

## Development and control of interactive reconfigurable robotic systems

Présentée le 29 octobre 2021

Faculté des sciences et techniques de l'ingénieur  
Laboratoire de robotique reconfigurable  
Programme doctoral en microsystemes et microélectronique

pour l'obtention du grade de Docteur ès Sciences

par

**Jian-Lin HUANG**

Acceptée sur proposition du jury

Prof. L. G. Villanueva Torrijo, président du jury  
Prof. J. Paik, directrice de thèse  
Prof. J. SEO, rapporteur  
Dr H. Hauser, rapporteur  
Prof. P. Reis, rapporteur









# Acknowledgments

It was a long and wonderful journey during my PhD study in Switzerland with many people's support and accompanied. First of all, I would like to express my earnest gratitude and appreciation to my supervisor Prof. Jamie Paik for providing me the chance to study at EPFL. Her continuous support and guidance motivate me to explore unique research topics and develop the perspectives and knowledge for formulating the shape of my PhD research.

I want to thank my thesis committee, Prof. Guillermo Villanueva, Prof. Pedro. M. Reis, Prof. Jungwon Seo, and Prof. Helmut Hauser for reviewing my work and providing insightful comments and suggestions.

I would like to thank all RRL members, especially Harshal, Zhenishbek, Matt, Chris, Sagar, Fred, Mete, Kevin. We are not only just like colleagues working together, but like good friends who share ideas, thoughts, and many pleasant moments while hangout, travel, or ski together. In addition, they always supported me while I was struggling with research problems and even career problems. I also want to thank our lab secretaries, Anouk, Carole, Joanna, Monica, and Julia, for the administrative support.

I am grateful to all my collaborators across diverse research fields. Especially Marius, Oleg, Thomas, Prof. Shea, Prof. Spolenak, Prof. Ermanni from ETHZ, and Prof. Concha from Adolfo Ibáñez University. The collaborative projects allow me to address the grand challenges with broader perspectives and fruitful discussions.

I would like to thank all my Taiwanese friends and Hongkongese friend in Switzerland, Shang-Jung, Kun-Han, Yi-Wen, Po-Jen, Henry, Chun Lam, Hsiang-Chu, Yen-Kai, and Gabriela. Without them, my PhD life may lose many colors. I will always remember the time that we had dinner, board games, hiking, climbing, and traveled together. I am thankful to my parents for always supporting my every decision and encouraging me to pursue my dreams. I am grateful to my sister for her support and for taking care of my parents while I am away for so many years.

Last but not least, I would like to thank my wife, Hsin-Tzu. She is always thoughtful of me and does whatever she can do to help me. Whether we can only talk on the phone because of the distance or live together every day, the time we spend together is the greatest treasure in my life.

*Lausanne, 29.09.2021*

*Jian-Lin*

# Abstract

Typical robotic applications are in tackling repetitive and precise tasks or for operating in hazardous environments; however, growing interests in bringing robots much closer to our everyday lives require a new generation of robotic systems. The new challenges demand robots to be reactive and adaptive in unconstructed environments and for dynamic human interactive applications. Future robotic systems then will not only be employed to function independently in factory cages; new forms of robotic systems will be proposed towards direct human interaction.

Reconfigurable robotic systems have emerged to address the many challenges of solving versatile tasks using their topological and functional reconfiguration. One of the most promising applications in reconfigurable robotic systems is a shape-changing interface, leveraging a user's perception and recognizing digital content and/or data rather than relying only on visual affordance for human-computer interaction. However, one of the critical obstacles is to make the interaction between human and reconfigurable robotic systems comprehensive and straightforward for end-users. In addition, the control and programming of robots require transferring abstract concepts, coordinates in space, or parameter definitions of various tasks using mathematics, physics, and computational skills. Furthermore, understanding how to generate suitable and efficient configurations for certain dynamic behaviors or tasks remains a barrier. Another critical challenge in the quest of creating seamless experiences in physical-virtual communication is developing compact hardware for the interactive system that enables multi-degree of freedom (DoF) actuation and multimodality input/output integration. In recent years, novel manufacturing technologies such as smart material-based actuators and additive manufacturing have offered opportunities for rapid, compact, and customizable design of multi-DoF robotic systems. However, much of the current research is still in its infancy and technology has limited capabilities for creating repeatable, reversible, and controllable motions.

While reconfigurable robots do provide a new and promising approach for interactive systems, the complexity of distributed actuation/sensing systems and coupled kinematics and desired functionalities bring fresh challenges and questions, both for control design and hardware development: *What design approaches enable direct human-robot interaction with morphological transformations and constraints of multi-DoF distributed activated systems? How can we implement controllable actuation toward complex ranges of motions and functionalities? How can we design multi-DoF robotic systems needed for operation in distinct real-world applications?* These problems and research questions formulate the objective and framework of my thesis. Namely, I explore methodologies for constructing reconfigurable interactive systems, including the hardware and control platform. I investigate control algorithms considering human-in-the-loop and evaluate the effectiveness of new integrated systems in different applications.

To address the above-mentioned challenges associated with the development of a reconfigurable robotic system for human interactions, I first outline the concept of an interactive interface between a human and a robot. I study design methods for intuitively and dynamically controlling multi-DoF reconfigurable systems and the algorithms required for integrating the mechanical characteristics of the core robotic components. Then, I investigate the design space and limitation of the gesture-based multi-modal interactions to further explore the controllability, scalability,

and versatility of functions for reconfigurable robotic systems. To realize the reconfigurable interactive robotic system, the design, capability, and limitations of the hardware system need to be established and evaluated. One of my research goals is to take advantage of the current non-conventional manufacturing technologies and materials and seek to overcome their limitations. Furthermore, I study and develop compact actuators and unique transmission mechanisms inspired by origami patterns, which can be integrated with multi-DoF robotic systems.

I start by designing, modeling, and validating experimentally the core functional components. Then, I investigate the fabrication process, which has additive manufactured structure and subtractive manufactured functional components integrated for compact, light-weight, and distributed activated mechanisms. Lastly, I propose strategies for configuring and controlling the functional components to achieve functionalities like multi-DoF distributed actuation, self-assembly, and tunable stiffness. Feasible functionalities are further examined in several application scenarios.

The main contributions of this thesis are:

- Development of an interactive control interface for reconfigurable robotic systems
- Design and validation of a distributed actuation solution and transmission mechanism for compact multi-DoF robotic systems
- Study of the synergy of additive manufacturing technique and smart materials to achieve customizable functionalities and for overcoming the limitations of conventional robotic systems

I believe that the control methods and hardware design investigated in this thesis bring a better understanding of interactive robotic systems and unleash potential for their future development.

# Résumé

Les applications robotiques classiques consistent à accomplir des tâches répétitives et précises ou à opérer dans des environnements dangereux. Toutefois, l'intérêt croissant pour un rapprochement des robots de notre vie quotidienne exige une nouvelle génération de systèmes robotiques. Ces nouveaux défis exigent des robots qu'ils soient réactifs et adaptables dans des environnements non construits et pour des applications dynamiques interactives avec l'homme. Les futurs systèmes robotiques ne seront donc pas seulement employés pour fonctionner de manière autonome dans des cages d'usine ; de nouvelles formes de systèmes robotiques seront proposées en vue d'une interaction humaine directe.

Les systèmes robotiques reconfigurables sont apparus pour relever les nombreux défis liés à la résolution de tâches polyvalentes grâce à leur reconfiguration topologique et fonctionnelle. L'une des applications les plus prometteuses des systèmes robotiques reconfigurables est une interface à changement de forme, qui tire parti de la perception de l'utilisateur et reconnaît le contenu et/ou les données numériques plutôt que de se fier uniquement à l'affordance visuelle pour l'interaction homme-machine. Toutefois, l'un des principaux obstacles consiste à rendre l'interaction entre l'homme et les systèmes robotiques reconfigurables complète et simple pour les utilisateurs finaux. En outre, le contrôle et la programmation des robots nécessitent le transfert de concepts abstraits, de coordonnées dans l'espace ou de définitions de paramètres de diverses tâches à l'aide de compétences en mathématiques, en physique et en informatique. En outre, comprendre comment générer des configurations adaptées et efficaces pour certains comportements ou tâches dynamiques reste un obstacle. Un autre défi crucial dans la quête de la création d'expériences transparentes dans la communication physique-virtuelle est le développement d'un matériel compact pour le système interactif qui permet l'actionnement à plusieurs degrés de liberté (DoF) et l'intégration d'entrées/sorties multimodales. Ces dernières années, de nouvelles technologies de fabrication, telles que les actionneurs à base de matériaux intelligents et la fabrication additive, ont offert des possibilités de conception rapide, compacte et personnalisable de systèmes robotiques à plusieurs degrés de liberté. Cependant, une grande partie de la recherche actuelle en est encore à ses débuts et la technologie a des capacités limitées pour créer des mouvements répétables, réversibles et contrôlables.

Si les robots reconfigurables constituent une approche nouvelle et prometteuse pour les systèmes interactifs, la complexité des systèmes d'actionnement et de détection distribués, la cinématique couplée aux fonctionnalités souhaitées posent de nouveaux défis et de nouvelles questions, tant pour la conception des commandes que pour le développement du matériel : *Quelles approches de conception permettent une interaction directe entre l'homme et le robot avec les transformations morphologiques et les contraintes des systèmes d'activation distribués multi-DoF ? Comment pouvons-nous mettre en œuvre une action contrôlable pour des gammes complexes de mouvements et de fonctionnalités ? Comment pouvons-nous concevoir des systèmes robotiques multi-DoF nécessaires pour fonctionner dans des applications distinctes du monde réel ?* Ces problèmes et questions de recherche constituent l'objectif et le cadre de ma thèse. Plus

précisément, j'explore les méthodologies de construction de systèmes interactifs reconfigurables, y compris le matériel et la plate-forme de contrôle. J'étudie les algorithmes de contrôle en tenant compte de la présence humaine dans la boucle et j'évalue l'efficacité des nouveaux systèmes intégrés dans différentes applications.

Pour relever les défis susmentionnés associés au développement d'un système robotique reconfigurable pour les interactions humaines, je présente d'abord le concept d'interface interactive entre un humain et un robot. J'étudie les méthodes de conception pour le contrôle intuitif et dynamique des systèmes reconfigurables multi-DoF et les algorithmes nécessaires pour intégrer les caractéristiques mécaniques des composants robotiques de base. Ensuite, j'étudie l'espace de conception et les limites des interactions multimodales basées sur les gestes afin d'explorer davantage la contrôlabilité, l'évolutivité et la polyvalence des fonctions des systèmes robotiques reconfigurables. Pour réaliser le système robotique interactif reconfigurable, la conception, la capacité et les limites du système matériel doivent être établies et évaluées. L'un de mes objectifs de recherche est de tirer parti des technologies et des matériaux de fabrication non conventionnels actuels et de chercher à surmonter leurs limites. En outre, j'étudie et développe des actionneurs compacts et des mécanismes de transmission uniques inspirés des motifs d'origami, qui peuvent être intégrés à des systèmes robotiques multi-DoF.

Je commence par concevoir, modéliser et valider expérimentalement les principaux composants fonctionnels. Ensuite, j'étudie le processus de fabrication, qui intègre une structure de fabrication additive et des composants fonctionnels de fabrication soustractive pour obtenir des mécanismes activés compacts, légers et distribués. Enfin, je propose des stratégies pour configurer et contrôler les composants fonctionnels afin d'obtenir des fonctionnalités telles que l'actionnement distribué multi-DoF, l'auto-assemblage et la rigidité réglable. Les fonctionnalités réalisables sont ensuite examinées dans plusieurs scénarios d'application.

Les principales contributions de cette thèse sont :

- Développement d'une interface de commande interactive pour les systèmes robotiques reconfigurables
- Conception et validation d'une solution d'actionnement distribué et d'un mécanisme de transmission pour les systèmes robotiques compacts multi-DoF.
- Étude de la synergie de la technique de fabrication additive et des matériaux intelligents pour obtenir des fonctionnalités personnalisables et pour surmonter les limites des systèmes robotiques conventionnels.

Je pense que les méthodes de contrôle et la conception matérielle étudiées dans cette thèse apportent une meilleure compréhension des systèmes robotiques interactifs et libèrent un potentiel pour leur développement futur.

# Content

Abstract .....	v
Résumé .....	viii
Content. ....	x
List of Figures .....	xii
List of Tables .....	xvii
<b>CHAPTER 0 Introduction.....</b>	<b>19</b>
<b>CHAPTER 1 Control and evaluation of Interactive reconfigurable system ..</b>	<b>28</b>
1.1 Interactive interface design for multi-DoF robotic systems.....	28
1.1.1 An overview of multi-DoF origami robot design and control .....	28
1.1.2 The concept for interactive control interface .....	31
1.1.3 Origami-based tangible interface for 3D model reconstruction .....	32
1.1.4 Gesture-based interface for controlling origami robots in a virtual environment .....	37
1.1.5 Experimental validation of interactive interface .....	43
1.1.6 Conclusion.....	50
1.2 An interactive control interface for reconfigurable modular robots .....	51
1.2.1 An overview of reconfigurable modular robot control overview .....	51
1.2.2 Interactive UI design for modular robots.....	54
1.2.3 Implementation and experiment .....	60
1.2.4 Conclusion.....	64
1.3 Interaction design and validation for a wearable haptic feedback device.....	64
1.3.1 An overview of soft wearable devices for haptic feedback .....	64
1.3.2 Wearable soft interactive interface design.....	65
1.3.3 Experimental evaluation and protocol design .....	67
1.3.4 Results and discussion.....	69
1.3.5 Conclusion.....	72
<b>CHAPTER 2 Multi-DoF reconfigurable structures' hardware                   developement .....</b>	<b>75</b>
2.1 Hardware design for multi-DoF reconfigurable robot .....	75
2.1.1 An overview of Actuation for multi-DoF robotic systems .....	75
2.1.2 Low-profile actuator development .....	77
2.1.3 Low-profile functional layer development.....	86
2.2 Flexural hinge design and characterization.....	88

2.2.1	An overview of additive manufactured hinges.....	88
2.2.2	Hinge material, design, and fabrication .....	89
2.2.3	Experimental characterization .....	90
2.2.4	Results, discussion, and design guidelines .....	95
2.3	Integration of active components and additive manufactured flexure hinge .....	101
2.3.1	Characterization of SMA torsional actuators embedded with flexure hinge.....	101
2.3.2	Development of actuated reconfigurable mechanisms.....	103
2.3.3	Prototyping and characterization.....	108
2.3.4	Conclusion.....	112
<b>CHAPTER 3 The design and demonstration of multi-DoF reconfigurable systems for customizable functionalities .....</b>		<b>113</b>
3.1	The multi-function enhancement of 4D printed 3DoF origami module .....	113
3.1.1	An overview of 4D printed structures and mechanisms .....	113
3.1.2	Design of multi-functional 4D printed origami module.....	114
3.1.3	Characterization and function validation of 4D printed origami module .....	117
3.1.4	Conclusion.....	124
3.2	A 4D printed active compliant hinge for space applications .....	125
3.2.1	An overview of 4D printed active hinge for space applications.....	125
3.2.2	Case study and function evaluation .....	126
3.2.3	Experimental validation.....	133
3.2.4	Results and discussion.....	136
3.3	Multi-agent control for reconfigurable power harvesting modules .....	139
3.3.1	Power harvest module and water management overview .....	140
3.3.2	Reconfigurable power module (RoPoM) design .....	140
3.3.3	Results and discussion.....	145
3.3.4	Conclusion.....	147
<b>CHAPTER 4 Conclusion and future directions.....</b>		<b>148</b>
4.1	Conclusion .....	148
4.2	Future research directions .....	150
References .....		151
Curriculum Vitae .....		165

# List of Figures

## CHAPTER 0

Figure 0. 1 Overview of the interactive reconfigurable robots and their contribution to the thesis.....	23
---	----

## CHAPTER 1

Figure 1.1 The schematic of origami robot-based interactive system .....	31
Figure 1.2 System overview of the two interaction modes .....	32
Figure 1.3 Kinematics of the origami tangible interface .....	34
Figure 1.4 The 3D model of the origami generated in LabVIEW .....	36
Figure 1.5 The architecture of physical objects for constructing a virtual environment in Unity.....	39
Figure 1.6 The flowchart of an approximate virtual rendering algorithm.....	40
Figure 1.7 Local interaction model for simulating the manipulation of robotic origami in a virtual environment.....	41
Figure 1.8 The flowchart of the algorithm for converting continuous folding motions to discrete folding sequences.....	42
Figure 1.9 Construction of two prototypes .....	45
Figure 1.10 The experimental setup and results of a single hinge of the tangible interface.....	45
Figure 1.11 Comparison between physical folding and the 3D model reconstruction. ....	46
Figure 1.12 The comparison of actual folding behavior of the origami robot with its real-time 3D image generated by virtual model reconstruction software .....	46
Figure 1.13 Experimental results of closed-loop control of robotic origami .....	47
Figure 1.14 Experimental results of the algorithm for conversion between digital data of manipulation and of control command.....	49
Figure 1.15 Experimental results of teaching a robot by demonstration in a virtual environment.....	50
Figure 1.16 The modeling with different geometries and hardware .....	50
Figure 1.17 A novel user interface designed for controlling reconfigurable modular robots can achieve the main features .....	54
Figure 1.18 Concept of control complexity in a human- multi-robot system[104].....	55
Figure 1.19 The proposed control methods for reconfigurable modular robots using hand gestures as input shown in virtual environment.....	56
Figure 1.20 The modular origami robot porotype, Mori.....	57
Figure 1.21 The proposed hand gestures for manipulating virtual model of reconfigurable robotic system.....	58



Figure 1.22 The sequences of selection and manipulation of the modules (left figure) and their corresponding rooted tree .....	59
Figure 1.23 The control parameters of (a) mode 1, (b) mode 2 (c) human-robot interaction mode for controlling three DoF platform .....	60
Figure 1.24 The system schematics of the proposed UI for controlling Mori .....	61
Figure 1.25 The experimental results of controlling Mori by mode 1 .....	62
Figure 1.26 The experimental results of using palm orientations to control motion of Mori .....	62
Figure 1.27 The mixed-reality implementation and multi-inputs for controlling modular robotic system .....	63
Figure 1.28 Wearable soft interactive interface .....	67
Figure 1.29 Experimental setup for interactive shape generation using SPA-skin and a playdough as a test object .....	69
Figure 1.30 Results of the shape reconstruction experiments .....	71
Figure 1.31 Image processing for shape creation accuracy calculation .....	71
Figure 1.32 Evaluation of capability and effectiveness of wearable haptic interfaces for virtual reality applications .....	73

## CHAPTER 2

Figure 2.1 Actuators for origami structures .....	77
Figure 2.2 The schematic of $\Omega$ -SMA torsional actuator .....	78
Figure 2.3 SMA characterization setup .....	80
Figure 2.4 Bending stiffness of SMA torsional actuator at full martensite .....	81
Figure 2.5 The maximum torque output with SMA torsional actuators .....	82
Figure 2.6 Maximum output of circular torsional SMA actuator with 0.345 mm <sup>-1</sup> curvature .....	83
Figure 2.7 Design and fabrication of self-heating torsional SMA actuators .....	84
Figure 2.8 Design parameter of SMA spring .....	85
Figure 2.9 Force output of SMA spring at austenite phase in the loading direction. ....	85
Figure 2.10 Force-deflection characterization of SMA spring at martensite state at loading direction .....	86
Figure 2.11 Fabrication process of SMP with customized heater attached .....	87
Figure 2.12 Bending stiffness of SMP at glass state .....	87
Figure 2.13 Laser engraved copper-Kapton flexible circuit and heaters .....	87
Figure 2.14 Investigated hinge classes, processes and design parameters .....	90
Figure 2.15 The custom-built setup used for characterization of the flexural properties .....	91
Figure 2.16 Mechanical properties of the different hinge classes .....	94
Figure 2.17 Property map comparing ULL and LFW of the different hinge classes .....	96
Figure 2.18 The prototypes for measuring torque output for SMA torsional actuators with different hinge gaps .....	102
Figure 2.19 Circular SMA actuator with different diameters and hinge gaps. D: Diameter of circular SMA, G: Hinge gap .....	102

## List of Figures

---

Figure 2.20 3D printed active hinge with actuator and heaters embedded .....	103
Figure 2.21 Torque output and torsional stiffness of the 3D printed active hinge .....	103
Figure 2.22 Water-bomb based origami joint and equivalent kinematic chain .....	105
Figure 2.23 Two range of motion due to different bistable states .....	105
Figure 2.24 Actuators for control the origami joints in two bistable states .....	105
Figure 2.25 Schematics of the crease pattern .....	106
Figure 2.26 Interpolated curve for mountain and valley folding angles .....	106
Figure 2.27 Potential energy of origami structure.....	107
Figure 2.28 Schematic of two different bistable states .....	108
Figure 2.29 Schematics for the design of functional layers.....	109
Figure 2.30 Characterization setup.....	109
Figure 2.31 Torsional stiffness measurement .....	110
Figure 2.32 Comparison between theoretical and experimental energy values.....	111
Figure 2.33 End-effector torque generated by the two torsional SMA actuators. ....	112

## CHAPTER 3

Figure 3.1 Design of 3 DoF origami module .....	115
Figure 3.2 Geometrical relationships of the equivalent spherical joint, adapted from[183] .....	116
Figure 3.3 Design of self-assembly origami module.....	117
Figure 3.4 Self-folding sequence .....	117
Figure 3.5 3-DoF force-displacement characterization setup .....	118
Figure 3.6 Axial stiffness measurements.....	119
Figure 3.7 Modeling results of linear axial stiffness.....	119
Figure 3.8 Lateral stiffness measurement .....	120
Figure 3.9 Lateral stiffness measurement with selectively activated SMPs .....	120
Figure 3.10 External load effect on the range of motion while selectively activating SMPs. ....	121
Figure 3.11 Reversibility of origami module by natural recovery .....	121
Figure 3.12 Reversibility of origami module by antagonistic actuation .....	122
Figure 3.13 Schematic of setup for closed-loop control experiments .....	122
Figure 3.14 Control results for closed loop with step input .....	123
Figure 3.15 Dual actuation experiments .....	123
Figure 3.16 The bending angle of origami module with different power input .....	124
Figure 3.17 Integration with a suction cup gripper.....	125
Figure 3.18 CubeSat hinge case study .....	127
Figure 3.19 Orientation of the satellite $\vartheta$ and of its panels $\alpha$ with respect to the incoming solar flux $\Phi$ .....	128
Figure 3.20 Schematic representation of the actuation strategies .....	129
Figure 3.21 Orientation of the satellite .....	131
Figure 3.22 (a) Demonstrator of the active compliant hinge, (b) exploded view of the active compliant hinge. ....	132
Figure 3.23 The schematics of the experimental setup .....	133

Figure 3.24 SMA spring force output with different power input and maximum force of 1.44 W for normalization .....	134
Figure 3.25 Heating/cooling cycle test of SMP .....	135
Figure 3.26 Deployment from the stowed configuration. ....	137
Figure 3.27 Bending and locking test of the active hinge .....	137
Figure 3.28 The schematics of the reconfigurable power module, which consists of two main components.....	141
Figure 3.29 The schematics of deployable origami floating structure .....	142
Figure 3.30 Folding pattern for origami module.....	142
Figure 3.31 The schematic of the top platform (a), and (b) the drawing of the platform. ....	143
Figure 3.32 The schematics of modular pneumatic actuators .....	143



# List of Tables

Table 1.1 The visual rendering and transformation between digital information and  
physical components ..... 42

Table 2.1 The radius of torsional SMA actuators and hinge material for each sample .....103

Table 3.1 Energy gained by proposed actuation strategies .....138

Table 3.2 Energy collected, energy consumed, net energy gain, and allowable actuation time  
for the considered actuation strategies .....138



# Introduction

Robots have been widely utilized in the manufacturing industry for the past few decades since they are greatly able to execute tasks precisely and rapidly, saving time and reducing costs. Conventional robots have been designed to conform with predefined tasks, both in software and hardware, for optimal performance. However, their adaptability to an undefined environment or unexpended circumstances is limited due to their fixed physical morphologies. Although this low flexibility and adaptability could be partially mitigated by adaptive control systems, safety and robustness remain questionable for many applications—primarily those related to direct human interactions. Thus, robots operate independently from humans in most typical applications. Modern robot design aims to resolve these limitations and progress toward a closer approximation to every human life, rather than just factory service. Robots can serve as coworkers, executing tasks with humans and wearable devices in power amplification or rehabilitation applications. These applications entail additional requirements for robots. Robots in these projects should provide better interactivity with humans and external environments, able to react causally to unstructured conditions or complex behaviors. These needs also bring new technical challenges to the next generation of robots, motivating new manufacturing, materials, and control methods.

For better interactivity and adaptability to external environments, new design paradigms have been proposed for robots. One promising approach is soft robots, which feature components and structures comprised of compliant materials. With the introduction of new functional materials and designs inspired by nature, soft robots offer unconventional approaches to overcome physical limitations. Soft robots' intrinsic compliance enables more adaptable, resilient, and safe interactions with humans and environments. Many conventional robots have highly stiff structures, motors, and relatively complex transmission mechanisms to achieve multiple degrees of freedom (DoFs) motions. In contrast, soft robots' bodies and joints usually comprise compliant materials, such as rubber, polymer, or other flexible materials. This composition allows soft robots to have continuum-deformable bodies, leading to higher DoFs, better conformity with external environments, better system stability by absorbing extra energy, and lower control effort to interact safely with humans [1]. Soft actuation design also benefits from the development of new materials and fabrication technology. Soft pneumatic actuators (SPAs) are among the mainstream soft robotic systems, with bodies mainly comprising elastic materials featuring hollow chambers or embedded porous material. Motion is generated via pressurized air input or vacuum-induced mechanical buckling. Controllable motion can be achieved by adding constraints or adjusting the stiffness of certain parts of the structure since deformations start at a lower stiffness. Various approaches—such as shell or fiber reinforcement, asymmetric chamber design and structural geometry, and stiffening materials—have been presented to create different forms of motions. Soft robotic systems' flexibility, robustness, and adaptability promise rich potential in diverse applications, such as soft manipulators in industry, wearable robotics in rehabilitation, performance augmentation, and virtual reality enhancement.

Soft robots reactively adapt to external environments with less controllable DoFs. However, the limited controllable DoFs have entailed some drawbacks in addressing real-world problems requiring complex and multi-DoF motions. On the other hand, an alternative solution, reconfigurable robots, providing multiple controllable and distributed DoFs, has been proposed allows excellent proactive adaptability to environments and various tasks. Conventional robots usually have fixed morphologies designed to perform desired tasks. In contrast, reconfigurable robots' fundamental concepts can reform their morphologies or functionalities to accommodate target tasks' requirements. This morphological reconfiguration can be conducted by (self-reconfigurable) robots themselves or external stimuli. Modular robotics is among the most significant research fields for self-reconfigurable robotics. It enables the reconfiguration of morphologies and functionalities by connecting or disconnecting and assembling self-contained robotic units. Changeable morphologies suggest a promising concept for versatile, highly flexible robotic solutions [2]–[4].

Origami robots have emerged as another example of reconfigurable robotic fields, in which robots can reconfigure from two-dimensional design (2D) to three-dimensional (3D) functional structures by folding. Complex motions could be achieved by combining a series of folding mechanisms with distributed actuators embedded in or on folding hinges. Since a relatively low thickness is required for folding designs, smart materials—such as shape memory alloys (SMAs)[5]–[9], shape memory polymers (SMPs)[10]–[13], electroactive polymers (EAP)[14]–[16], and piezoelectric (PZT) materials [17], [18] have been widely applied to develop origami robots and reconfigurable robots. Their excellent compatibility with both additive and subtractive manufacturing processes provides tremendous potential to create miniaturized mechanisms, which may be a significant challenge for conventional electromagnetic motors. However, smart-material-based interactive systems are still in an inception phase, and many recent studies have limited their capabilities to creating repeatable, reversible, and controllable motions. The control of smart-materials-driven robotic systems presents a significant challenge to the field. This control difficulty has arisen due to the materials' non-linear mechanical properties, and their reactive behaviors could also vary with external factors, such as load and temperature. Furthermore, their manufacturing process and integration with structural materials also have an unignorable impact on built mechanisms' performance. The same influence applies to integrated robotic systems; few attempts have sought to validate models experimentally using physical devices, and this lack of implementation with robotic components has hindered the comprehensive understanding of origami-inspired systems' behaviors.

One promising application for reconfigurable robotic systems is shape-changing interfaces that leverage users' perception and recognize digital content or data, rather than only relying on visual affordances for human-computer interaction (HCI). Shape-changing interfaces can change their physical shapes to support either the input or output of digital information, and they have become a significant preoccupation among the HCI community. Shape-changing serve several primary purposes: (a) hedonic aims, such as kinetic sculptures, (b) explorative or simulation tools for materials and objects, (c) functional aims, such as haptic and tangible feedback to communicate information; and (d) toolkits for programming shapes [19], [20]. To simultaneously recreate a realistic and immersive interaction with digital information, multi-modal sensations or actuation systems must be developed and integrated. Nonetheless, many developed shape-changing interfaces have limited controllable DoFs, workspaces, resolutions, and dimensionalities. Thus,



scalable and generalizable designs of shape-changing interfaces to accommodate different user behaviors and provide various visual or tactile experiences are even more challenging [21].

While the systems' complexity has arisen due to high DoFs, coupled with kinematics and distributed actuation systems, considerable efforts have sought to study the generation of suitable configurations, motion control, and high-level task planning. Still, the control and programming of multi-DoF reconfigurable robots are difficult and time-consuming when bringing control interfaces directly to end-users. Furthermore, many studies have focused on modeling to generate and simulate the morphological transformation of multi-DoF distributed activated systems, but fewer studies have focused on evaluating physical prototypes. Moreover, quantifiable evaluation methods for human-in-the-loop, interactive control systems are challenging to define and develop since a shared standard is lacking across different devices. Therefore, many studies have relied on user studies, which usually qualify results using questionnaires. However, comparing performance among interactive control systems could be questionable and difficult if relying on quantification alone, without measurable characteristics.

## Problem statement

Over the past two decades, multi-DoF reconfigurable robots have shown great potential for applications involving direct human interactions with the introduction of new materials and manufacturing technologies. Nevertheless, building interactive, reconfigurable robotic systems remains challenging since the integration of multidisciplinary knowledge—including material science, mechatronic engineering, graphical computation, and user experience design—is significantly required. Although roboticists might have excellent knowledge of constructing and controlling physical robotic systems, knowledge of designing, creating, and evaluating interactions might be inadequate. Interaction developments and research has focused on well-established robots, rather than the new generation of robots for human-robot interaction in society. Because the new, materials-based robots are still in their infancy, the challenges of controlling and characterizing their behavior have prevented these functional, material-composed robots from serving as suitable platforms for human-robot interaction research[22]–[24].

Similarly, current HCI researchers face several technological limitations: (a) design concepts are more user-centered and specific to a uni-function, (b) the manufacture of miniaturized, distributed actuation for high-resolution interactions presents challenges, (c) a comprehensive understanding of multi-DoF actuated systems' properties and behaviors, as well as their composite materials, remains elusive[20], [25], [26]. Many recent HCI studies have focused on implementing novel materials and manufacturing technologies to create interactive devices and experiences with relatively simple electronics and design mechanisms. Their primary purposes are usually to present new technologies' applicability to interactive design rather than extensive studies examining integrated interactive systems' capabilities.

My thesis seeks to fill these research gaps by answering the following research questions.

***What design approaches enable direct human-robot interaction with the morphological transformations and constraints of multi-DoF distributed activated systems?***

Multi-DoF distributed activated systems' shape-changing behavior can be complex and difficult to understand. Since substantial works have modeled multi-DoF systems, such as origami folding models, can a further step be taken to simulate and understand actuated multi-DoFs, based on prior knowledge? That is, is the creation of a comprehensive interface that enables humans to interact with multi-DoF distributed activated systems possible?

***How can the controllable actuation of complex ranges of motions and functionalities be implemented?***

Since mesoscale actuators could be achieved through the introduction of novel functional materials, we would like to investigate whether the controllable actuation of complex ranges of motions and functionalities can be implemented. Challenges stem from all the factors involved in this question—including a comprehensive understanding of functional materials' characteristics, manufacturing process, installation, and integration approaches—and these factors are cross-linked together for consequential behaviors. Thus, characterization protocols and platforms must be established for multi-DoF actuation. Models that consider not only mechanisms' kinematics but also functional materials' behaviors should also be studied to enable a better understanding of how to control multi-DoF mechanisms.

***How can the multi-DoF robotic systems be needed to operate in distinct, real-world applications be designed?***

Reconfigurable multi-DoF systems with morphological adaptivity benefit by increasing the achievable functions. However, this benefit increases their complexity in terms of design, control, and fabrications. Thus, a balance between satisfactory functionalities and the removal of unnecessary complexity from systems much be achieved. Also, challenges could vary among different systems and applications for different scales and environments. We would like to investigate the design of multi-DoF robotic systems that can operate in distinct, real-world applications.

## Thesis statement and structure

My thesis aims to extend the understanding of design, control, and interaction with multi-DoF reconfigurable systems, based on recent progress in manufacturing technologies, functional materials, and HCI design. Motivated by the substantial movement that origami folding can accomplish—as well as its potential to create miniaturized, actuated interactive structures—we use origami-inspired structures as a platform to begin the study of multi-DoF systems' morphological transformation. We propose interactive graphical interfaces with the origami platform to both simulate and control multi-DoF systems. To experimentally validate the proposed platform, simulation, and control algorithms, we adopt cutting-edge manufacturing technologies for creating physical prototypes. Additionally, we systematically study the characterization process from the component level to the performance of integrated active structures. With the proposed platform, we can further estimate human-robot interaction systems' effectiveness. Finally, we examine

multi-DoF reconfigurable systems' scalability and capability with several existing, real-world challenges as shown in Figure 0.1. The main contributions of my thesis are:

- The development of interactive interfaces to intuitively and dynamically control multi-DoF reconfigurable systems and algorithms, integrating the core robotic components' mechanical characteristics
- The experimental validation of interaction design and evaluation protocol development, considering human-in-the-loop to study interactive reconfigurable robotics systems' effectiveness and capabilities
- The design, fabrication, and demonstration of multi-DoF actuated reconfigurable systems for customizable functionalities in various applications

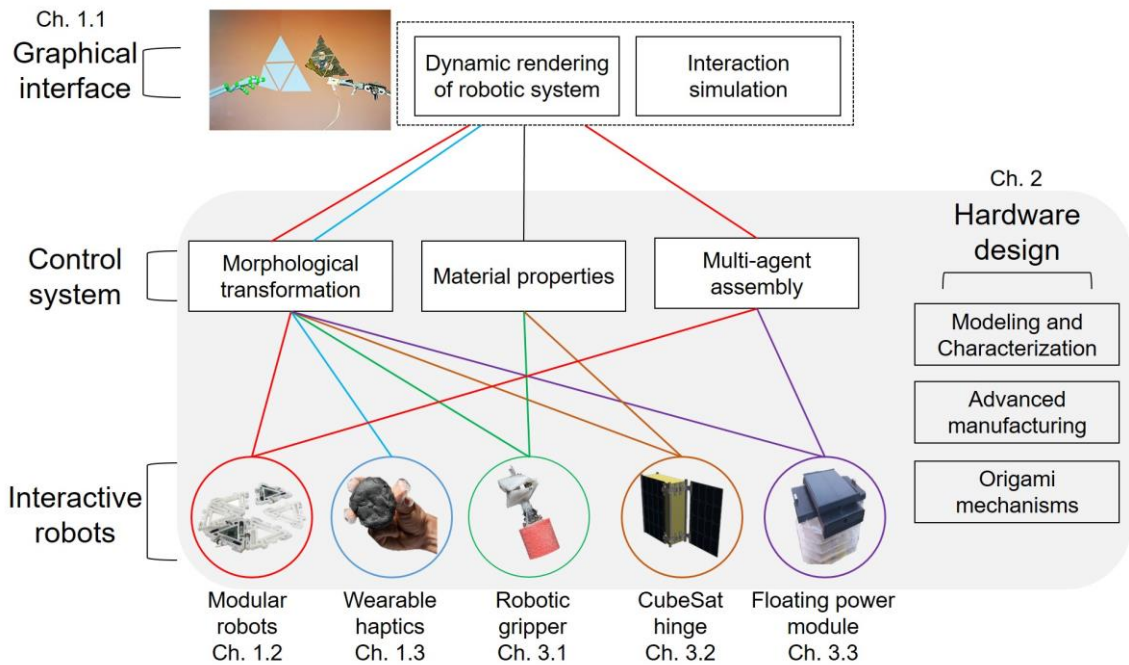


**Figure 0. 1 Overview of the interactive reconfigurable robots and their contributions to the thesis.** The graphical interface for simulating the behavior of robots and interaction with humans was integrated with the control system for achieving the three functionalities of reconfigurable robots. For attaining the desired functionalities, hardware design considering the factor that including material properties, manufacturing process, and mechanisms has been discussed in chapter 2. Finally, we examined the capabilities of the proposed control system, interface, and hardware design on developing new robots (Ch. 3.1, 3.2, 3.3) or developed robotic platforms (Ch. 1.2, 1.3, 3.1).

## Thesis outline

### Chapter 1. Control and evaluation of interactive reconfigurable systems

Motivated by interactive user interfaces' effectiveness and intuitiveness, we introduce a design concept for interactions with reconfigurable robots. We present the development of algorithms integrating essential robotic components, such as sensors and actuators, to adapt to different hardware. For our interface design, we developed multiple control modes to further enhance

reconfigurable robotic systems' controllability. We demonstrate the design concept's applicability with three different robotic systems.

### 1.1. Interactive interface design for bi-directional communication between virtual and physical environments

In the first part of this chapter, we present a physics-based, interactive modeling control interface to explore reconfigurable robots' design space using origami robots as a platform. We developed two interactive modes as proofs of concept for a bi-directional communication interface between virtual and physical environments. The first interaction mode is origami-inspired, foldable surfaces with distributed sensors that can recreate folding sequences and shape transformations in a virtual environment via a hardware-in-loop simulation. This mode's complementary digital transcription lays the foundation for a robotic origami design tool that visually represents various design formulations, as well as an intuitive controller for robotic origami. In the second interaction mode, we construct a physics-based modeling interface for the intuitive user manipulation of robotic origami in a virtual environment. Algorithms for graphical representation and command transformation are also developed for robotic interaction.

- The development of an interface provides intuitive control methodologies that can adapt to different hardware designs
- Algorithm for rapid 3D model reconstruction by solving kinematics of origami structures embedding distributed sensors
- Demonstration of two-way communication interaction for human-robot interface

### 1.2. An interactive control interface for reconfigurable modular robots

In the second part of Chapter 1, we propose a gesture-based, interactive user interface to control configurable modular robotic systems using hand gestures with visual feedback. We achieve this interface with a 3D real-time simulation of the manipulation on a graphical interface. Moreover, we develop gesture sets and interactive control methods to achieve scalable controllability and the main functionalities of a reconfigurable modular robotic system. We also develop algorithms for visual representation and control command transformation that adapt to different hardware components' characteristics. With the hardware platform Modular origami robots, MORI, a modular origami robot, we demonstrate the capabilities of this novel interactive user interface. Finally, we validate the user interface's effectiveness experimentally and explore its capability of integrating multi-modalities for human-robot interaction applications.

- The development of a control interface to intuitively and dynamically control a multiple-DoF modular robotic system in real-time
- The design of suitable gesture sets and interaction strategies to address functions' modularity, reconfigurability, and versatility in a modular robotic system
- An experimental validation of the interaction design on a robotic platform

### 1.3. Interaction design and validation for a wearable haptic feedback device

In the third part of the first chapter, we design a comprehensive and coherent tactile information transfer system and an experimental protocol to validate tactile feedback. Our approach utilizes a novel soft interactive interface linked to a soft, malleable object. The controlled feedback can generate texture and auxiliary tactile responses through actuation frequencies proportional to the distance from the target shape, thereby guiding users toward the intended shape. Then, an association with a moldable test object (Modeling clay) confirms, through its plastic deformation, the user's applied actuation forces in response to the sensed feedback from the active interface. Together, this unique experimental setup and protocol produce tangible tactile feedback, instantly validating the cogency of the user's experience in three different modes of tactile actuation: texture, size, and shape.

- The design of a comprehensive, coherent tactile information transfer system and an experimental protocol to validate tactile feedback for a human-in-the-loop system
- A testbed to reconstruct a virtual 2D shape using guided, multi-frequency tactile feedback and active finger tracking

## **Chapter 2. Multi-DoF reconfigurable structures' hardware development**

Thanks to the advance in manufacturing technologies and the development of functional materials, compact actuation design can be realized. In this chapter, we comprehensively study origami-inspired reconfigurable structures from the core-component level to the overall mechanisms' designs. We start by introducing the design, model, and experimental validation of origami's core functional components. Then, we conduct parametric studies of folding hinges since they dictate origami structures' overall performance. Finally, we design an origami mechanism with reconfigurable functionalities.

### **2.1. Low-profile functional components developments**

In the first part of Chapter 2, we develop low-profile actuators and functional components embedded and integrated into 2D origami design. To integrate the additive manufacturing process, our functional component design must avoid collisions with an extruder and ensure minimal interference with the subsequent printing layers. We design flat torsional SMA actuators that can be laser-cut from a nitinol sheet, as well as an alternative design for heater-free and minimal-effort assembly. We model and experimentally validate the proposed design's performance.

- The design, model, and characterization of integrable actuators for multi-DoF reconfigurable structures
- A controller design and validation of the actuators' performance

### **2.2. Flexural hinge design and characterization**

In the second part of this chapter, we focus on testing and characterizing flexural hinges' mechanical properties so that our findings can immediately apply to 3D printed origami structures. We introduce an aramid-fiber composite hinge and compare it with a single-material polyamide hinge and a multi-material photopolymer hinge. Next, we investigate the impact of the materials

and the geometric design parameters on the hinge's load-carrying capability and flexural properties. Furthermore, the hinge's fatigue behavior is characterized, identifying its constitutive mechanisms.

- A comparison of additively manufactured flexural hinges made from different materials and an investigation of the design parameters' dependence on load-carrying capability and flexural properties, respectively
- Guidelines for material and design parameter selections to meet the mechanical properties required in hinge design

### 2.3 Development of actuated reconfigurable mechanisms

In the third part of Chapter 2, we quantitatively study the bistable behavior of a six-bar kinematic chain origami prototype, based on the waterbomb pattern, by conducting a geometric and potential energy analysis of the pattern and its stable positions. We develop a kinematic model to describe the behavior of the joint and suitable actuators that generate the desired motions. Secondly, an SMA-actuated solution is proposed to change between our structure's two stable states and control its end-effector position. The lightweight, SMA-actuated, bistable, two-mode-stiffness origami joint with a high workspace can rapidly change between its two stiffness modes and serve as a reconfigurable mechanism in robotic applications.

- The design and integration of an actuation system for waterbomb-based, spherical origami joints
- The adoption of various bistable states to adjust the joints' stiffness and the mechanism's workspace

## Chapter 3. The design and demonstration of multi-DoF reconfigurable systems for customizable functionalities

In this chapter, we demonstrate the design capabilities of reconfigurable robotic systems for additive manufactured structures across various applications. Additive manufactured active structures' major challenges, and limitations are generating controllable, reversible, distributed actuation, load-carrying abilities, and additional functionality other than shape morphing. To overcome these limitations, we investigate the fabrication process, which has an additive manufactured structure with subtractive manufactured embeddable functional components. We also propose a strategy to configure functional components in order to achieve desired functionalities, such as self-assembly, manipulation, load-carrying, and variable stiffness. Finally, we present how we implement these functionalities across applications on different scales.

### 3.1. The multi-function enhancement of a 4D printed 3DoF origami module

In the first part of Chapter 3, we aim to investigate a strategy for how to implement additional functionalities for a known multi-DoF mechanism, overcoming the limitations of conventional manufactured structures. We choose a 3DoF origami-inspired parallel mechanism to study its behavior. This robotic origami mechanism has been proposed for robotic arms and graspers in

medical applications with SMA actuators or tendon-driven systems. However, its challenges vis-à-vis module assembly, actuator integration, and ability to withstand external loading persisted. Therefore, we propose a strategy that suggests the synergy of additive manufacturing origami structures and low-profile functional materials. The study of the configuration of functional components and control schemes provides a cue for the functional enhancement of integrated multi-DoF reconfigurable systems.

- The design of a self-assembly 3DoF origami module that can be fabricated in full 2D and as a self-folding active functional structure through selectively distributed actuation
- A study of the proposed origami module's compliance and performance with different configurations of functional components and activation strategies

### **3.2. A 4D printed active compliant hinge for space applications**

In the second part of this chapter, we present a concept for a 3D printed, active compliant hinge with variable stiffnesses suitable for deployment, as well as the reorientation of satellite appendices. The concept has no moving parts, so it requires no lubrication and prevents shocks, allowing for smooth and controlled movements. The hinge's deployment and reorientation are achieved by exploiting thermally induced variations in stiffness for one of the constituting materials and using two antagonistic SMA springs as actuators.

- The development of an active compliant hinge with selectively variable stiffnesses for deployment, as well as appendages suggesting space applications
- An experimental validation of the hinge concept's feasibility, showing the hinge's ability to fulfill stowing requirements and proposed actuation strategies

### **3.3. Multi-agent control for reconfigurable power harvesting modules**

In dry regions, water resources' efficient use is critical for survival, and it plays an important economic role. One major problem of water storage and distribution in countries with very high radiation indexes is that much water is lost due to evaporation from artificial and natural reservoirs. To reduce water evaporation while harvesting solar energy for efficient and sustainable energy management in dry areas, in this part of Chapter 3, we develop a modular floating photovoltaic power system that can self-reconfigure, forming a 2D surface to cover reservoirs with arbitrary geometries. In this project, we propose to build a reconfigurable power module (RoPoM) that is reconfigurable by two folds: surface-wise reconfiguration via magnetic interactions and soft actuation. The module forms a reconfigurable surface that minimizes water evaporation from reservoirs while harvesting solar energy. This modular system can be self-sustainable and self-reconfigurable to any arbitrary geometry. With this research, we also demonstrate a novel approach to achieving scalable, efficient, and controllable self-assembly.

## **Chapter 4. Conclusion**

In this chapter, we summarize how we have addressed the stated research questions through the proposed approaches in my thesis. A discussion section addresses future research directions.

# Control and evaluation of Interactive reconfigurable system

In this chapter, we introduce a design concept of an interactive interface for control reconfigurable robots. We first introduce the design concept for an interactive interface that allows users to manipulate the robots both in virtual and physical environments. We adopt robotic origami as the platform for demonstrating the proposed interface. We also develop algorithms for integrating essential robotic components such as sensors and actuators for adapting different hardware. For the interface design, we develop multiple control modes for further enhancing the controllability of reconfigurable robotic systems. Finally, we demonstrate and evaluate the applicability of the design concept with three different robotic systems.

## 1.1 Interactive interface design for multi-DoF robotic systems

To understand the morphological changes of multi-DoF robotic systems and bring such systems for direct human interactions, we investigate the design of an interactive interface that allows humans to manipulate multi-DoF robotic systems by hand directly.

### 1.1.1 An overview of multi-DoF origami robots design and control

Industrial robots provide high precision, efficiency, and fast execution of programmed tasks for reducing cost both in time and workforce. In contrast to conventional mass production, the need for customized and flexible production systems has increased due to product variety, globalization, and a shorter product development period. Thus, robots need to be reprogrammed or re-arranged more frequently, which usually demands highly-trained specialists involved. Robots programming requires transferring abstract concepts such as coordinates in space or parameter definitions of various tasks using mathematics, physics, and computational skills. This prevents robots from entering different markets, such as small and medium-sized enterprises (SMEs), as the cost associated with reprogramming is quite high. Because workers usually have high expertise for their work but without any experience in

---

The material of this chapter is adopted from the following self-authored publications.

**Jian-Lin Huang**, Zhenishbek Zhakypov, Harshal Arun Sonar, Jamie Paik 'A reconfigurable interactive interface for controlling robotic origami in virtual environments' *The International Journal of Robotics Research*, 2018

Harshal Sonar, **Jian-Lin Huang**, and Jamie Paik, 'Soft touch using soft pneumatic actuator (SPA)-skin as a wearable haptic feedback device' *Advanced Intelligent systems*, 2021

The contribution of Jian-Lin Huang were design of shape reconstruction experiments, results analysis, and writing.



robot programming. Additional expenses for hiring programming experts are not favorable for SMEs.

To reduce the obstacles in the development and control of robots, many approaches have been investigated. For instance, to simplify robot programming and manipulation, high-level or task-oriented programming methods [27], [28] provide intuitive and comprehensive programming interfaces. Recently, the interaction interfaces between robots and humans, based on virtual reality (VR) and gesture-based control, provide natural ways to program or telemanipulate robots [29], [30]. Several commercially available examples have been proposed for ease of robot programming [31]: (1) Icon-based control interface, which allows users to configure the functional blocks in the graphical interfaces for defining the program flow. (2) Wizard-based programming, where users are provided structured guidance/steps for programming the robots by selecting the suitable parameters and settings. (3) Computer-aided design (CAD)-based programming interface, which provides 3D graphical simulation environments for programming the robots. (4) Lead through programming, where the user moves the robots by hands, and the performed motions are recorded. The recorded trajectory could be modified and arranged for matching the desired tasks. The approaches motioned above could also cooperate with each other for creating a more comprehensive programming and control interface. However, the scope and level for simplification of robot programming could be different depending on a different level of users and applications.

In order to approach the first research question proposed, *‘What design approaches enable direct human-robot interaction with morphological transformations and constraints of multi-DoF distributed activated systems?’* We first need to define the scope, platform, and scenario for investigating the question. In my thesis, I investigated a control/programming interface that allows users to manipulate multi-DoF robotic systems even they don’t have much experience with robot programming. A very initial idea for novice users to experience a morphological transformation system would be linked to real-life experiences such as playdough or origami. The control objective is to achieve shape-changing via the control interfaces.

### **Multi-DoF reconfigurable robotic origami**

Origami is the art of paper folding that has also inspired dozens of engineering applications. Origami robots, robotic origami, can self-transform into desired three-dimensional (3D) shapes from nominally flat structures without manipulation by external torques or forces [32]–[34]. This technology has appropriated the foldable and reconfigurable structures, to adapt to undefined environments or tasks. Several self-folding devices have been developed that employ shape memory alloy (SMA) or shape memory polymer (SMP) actuators[5], [35]–[37]. Besides the hardware, planning and control algorithms have been proposed to generate automatic design processes to fold origami into the desired shape [38]. However, sensing feedback has relatively rarely been considered in the presented designs[39], which is crucial to achieving more complex shapes with many folding steps; it is beneficial to know and control each folding step towards a more complicated design.

Robotic origami can serve as a platform to investigate synergy between virtual and physical reality. Due to its unique structure, kinematics, and corresponding control strategies, we can

gain valuable insights into different interactive methodologies via the physical interface of origami robots.

To construct a virtual model, the critical step is to understand the kinematics of origami. This has been extensively studied by various research groups in mathematics, computer sciences, and even architecture. To classify the different origami patterns, several works exist on kinematic analysis or representation by equivalent mechanisms, and a spherical mechanism modeling is commonly used to differentiate the particular classes of origami kinematics[40], [41]. Rigid origami models regard the crease as a compliant hinge and the facet as a rigid panel that can effectively model the trajectories during folding [42], [43]. In origami structure, numerical analysis and finite element simulation involving active components have been proposed by several groups[44], [45]. However, finite element simulation does not allow rapid responses to dynamic input. While considerable attention has been paid to kinematic models and computational simulation, there have also been some attempts to experimentally validate models using physical devices [46]–[50]. While these studies are significant for the modeling of robotic origami application, they lack sensing and actuation components. To incorporate a control feedback loop, we need a more extensive origami platform that includes additional parameters such as weight, structure thickness, the torque of actuators, and hinge stiffness. A progressive understanding of the realistic and physical model-based mechanics of robotic origami folding is needed to design robots from the concepts of origami. Therefore, we need a design tool that considers both the robotic hardware components as well as the origami folding mechanisms.

As well as simplifying and understanding the kinematics of foldable structures, the distributed sensing approach on deformable devices facilitates self-sensing, which could be employed as multiple DoF input devices for virtual model construction and could be compared with the kinematic model or computational simulation. This type of 3D model acquisition and the input devices could have a wide range of applications, such as reverse engineering, virtual and augmented reality, and human-computer interaction. Optical sensors, such as laser scanners or cameras, are common methods for reconstructing 3D models. Several groups have investigated the 3D construction of physical structures by distributing sensors on the object itself so that the user can manipulate the object as a tangible input device for constructing the 3D model [51]–[53]. However, due to the size of the device and the limited number of physical pieces, it inevitably has a restricted realizable DoF (below 10). Thus, distributed miniaturized sensor networks over a deformable surface for high DoF input devices were developed [54]–[56]. Although these devices provide the interface for high DoF, even up to 50, input at a manipulable scale, these kinds of distributed sensing systems lack a self-actuation mechanism. Recently, actuated tangible interfaces have begun to emerge. These new types of tangible interfaces provide not only one-way communication but also enhance the interaction experience with digital information, making use of shape change to embody digital information in ways such as changing orientation, texture, volume, or form [19], [57], [58]. A number of studies were conducted in the context of educational toys[59], spatial augmented reality [60], [61], tangible remote collaboration [62], and even conveying emotions [63]. Many of these devices, however, have limited DoF in 3D space and quite often non-portable tabletop tangible user interfaces, especially in virtual reality and augmented reality applications. For these types of actuated tangible interfaces, robotic origami could have advantages, namely:

(1) multiple DoF actuations and DoF in 3D space, (2) light weight portable structures, and (3) are reprogrammable and reconfigurable.

Hence, in this section, we have developed an interactive interface to bridge robotic origami and human communication in both digital and physical environments.

### 1.1.2 The concept for interactive control interface

For control and manipulation of high-DoF robotic systems, the kinematics and dynamic behavior of the robots need to be well studied and modeled. Inspired by the concept of virtual reality-based interaction interfaces and hardware-in-loop simulation, which helped developers to reduce time, effort, and cost for designing and controlling robots [64], we propose a framework that enables users to interact with robots in both physical and digital domains. For an interactive system, the interaction may be expressed by three stages: (1) stimulus processing, (2) behavior modeling, and (3) response generation[65]. This framework consists mainly of an interactive interface involving hardware characteristics visualization and physics-based modeling for bridging the stimulus and response, as shown in Figure 1.1. The physics-based modeling governs the behavior of the robotic system and can be divided into different levels of modeling: (1) the geometry of the robot body that achieves the desired functionality, (2) the mechanism employed for the geometry, which describes the relation between the robot's body, (3) the critical components of the robotic system, such as actuators and sensors, and (4) the control method implemented in the robotic system. As discussed in the Introduction, most existing origami software only focuses on the first two levels; modeling the kinematics and dynamics of origami structure.

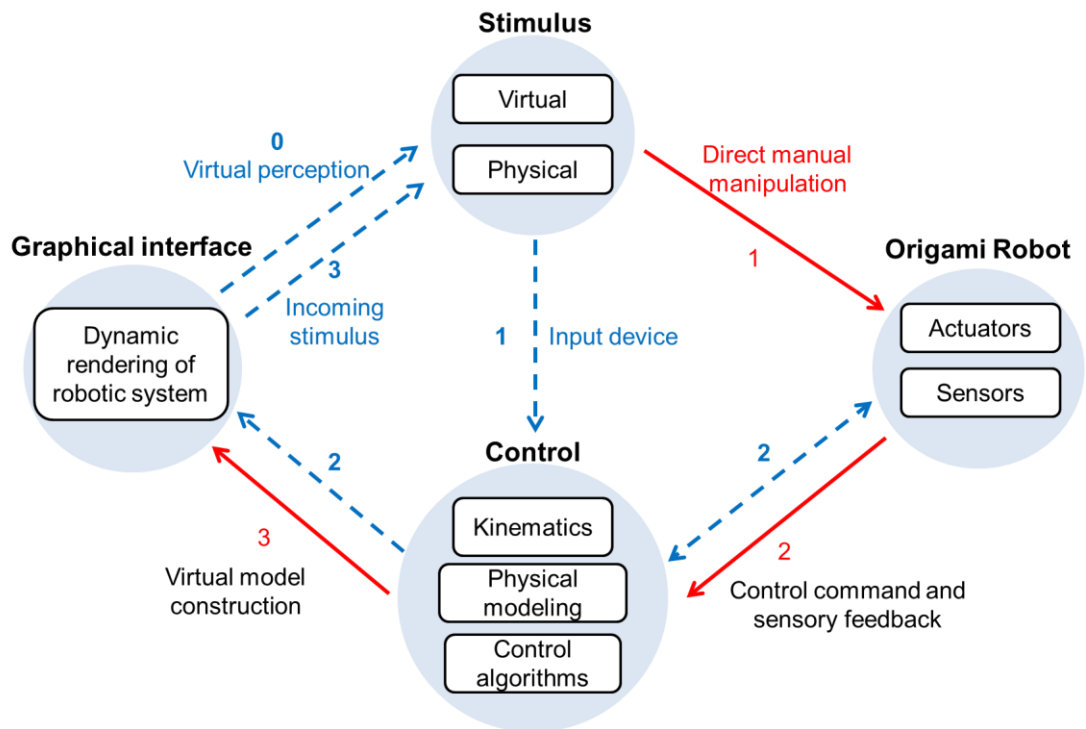


**Figure 1.1 The schematic of origami robot-based interactive system.** This behavior-based robotic interaction system can be expressed by three states. With a robotic origami platform, the stimulus can be virtual and physical. The physics-based modeling forms the behavior of the robotic system that governs the responses of

the robot in both the physical and graphical simulation worlds. The solid red arrows show the process of interaction mode 1, and the dashed blue arrows show the process of interaction mode 2.

Here, we introduce hardware-in-loop simulation into the origami modeling that involves feedback from the characteristics of physical components and the control system of the robot. The algorithms for different levels of visualization of physical objects and for the conversion of the virtual information to command the robots to generate response are also proposed. The response can be represented visually by the graphical interface or in the robotic system. To illustrate the bidirectional communication between the robot and humans, we developed two modes of interaction with the novel robotic origami system, shown by the solid (red, mode 1) and dashed (blue, mode 2) arrows in Figure 1.1 Below, we describe the two interaction modes that show the possibility of interacting with the robotic system in physical (mode 1) and visual (mode 2) platforms.

The ultimate goal of the proposed concept and framework is to control different types of multi-DoF robotic systems, such as modular robots. Although various software and hardware tools exist for origami design, there are only fundamental structural and kinematic assumptions that limit their usability in dynamic robotic origamis. The principal contribution of this work is creating interactive control methodologies that consider the characteristics of physical components of the origami robot, such as sensors and actuators. We decipher the physics of two distinct materials of origami robots that make up the rigid tiles and compliant joints. This is important because the tiles should be flat and non-deformable during the folding motion, and the joints should only allow single-axis rotation along the creases.

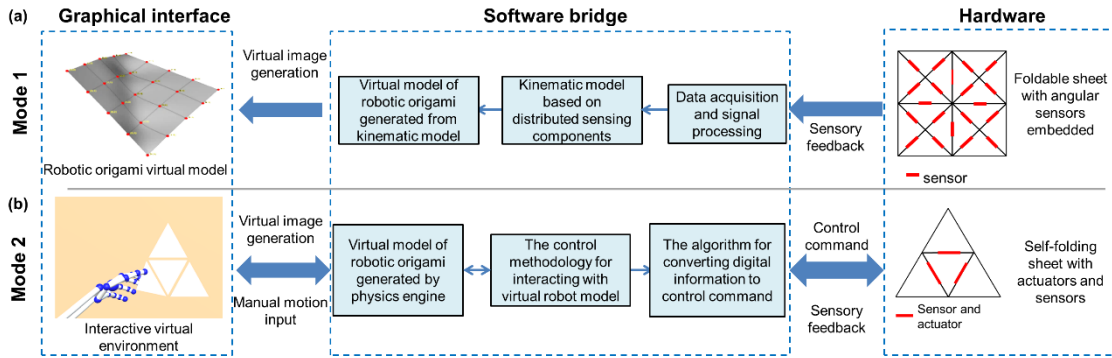


**Figure 1.2 System overview of the two interaction modes.** Interaction mode 1 is an origami-based tangible interface (a). This tangible interface collects the onboard sensory data to reconstruct a virtual 3D model of origami structure. Interaction mode 2 shows the interactive interface for controlling robotic origami in the virtual environment (b)—the software bridges the graphical control interface built in a virtual environment between human and robotic systems.

### 1.1.3 Origami-based tangible interface for 3D model reconstruction

In interaction mode 1, we create a physical interaction method that allows the user to operate digital model of robots manually. The solid red arrows in Figure 1.1 show the interaction mode 1 process. The stimulus (stage 1) is given physically to the origami robot, and the response (stage 3) is generated visually by the graphical interface through the control system (stage 2). To create interaction mode 1, understanding the kinematics and constructing a virtual model for the robotic origami is required. We developed an origami-based tangible interface, which is a combination of hardware and software components, as shown in Figure 1.2(a). The system

involves not only 3D model reconstruction of the robotic origami but also their design and control. The prototype is a low-profile, multi-DoF self-sensing device where the software runs sensor data processing, the algorithm for sensor localization, calculation of the kinematics and 3D model construction, as shown in Figure 1.2(a). The process following the arrows in Figure 1.2 illustrates the workflow of this tangible input device consisting of compliant hinges and rigid tiles with embedded sensors on the hinges. The distributed sensors on the foldable sheet provide the bending angles data at each hinge, and each sensor reading is collected to construct the kinematic model. Then, the software computes the relative position of each tile based on the kinematic model of the origami. Finally, the software generates a 3D image that is displayed on the graphical user interface.

Theoretically, an origami can have an infinite number of DoF, but in practical applications, we aim to have a finite number of DoF with sensors to detect all the actuated folds, rather than having arbitrary creases. Our prototype has rigid triangular tiles interconnected by compliant hinges with sensors. While this design is highly feasible and simple to fabricate, it is capable of being folded into a variety of 3D shapes. The crease pattern of the foldable sheet is shown in Figure 1.2(a). It has a square shape and is divided into 16 equally-sized isosceles triangles. This crease pattern design is inspired by [32], [46], [66]. Each triangle is a basic module for constructing the 3D model. The triangular tiles are regarded as rigid bodies that cannot be folded further. A flexible joint connects two adjacent tiles and enables bi-directional folding along the joint. To get a dihedral angle between two adjacent tiles, we distribute 20 bending sensors along each joint, and by measuring the bending angle, the relative position and orientation of adjacent tiles are calculated by the software. This tangible interface is not only a methodology for interacting with digital information but also a kinematic modeling tool of robotic origami involving feedback hardware components.

### **Model and implementation for robotic origami platform**

In interaction mode 1, we evaluate the position of each tile on the surface and adapt the origami folding sequence using the data from angular sensors for dynamic modeling of the robotic origami on a graphical interface. Therefore, the bending angles on the creases become the input of the kinematic model. We employ the rigid origami model[67] to present an equivalent mechanism of robotic origami. The rigid origami model treats planes of the origami as rigid links and their creases as revolute joints. The crease pattern and the equivalent mechanism of robotic origami are illustrated in Figure 1.3, where the creases are represented as dashed lines (see Figure 1.3 (a)), and the solid link lines in Figure 1.3(b) are equivalent to the triangular facets in Figure 1.3(a). For instance, link  $A$  in Figure 1.3(b) represents the triangular facet  $A$  in Figure 1.3(a). According to the terminology used in origami, the point where bending crease converges is called the vertex, i.e. point 1 in Figure 1.3(a). The vertex in origami is also the center of the spherical mechanism. The spherical mechanism is a mechanical system in which any point in a moving body is constrained on concentric spherical surfaces. This mechanism is helpful for understanding the kinematics of origami. In Figure 1.3(b), the rectangles are the revolute joints rotating along the folding creases, represented as dashed lines. For example, rectangle  $J_{AB}$  is the joint between link  $A$  and link  $B$ .  $J_{AB}$  rotates along the axis, passing through point 1 and point 2. The trajectories of points on links lie on concentric spherical surfaces, and all the axes of revolute joints pass through the vertex. The

intersections of the dashed lines are the vertices, such as points 1, 2, 3, 4, and 5. The vertex 1 is the spherical center of link A to link H, which means the trajectories of points on link A to link H will lie on concentric sphere surfaces. However, the kinematics of origami structure within multiple spherical mechanisms is not easy to solve. Since we have the rotation angles of each joint from the angular sensor data, we can simplify the analysis of multiple spherical kinematics.

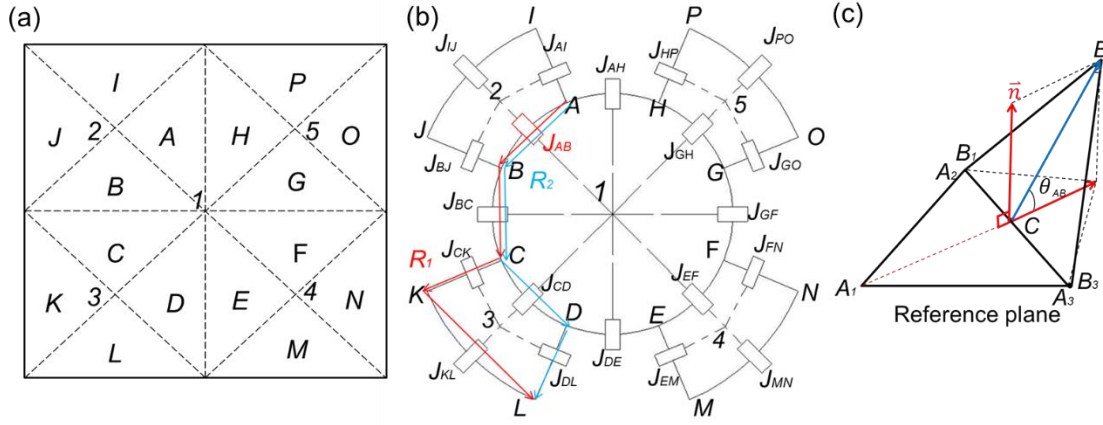


**Figure 1.3 Kinematics of the origami tangible interface:** The crease pattern (a), the equivalent spherical mechanism (b), and the schematics for coordinate calculation of two adjacent tiles (c).

Since an equivalent mechanism of the reconfigurable sheet has been found, we can coordinate each tile based on this mechanism using the revolute angle of the joint. Thus, we can include sensor data into the kinematic model. The measured data taken from angular sensors represents the dihedral angle of two tiles, which is also equal to the revolute angle of a joint in the spherical equivalent joint. To calculate the relative position of tiles, we set point 1 as origin of the Cartesian coordinate system. Then, given the position vectors of each of the vertices on the triangular tiles as  $V = [v_A, v_B, \dots, v_P]$ , and  $v_A, v_B, \dots, v_P$  are  $3 \times 3$  matrices.  $v_A$  can be shown as  $v_A = [v_{A1}, v_{A2}, v_{A3}]$ , where  $v_{A1}$ ,  $v_{A2}$ , and  $v_{A3}$  are the position vectors of three vertices of the triangle, respectively.

To find the position of all the tiles, we calculate the relative position between two adjacent tiles, as shown in Figure 1.3(c). In the beginning, link A is chosen for the reference plane. Then, we compute the  $v_B$  from  $v_A$  by (1.1)

$$v_B = f(v_A, \theta_{AB}) \quad (1.1)$$

$\theta_{AB}$  is the revolute angle of  $J_{AB}$ , and also the dihedral angle between link A and link B. Function  $f$  was derived from vector operations. Where  $v_{B1} = v_{A2}$ , and  $v_{A3} = v_{B3}$ . The coordinates of  $v_{B2}$  can be expressed in terms of the cross and inner products of  $v_A$  and  $\theta_{AB}$ :

In Figure 1.3(c), if C is the midpoint of  $A_2$  and  $A_3$ , then the position vector of point C is written as  $C = \frac{v_{A2} + v_{A3}}{2}$ . Since the plane defined by points  $A_2$ ,  $B_2$ , and C is perpendicular to  $\overline{A_2A_3}$ , we can divide the vector  $\overline{CB_2}$  into two components. One is the projection of  $\overline{CB_2}$  onto  $\vec{n}$ , and

another is the projection of  $\overrightarrow{CB_2}$  onto  $\overrightarrow{A_1C}$ . Where  $\vec{n}$  is the normal vector of link A, and can be calculated as

$$\vec{n} = (v_{A3} - v_{A1}) \times (v_{A2} - v_{A1}) \quad (1.2)$$

We can get  $\overrightarrow{CB_2}$  from the addition of two components has mentioned before by

$$\overrightarrow{CB_2} = |\overrightarrow{CB_2}| \cos \theta_{AB} \frac{\overrightarrow{A_1C}}{|\overrightarrow{A_1C}|} + |\overrightarrow{CB_2}| \sin \theta \frac{\vec{n}}{|\vec{n}|} \quad (1.3)$$

Finally, we can find

$$v_{B2} = \begin{bmatrix} v_{A2} \\ C + \overrightarrow{CB_2} \\ v_{A3} \end{bmatrix} \quad (1.4)$$

Next, we can describe the relative position of any random two tiles. For example, we calculate the relative position of link  $L$  based on link  $A$  iteratively. That is, from Eq. (1.1), we find  $v_B$  from  $v_A$ . Similarly, the position vector of link  $C$ ,  $v_C$  is expressed as  $v_C = f(v_B, \theta_{BC})$ . Then, the position vector of link  $L$ ,  $v_L = f(f(f(v_A, \theta_{AB}), \theta_{BC}), \theta_{CK}), \theta_{KL}$ , takes the route  $R_1$  as shown in Figure 1.3(b). The mechanism passing through  $R_1$  is considered as a chain, and each tile can use the position of the adjacent tile as a reference. The relative position between the terminal and the initial tiles is calculated iteratively based on the two adjacent tiles' kinematics. For a given folding pattern, the chain configuration is not unique. For example, another alternative route,  $R_2$ , can calculate the relative position between link  $L$  and link  $A$  as  $v_L = f(f(f(v_A, \theta_{AB}), \theta_{BC}), \theta_{CD}), \theta_{DL}$ . We can simplify the kinematic model by hardware design parameters such as the dimension of tiles and dihedral angles from sensory data.

The positions of links are imposed by the rotation angles on the revolute joints. The rotational angle can be measured by the angular sensor described in the next section. In contrast to the 3D scanning technique or the gesture-based 3D modeling technique, our 3D model construction does not employ a marker or external sensing device to create a geometric model on a coordinate system. Instead, we select a tile as a fixed reference plane and calculate coordinates of adjacent tiles through the bending angle of the joint.

When considering the entire structure, several routes of kinetic joints can be applied for getting the coordinates of the standard rule of route selection to find all position vectors on the tile vertices. Our distributed sensing system has a central processor, which is usually known as the fusion center, to collect and convert the sensory data to position[68]. The sensors are independent, and there is no feedback from the fusion center to the sensors. No sensor has a pre-configured global coordinate, but we assigned coordinates for one of the tiles from the reference plane. The fusion center collects relative position data that integrates with absolute location sensors to merge multiple distributed sensing systems. Here we investigate the tiles adjacent to the center vertex in Figure 1.3(b), link  $A$  as start nodes. By assuming the path finding problem is a single-source unweighted graphs problem, we calculate the relative

position of other tiles from the nearest to the farthest tiles by the shortest path, based on breadth-first search trees [69].

There are two main functions of the software bridge. The first one is to reconstruct a 3D model of the physical device, and the second is to control the actuation of the self-folding sheet. The two main functions are described below. The software uses the distributed sensor data for reconstructing the 3D model. First, the collected sensor reading is filtered by a digital signal filter. In our experiments, we employ a moving average filter to reduce the low-frequency noise ( $< 5\text{Hz}$ ) corresponding to the actuator operational frequency. Second, the software converts sensory data into bending angles based on the sensor calibration data. The calibration data of each sensor embedded in the prototype is stored in a software database before the model construction. A surface model is generated beforehand according to the kinematic model of the prototype for simulating the physical sheet where the surface model nodes cover all vertices of the triangular tiles. Last, the program updates the coordinates of each tile and generates the 3D model iteratively. For feedback control of the robotic origami, the sensory data is sent to the software controller. Then, the folding sequence of the robot is converted to the angular set points.

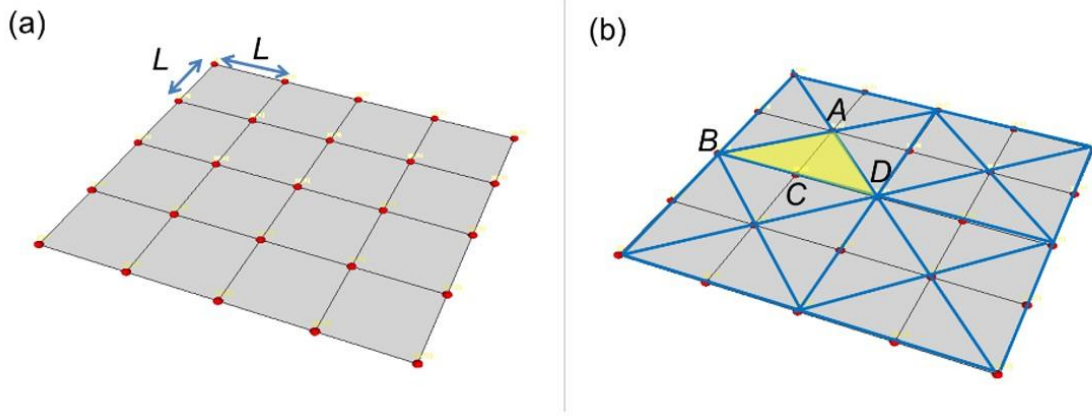


**Figure 1.4 The 3D model of the origami generated in LabVIEW.** (a) A square, flat surface is predefined by a 2D array of nodes. (b) The crease pattern of the origami pattern within the triangular tiles overlays the predefined surface. The nodes used to describe the coordinates of the tiles.

For visualizing the kinematic model, we developed 3D model visualization software in *LabVIEW*. Since the proposed kinematic model can provide the relative coordinates of all the tiles by sensory feedback, developers can use any 3D graphics software to reconstruct the 3D model of robotic origami.

We employed a 3D surface editor by Wojtek Golebiowski (<https://forums.ni.com/t5/Example-Program-Drafts/3D-Picture-Interaction-3D-Surface-Editor/ta-p/3494179>). This 3D surface editor uses a 2D array of nodes to describe the 3D surface. The surfaces between nodes are calculated by spline interpolation. To generate the surface model of each single triangular origami tile, we need the full coordinates of vertices of the triangle tile. We generated a planar surface that contains  $5 \times 5$  nodes which has enough nodes to cover all the tile vertices with a predefined distance,  $L$ , between nodes, as shown in Figure 1.4 (a). Thus, these nodes can be used to describe the coordinates and generate the surface of the triangular tiles, with a base length,  $2L$ , and a height,  $L$ , as shown in Figure 1.4 (b). For example, the highlighted tile can be



described by nodes A, B, C, and D, and we can fix this tile to calculate the relative coordinates of the other tiles. By reading all bending angles between tiles from the sensors, the 3D model can be updated simultaneously. We can use different crease patterns not only in triangular shapes but also in other arbitrary patterns such as polygons since the nodes are enough to describe the shape of each tile.

#### **1.1.4 Gesture-based interface for controlling origami robots in a virtual environment**

The design and control of robotic origami can be challenging due to their multiple DoF and complex kinematics. Moreover, the users or developers may not have adequate knowledge of the kinematics of origami structures. Hence, in interaction mode 2, an interface was developed that provides a more intuitive way to command as well as simulate the kinematics of robotic origami, as shown by the dashed arrows in Figure 1.1. A graphical interface provides virtual perception for the user to move and manipulate the virtual robot, meaning the stimulus is given virtually to the control system. The responses are generated in two ways. First, the visual responses are generated by physics-based simulation on the graphical interface, shown by the two-way arrow between the graphical interface and the software bridge in Figure 1.2(b). Second, the control algorithms transfer the virtual stimulus to the control commands to control the motions of the physical robot and bring onboard sensory feedback for closed-loop control and virtual model construction of robotic origami, shown by the two-way arrow between the Software bridge and hardware in Figure 1.2(b). In interaction mode 2, we created an interactive virtual environment on the graphical interface to control a physical robotic origami, as shown in Figure 1.2(b).

The virtual environment is constructed from the 3D model of the robotic origami, the 3D model of the hands and the interaction mechanisms between the hands and robotic origami. This virtual environment enables users to interact with the robotic origami in a similar way to folding origami directly. The software is independent of the hardware. The current virtual environment setup is built on Unity. Unity is a game development platform that also provides built-in support for VR development. Leap motion(Leap Motion, Inc.), a hand motion-tracking sensor works as the input device for generating the corresponding virtual 3D model of the hands on the graphical interface. To fold an origami structure, the position of the crease pattern and movement direction is required. With this virtual model of hands, users can transfer their hand motions into the virtual world, including positions and gestures, that is to say, a pathway to manipulate virtual objects precisely and intuitively. For physics simulation of interaction mode 2, Nvidia's PhysX physics engine built in the Unity platform has several key features that are suitable for simulation of the interaction between the robot and the human, such as rigid body kinematics and collision detection. Furthermore, using the kinematic model in mode 1, the graphical interface is not only used to input control command to robotic origami but also to get information from the robotic origami as visual feedback for interaction.

There are several challenges to building a virtual environment with reasonable interaction for users. The first is to create the virtual model of the robotic origami for simulating kinematics of the robotic origami. Second, the interactions between the virtual robot and virtual hands

may be slightly different from those of the physical robotic origami manual folding but still need to be intuitive to the user. That is, most of the movements and reactions in the virtual environment should represent physics as close as possible; some physics, however can be modified to make the manipulation easier and more fluent in the virtual environment. These changes should not increase the learning barriers and should be understood immediately, even without extra instructions. Third, the reactions of the virtual world should be in real-time, or the user will tend to stop or keep moving until they see the desired motion finished. We addressed these three challenges using the following methodologies: (1) the virtual robotic origami model was generated based on rigid origami theory with a foldable structure of rigid flat facets connected by revolute hinges. We can calculate the dihedral angle between the tiles for the robot's control system use. (2) Rigid body modeling and collision detection between the virtual robot and the virtual hands enables users to fold and move the virtual origami tiles without penetrating the origami object. Moreover, the friction simulation of objects allows the user to manipulate or grasp the tiles of the virtual robotic origami more easily. Therefore the user can manipulate and understand the mechanics in a very intuitive way. (3) The infinite virtual air drag force acting on the robotic origami opposes the motion direction and can stop the movement of the robotic origami immediately after the end of collision between the hands and tiles. This function enables the user to fold robotic origami to the desired shape and to operate more easily in virtual environments.

Then comes the challenge of transformation of the visual information to command the physical robot. The virtual presentation needs to consider not only the kinematics of origami structure but also the characteristics of physical components on the robots such as actuators and sensors.

To demonstrate the capability of the interactive control interface, we built an active, reconfigurable, self-sensing, and self-folding prototype. This prototype consists of four rigid equilateral triangular tiles with sensors and actuators attached at the edges of the triangles, as shown in Figure 1.2(b). This design allows bending along the edges of the triangular tiles; in other words, all the elements connected between two tiles are foldable. The folding is done by torsional actuators that generate motion about the central axes along the edges of the tiles.

### **Virtual model for robotic origami generated by a physics engine**

The first step to create a virtual environment is to construct the physical model for simulating and visualizing the kinematics of robotic origami, and this physics model should be capable of simulating kinematics of origami and interactions between humans input and the robot. Thus, we created the physics-based modeling based on rigid origami and multibody system. Multibody systems utilize a set of elements such as rigid parts, joints, actuators, and forces. The interaction can be given by a joint, a force actuator, or a sensor[70]. The kinematics of a single vertex rigid origami system could be simulated by a matrix model or Gaussian curvature model [71], [72]. For the kinematics, multiple vertices origami structure is modeled by the physics engine. In this framework, physics engines are not only used for visual rendering but can also be the modeling tool of rigid origami structure.

For visualizing the physical world and building an understandable interaction model in the virtual environment, we adapted the virtual rendering algorithms [73]–[75] to approximately

simulate the physics of the real world. The virtual interface is more focused on providing users with a control interface with perceptually-correct, immediate feedback, and interactivity rather than simulating physics precisely in the common simulation tool. Furthermore, since we can create the virtual model of robotic origami from the on-board sensory feedback, these data can be used to fix simulation errors and refine the behavior model in the virtual environment in the future. Thus, the algorithms for building the virtual model will not be exactly the same as the physics rules, which usually simplifies the kinematics of the system. We built the model in a discrete-time system with the virtual rendering rate 30 Hz, which can adequately create virtual perceptions for humans. The architecture for building a multibody system and rigid origami theory under *Unity* is shown in Figure 1.5 [76]. We defined the rigid part of robotic origami as a rigid body, which enables the objects to simulate rigid body dynamics under the control of the physics engine. This is a component that can simulate the conjunction relation between adjacent rigid parts of the models.

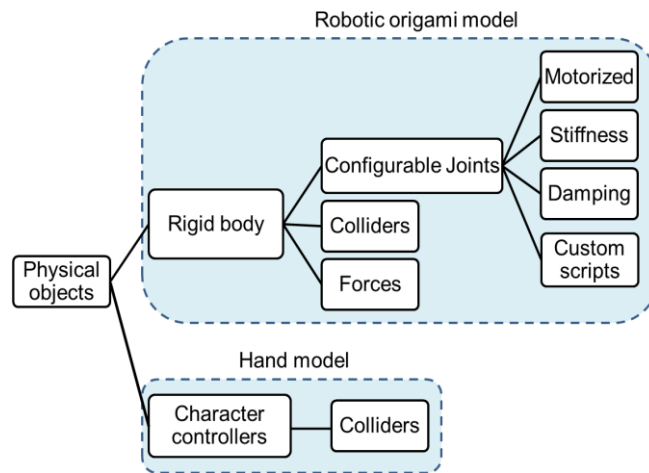


**Figure 1.5** The architecture of physical objects for constructing a virtual environment in Unity.

### Customizable hinge properties

Due to differences in types of connecting joints of robots, they can be functional joints implemented with customized algorithms. For example, we used a Kapton layer as a passive hinge to connect tiles in our robotic origami prototypes. In this case, we developed an algorithm to simulate the bending and restorative behavior of the Kapton material [77]. The approximate mechanical behavior and corresponding algorithm are described in Figure 1.6. We could implement this algorithm in the robot behavior model to give the visual perception of material properties when the user interacts with the passive hinge, even without sensory feedback from the physical prototype.

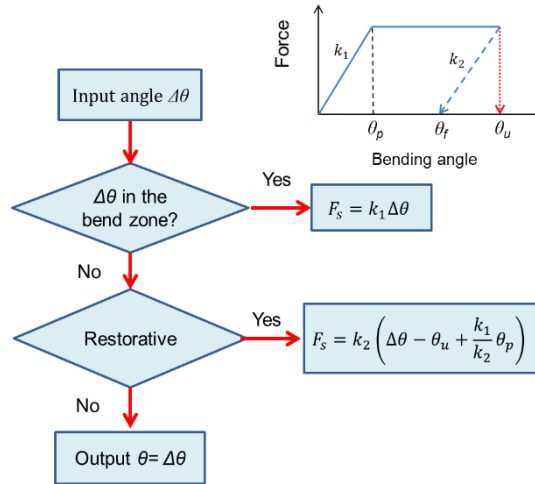


**Figure 1.6 The flowchart of an approximate virtual rendering algorithm** for the restoration of the origami robots' Kapton hinges.

The character controller is not affected by forces and will only move when called by the move function, which receives command from human motion input. It will then carry out the movement but be constrained by collisions. The collider allows virtual objects to collide with each other. One object can apply forces to the other via collision. It is the main mechanism to manipulate virtual objects with a user's motion.

The localized interaction model for indicating the kinematics during manipulation in the virtual environment is shown in Figure 1.7. The behavior of the virtual model of the origami robot is not only dominated by the kinematic constraints but also by the forces in the virtual environment. In interaction Mode 2, the robotic origami model moves by collision forces generated by the hand model. The folding motion not only follows the user-input trajectory but is also affected by the virtual forces that are listed in Table 1.1. Apart from the force generated by the hand, other virtual forces like the spring force on the unactuated hinges in Figure 1.6 contribute to unfolding motion. The collisions between the hand model and robot are assumed to happen on part  $i$ . The motion of virtual part  $i$  is decided by force exerted, which  $F_c$  is the collision force generated by the hand model,  $F_f$  is the friction force between the hand and part  $i$ , the air drag on the rigid body. The constraints describe the relations between the parts. The virtual components generating visual rendering and converting the digital information to physical parameters for controlling robots are shown in Table 1.1. Once the virtual hand model collides with the robot model, it generates the collision force on the robotic origami model. The motion of the virtual hand model is only governed by the input signal from the motion tracking system. The hand model does not receive any force, and the generated force can only be described by the velocity of hand motion,  $F_c = M \frac{V_h}{dt}$ . The generated forces are proportional to the speed of the hands when the collision happens. However, the collision force generated by the hand model will make the robot move endlessly. Thus, we created air drag force on the rigid body, which is proportional to the square of velocity, which can be expressed by  $F_d = V^2 D$ . Where  $V$  is the velocity of the object and  $D$  is the drag coefficient. The movement of the tile is dominated by the collision force exerted by the hands. In the actual prototype, we achieve desired folding angles thanks to the distributed sensing and consequent closed-loop control. In order to recreate the same motion of origami in the virtual

environment, we need to make sure that each folding is completed when the hand makes no contact with the virtual model. To achieve this effect, we add an air drag effect on the origami surface after the contact is lost.

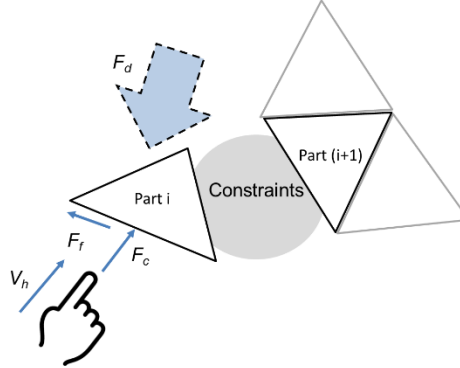


**Figure 1.7 Local interaction model for simulating the manipulation of robotic origami in a virtual environment.**  $V_h$  is the velocity of hand motion.  $F_c$  is the contact force exerting on part  $i$ .

The general equation of motion used for describing the visual rendering representation of a multibody system is performed by a position-based approach. The vectors of generalized coordinates are denoted by  $q$ . The velocity vector can be denoted as  $v = dq/dt$ . From Newton-Euler equations and Lagrange's equations; we can describe the general equation motions of the rigid body by  $\ddot{q} = M^{-1}f$ . The mass matrix is described by  $M(q)$ , which depends on the deviation of constraints.  $f$  is the force exerted on the central of mass. Given a known position  $q_0 = q(t_0)$  and velocity  $v_0 = v(t_0)$  at time  $t = t_0$ . Then, we define  $\Delta q = q(t_0 + h) - q(t_0)$  and  $\Delta v = v(t_0 + h) - v(t_0)$ , where  $h$  is the updating rate of virtual rendering. The time integration is performed by implicit backward Euler method, which leads to  $\Delta q = h(v_0 + \Delta v)$  and  $\Delta v = hM^{-1}f(q_0 + \Delta q, v_0 + \Delta v)$ . We use Talyor series expansion to make the first-order approximation of  $f$ :

$$f(q_0 + \Delta q, v_0 + \Delta v) = f_0 + \frac{\partial f}{\partial q} \Delta q + \frac{\partial f}{\partial v} \Delta v \quad (1.5)$$

Then, we can get the virtual model of each time frame based on a fixed initial state.

To create the rigid parts of robotic origami, we predefined the geometries of rigid parts by 3D CAD software such as *Blender* and imported them to *Unity*. In addition, simple geometry such as spheres and cubes can be directly edited in *Unity*. After the definition of geometry, we added the rigid body components to the physical objects so that the objects can receive force and torque and act accordingly following physics in the real world. An important step in simulating robotic origami structure is to define the relationship between each rigid tile. We attached joints at every connection between the rigid tiles. The connected joints were defined as a revolute joint, and the properties of these connected joints can be configurable as described in the previous paragraph. The integration of dynamics is performed by the symplectic Euler method for physics-based modeling, which is a popular method in computer graphics and the integration results are close to the implicit backward Euler method.

**Table 1.1 The visual rendering and transformation between digital information and physical components**

Virtual components	Data description	Physical components
Spring force of joints	$F_s = k\Delta\theta$	Kapton passive hinges (Elastic deformation)
Air drag	$F_d = V^2 D$	n/a
Torque of motorized joint	$T = M \frac{\omega}{dt}$	Bending sensor
Constant force	$F_c = M \frac{V}{dt}$	n/a
Hinge angle	$\Delta\theta$	SMA torsional actuator
Dynamic friction force	$\Delta V = \mu \cdot dt$	n/a

### Converting virtual information to the control command of robotic origami

In robotic control systems, the time delay for closed-loop control could result in instability of the system. Therefore we propose an algorithm to convert a continuous-time system to a discrete-time system. This algorithm includes signal processing, components behavior adaption, and response generation that can divide continuous folding motions to discrete folding sequence control commands to the actuators. The algorithm enables user teaching for robotic origami by demonstrating in the virtual environment. Then, the collected data will convert to control command to control robotic origami. This is an early step towards task-oriented programming in robotic origami for high DoF mechanism control.

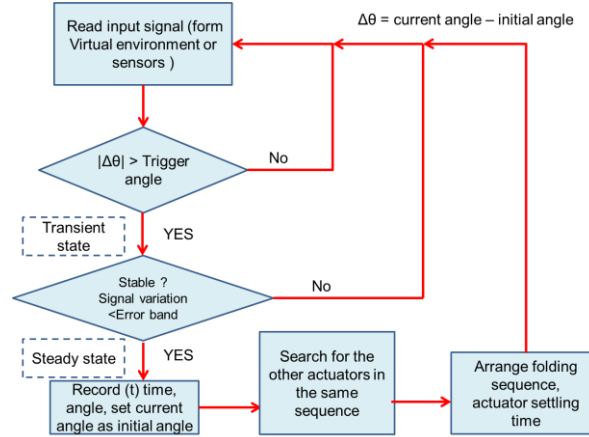


**Figure 1.8 The flowchart of the algorithm for converting continuous folding motions to discrete folding sequences.** This algorithm converts the recorded folding angles from the virtual environment to control commands of the robotic origami, adapted to the characteristics of the hardware. In addition, this algorithm can also use the sensory data as input while folds the physical prototype to demonstrate the folding tasks.

As shown in Figure 1.8, the algorithm considers the mechanical characteristics of actuators and sensors in the robotic origami that can be divided into the following steps: First, the user demonstrates the folding behavior in continuous motion by the hands, and the performed motions are transferred to virtual modeling by Leap motion. The graphical interface gives users immediate visual feedback of the folding process. In the first phase, the physics engine takes the simulation of interactions between user input and virtual model of robotic origami,

and the status of physical robotic origami does not simultaneously change while the user manipulates the virtual model. Then, the control system takes the recorded folding angles of the virtual robotic origami model and time data from the simulated results to control robotic origami. In addition to Interaction Mode 2, this algorithm uses the sensory data from the prototype during direct physical manipulation. Second, the control system transfers the recorded data to task structures in symbolic level representations that are the transient and stable states of robotic origami. The transient states confirm the folding motions are executed, whereas the stable state is the end of the folding sequence. Therefore, a transient state with a stable state represents a complete folding sequence. When the change of a joint angle  $\Delta\theta >$  trigger angle, the task goes to a transient state. When the signal variation is smaller than the error band for a predefined settling time, the task goes to a stable state. The trigger angle, error band, and settling time can be tuned to the proficiency level of the users in the virtual environment. Third, the extraction of folding sequences represented by the task structures is relayed to actuation commands to control the robotic origami. The averaged angles of stable states will be the set points of each folding sequence for the controller. The final step of generating a discrete folding sequence is applying the converted virtual tasks on the physical robotic origami. For this robotic origami, a PID controller is employed to control the folding angles where the sensor readings dictate when to start the next folding sequence – when each sensor reading reaches a steady state. In this step, a kinematic model developed in Interaction Mode 1 can be implemented in the same graphical interface for monitoring the task sequence.

### **1.1.5 Experimental validation of interactive interface**

In this section, we discuss the experimental verification of the proposed interaction methodologies, including hardware construction, software development, and integration of the robotic systems.

#### **Summary of required experiments**

To validate the applicability of the robotic origami kinematic model based on a distributed sensing system, we prototyped a multi-DoF, physical input interface and compared the actual 3D shape with the reconstructed 3D virtual model.

To achieve reconfigurability of robotic origami, we implement a distributed sensing system on the robotic origami for feedback control so robotic origami can transform into different configurations from the same hardware, which is still rarely applied in robotic origami research.

To demonstrate the intrinsic control methodology for robotic origami, we created a software platform with physical prototypes to teach the robot in a virtual environment and then replicate the demonstrated task on physical robots. The experimental results show the algorithm's capacity to control a multiple DoFs system in an intuitive way, as well as providing a platform for telemanipulation of the robotic origami.

#### **Experimental platform**

We prototyped two different hardware interfaces to experimentally validate the interactive interfaces: a tangible interface with distributed sensors and a robotic origami with embedded actuators and sensors. Both prototypes are assemblies of rigid tiles, foldable joints, and

sensing elements in a planar structure that employ a layer-by-layer fabrication method. The prototype consists of two glass fiber layers, a strain gauge, and a Kapton layer for foldable joints, as depicted in Figure 1.9 (a). The sensory and linkage components are sandwiched between two glass fiber layers that provide a structural backing with minimal weight. The glass fiber layers, each less than 1 mm thick, form the mechanical foundation of the tiles. The shape of the glass fiber layer is an isosceles triangle of 20 mm base length and 10 mm height. The Kapton layer serves as a foldable joint between the tiles. This layer is flexible and provides rotational DoF whose axis is parallel to the edges of two adjacent tiles. We adopt 120  $\Omega$  strain gauges (RS components) as bending sensors and attach them to the Kapton layer to sense the bending behavior of the layer; the sensitive direction of each strain gauge is perpendicular to the edges of two adjacent tiles.

The construction of the prototype requires several steps. We first design a 2D pattern for the glass fiber and Kapton layers and then laser micro-machine the designed pattern. The machined layers are stacked layer-by-layer and bonded by adhesive layers, and after applying heat and pressure, the whole structure is cured. Finally, we connect electrical wires to the strain gauges for the readout.

The actuated prototype uses shape memory alloy (SMA) torsional actuators within the layers as shown in Figure 1.9(b). The detailed design and fabrication of SMA will be introduced in Chapter 2. The torsional SMA actuator generates the folding motion when it is thermally activated via a customized Copper-Kapton micro-heater. The details of the heater and SMA actuator fabrication process are discussed in Chapters 2 and [78], [79]. Here, strain gauges are placed along with the Kapton. All the stacks are aligned and mechanically fixed with screws and nuts that allow easy and fast assembly and dismounting. The drawing of the structure of the actuated prototype is shown in 1.9(c). The strain gauges were chosen for angular sensing, and the resistance changes of the strain gauges are expected to be quite small. A multiple channel resistance measurement setup with high accuracy and suitable resolution is required. For quick implementation, we selected some commercial modules to measure the sensor array rather than design and fabricate a new electrical circuit based on a Wheatstone bridge or potentiometer. Resistance measurement was accomplished with a commercial instrument (National Instruments NI USB-4065) with resolution down to 1 m $\Omega$  in the range of 1 k $\Omega$ . For multi-channel measurement we used a digital I/O device (NI 6008) to control a multiplexer (CD74HC4067). We connected the electrical measurement setup to a single sensor and measured the resistance of an unfolded sensor. The measured standard deviation was about 12 m $\Omega$  and peak-to-peak noise was about 75 m $\Omega$ .

We present an experiment to confirm and test the compatibility of the distributed sensors on the tangible interface and to evaluate the performance of the distributed sensing system. We constructed an angular sensor testing setup as shown in Figure 1.10(a). It consists of a DC motor with a rotary encoder and two plates; one is fixed, the other is movable, connected by a rotary hinge. The movable plate rotates along the hinge and is driven by the DC motor; the angle between the two plates is calculated from the rotary encoder data. We attached our prototype to both plates and aligned its bending axis along the rotary hinge. The prototype is folded by the DC motor, and its folding angle is recorded and calculated simultaneously.



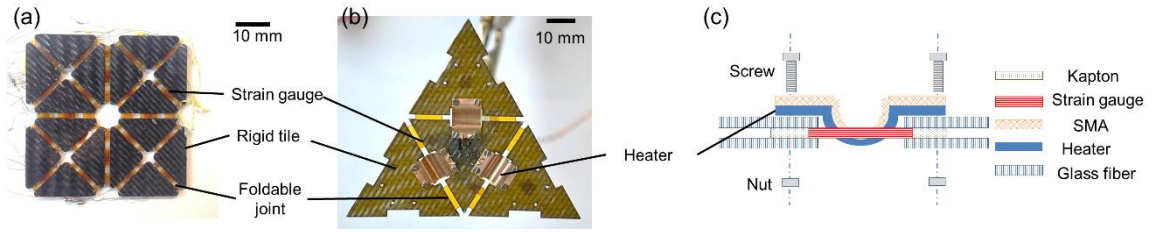


**Figure 1.9 Construction of two prototypes:** (a) A tangible origami input device (only with sensors), and (b) robotic origami (complete with sensors and embedded actuators). The side view of the robotic origami prototype consists of 5 functional layers (c). The robotic origami contains several functional layers, including SMA actuators and sensors that enable the self-folding and self-sensing.

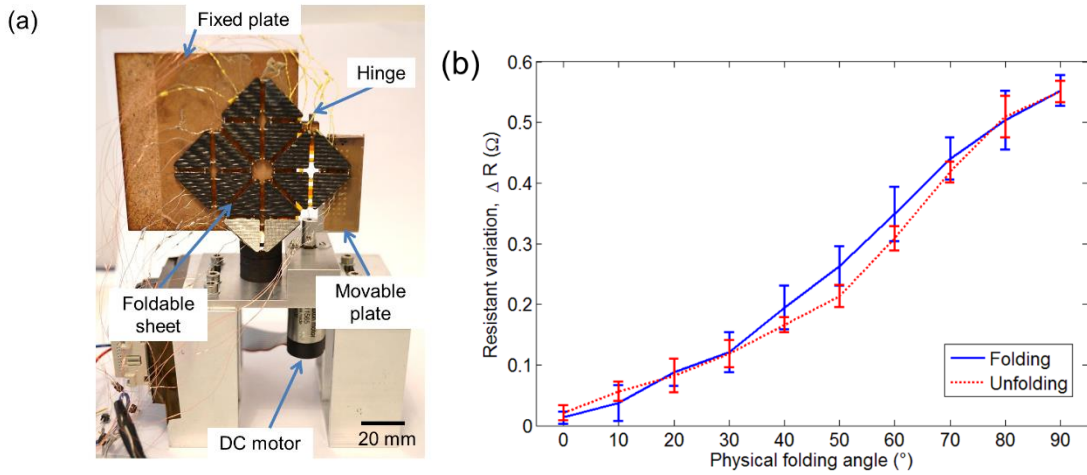


**Figure 1.10 The experimental setup and results of a single hinge of the tangible interface.** Experimental arrangement for angular sensor testing (a) and the measured resistance variation of the strain gauge versus the bending angle (b).

We set the DC motor to fold the prototype to 90° and unfold at a constant angular speed in a single testing cycle, and we conducted five testing cycles. At the same time, the folding angle and resistance of the sensor are recorded. The resistance variation of the strain gauge is proportional to the folding angle, as shown in Figure 1.10(b). The resistance variation is calculated as  $\Delta R = R - R_0$ , where  $R_0$  is the average resistance of the sensor in an unfolded state (with bending angle 0),  $R$  is the measured resistance, and  $\Delta R$  is the resistance variation corresponding to the bending angle. The sensitivity of the angular sensor as estimated from linear regression was 6 mΩ/°, and the hysteresis was 9 % of the full scale. We then use the sensitivity of the angular sensor to calculate the dihedral angle between two tiles in the virtual model, and after measuring the sensitivity of all angular sensors embedded in the foldable sheet, we add these calibration results into the software.

### Virtual model reconstruction of robotic origami experiment (Mode 1)

We validated the applicability of the multi-DoF physical input interface by comparing the actual 3D shape and the reconstructed 3D model. In the first experiment, we fold two tiles together at the corner of the sheet to 90° bi-directionally. The visualization results are shown in Figure 1.11(a). In the second experiment, we fold eight tiles at a time. The 3D reconstruction results are shown in Figure 1.11(b) and indicate that the generated virtual images are comparable to the real folding angles. However, we do observe some discrepancies on the

sheet's surface that are due to signal noise. Nevertheless, the peak-to-peak noise is reduced below  $5^\circ$  by implementing the moving average filter.

We also tested multiple shapes, and the comparisons between the physical folding state and the 3D reconstruction results are shown in Figure 1.12. Figure 1.12(a) to (c) show results for the W-shape and 1.12(d) to (f) show results for corner-shape folding. The folding angles of creases are shown in figure 1.12(a) and (d). For the first folding, we fold the prototype into a W-shape by attaching the prototype to a wooden reference block to ensure that adjacent planes of the sheet are perpendicular to each other, as shown in Figure 1.12 (b). The image generated by the software is shown in Figure 1.12(c). The virtual image shows our visualization algorithm works with this multiple-DoF folding shape. Figure 1.12(d), (e), and (f) show another multiple-DoF folding. The prototype is laid flat against the corner of the cube. Two of the angular sensors are fully bent to  $180^\circ$ . These results show that the reconfigurable sheet could be a 3D shape measurement tool with the ability to measure curvature or complex topography of object surfaces while increasing the DoF of the tangible devices. Refer to the Multimedia Extension for the demonstration of interaction mode 1.

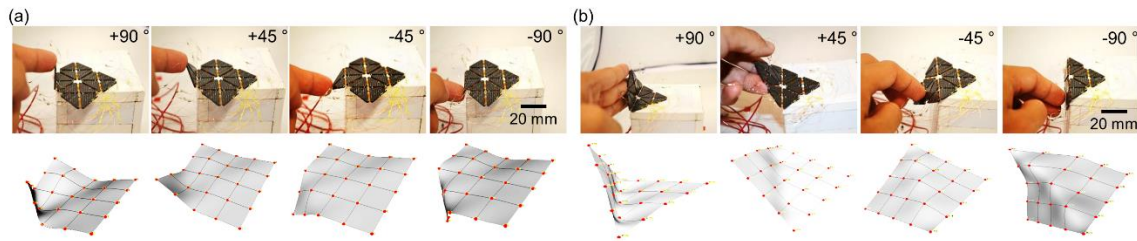


**Figure 1.11 Comparison between physical folding and the 3D model reconstruction.** Bi-directional folding of two joints (a), bidirectional folding of four joints (b).

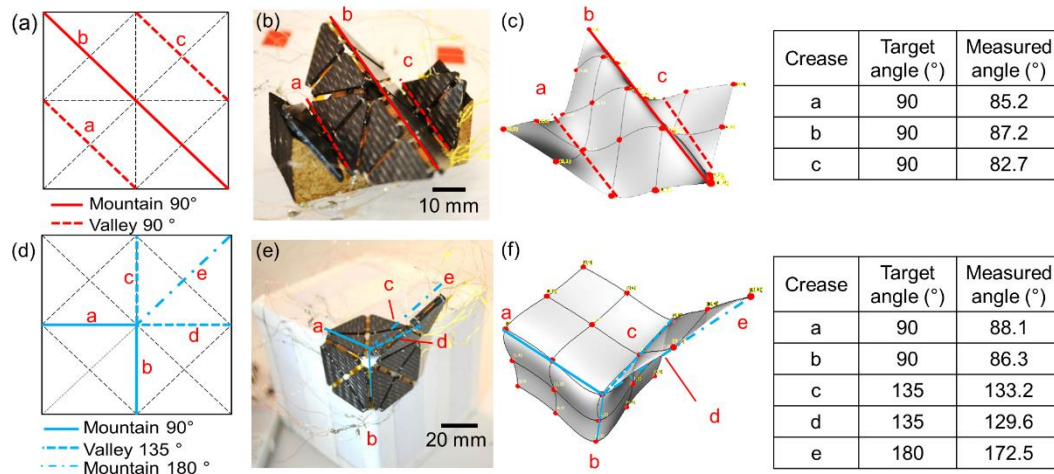


**Figure 1.12 The comparison of the actual folding behavior of the origami robot with its real-time 3D image** generated by virtual model reconstruction software. (a) to (c) show W-shape folding and (d) to (f) show the corner shape. The folding angles of multi-DoF folding shapes in W-shape from side view (a), and a corner shape (d). The prototype is affixed on two different reference blocks to generate different folding shapes (b) and (e). The 3D model and measured bending angle of each crease from sensory feedback are shown in (c) and (f) closely following the actual shape of the prototype.

### Closed-loop control of robotic origami

Using controllable actuators with feedback from distributed sensors gains much flexibility for system reconfiguration design for any robotic origami. To control the SMA actuator, a microcontroller board (Arduino Mega) which provides pulse-width modulation (PWM) output, is employed. The input power of the heater is controlled by the tuning duty cycle of PWM. The electronics design was proposed in [78]. However, we implemented a PID controller in *LabVIEW* for closed-loop control. The PID values were tuned manually for getting acceptable performances. The experiment includes folding the prototype into two different shapes, starting from a flat configuration. The first folding attempted to valley-fold the prototype to  $60^\circ$  along one crease, illustrated in Figure 1.13 (a). The second folded all the creases to  $110^\circ$  to form a Tetrahedron, as shown in Figure 1.13 (b). This design-by-showing process is then transferred to the control command to control robotic origami. The setpoint values and responses in this experiment are shown in Figure 1.13. The dashed line is the control input, and the solid line, solid line with crosses, and the solid line with points are the readings of sensors 1, 2, and 3, respectively. We can see that the module-to-module amplitudes of shape 2 have some discrepancies from the fabrication, loading effect, and from the customized SMA actuators. However, this “mechanical noise” can be reduced to less than  $5^\circ$  by tuning the control parameters.

The images of the physical folding are shown in Figure 1.13, and the 3D model reconstruction is generated simultaneously with the physical folding. Simultaneous visual feedback can be employed in interactive interfaces. The folding processes of the prototype are recorded by a camera, and we calculate the folding angle in the physical image by tracking the red marker on the tip of the tiles. The calculated angle differences between sensor readings and results from video analysis are below  $5^\circ$ . Experimental results show the capabilities of the robotic origami for multiple sequence folding and possibilities for employing reinforcement learning in robotic origami with studies on the mechanism kinematics and trajectories.

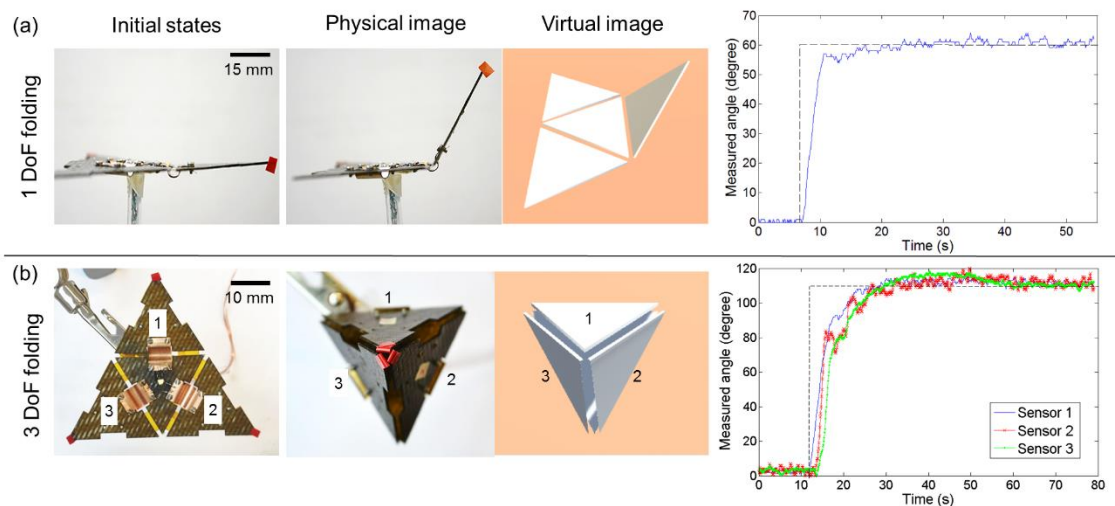


**Figure 1.13 Experimental results of closed-loop control of robotic origami.** The pictures from left to right are i) the initial state of the prototype, ii) the physical folding photo, iii) the reconstructed virtual model of the folding shapes, and schemas, the sensor readings for shape 1 (a), and shape 2(b). Shape 1 folded one tile to  $60^\circ$ , and shape 2 folded three tiles to  $110^\circ$ .

### Manipulation of robotic origami in a virtual environment (Mode 2)

To evaluate the capabilities of the interface for controlling robotic origami, the proposed algorithm for transforming digital information into control commands is implemented in the interface. We tested the algorithm with the four-tile actuated prototype, shown in Figure 1.9(b). We manipulated the virtual robotic origami model through a motion-tracking device. We intended to fold tiles to a tetrahedron shape in 5 steps, and the recorded data from this are shown in Figure 1.14. First, we folded hinge 3, then the bent hinge 1 and 2 together. Third, we folded hinge 1, then folded hinge 2 and 3, respectively. The scenario of folding sequences is shown at the bottom of Figure 1.14(a). The recorded bending angles in the virtual environment are shown in Figure 1.14(a). Then, the algorithm in the control system converts the recorded motion data from the virtual environment to control the commands for the robotic origami prototype, and this is shown as the dashed line in the Figure. The conversion algorithm is adapted to the human factors for manipulation in virtual environments, as well as the characteristics of the prototype, such as sensor sensitivity or settling time of the actuation system. The control results of the physical prototype from sensory feedback are shown in Figure 1.14(b). The control command will only forward to the next sequences when all target values are achieved at a stable state. This algorithm is prominent to thoroughly fold robotic origami in multiple sequences, especially with SMA actuators whose motion is nonlinear and hardly controlled. The largest oscillation in Figure 1.14(b) up to  $20^\circ$  all the actuators were turned on. The larger oscillation is mainly caused by the shared power sources. However, it could be decreased by changing the design of electronics and tuning PID parameters. To extend to higher DoF robot system manipulation, we demonstrate a control interface with manipulation of the dual module prototype, which consists of two four-tile prototypes. The manipulation steps in the virtual environment are shown in Figure 1.15(a) to (d). The prototype was self-folded into the sequences from the teaching in the virtual domain, as shown in Figure 1.15 (e) to (h). This interactive graphical interface to manipulate robotic origami can adapt to any kind of actuator, and these experimental results open up opportunities for a graphical and high-level programming interface for robotic origami. Refer to the Multimedia Extension for the demonstration of interaction mode 2.

The physics-based virtual environment can adapt to different origami structures and robotic origami, as shown in Figure 1.16. For interaction mode 2, we can predefine the arbitrary geometry of the rigid origami structure and then fold it in the virtual environment, as shown in Figure 1.16(a) to (c). This virtual environment could also serve as a simulation tool for robotic origami. Figure 1.16(d) to (f) show the dynamic simulation of Tribot's jumping gait [80]. Tribot has three SMA springs connected between each leg, and we can set the spring hinges in the virtual model. Figure 1.16 (d) shows Tribot standing state. Then, the two SMA springs connecting the top leg and two bottom legs are virtually activated to store the energy of the bottom SMA spring, shown in Figure 1.16(b). We release the stored energy by virtually deactivating the two SMA springs connecting the top leg and two bottom legs to activate the bottom SMA spring. The energy release makes Tribot jump, as shown in Figure 1.16(f). The gait control system can be performed in virtual modeling code and shows the capability of the interface to adapt to different geometries, hardware components, and control systems to manipulate and simulate.

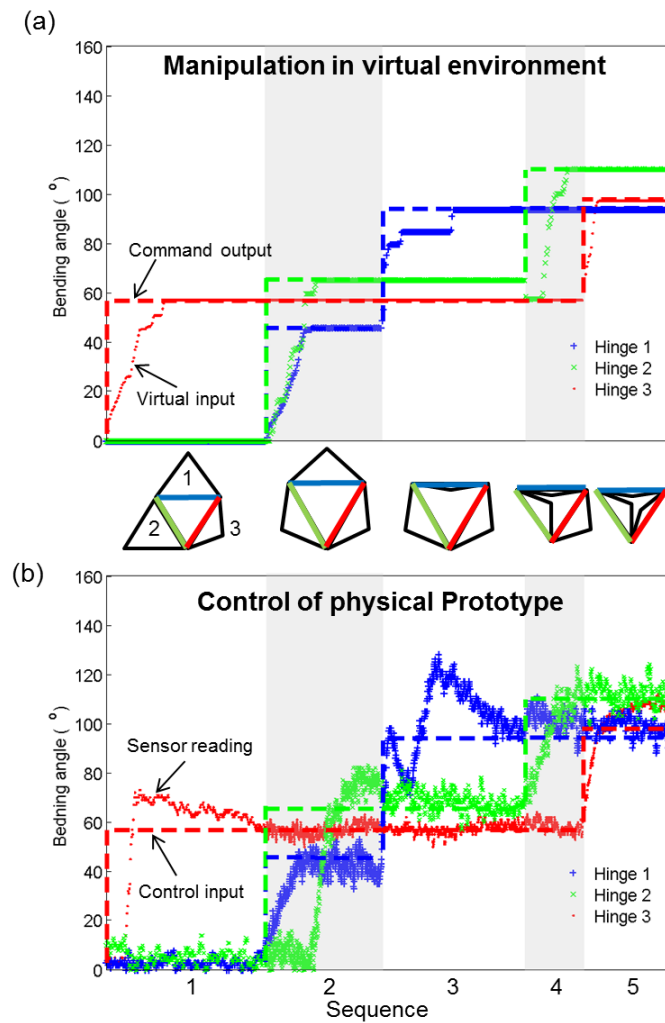


**Figure 1.14 Experimental results of the algorithm for conversion between digital data of manipulation and of control command.** (a) The scenario of folding sequences and the schematics of folding shapes are at bottom of the figure. The bending angles acquired from the virtual environment are shown in different marks and the solid line shows the converted control commands from recorded data by the algorithm of control command conversion. (b) The control results of the physical prototype are recorded from bending sensory feedback. The solid lines show the control input for control physical prototype.

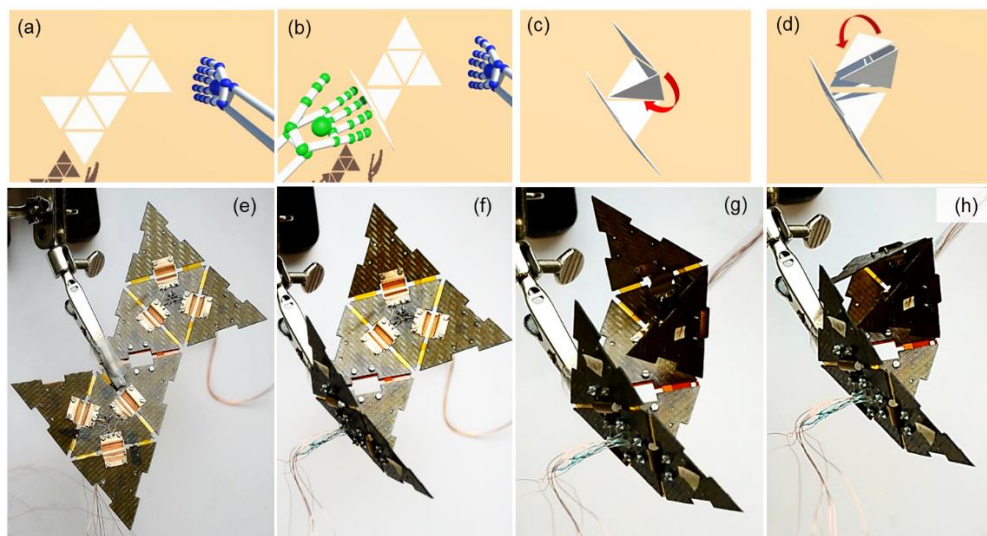




**Figure 1.15 Experimental results of teaching a robot by demonstration in a virtual environment.** The folding motion in the virtual environment is shown in (a) to (d), and the self-folding robotic origami was achieved following the sequences that we demonstrated in the virtual environment, in (e) to (h.)

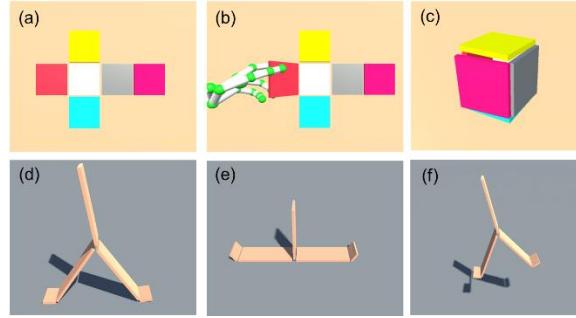


**Figure 1.16 The modeling with different geometries and hardware.** (a) to (c) show the process of folding an origami cubic box, and (d) to (f) show simulation of Tribot jumping.

### 1.1.6 Conclusion

#### Capabilities and limitations of the current system

In interaction mode 1, the effectiveness of the kinematics model is in calculating the relative coordinates of all the tiles on the robotic origami and reconstructing the geometry of robotic origami using sensory feedback. The sensory feedback provides the bending angle of each foldable joint on the robotic origami. This individual angular reading is the input for the kinematic model. Another required input is the dimensions of each tile. This model can be applied to multi-vertices and arbitrary crease pattern design. The limitations of the origami structure used in this kinematic model are assuming rigid tiles, and it should be in one piece. Kinematically, this dictates the thickness to be non-zero and the creases to be straight, not curved.

The software we developed for validating the kinematic model can generate the 3D virtual model of robotic origami simultaneously with the corresponding robotic origami prototype. To generate the 3D model, all the tiles on the crease pattern of the origami structure must be described by the nodes. Since we assume the origami structure thickness is zero, the 3D model construction has a geometric bias when stacking multiple layers.

For the hardware, the fabricated prototype with 1.5 mm thickness can fold and sense the bending angle to  $\pm 180^\circ$  on single joint folding. However, it faces foldability problems when stacking several layers due to the thickness of the tiles and length of the joints that may be solved by structural design or kinematic synthesis.

In interaction mode 2, the kinematics of interaction is managed by the physics engine, built in Unity system. The physics engine can handle origami structures that contain up to three vertices rather than a single vertex tree structure. The created virtual environment allows the user to manipulate the virtual origami model through hand motion input. However, numerous mechanical constraints increase the calculation load for a real-time simulation. The simplification of the interaction model can upgrade the robustness of the tool for handling more complex structures. Although the physics engine can handle more than tree structures

only, the control methodologies and algorithms for multiple-vertices origami structures have not been thoroughly investigated.

The developed prototype is a low-profile, lightweight actuated tangible interface that has the ability to transfer to different 3D geometries from a single 2D configuration. While the presented origami hardware platform only folds in a single direction, control systems and algorithms allow the robotic origami to fold to static shapes within controllable bending angles on the joints in multiple folding sequences. However, the current system lacks the ability to follow a trajectory or folding speed. Also, the folding motion is not reversible since it does not have antagonistic actuators.

## **Conclusion and outlook**

In part 1, we present an interactive graphical interface for controlling and simulating robotic origami. We created a virtual environment and interactive methodology to manipulate a virtual robot that enables the user to intuitively control robotic origami. For simulation, we developed an algorithm to solve the kinematics of origami using distributed sensory feedback. We designed and fabricated two prototypes to validate the capacity of the interactive interface. The first prototype is a foldable sheet with distributed angular sensors, and experimental results show that it can reconstruct various 3D shapes. The second prototype uses sensors and actuators to produce a virtual model-based graphical interface to command and control the folding process of the robotic origami. These interactive interfaces and their kinematic model simplification algorithms for folding as well as sensor/actuator embedded prototypes could improve the often intuition-based origami robot design process. This implies an approach for tackling one of the research questions that we proposed: *How can we implement controllable actuation toward complex ranges of motions and functionalities?* The distributed sensing-based algorithm helps us to understand the behaviors of multi-DoF active systems. The experimental results also reveal opportunities for further applications such as high DoF tangible interfaces and actuated tangible interfaces. In the future, we will work on the amalgamation of the two interaction modes to achieve tight two-way communication and high-fidelity interaction for human-robot interfaces. However, the current virtual environment still has some restrictions, including the soft component modeling, and a higher DoF interaction may be challenging to perform accurately. Algorithms and control methodologies for more complex origami structures as well as nonlinear actuators and components are needed to push forward modeling-based control interfaces.

## **1.2 An interactive control interface for reconfigurable modular robots**

Since we have developed the control interface for multi-DoFs robotic systems in part 1, we would like to extend the capability of the control interface for modular robotic applications. The unique control scheme and the multi-agent systems could be challenging for direct human interaction.

### **1.2.1 An overview of reconfigurable modular robot control**

Many advanced robots provide a wide range of abilities for programmed tasks such as grasping, running, jumping, or even specific skillsets for house services or exploring undefined environments. Although these robots have highly specialized designs to perform tasks well in specific domains, they are often not designed to have the flexibility to adapt the design to different tasks or changing environments. As well as a trend for high complexity robotic system designs, the field of reconfigurable modular robots provides a flexible solution based on rearrangeable connectivity of modular parts [81]. Reconfigurable modular robots are composed of a set of simple modules that can be disconnected and reconnected to form diverse arrangements to empower new functionality. The modules contain active connecting mechanisms that enable them to morph their shapes to adapt to the task needed. Another versatile platform is origami design: origami-inspired engineering has been influential in many engineering fields, including architecture [82], deployable structures in space[83], and biomedical devices for drug delivery [13]. Origami-inspired robots have given researchers innovative ways to design mechanical components and structural transformations that overcome conventional design constraints [84]. The concept of folding offers an effective method to form three-dimensional (3D) geometries from two-dimensional (2D) lightweight structures to rapidly achieve desired shapes [38], [85] or functionalities such as grasping [86], crawling, jumping, and flying [87]. Mori, a modular origami robot developed at the Reconfigurable Robotics Lab (EPFL, Switzerland), merges the features and advantages of origami robots and reconfigurable modular robots with its quasi-2D robotic modules [88]. While connecting one module to another, Mori can fold into various 3D shapes for reconfigurability and meeting the requirements of target tasks. The key characteristics of Mori being, modularity, mobility and provide promising features for a versatile deployable structure for space exploration, adaptive morphing structures, and human-robot interaction (HRI).

One of the research visions for Mori has been to bring modularity and reconfigurability for better HRI applications in daily life. However, one of the critical issues to address is the high-complexity and time-consuming programming and controlling of robots for non-experts. Robot control and programming require transferring abstract concepts such as coordinates and coordination in space or parameter definitions of different tasks using mathematics, physics, and computational skills. Furthermore, understanding how to generate suitable and efficient configurations for certain dynamic behaviors or tasks also remains a barrier. The development of high-level programming methods and tools has reduced the obstacles for novice users to a certain extent. For instance, 3D CAD-based programming, icon-based graphical control interfaces, and program by demonstration have been developed for research[89] and also applied in the industry[27]. Recently, gesture-based interactive **natural user interfaces** (NUI) revealed a potential solution for primary and expressive communication with modular robotic systems[90]–[93]. Researchers used palm orientation to control different pre-programmed locomotion modes of chain-like robots[91] and used arm directions to set destinations for robots to move to [93] or to move their end-effector towards the desired direction [90]. These studies provide promising ways to control entire configurations or to perform preprogrammed tasks for modular robots; however, they do not provide a comprehensive control method for reconfigurable modular robots. That is, the possibility to reconfigure the entire geometry of a robotics system by assembling or disassembling the modules for different functionalities is not possible. Moreover, even if it were to be possible, this gesture-based control system has a



common issue that is too many gestures would be counter-intuitive and difficult to learn and to memorize for practical use.

For improving the user experiences and controllability of the control interfaces, [94] presented a modular robotic system with mixed-reality interaction, which allows users to design and assemble the modules with different functionalities by hand gestures with virtual guidance through augmented reality (AR) headset. This research proposed a well-defined workflow and user interface (UI) design for interactively control the robots. The UI design focuses on the instructive and informative assembly of different functional modules for DIY robots. In contrast, [95] developed a virtual reality (VR) environment for building arbitrary structures by robotic modules with immersive interactions. However, the previous research did not have the flexibility for selecting and commanding individual modules and a method reconfiguring the entire robotic system with larger numbers of modules. High-level intuitive control of a multi-robot system is still an open problem due to its high DoF and complex kinematics. To upgrade the controllability of NUI in modular robots, implemented kinematics and planning algorithms with reconfigurability, modularity, and functional adaptability should be further investigated. Although there are substantial studies on the theory and software for helping or even automating the design of origami [96] or modular robots [97], [98], there has been relatively little research so far that considers both the kinematics of origami and characteristics of robot components. Thus, the barriers to controlling modular origami robots for non-expert users still remain. Motivated by the effectiveness and intuitiveness of NUIs, in this manuscript, we introduce a novel interactive UI to interact with modular robots using hand motions. For the interface design, we developed multiple interaction modes for further enhancing the controllability of modular robotic system.

While we tried to address the challenges for controlling reconfigurable robotic systems, the applications related to HRI are also the major importance in this research. One of the promising applications would be the shape-changing interface that leverages users' perception and recognizing the digital content or data. Recently, several researchers investigated collaborative tools for immersive and rich sensation rendering through VR or AR techniques [99]. [62] proposed an actuated tangible interface that can enable synchronized physical interaction and real-time embodiment and manipulation for collaborative works. There are several grand technological challenges that should be addressed, such as toolkit and cross-platform software interface for development, higher resolution with miniaturized devices, and integration of multiple modalities [100]. Reconfigurable modular robots could be a suitable candidate for addressing such challenges in current researches with their versatility and potential of scalabilities for shape morphing. [101] proposed a 2.5D robotic assembly system for enhancing the tangible interaction with VR. [102] demonstrated a homogeneous self-reconfigurable modular system that can dynamically change its geometry to fit different functionalities. However, these systems still have some limitations, such as discrete motions and limited dimension and DoFs of movements which limit the possible topologies. Furthermore, the restricted dynamic user interactions during reconfiguration also hinder the smooth and continuous interactions.

Thus, we also investigated the design of dynamic multi-modalities interactions using Mori to overcome the constraints of limited DoFs and discrete controlled motions.

### 1.2.2 Interactive UI design for modular robots

In this section, we first describe the principles and overall system design. Then, the detailed interactions design, virtual environment constructions, and hardware are discussed in the following subsections.

#### Overview of interactive UI

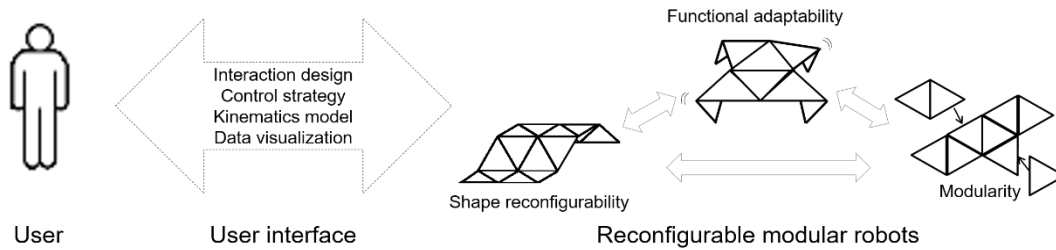


**Figure 1.17** A novel user interface designed for controlling reconfigurable modular robots can achieve the main features of the reconfigurable modular robots through intuitive interactions.

The main motivation of this research is to create an intuitive and interactive UI for controlling reconfigurable modular robots, as shown in Figure 1.17. To tap potential capabilities of modular, reconfigurable robots, the control methods should provide controllability for modularity, reconfigurability, and functional adaptability. That is, the proposed control methods need to be able to separate or combine modules as well as to deliberately morph the geometries or configurations for desired functionalities. The UI we propose contains kinematics modeling for understanding the behavior of robots, an interaction design for people using intuitive gestures to command the robot, and control strategies that transform between the kinematics of robots and human input. Furthermore, we also added data visualization, such as a 3D virtual model of the robot for effective communication between humans and robots.

#### Control sharing in human-robot interaction

Humans and robots have complementary abilities for performing tasks. Humans have great capability in rational design and high-level planning in an unknown environment. In contrast, robots have the competence for performing programmed tasks precisely and reacting rapidly [103]. How to fuse and maximize the performance of a human-robot interactive system is a challenge, especially for a multi-robot system. The design of interaction, intuitiveness, cognitive limitation of human, and autonomy level is coming into the picture to build an interactive UI for multi-robot systems. The relations of cognitive complexity with the number of robots were described in [104], as shown in Figure 1.18. The complexity  $O(n)$  for a human to manipulate a multi-robot robotic system arises exponentially while the number of independent activity  $n$  that needs human to perform for each of the individual robots increase. It is especially critical for designing the interaction that scalable for the system with many independent robots.

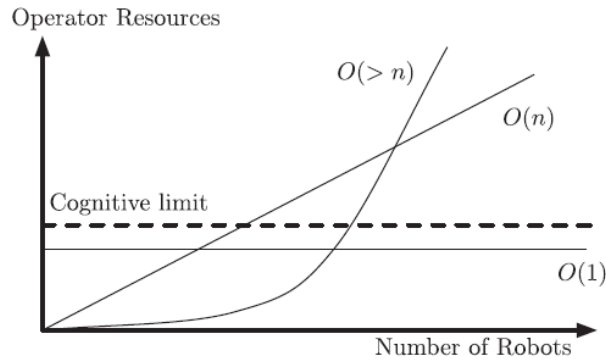


**Figure 1.18 Concept of control complexity in a human– multi-robot system[104]**

We use Mori as the physical modular origami robotic platform to demonstrate the proposed control methods. Previously, Mori was controlled by: (1) using a remote-control pad for manually folding up each hinge, (2) implementing an onboard accelerometer and proximity sensor for autonomously programming the tasks. The first method is good for controlling three active folding joints on a single module. However, it is hard to extend to multiple module control due to too many buttons to manipulate at the same time. The second method is only suitable for developers who can preprogram the task for closed-loop control. To meet the need for an intuitive way to control robots, we propose a new interactive UI in this section. To develop an interface for intuitively controlling and manipulating modular origami robot systems, the kinematics and dynamics of the robot should be well understood and modeled. However, the kinematics of origami robots is complex for a novice because of their coupled actuation and high DoF. For users, the easiest way to manipulate origami is by hand. So, we developed an interactive graphical interface to control and interact with Mori in a virtual environment.

To use hand gestures as system input, we propose a gesture set and corresponding algorithms for recognizing hand gestures interacting with a virtual model of Mori. We propose two major interaction modes for manipulating virtual Mori to achieve the scalability and flexibility of control for both the whole robotic system and individual module, as shown in Figure 1.19. The first interaction mode is to globally manipulate the robots model by the way similar to folding origami directly with hands in reality. This mode allows users manipulate the robot without memorizing any gestures and understanding of complex coupling kinematics of connected modules, which relieve the obstacles for the usage of the control interface, as shown in Figure 1.19(a). The second interaction mode is for selecting and controlling the individual module or a subset of the modules among the whole robotic system. Users can use the index finger to select which module to manipulate and palm orientation to control the orientation of the selected module in 3D space, as shown in Figure 1.19(b). At the same time, users receive the feedback of their commands visually by interaction simulations. This simulation not only provides an intuitive pathway to control the robot but also informs the dynamic status of the robotic system. Then, the virtual simulation results are transformed to the control commands of the physical robot.

To enable the bi-directional multi-modality interactions for tele-collaboration applications, we designed interaction mode 3 to use robot modules to be both the control output and output platform: it produces and displays the control output as well as it receives control input. We

achieve this by embedding sensors on the robot modules for detecting hand gestures, as shown in Figure 1.19(c). Thus, the robot can be used as the input/output interface for controlling and displaying digital information. We integrated the distance sensors to detect the distance between hands and modules, and the distance information could be transferred as the 3D position information for the module (i.e. height between ground and module center). Thus, the robot reacted as similar to be pressed down while the user's hand approaching. Although the current integration is straightforward, it implies the capabilities and flexibilities for integrating multi-I/O system to further enhance to immersive interactivity of UI.

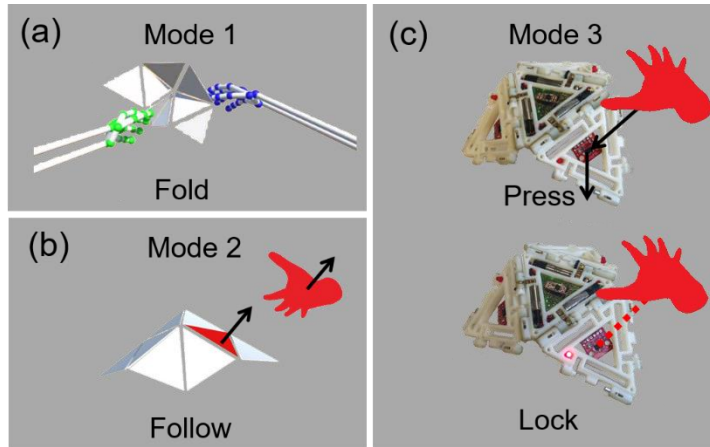


**Figure 1.19 The proposed control methods for reconfigurable modular robots using hand gestures as input are shown in the virtual environment.** There are two main interaction modes for manipulating the virtual model. (a) Mode 1: for global geometry changing, this mode allows the user to fold the virtual model directly. (b) Mode 2: for individual module control, this mode allows the user to use the orientation and position of the palm to move the selected tile in 3D space freely. (c) Interaction mode 3: HRI mode allows users to interact with robots directly. The module acts as pressed down while the hand approaches and the modules are locked in 3D space while the user's hand holds at the same position for a period of time. The LED on the module indicates the locking status of the module.

### Modular robotic origami platform

The modules of the modular origami robot, Mori, as first presented in [88], are quasi-2D triangles that can be connected to one another and then reconfigure into any desired configuration, as shown in Figure 1.20. The body of each robot has the shape of an equilateral triangle, such that any side of one module can be connected to any side of another. Each edge accommodates two genderless mechanisms that allow the system to be reconfigured.

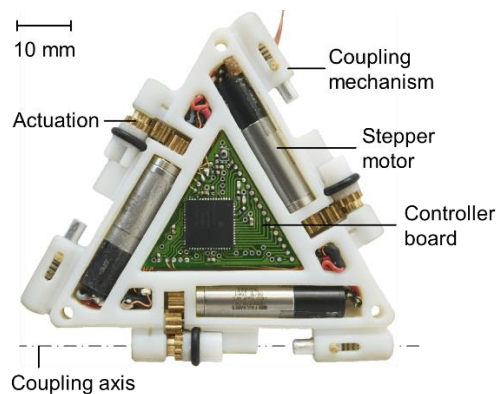


**Figure 1.20 The modular origami robot porotype, Mori.** Contained with the single module are three actuators, sensors, and on-board controller. The symmetrical and genderless coupling mechanism allows a module to attach to another on any side. The dashed line is the axis for engagement and folding [14].

### **The interactive control method constructed in a virtual environment for reconfigurable modular robots**

To create an interactive control method, the virtual environment serves as a telemanipulation interface for visualizing the manipulation process. The physics-based simulation and the transformation of physical reality can greatly augment the immersive sensation of interactivity in virtual manipulation scenarios.

The first step for creating the virtual environment for simulating and visualizing the interactive manipulation process is to create the virtual model of the robot. The virtual environment setup is constructed on Unity. Unity is a game development platform that offers physics-based simulation by a built-in physics engine. It has also been used for virtual reality development and has good capabilities for robot behavior simulation to especially include human-in-the-loop for HRI applications[105], [106]. Thus, we used the built in physics engine of Unity to simulate the kinematics of Mori based on the rigid origami kinematics and the multibody system. The rigid origami model treats each facet of the origami as rigid links and their creases as revolute joints. The multibody system describes the dynamics of interconnected rigid or flexible bodies, and motions of the bodies are described by their kinematic behaviors. We defined each triangular module of Mori as a single rigid body which is the basis block for the simulation. The interconnection between modules is revolute hinge joints. The detailed model, setups, and methods of virtual environment construction have been discussed in part 1.

To achieve the modularity of the modular robotics system in the virtual environment, each virtual module should be able to connect to another to form a new configuration. Thus, the first step of the manipulation is to create modules for manipulation. We use both hand pinch move as the command gesture for creating the new modules, as shown in Figure 1.21(a). The module is created at the mid-point between the index fingertips while the pinch distance is smaller than the threshold. That is, thumbs and index fingers are touched. The second step is constructing the desired configuration by connecting modules together, as shown in Figure 1.21(b). The virtual hand model generated in the virtual environment utilizes the tracking data from Leap motion, (Leap Motion, Inc.), an optical hand motion tracking device. The user can grasp the virtual module to contact another module. The contact point and orientation of the module are analyzed for generating the connecting joint while the collision happens between two virtual modules. A revolute hinge for connecting two modules is implemented after the contact between two modules. This step allows the user to design and build arbitrary 2D configurations to achieve the inherent scalability of the modular robotics system.

In order to achieve the desired functionalities by morphing the geometries through interactive manipulation, here we propose two main interaction modes for reconfigurable modular robots by using hand gestures, as shown in Figure 1.19. As mentioned in the Section II. A, mode 1 is inspired by the very beginning of the idea of origami, using hands to fold the paper. The ultimate goal of mode 1 is to have a virtual deformable sheet with infinite DoFs that can be folded by hands and change the overall geometry. Direct manipulation of objects is one of the most intuitive ways to form arbitrary geometries. The mode 2 mainly uses the index finger for

selecting the target module and controlling the selected module in 3D space. While moving the target module, other modules in the system move accordingly based on the kinematic constraints. We can control any module in the system by applying mode 2. With these two modes, we can have scalable controllability from individual module to entire robotics structure with multiple modules for reconfigurable modular robotic systems. Similar to the step of constructions, mode 1 also enables users to manipulate the virtual model of Mori with hands. Through the folding motion, we can teach or program the folding sequences to transform to the target geometries or the final configuration in the virtual environment. The virtual model of Mori is floating in midair without gravity effect and the virtual model stops movements after the user stops touching it. Finally, the dihedral angles between the modules are calculated for robot control. Mode 1 could be an effective solution for morphing static geometries while simplifying the gesture and task-abstraction for manipulation is the trend for gesture-based interactions. In order to improve the precision and maneuverability of mode 1, we proposed a gesture set for locking selected modules in place, as shown in Figure 1.21(c) and (d). Sometimes undesired motions occur while manipulating the modules. This is mainly due to the complex coupled kinematics. This proposed gesture set is helpful for this case, in order to fix certain formation and to designate modules to manipulate. This gesture set employ right-hand index finger to select a module and with left-hand fist to change locking status. First, one module can be selected by pointing with the right-hand index finger. On the simulation, there would be a ray casted from the index fingertip and along with pointed direction. The module becomes a provisional target while the ray hits on it. There is a light point at hit point the object's surface to highlight which module is selected. Second, we use the left-hand fist gesture hold for 2 seconds for changing the locking status of selected modules. The locked module is set to kinematics mode that is not governed by the rigid body simulation. Thus, the locked modules are fixed in 3D space, and the hinges connected to the unlocked modules are still valid for the kinematic constraints for calculating the motions of unlocked modules. The sequences of selection and manipulation of the modules are shown in Figure 1.22.

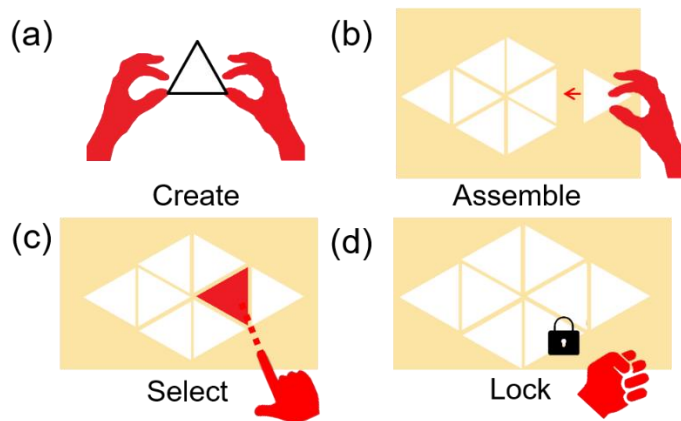


**Figure 1.21 The proposed hand gestures for manipulating the virtual model of the reconfigurable robotic system.** The creation of the modules by both hands pinch move (a). The construction of the desired configuration is done by connecting the modules held by hand (b). For individual control in mode 2. The target module can be selected by using pointing gesture (c). Then, the selected module can also be locked in 3D space for giving constraints using fist gesture (d).

For continuously and dynamically controlling the selected modules of Mori, we designed mode 2 using palm orientations and positions, as shown in Figure 1.19(b). The palm position and orientation are commonly used in hand gestures, and they can be easily and effectively detected by Leap motion. First, the initial 2D planar configuration of Mori modules lies on the x-y plane (z-axis out of the plane of the paper). The user's index points at the virtual model of Mori for selecting control target, as shown in Figure 1.21(c). While the target module is selected, the user can use palm orientation for moving the selected virtual module. The vector of out of the front surface of the palm is extracted for generating the normal vector of module plane, as shown in Figure 1.19(b). Thus, the orientation of the surface plane of the virtual Mori module follows the palm. By applying this mode for robot motion control rather than using other gestures, we can reduce recognition errors and tracking loss. Furthermore, this mode provides more agile motions control that could be a step towards locomotion control.

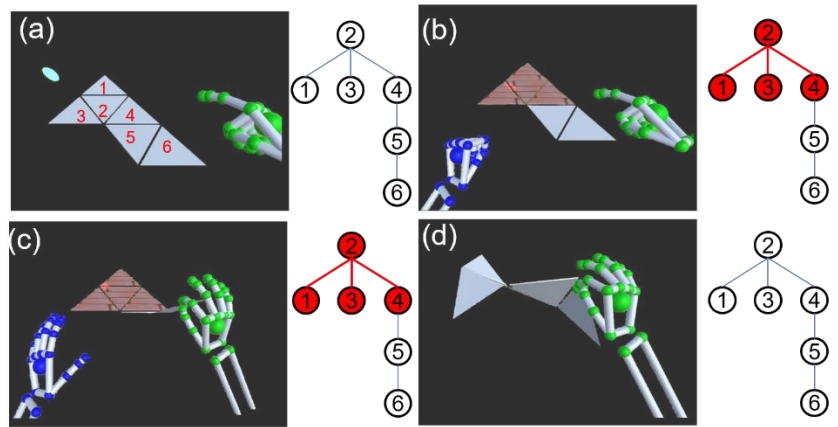


**Figure 1.22 The sequences of selection and manipulation of the modules (left figure) and their corresponding rooted tree (right figure).** The rooted tree shows hierarchical structure of the layout. The modules are represented as circle in the rooted tree and the joints between modules are represented as the lines between the states. Initial configuration of the modules without any module locked (a). The user used the left hand fist gesture for changing the locking/unlocking status and right hand to point to the module to control (b). The red color in the rooted tree shows the locked status of the joints and modules. The joints can be still active while modules are locked. However, the movements of the children are constrained by parents (c). The locked modules can be unlocked again and moved by hands without constraints (d).

### Implementation of control methods and transferring hand gestures to robot control commands

The interactive interfaces and control methods we propose are independent of the hardware components. In other words, it is possible to implement algorithms that can adapt to the various hardware components (i.e., sensors and actuators) to generate control commands. However, for transferring the hand gesture input, not only the kinematics of the robot should be analyzed the equipped sensors and actuators should also be considered.

The configuration of Mori we used in this section has a central module attached to three passive modules on each side, as shown in Figure 1.19(c). This floating three-DoF platform demonstrates one of the real-life applications that could be achieved by Mori. The proximity sensor mounted on the bottom and accelerometer mounted on the top can be used for closed-loop control of the three DoF platforms. The onboard sensors provide the row, pitch, and height of the central module, which can be denoted by  $\alpha$ ,  $\beta$ , and  $h$ , respectively. We have constructed the kinematics model based on these three parameters [88]. The control

parameters used for controlling the three-DoF platform are shown in Figure 1.23. In mode 1, the user folds the virtual model and the dihedral angles between modules extracted for control input for the robots. The dihedral angles can be converted to  $\alpha$ ,  $\beta$ , and  $h$  by solving the kinematics of three DoF platform. In mode 2, the user uses the palm position and orientation as control input for constructing the virtual model and generating control commands. Mode 3 uses the distance between hands and sensor,  $D$  as a control input. Then,  $D$  is transferred to the bending angles of the hinge for generating affordance as being pushed down by the hand. However, the inherent perceptive limitations of humans, such as distance perception and the limitations of the physical prototypes, such as backlash of atics of three DoF platform. In mode 2, the user uses the palm position and orientation as control input for constructing the virtual model and generating control commands. Mode 3 uses the distance between hands and sensor,  $D$  as a control input. Then,  $D$  is transferred to the bending angles of the hinge for generating affordance as being pushed down by the hand. However, the inherent perceptive limitations of humans, such as distance perception and the limitations of the physical prototypes, such as backlash of gears and errors of sensors, reduced the precision and fluency of the interactive UI. To improve the control experience, we applied two scaling processes between the user's-hand workspace and the robot workspace. The scaling factor  $S$  is smaller than one for precise height control, and adaption of the workspace of the three DoFs platform since the workspace of hands is larger than the robots. The proposed UI can be customized for different types of reconfigurable robotics systems by the implementation of the kinematics model and modifications of interaction mechanisms. The control parameters and the transforming algorithms can also be customized to adapt to different hardware components (e.g., using bending sensors on the hinges) implemented with the proposed interactive UI.

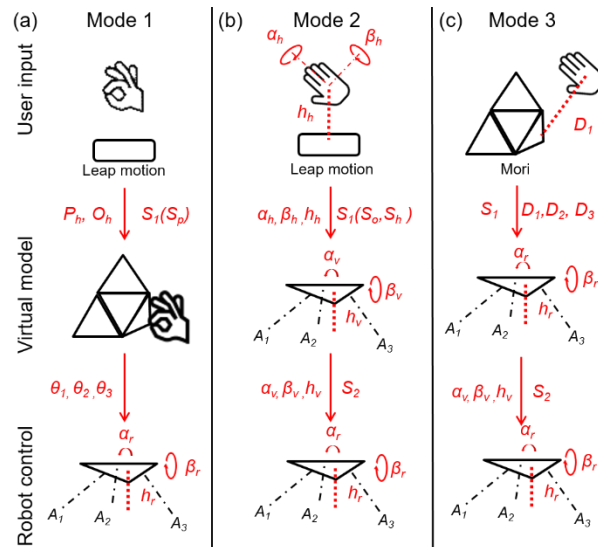


**Figure 1.23 The control parameters of (a) mode 1, (b) mode 2 (c) mode 3 for controlling three DoF platform.**  $P_h$  and  $O_h$  are the positions and the orientations of hands.  $S$  is the scaling factor for transforming the parameter in different systems.  $A_1$ ,  $A_2$ , and  $A_3$  are the end points of three legs.  $\alpha$  and  $\beta$  are the row and pitch angles.  $h$  is the height between surface and ground.  $D$  is the distance between hand and controlled modules.

### 1.2.3 Implementation and experiment

In this section, we evaluated capabilities of the proposed UI for modular reconfigurable robots. With the proposed control methods with software and hardware setup integrated, we



designed several experimental scenarios to demonstrate the capabilities of the proposed control methods.

The system schematic of the proposed UI for controlling reconfigurable modular robots is shown in Figure 1.24. This interface consists of a display showing a virtual environment for manipulating robotic origami, motion capture devices for the user to give the input by hands and algorithms for transforming the information from the virtual environment to control the physical prototypes. The virtual environment consists of a 3D model of the robot, a 3D model of the hands and the interaction mechanisms between the robot and hands to give users visual perceptions. To track the user's hand gestures, we use Leap motion to acquire system input. The proposed control methods and the construction of virtual environments are implemented in *Unity*. The proposed algorithms for converting the virtual simulation results to control commands are programmed by Labview. A microcontroller board Arduino Uno is used for sending commands and receiving the sensor readings. For the collaborative shape changing interface.

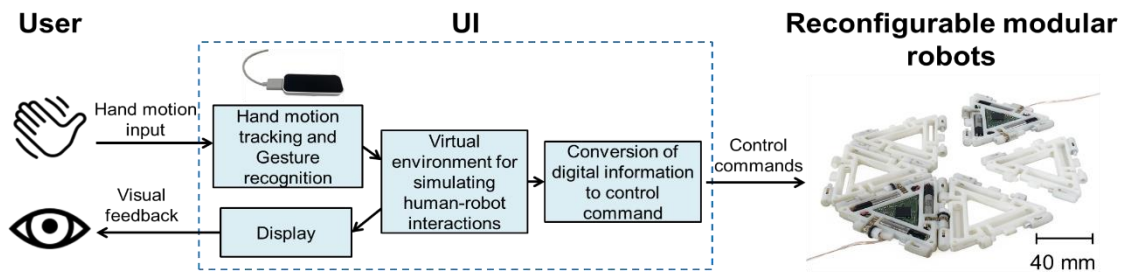


**Figure 1.24 The system schematics of the proposed UI for controlling Mori.** The user's hand gestures are tracked and modeled in a virtual environment using a hand motion tracking system, Leap motion. The tracking data and virtual hands are used for manipulation of the virtual model of Mori in the virtual environment, and the simulation results generate the control command for the physical robot to execute.

### Experimental evaluations of the capabilities of interactive control methods

We examined the effectiveness of two control modes with the three-DoF platform configuration and compared the control input by users with the control performance executed by the physical prototype. First, we tested control mode 1. The comparison between virtual simulation on display and the task execution is shown in Figure 1.25. The folding sequences are divided into two steps. First, we folded the right hinge as shown in Figure 1.25 (a), then folded hinges 1 and 2 together as shown in Figure 1.25(b). The corresponding folding motions performed by the physical prototype are shown in Figure 1.25(c) and (d). The physical prototype can efficiently change its geometry along with the folding behaviors of users. However, mode 1 might not be the best solution for continuously and precisely controlling a specific module among the entire system. In this case, the orientations of the three-DoF platform are not easy to manipulate due to the complexity of manipulating three hinges simultaneously with two hands.

To evaluate the capabilities of continuously manipulating individual modules in the system using mode 2, we designed a specific system input that moves and rotates the selected modules at the same time during the experiment. The generated virtual model of the hands and Mori can serve as a telemanipulation, and the photo of the hand gesture for mode 2 is also shown in Figure 1.26(a). The user slowly lifts up the height of the palm while rotating the

palm orientation to create a helix-like pattern in Row-Pitch-Height space, as shown in Figure 1.26(b). Finally, the performances of the control results are shown in Figure 1.26(c). The mean differences between control inputs and sensor readings are  $M_{Row}= 4.67^\circ$ ,  $M_{Pitch}= 2.31^\circ$  and  $M_{Height}= 2.11\text{mm}$ . The large difference in the row angle happened with input angles higher than  $20^\circ$ . This is due to the limitation of tilt angles we set in the controller to keep the stability of the system. A small delay in the tracking data might due to the backlash of the gears. The experimental results show the capabilities of conversion of the hand gestures to the control of the modular origami robot geometry transformation.

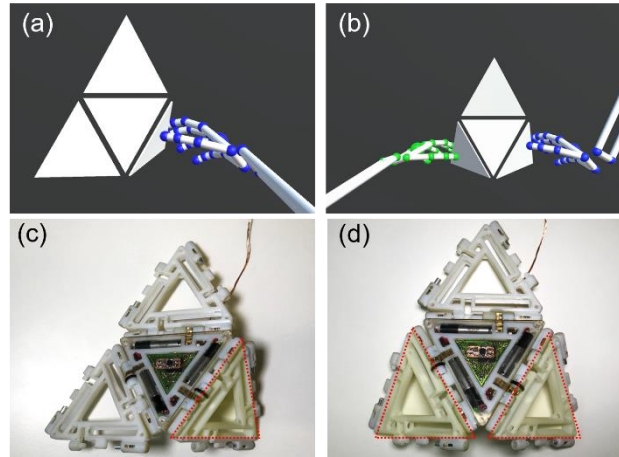


**Figure 1.25 The experimental results of controlling Mori by mode 1.** The folding motions in the virtual environment are shown in (a) and (b), and the physical prototype achieved the folding motions in (c) and (d) which we demonstrated in the virtual environment.

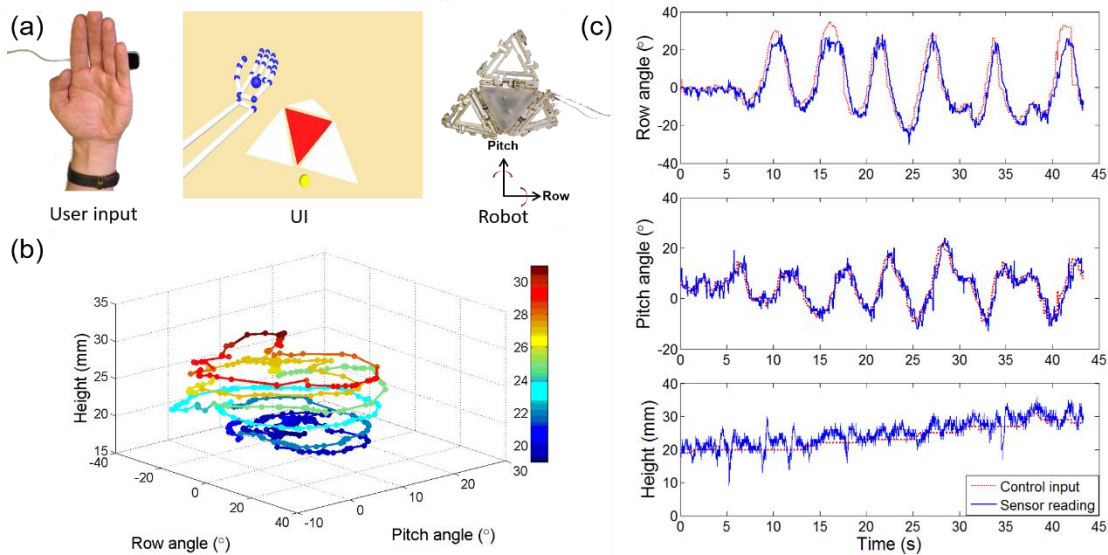


**Figure 1.26 The experimental results of using palm orientations to control the motion of Mori.** (a) The 3D graph of input signals for commanding Mori. (b) The virtual environment generates the models of Mori and hands on display. (c) The physical prototype followed the orientations of the palm. (d) The control results of the physical prototype are recorded from the accelerometer and proximity sensor installed on the central module. The dashed lines show the control input for controlling the physical prototype.

### The implementation of mix-reality and the capabilities for multi-module control

The developed UI can implement the mix-reality technologies to more effectively convey the dynamic status of Mori by visualization, on-board sensor reading rendering on the real image.

Mix-reality is the merging of real and virtual worlds to generate a new environment. And the physical objects not only can exist but also react with one another [107].

We added an external camera for tracking the image tag on Mori and monitoring the control performance on display, as shown in Figure 1.27(a). The coordinate system in black color was attached to the ground surface, and the coordinate system in red color was attached to the image tag. Then, we transferred the on-board sensor reading to create virtual objects that render on the real image of the robot. We created a virtual plane that is attached to the surface of the central module. Although the virtual plane could rotate along with the image tag, the physics for virtual objects did not change according to the image captured by the camera. That is, the direction of gravity in the virtual environment was toward the ( $-z$ ) direction in Fig 1.27(a). For connecting the physics with the real image, we used the tilt angles from on-board sensory feedback to calculate the coordinate transformation. Then, we could generate a gravity along the ( $-z$ ) direction in the virtual system. A virtual ball was placed on the virtual plane. The rolling direction of the virtual ball provides a common frame for visualizing the changing of tilt angles. The results show a visual representation for understanding the dynamic status of the robot and also reveal the potential of utilizing the proposed UI integrated with reconfigurable modular robots for creating a data physicalization interface [108]. To extend the controllability to higher DoF systems using both hands, we demonstrate an experiment manipulating a six-module prototype, as shown in Fig 1.27 (c) and (d). The two central modules were controlled by both hands using mode 2. The two virtual central modules are highlighted by the red dashed line in Figure 1.27(d). The row angles for both modules were controlled by the left hand only due to the kinematics coupling. Because only a single motor was used to connect the two central modules in this experiment, the mean differences between control inputs and sensor readings increased, especially in the pitch direction ( $M_{Pitch}=5.26^\circ$ ). However, continuing work to minimize the coupling effect and optimize the control parameters will open up opportunities for high DoF system control.

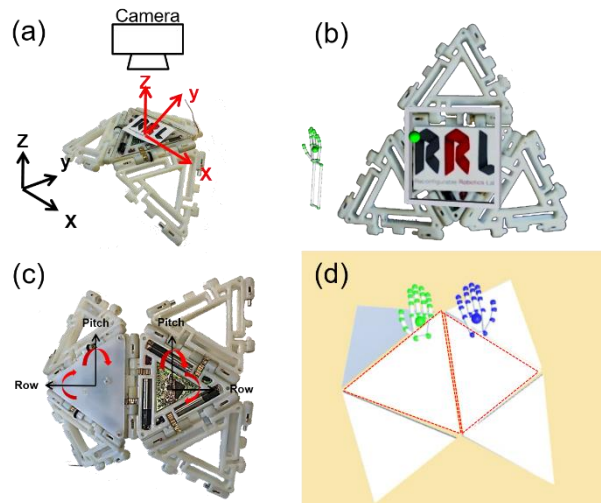


**Figure 1.27 The mixed-reality implementation and multi-inputs for controlling modular robotic systems.** (a) The experimental setup for implementing mix-reality technology with the control interface. (b) shows that the virtual objects are added to real images. The rolling directions of the green ball reveal and visualized the onboard sensory data. A six-module robot was controlled by the two central modules using both palm orientations shown in prototype (c) and virtual environment (d).

### 1.2.4 Conclusion

In part 2, we described an interactive UI developed and studied for reconfigurable modular robots is presented. We introduced a design of interaction mechanisms for using hand gestures to manipulate reconfigurable modular robots complying with the robot's kinematic constraints. The proposed control methods can bring about the three key characteristics of reconfigurable robots: Modularity, reconfigurability, and functional adaptability can be achieved by module reassembly, individual module control mode, and global-geometry control mode. We integrated the hardware/ software to demonstrate the proposed control methods on a physical prototype. The experimental results show the efficacy of the proposed control interface for HRI applications and the capacity of a modular origami robotic system. Furthermore, the implementation of mix-reality techniques and multimodal I/O reveals that the proposed UI could be a bridge for two-way communication between the physical and digital worlds. In the future, we will work on the development of control methods to further exploit the capabilities of Mori, such as its mobility and autonomy, as well as for high DoF robotic systems control. The capabilities of the system should be quantitatively verified with user studies. The module assembly function should be further validated with mobile prototypes with automated attachment mechanisms. Similarly, the function for separation of the modules should also be developed and tested for accomplishing better control for modularity. Another future goal is the amalgamation of gesture and autonomous control modes for achieving intuitive high-level task programming.

## 1.3 Interaction design and validation for a wearable haptic feedback device

We have described the control interface design for human-robot interaction with different robotic systems. In the third part of this chapter, we would like to study the how can we exam the effectiveness of a human-robot interactive system. We design a comprehensive and coherent tactile information transfer system and an experimental protocol for validating a soft wearable robotic system with tactile feedback.

### 1.3.1 An overview of Soft wearable devices for haptic feedback

Soft robotics has become a tempting field in robotic research in the past decade. Soft robots provide safer interaction with humans due to their compliant material properties. The advance in actuator/sensor design, materials, fabrication process, and control methods of soft robotics brings a new paradigm, especially for wearable systems. Soft robots' inherent compliance provides flexibilities for adapting to the human body and abilities to conform to complex human motions. Soft wearable system has been developed for task assistance, haptic feedback, rehabilitation, and various applications.

Haptic feedback plays an essential role in human-robot interaction and human-computer interaction. Haptic feedback fulfills the interactive experience rather than only limited to visual feedback, especially for virtual reality applications. Haptic perception consists of multiple experiences which can be categorized in temperature, stiffness, roughness, size,

shape, and weight [109]. In order to create a realistic sensation of touch in a virtual environment, a haptic device that can generate multimodal feedback would be promising.

Translating a virtual object's shape has been another principal focus of the haptics field. One way of recreating a shape is by actuating a 2.5D shape display, which consists of actuated pin arrays that can alter the heights of multiple pins in a grid [110]–[112]. Some of these devices not only render the shape but further expand possibilities by integrating force control for dynamic interpretation of force and stiffness of materials [60], [113]. Although these pin-based shape displays allow multi-point and multimodal cutaneous feedback for exploring virtual environments, the interactions are limited to a plane and a modulated height - 2.5D experience. In addition, this type of shape display needs a large number of actuators (from 50 to several hundred), which with a high aspect ratio (usually higher than 30) to map the shape of objects; this solution cannot be applied to a fully-3D environment. To generate shapes entirely in 3D, there are several interactive interfaces based on unconventional materials and actuators, such as soft pneumatic actuators[114]–[116], jamming materials[117], or shape-memory materials[37], [106]. Shape generation, however, is still restricted by the number of actuators, despite a few model-based designs achieving target shape with relatively small numbers of actuators[118], [119]. Some wearable/handheld devices[120]–[123] provide an alternative solution for tangibly perceiving shapes and spatial information. They enable a more natural interaction and larger workspaces for shape exploration in contrast to tabletop devices, which have limited workspace.

In this chapter, we present the design of a comprehensive and coherent tactile information transfer system and an experimental protocol for validating tactile feedback. Our approach utilizes a novel soft interactive interface linked to a soft malleable object. The soft interactive interface consists of a soft pneumatic actuator (SPA) layer integrated with a layer of piezoelectric lead-zirconate-titanate (PZT) sensors to form a SPA-skin, providing a wide range of controlled vibratory feedback to the fingertips. The controlled feedback is able to generate texture and auxiliary tactile response, bought about by actuation frequencies being proportional to the distance from the target shape, therefore guiding users towards the intended shape. Then, association with a moldable test object (playdough) confirms, through its plastic deformation, the applied actuation forces of the user in response to the sensed feedback from the active interface. Together, this unique experimental setup and protocol produce tangible, tactile feedback and instant validation of its cogency in the user's experience, of three different modes of tactile actuation: texture, size, and shape.

### **1.3.2 Wearable soft interactive interface design**

Many of today's virtual reality (VR) interfaces rely only on visual and auditory modes for user interaction, limiting the user's level of immersion due to a lack of haptic feedback. Developing a human-in-loop interactive system requires realistic tactile feedback producing a range of tactile experiences, such as perception of shape, size, surface texture, and stiffness [124]–[126]. Especially in the case of tactile exploration, texture and shape perception play inherent roles in gaining more information about the object being touched. The texture is perceived through the Meissner and Pacinian corpuscles (PC), which can detect variations in roughness and texture while contacting the surface [124], [127]. The range of detection frequencies of

Meissner (slowly adapting type) and Pacinian corpuscles (rapidly adapting type) is from 10-40 Hz to 60-400 Hz, respectively, with maximum sensitivities around 30 and 250 Hz, respectively. As these frequencies demand a high-fidelity response from a device with appropriate actuation at the fingertips, only a few wearable platforms can currently render texture. Shape is the second fundamental property of an object necessary for human-computer interaction both for input and output devices. The ability to interact bidirectionally with shapes is essential for applications such as computer-aided design (CAD) and interactive digital fabrication [128]. Tabletop shape displays provide possibilities for bidirectional interaction[129], [130] that make both perception and creation of shapes accessible, while most of the wearable/handheld haptic research has mainly focused on just perceiving the direction of shapes.

Another uninvestigated problem is the way to quantify spatial or textural accuracy of haptic stimuli in wearable devices, despite the well-studied on precision of motion-tracking systems. There is some research examining the potential of digital shape recreation using wearable haptic devices in VR environments [131]. However, the possibility of both perceiving and recreating shapes in a single human-in-the-loop integrated haptic system has rarely been considered or quantitatively evaluated. Closing the haptic feedback loop with human action triggered by the tactile feedback would bring essential measures of applicability of the haptic feedback system and level of immersion. A platform, aware of human action and having active feedback control could be coupled to quantitative analysis of the integrated system. To achieve the broad range of tactile perception frequencies and active feedback control, we propose a two-component system (Figure 1.28) consisting of an active wearable component and a passive soft and pliable test object to tackle the challenges of multi-modal tactile exploration:

**Sensor-actuator bidirectional interface component:** We used an interactive soft pneumatic actuator (SPA)-skin with integrated hi-fidelity actuation and sensing capabilities as the active component [132]. The SPA-skin is a low-profile soft interface containing a PZT sensor layer, an SPA layer, and a controller controlling the SPA layer with a pneumatic regulator and high-speed on-off solenoid valves. The integrated sensing layer makes it possible to gather information about the local environmental loading conditions in order to modify the output required for coherent feedback. Together, the integrated sensing layer and an external finger tracking system provide a bidirectional interaction between the SPA-skin and the user.

**Test object component:** A second challenge for system design lies in producing a static force-feedback allowing a sense of touch. A virtual shape may be perceived using a heavy and bulky electro-mechanical glove-like design, but this has limited wearability. Here, we propose a test object made using playdough, which may be molded plastically into the desired shape according to the applied forces. Uniting the active interface and the test object provides coherent tactile feedback for an immersive experience.

While shape recognition could be augmented by a kinesthetic haptic device with passive haptic assistance as discussed in[121], the integration of cutaneous sensation using playdough might be effective, as the spatial precision for macro-features of objects mainly relies on SA1 afferents, which have a lower frequency of peak sensitivities. The playdough not only grants a response to the perception of the shape but also serves as an output device for quantitatively

evaluating the spatial resolution via the human as an intermedium, as depicted in Figure 1.28b. Playdough in fact serves as a means of data physicalization[108], a process transferring digital data to a physical/tangible form that people can explore and communicate with.

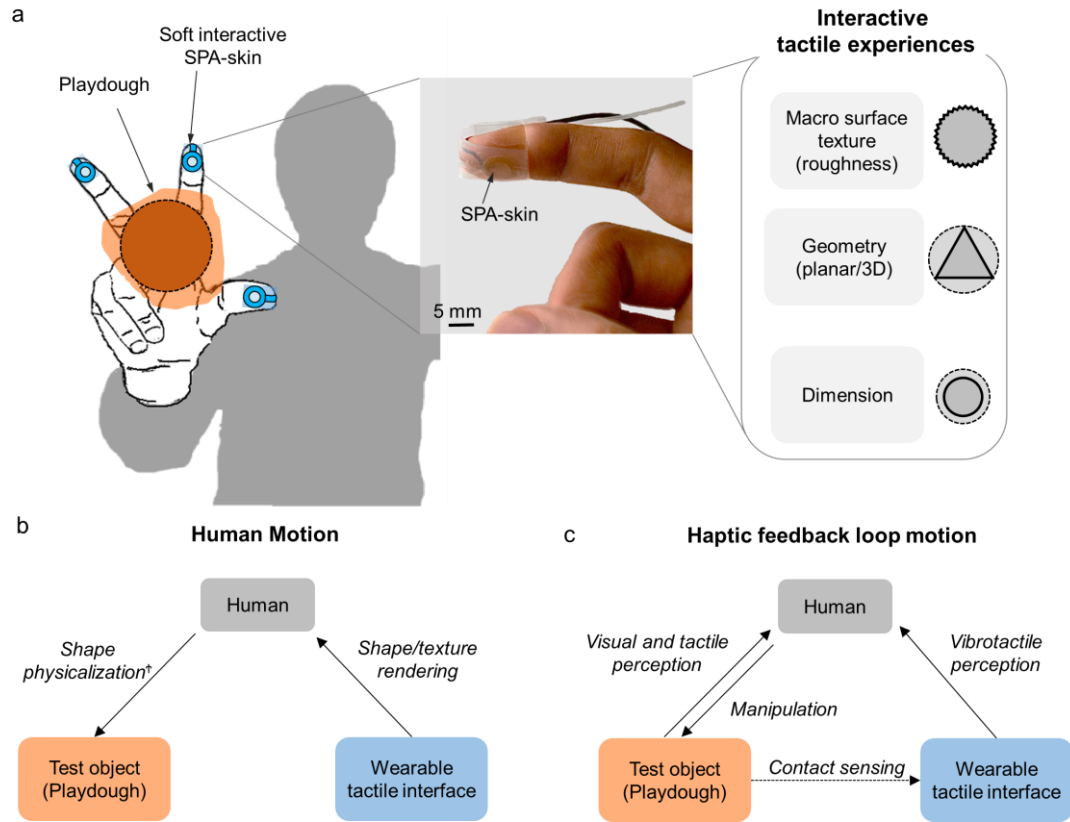


**Figure 1.28 Wearable soft interactive interface** (a) A two-component system combining a wearable interactive SPA-skin with a passive soft playdough object to generate multi-experience tactile feedback of macro-surface textures, planar shapes, and size tracing. The SPA-skin interface is composed of a SPA actuation layer and a PZT sensing layer with 8 mm-diameter actuators and 2x2mm<sup>2</sup> PZT sensors. Integrated high-sensitivity (0.3 V/N) sensing allows closed-loop feedback control and simple texture classification. Multi-level tactile feedback is used for directed spatial localization of planar virtual shapes via a: (b) Human motion side and (c) Haptic feedback-loop motion side. Human motion and haptic feedback-loop motion block diagrams illustrate the separate actions of the human and computer units. The wearable tactile interface triggers the human motion to help in physical shape rendering, physicalization<sup>\*</sup>, of the moldable test object (b). The haptic feedback motion loop senses the location of the human fingers and the contact with the test object boundaries to generate multi-level tactile feedback (c)

### 1.3.3 Experimental evaluation and protocol design

Humans combine touching and physical exploration of an object to gain detailed information about the properties of the object being inspected. The surface exploration generates varying contour, hardness, and roughness profiles by dynamic shape exploration in space stimulating the particular mechano-receptors. In this section, we developed a protocol to produce realistic tactile feeling and to close the haptic loop with human interaction. For the first time, we can validate tactile feedback in a physical manner. We used a SPA-skin interface granting actuation at required frequencies without losing on output amplitude combined with a human-in-loop exploration to generate a realistic feeling of two of the most important modes of dynamic exploration: texture and shape of a physical object recreated virtually.

#### Shape reconstruction experiment

Indeed, shape perception is especially challenging for wearable devices due to the multi-modality of cutaneous sensation in bidirectional interaction, involving active exploration of the object's surface linked to intended motion coupling (sensory-motor coupling). Sense of shape relies on both slowly adapting type 1 (SA1) and rapidly adapting (RA) afferents [133]. SA1 and RA afferents are two different types of mechano-receptive afferent fibers found in human skin, which convey tactile information. In addition, perceptions at these fibers have varied peak sensitivity frequencies, not easy to integrate into a single wearable haptic system. Most of the current haptic research is focused on creating perceptions and qualitatively evaluating the feeling by haptic devices. In fact, quantitative studies of the perception received and how humans respond are rare; it is especially challenging to quantify performance with human-in-the-loop; human behavior is not usually reproducible and is difficult to measure. Here we propose a test protocol and quantify shape sensation at the fingers.

The objective of the experiment is to evaluate the capacity of the active, interactive interface to deliver spatial information sensations of virtual objects in terms of shape and size to the user who simultaneously physicalizes the sensations via the test object. We used vibrotactile feedback through SPA-skin as the active interactive interface and playdough as the test object, as shown in Figure 1.28b and c.

The assumption for the experiment is that active exploration of shapes and concurrent hand motion control shaping the playdough can be achieved using the SPA-skin due to its soft material properties and broad vibration frequency bandwidth; the rigidity of other wearable devices might be an obstacle for exploring and creating virtual shapes. We also presume that playdough can be a base for shape sensation in active exploring, and the effectiveness is comparable to other wearable devices having kinesthetic feedback assistance [122].

The experimental setup is shown in Figure 1.29. The proposed task was to shape the playdough to match pre-defined geometries, guided only by the vibrotactile feedback through the SPA-skin and feel of the playdough. There was no visual feedback or shape contour information. The target shapes were limited to 2D contours instead of 3D geometries to simplify the task, cancel undesired noise, and relieve the workload. The playdough was placed on a smooth, transparent glass platform. A camera was installed underneath the glass platform to track colored markers attached to the fingers. The sampling rate of finger position was 10 Hz. The captured images provided spatial information, allowing the tactile sensation of the virtual objects by the SPA-skin in real space. The SPA-skin vibrated when the fingers approached or reached the 2D contour of the virtual object. Then, the 2D contour of the virtual object was recreated physically, manipulating the playdough by the users. Finally, the trajectories of fingers and the final contours of the playdough were recorded to examine the effectiveness of spatial information delivery.

We defined three different target contours: rectangle, trapezoid, and circle, to provide flat lines, inclined lines, and curves with respect to the grasping motion of the fingers. We gave one target contour per test. The target contours were relatively simple without detailed features or concave lines, designed mainly to promote simple grasping gestures, avoiding complex manipulation and thereby, interference from other factors. Furthermore, there were two horizontal cuts on the glass as boundaries to the shape generation motion, as shown in Figure 1.29. With the boundary constraint, shaping progress was focused on grasping motion



control and tactile perception of the fingers, without larger movements of entire hands or arms. The shaping process lasted 2 minutes per test. Nine tests for each target contour were carried out on three subjects whose ages ranged from 28 to 34 years. Subjects were informed to follow the vibration guidance to shape the playdough without any information of the target shapes.

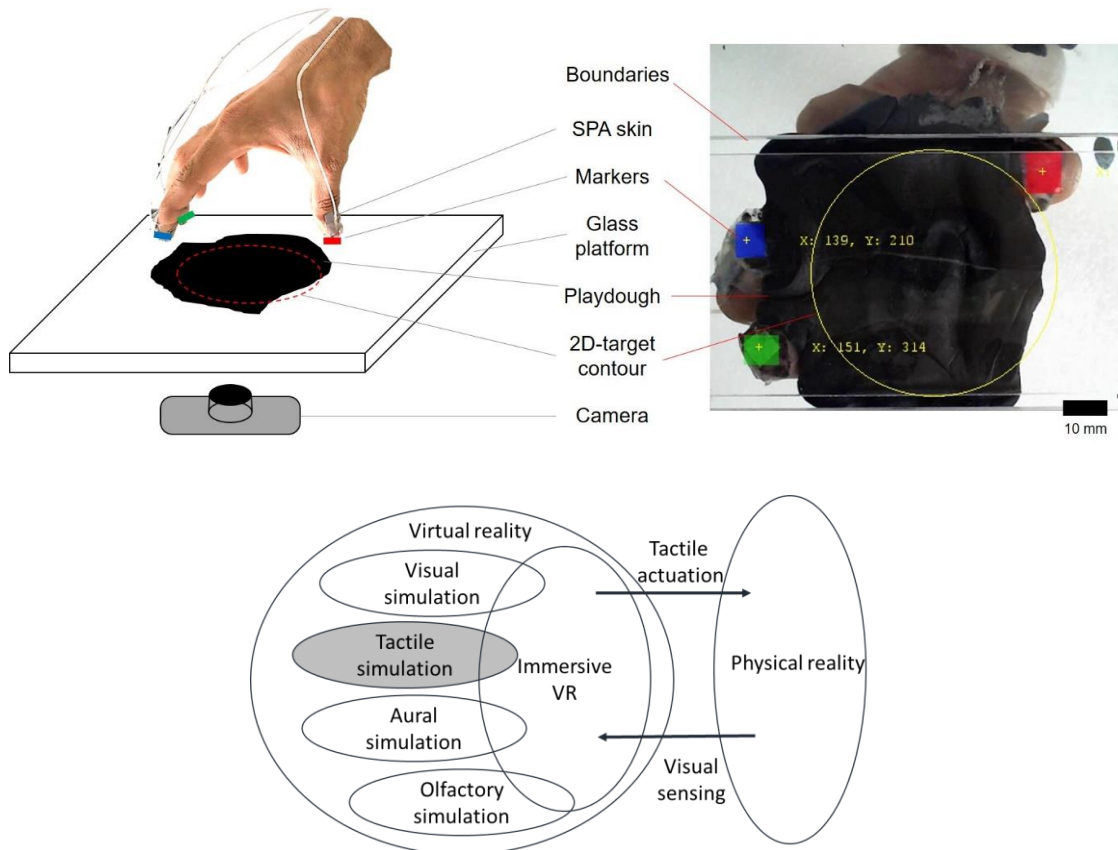


**Figure 1.29 Experimental setup for interactive shape generation using SPA-skin and a playdough as a test object.** The image on the right is the computer vision of the control system (A). SPA-skin setup with tactile actuation and visual sensing closing the loop with tactile simulation, a part of virtual reality environment, and physical reality (B).

### 1.3.4 Results and discussion

To evaluate the spatial accuracy and effectiveness of the tactile exploration, the final contour of the playdough after the shaping process was compared to the target contour, as shown in Figure 1.30b. The accuracy of the shaping process was defined as the correlation coefficient of the area. The finger trajectory shaping process was recorded, and the sets of experimental results are shown overlapping in Figure 1.30a, for multiple test subjects and for three shapes and sizes. The temporal exploration by the human fingers during the reconstruction process is shown in Figure 1.30b. The two red dashed lines are boundaries limiting the workspace of the shaping process. The playdough contour outside of the workspace is removed in the figure for the accuracy calculation. The colored dots from light to dark represent the finger center locations from the start to the end of one set of experiments. There are three concentric

circles, representing the boundaries of the 1st feedback edge, 2nd feedback edge and the target contour, respectively. The 1st and 2nd feedback edges were defined as 20 pixels and 10 pixels from the target, respectively, as shown in Figure 1.30b. The control system gave a 15 Hz vibrotactile signal signifying the approach of the target contour when the fingers reached the 1st feedback edge. A higher 35 Hz frequency signal was generated on the SPA-skin to give the sensation that fingers were really touching the boundary of the target shape when the finger center reached the 2nd feedback edge. As mentioned previously, both SA1 and RA afferents are relevant in grasping control. The vibration frequency of the 2nd feedback edge was close to the frequency of peak sensitivity for RA afferents and could be an effective stimulus for grasping control. The 10-pixel distance from the target contour was the definition as we roughly defined a 6 mm thickness for fingertips, and one pixel equaled 0.29 mm in the region of interest. In Figure 1.30b, most of the finger-tracking points are located between the 1st and 2nd feedback edges and only a few of them between the target and 2nd feedback edge. It shows that the system gave an effective vibrotactile signal for acknowledging the appearance of virtual boundaries. The contact forces from grasping the playdough were also present at the same time in this case.

Horizontal grasping motions were frequently used to shape the playdough, observed by the trajectories of fingers in Figure 1.30b. Thus, the spatial accuracy of the grasping motion could also be evaluated by calculating the area difference as the area is the horizontal difference integral along the y-axis. The calculated accuracy of all data sets is shown in Figure 1.30c and the image processing for accuracy comparison in Figure 1.31. The participants achieved almost 90% accuracy for the rectangle contour and almost 80% accuracy for the circle contour using vibrotactile feedback. The circle contour had a lower average accuracy, and we also saw a possible outlier for the circle case. A suggested reason for the lower accuracy could be the stop of airflow in the SPA-skin due to the large bending on the rubber tube, which led to a lower amplitude vibrotactile feedback.

In order to investigate the effectiveness of the proposed SPA-skin feedback system in grasping control, we studied the distribution of the error area to find the ratio of the error area inside the target boundary to that outside the boundary and the image processing as shown in Figure 1.30a and Figure 1.31d. The error distribution showed that there was no significant difference between error inside the target boundary (8.5%) or outside the boundary (7.8%), which suggested that the vibrotactile feedback from the SPA-skin is effective for grasping control.

To further examine if outside factors had a significant effect on the accuracy, we performed one-way analysis of variance (ANOVA) tests [134] on the target shapes, participants, and test order (divided into three groups: tests 1 to 3, tests 4 to 6, and tests 7 to 9). In these cases, F critical value,  $F_{crit} = 3.4$  at  $\alpha = 0.05$ . The F-ratios were 3.2, 2.3 and 0.4 respectively, namely  $F_{crit} > F\text{-ratio}$ ; hence, the results showed that none of the factors had a significant effect on the accuracy with a 95% confidence interval. The influence of the tested shapes on accuracy was minor; however, the contours tested were designed for rough geometries without detailed features, mostly composed of straight lines and uniform curvature lines. The accuracy of reconstructed shapes with detailed features with respect to dimension and geometry of the fingertips could be further studied. In addition, we observed that the learning factor was not significant in ANOVA tests of test order. Further studies could be done with more sets of

experiments and changing the design of the test-shape order to examine learning factor influence on the same shape, as the current test shapes were hidden, picked at random before each test.

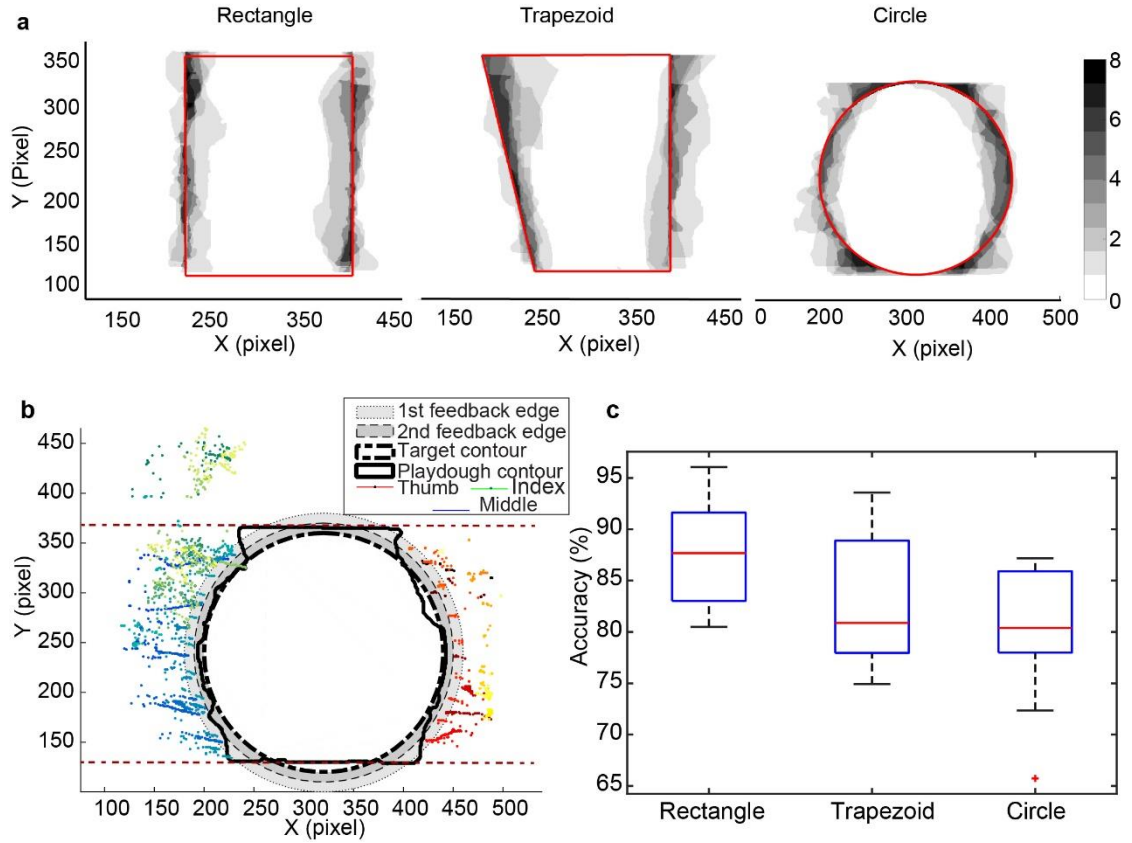


**Figure 1.30 Results of the shape reconstruction experiments.** (a) Intensity map of the shape difference between the playdough shape and target shape. The error intensity mapping for the shape reconstruction experiments for three target shapes: rectangle, trapezoid, and circle. The darkest color represents the higher trends of error distributed in the 2D-plane. The red line is the target contour. (b) The finger trajectory shaping process and the comparison between target and playdough contours. The different feedback frequencies acknowledging approaching the target contour or reaching the target contour are shown as different shaded areas. The two horizontal red dashed-lines are the boundaries limiting the workspace of the grasping motion. (c) Calculated average area accuracy of shape reconstruction.

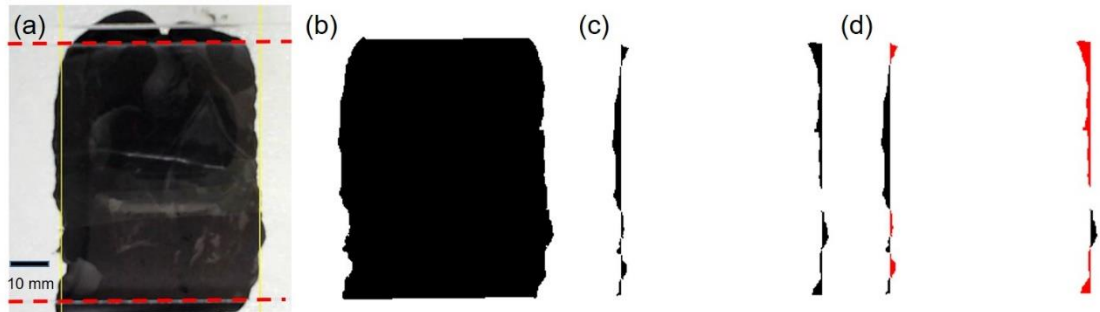


**Figure 1.31 Image processing for shape creation accuracy calculation.** (A) The image of playdough after the shaping process. The yellow lines are the target contour, and red dashed lines are the upper/lower boundaries limiting the workspace. Then, (B) the filtered image of playdough for shape comparison is generated. It is transferred to a binary image with the background removed. (C) The area difference between the playdough shape and target shape. The shape creation accuracy is calculated as:  $\text{accuracy} = 1 - (\text{area difference} / \text{area of target shape})$ . (D) The area difference inside of the target contour is shown in red and outside of the target contour in black.

### 1.3.5 Conclusion

For an effective wearable haptic feedback device, we require an accurate understanding of the physical interactions between the device and the wearer's perception. We propose a two-component system to achieve multi-experience tactile feedback and, for the first time, human-in-loop 'physical' validation of user actions, closing the haptic feedback loop. We use SPA-skin for its low profile form factor, high-bandwidth capabilities, and integrated sensing as an active bidirectional interface. Special design measures in PZT sensor signal conditioning like high sensitivity instrumentation amplifiers with noise filtering using coaxial cables and line noise notch-filters allow for on-body placement and accurate measurements.

We then designed and validated a haptic system in which the delivery of tactile feedback and spatial accuracy was quantitatively studied for bi-directional human-in-the-loop system. A 2D planer platform was used to *physicalize* a given virtual shape using a soft test object based on two-level tactile cues guiding the human actions. The test object play dough, on being molded, provided the sense of shape and size whereas active tactile feedback from SPA-skin overlaid the texture cues. The results showed almost 90% accuracy for the rectangular shape and greater than 80% for the trapezoidal and circular shape physicalization using SPA-skin for tactile guidance. We employed a two-stage actuation with a low-frequency stimulation when approaching the contour shape, followed by a high-frequency vibration when reaching the actual contour for ease of exploration.

The experiments showed that SPA-skin is an effective haptic platform and provided rich tactile feedback in a wearable scenario. The tactile feedback loop was closed with human actions and was quantitatively validated for the level of immersion and quality of tactile feedback. There is plenty of room for further studies of multimodal perception with wearable soft haptic devices due to the customizability of both material properties and control frequencies. For example, we could integrate the evaluation protocol with a 3D VR environment to understand the effectiveness of tangible interaction, as shown in Figure 1.32. The current studies are focus on 2D geometries; the challenges for how to recognize the 3D gesture with the interference of test objects will be interesting to tackle. Furthermore, these preliminary studies open up discussion for the next generation of haptic feedback devices, which are not only mechanically transparent for human wearability but also provide ranges of tactile sensations inherent to the object and perceived by the human sense of touch.



**Figure 1.32 Evaluation of capability and effectiveness of wearable haptic interfaces for virtual reality applications**



# Multi-DoF reconfigurable structures' hardware development

To realize this research project's reconfigurable interactive robotic system, the hardware system's design, capability, and limitations must be established and evaluated. In this chapter, we investigate a hardware design that enables the multi-modal interaction proposed in Chapter 1. Accordingly, finding solutions to implement controllable actuation and transmission mechanisms for the desired range of motion and functionalities is important. Motivated by the advantages of non-conventional fabrication technologies and origami-inspired engineering, we explore possibilities to develop compact, lightweight, mesoscale (mm to cm), and multi-DoF active structures using different materials and fabrication approaches.

In this chapter, we study origami-inspired reconfigurable structures from the core-component level to the overall mechanisms' design. We start by introducing the design, model, and experimental validation of origami's core functional components. Then, we conduct parametric studies on folding hinges since they dictate origami structures' overall performance. Finally, we investigate a waterbomb-based origami mechanism that enables reconfigurable functionalities through varying actuation strategies.

## 2.1 Hardware design for multi-DoF reconfigurable robots

In the first section of this chapter, we begin with the design of core functional components for multi-DoF reconfigurable robots. In order to activate multi-DoF systems, actuators selection will be described in the following sections.

### 2.1.1 An overview of actuation for multi-DoF robotic systems

---

The material of this chapter is adopted from the following self-authored publications.

Marius Wagner, **Jian-Lin Huang**, Philipp Okle, Jamie Paik, Ralph Spolenak 'Hinges for Origami-Inspired Structures by Multi-Material Additive Manufacturing' *Materials and Design*, 2020.

The contribution of Jian-Lin Huang were design and execution of experiments, results analysis, and partial writing.

Zhenishbek Zhakypov, **Jian-Lin Huang**, Jamie Paik 'A Novel Torsional Shape Memory Alloy Actuator: Modeling, Characterization, and Control' *IEEE Robotics & Automation Magazine*, 2016

The contribution of Jian-Lin Huang were measurement setup programming, control experiments, results analysis, and partial writing.

Hongying Zhang, Huijuan Feng, **Jian-Lin Huang**, and Jamie Paik 'Generalized modeling of origami folding joints' *Extreme Mechanics Letters*, 2021

The contribution of Jian-Lin Huang were measurement experiment.

In computational origami and the mathematics of origami folding, a *fold* is considered as a surface with zero thickness deformed along a crease without stretching or compression [26], [71]. [26, 71]. To apply the design concept to real prototyping, an origami structure should have a relatively low thickness, enabling folding with a high folding angle (maximum  $\approx 180^\circ$ ). This thickness also determines the design's requirements for its actuation and transmission mechanisms.

Depending on the controllable DoFs, scales, and applications, various actuation solutions have been proposed to activate origami structures, as Figure 2.1 shows. Origami's actuation systems can be divided into two different approaches [135]: (1) direct methods, in which an actuator generates torque directly at the hinge to fold a structure, and (2) indirect methods, in which the actuation force is applied to the entire or partial origami structure. Single actuation may involve multiple folds instead of only activating single-hinge folding. Indirect methods entail simpler actuation control systems but also limited controllable DoFs. Moreover, indirect methods share more similarities with traditional robots, for which fewer actuators are needed [136]. Indirect methods are often applied while self-assembly is not the structure's main function because discrete and sequential actuation is not needed. Commercially available actuators—such as electromagnetic motors—can also often be used in this method.

Tendon or cable-driven systems provide examples of indirect methods[135], [137], [138]. Tendon-driven systems allow rapid, accurate, and high-force actuation, providing a simple control solution even for origami structures with complex kinematics. Additionally, tendon-driven systems are often installed on folded or assembled origami structures, which may require post-manufacturing processes. In some cases, tendon systems can be integrated into origami structures during the manufacturing process[86], [139]. However, a sufficient distance must be ensured between the neutral plane and tensile force direction generated by the tendon to create enough torque to fold the hinge. This requirement has led to an increasing structural thickness, which may result in foldability limitations.

In contrast, direct methods distribute actuators at origami structures'. These methods have higher controllable DoFs, variable motions, and possibilities for integration in origami structures during the manufacturing process. Several different actuation principles have been proposed to fold hinges directly. Pneumatic actuators can be powered by positive pressure [140], [141], or negative pressure[142]. Smart materials such as SMAs and SMPs [143], [144] have also offered promising solutions in this decade. Pneumatic actuators have a higher operating frequency than most smart materials-based solutions, which are slow ( $< 1$  Hz). However, pneumatic actuators' need for valves and pumps in every individual actuator may hinder a system's portability and scalability. In particular, building a system with high DoFs using a pneumatic approach could be challenging due to the size of the pumps and valves. The volume needed for pneumatic actuators to expand may affect foldability for structures with compact folding patterns. Smart materials-based actuation can provide better scalability and foldability since the miniaturization of power electronics and a high range of motion can be achieved with a smaller cross-section area. Although SMPs generally have larger reversible strains than SMAs ( $< 5\%$ ), SMAs have some of the greatest bending movements and actuation



stress among the functional folding materials [5]. Therefore, we chose an SMA as our active material to investigate multi-DoF reconfigurable systems.

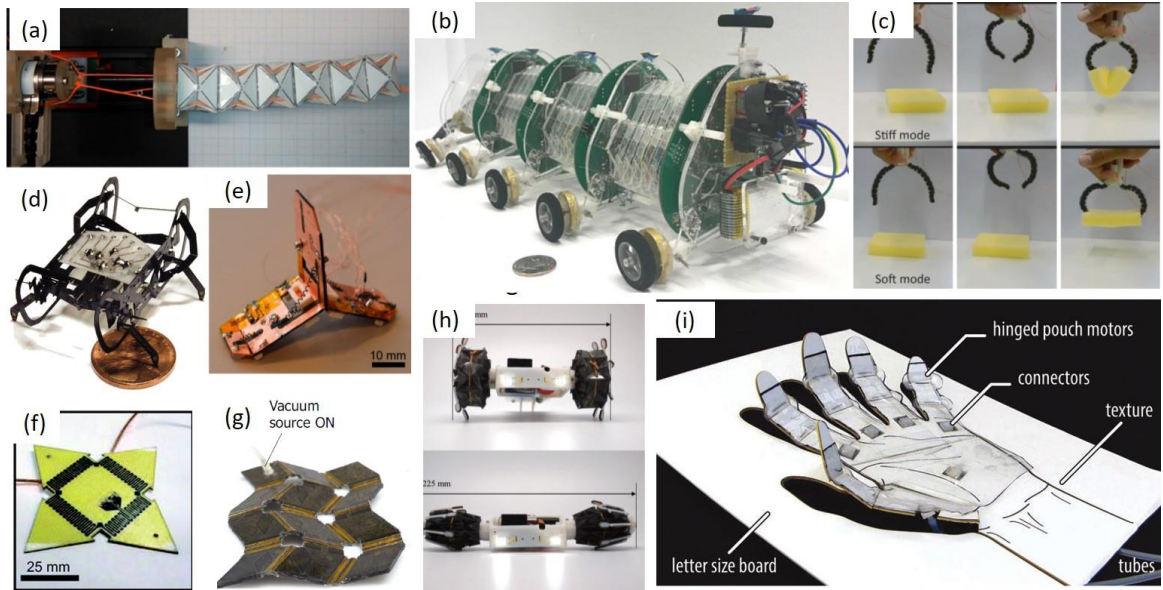


**Figure 2.1 Actuations for origami structures:** (a) Tendon-driven origami continuum robot [137], (b) origami cable-driven snakerobot [138], (c) Tendon-driven underactuated origami gripper [86], [139] (d) piezoelectric driven quadrupedal microrobot [18], (e) SMA actuated multi-modal locomotion robot [80], (f) self-folding origami by SMP [143], (g) fluidic network for self-folding origami [142], (h) variable diameter origami wheel [145], (i) pouch actuators [140]

### 2.1.2 Low-profile actuator development

For achieving good foldability and scalability, we investigate low-profile functional components for the active multi-DoF origami structures. First, we start with the actuator for creating folding motion

#### Shape memory alloy actuators

In order to empower origami folding, the actuators should generate enough torque to lift up several tiles as well as high bending angle to fold hinges (approximately  $180^\circ$ ) for some cases. As mentioned in the previous sections, we chose SMA as the actuator due to its high force-to-volume ratio, high force-to-weight ratio, and it could be compatible both with subtractive and additive manufacturing processes.

#### SMA torsional actuators design and fabrication

There are several SMA-based approaches that can achieve bending motions, such as torsional SMA sheet [78], [146], [147], torsional coil [7], [148], SMA wire [44], and SMA spring [149], [150]. The bending performance is not only dedicated by the morphology of SMA but also by the way installed with structural materials (e.g., outside or embedded in the hinge) and hinge type (mechanical joint or flexural hinge) [9].

As presented in chapter 1.5, we have developed and characterized a low-profile torsional SMA actuator based on our previous design, an  $\Omega$ -SMA actuator [78], and the work presented in [147], an SMA strip-based actuator. The proposed SMA actuators are made from a NiTi SMA

sheet (M alloy, Memry GmbH) with 100  $\mu\text{m}$  thickness. The SMA sheet is cut on a laser micro-machining station (LAB 3550, Inno6 Inc.). The machined SMA actuator has a rectangle shape geometry with the dimension  $14 \times 8 \times 0.1 \text{ mm}^3$  and 0.7 g weight. Since we would like to generate torque while giving heat excitation, the desired programmed state, austenite state with a closed shape, and it can be flattened at the rest state for integrating into a flat sheet-like structure, as shown in Figure 2.2(a). Thus, we programmed by bend the machined along steel rod with three different diameters, 2 mm, 2.9 mm, and 4.2 mm, forming a circular shape. The diameter of the programmed circular shape has a significant impact on the output torque, which will be discussed in the later section. The circular 2-mm diameter circular SMA actuators share the same dimension and curvature with the  $\Omega$ -shape torsional SMA actuators we proposed in [78]. Thus, the performance and modeling results should be comparable. To integrate with the additive manufacturing (3D printing) process, our design of the functional components need to avoid collisions with an extruder and ensure minimal interference with the subsequent printing layers. Thus, The circular shape actuator proposed here can be flattened easily, unlike the  $\Omega$ -shape SMA actuators. The subsequent integration process will be discussed in Chapter 3.2. Then, we insert the bent SMA with steel rod into a customized jig for ensuring the shape during the programming process. To program the desired geometry, the SMA is annealed in a high-temperature furnace (Nabertherm GmbH) at 405  $^{\circ}\text{C}$  for 30 minutes. Finally, the annealed SMA could be flattened again after cooling down for the following assembly process.

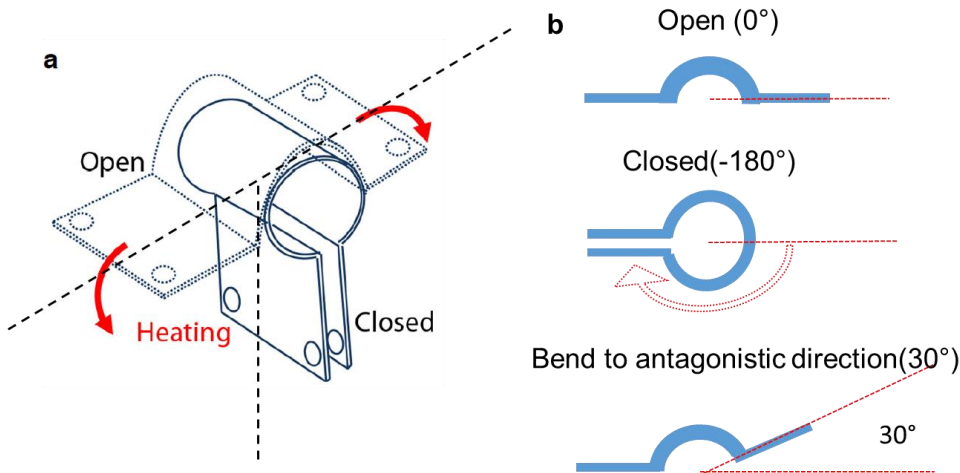


**Figure 2.2 The schematic of  $\Omega$ -SMA torsional actuator.** (a) The SMA actuator is set to open configuration at room temperature, and it closes while heating up. (b) The bending angle definition for the torsional SMA actuators used in this chapter.  $0^{\circ}$  while open to a flat configuration and it closed and programmed at  $-180^{\circ}$ . It has a positive bending angle for bending toward the opposite direction from the programmed direction.

### SMA torsional actuators model

For the SMA torsional actuator proposed in this chapter, the programmed curvature is significantly larger than actuator thickness. So, we assume it is a pure bending for the geometric model.

$$\epsilon = \frac{y_n}{l} \underbrace{\text{atan2}\left(\frac{y}{x}\right)}_{\theta} \quad (2.1)$$

$$\sigma = \tau \frac{6}{\underbrace{wt^2}_{C_2}} \quad (2.2)$$

Where  $\theta$  is the bending angle, and  $\epsilon$  and  $\sigma$  are the strain and stress.  $y_n$  is the distance to the neutral plane.  $l$  is the curvature length and  $\tau$  is the torque.  $w$  and  $t$  are the width and thickness of the actuator.

Then we adopted the one-dimensional model of SMA proposed in [151]. Where the thermo-mechanical model is given by:

$$\sigma - \sigma_0 = E(\epsilon - \epsilon_0) + \Omega(\xi - \xi_0) + \Theta(T - T_0) \quad (2.3)$$

Where  $E$  is Young's modulus.  $\Omega$  and  $\Theta$  are the transformation and thermal expansion coefficients, respectively.  $\sigma$ ,  $\epsilon$ ,  $\xi$ , and  $T$  are the stress, strain, martensite volume fraction, and temperature, with their initial conditions  $\sigma_0$ ,  $\epsilon_0$ ,  $\xi_0$ , and  $T_0$ , respectively. This equation can be simplified by removing the thermal part since the strain caused by phase transformation is much larger than thermal expansion. For an SMA material, Young's modulus changes with phase transformation, and it can be written as  $E_M$  and  $E_A$  for the full martensite state and full austenite state, respectively. The phase transform coefficient can be expressed as  $\Omega = \epsilon_L E$ , and  $\epsilon_L$  is the maximum recoverable strain.  $C_A$  and  $C_M$  are the stress-induced coefficients that can be computed by the heating and cooling process ( $M$  to  $A$ , and  $A$  to  $M$ ).

$$C_A = \frac{E_A}{A_f - A_s}, C_M = \frac{E_M}{M_s - M_f} \quad (2.4)$$

Where  $M_s$ ,  $M_f$ ,  $A_s$ ,  $A_f$  are the martensite start, finish, and austenite starts and finish temperature. Then, we substitute Eq. 2.1 and Eq. 2.2 into Eq. 2.3. Finally, the martensite fraction composition can be express by the following form.

$$\xi = \begin{cases} \frac{1}{2} \cos \left[ \frac{\pi}{A_f - A_s} (T - A_s - \frac{C_2}{C_A} \tau) \right] + \frac{1}{2} & M \text{ to } A \\ \frac{1}{2} \cos \left[ \frac{\pi}{M_s - M_f} (T - M_f - \frac{C_2}{C_M} \tau) \right] + \frac{1}{2} & A \text{ to } M \end{cases} \quad (2.5)$$

These eight parameters,  $M_s$ ,  $M_f$ ,  $A_s$ ,  $A_f$ ,  $E_M$ ,  $E_A$ ,  $C_A$ , and  $C_M$  can be found by experimental characterization.

### SMA torsional actuators characterization

The performance and model of SMA torsional actuator need to be verified. Indeed, the output torque and bending displacement are the major concerns in practical robotic applications. We have found the material parameters including  $M_s$ ,  $M_f$ ,  $A_s$ ,  $A_f$ ,  $E_M$ ,  $E_A$ ,  $C_A$ , and  $C_M$  and verified the thermal-mechanical model through characterization proposed in [78]. Here, we would like to apply the obtained parameters to examine the model for SMA bending stiffness and blocked torque at different angles. Blocked torque is defined in the later paragraph.

We built a force measurement setup depicted in Figure 2.3. It consists of two plates to form the opening and closing motion of a hinge. One of the plates is fixed on a 6-axis transducer (Nano17, ATI industrial automation), and the moving plate is driven by a DC motor with an

encoder (A-max16, Maxon Motor AG). The moving plate can be positioned at desired angle with the controllable angular speed and acceleration with a controller board (ECON 36/2 DC, 4-Q Sevocontroller, Maxon Motor AG). The bending stiffness SMA can be measured by driving the motor at a constant rate, and blocked torque tests for realizing the torque output of SMA actuators can be realized by holding the motor at various angles while activating the actuator. An infrared thermal imaging camera (a FLIR A35) is employed for recording the temperature of SMA. SMA actuator was clamped on one side of the stationary plate, and the other side was secured on the moving plate.

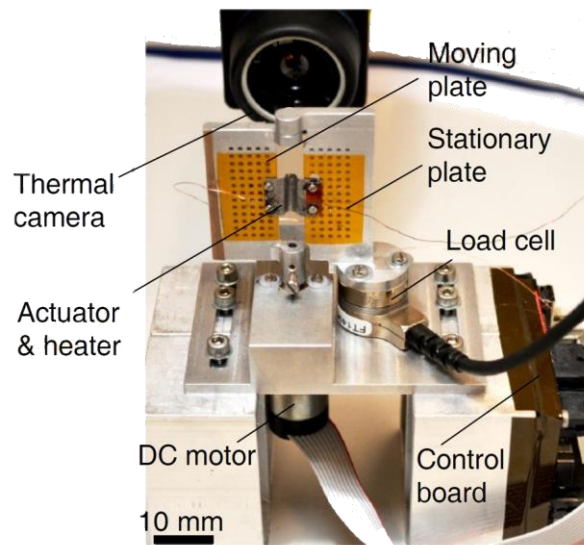


**Figure 2.3 SMA characterization setup.** The loading setup with temperature measurement using the IR thermal camera, angular position by the motor encoder, and force measurement is measured by a load cell.

First, we conducted the force measurement for obtaining the bending stiffness of SMA. Since we have measured the blocked torque with the range from  $0^\circ$  to  $-150^\circ$ , we would like to verify that the bending stiffness is similar if we bend the SMA actuator towards the opposite direction from the programmed direction in the pseudoelasticity region. We set the initial bending angle at  $45^\circ$ . Then, the moving plate is rotated at a constant speed  $-5^\circ/\text{s}$  and applies load towards  $-45^\circ$ . When the bending angle reach  $-45^\circ$ , the rotation speed of the moving plate change to  $5^\circ/\text{s}$  until the bending angle reaches  $45^\circ$ . The measurement result is depicted in Figure 2.3. It shows a similar loading and unloading curve in both bending directions. The results are similar to the experimental results obtain in our previous publication[78] while bending towards the programmed direction. It also meets with the model prediction suggested in the previous section. In addition, It shows the hysteresis cycle, which has been found in stress-induced transformation both for single crystal and polycrystal SMAs [152]. However, we can also see that the overall bending stiffness towards the programmed direction is lower than the opposite directions, especially at larger bending angles.

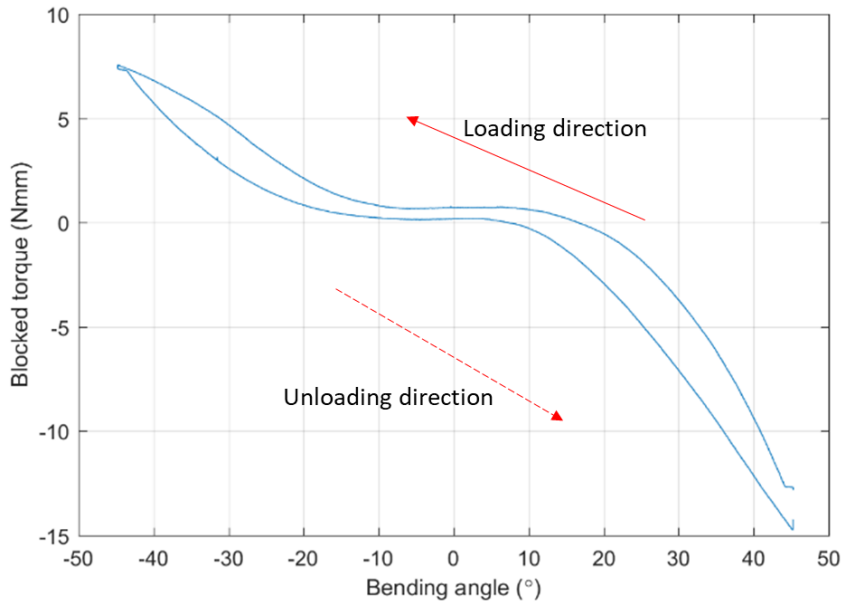


**Figure 2.4 Bending stiffness of SMA torsional actuator at full martensite**

Then, we would like to examine the blocked torque at the full austenitic state to verify the maximum torque that torsional SMA actuators can give for bending the hinge at different angles. We have examined the torque generated by  $\Omega$ -SMA actuator with  $1 \text{ mm}^{-1}$  curvature for the bending angle range from  $0^\circ$  to  $-150^\circ$  with  $30^\circ$  of an interval, as shown in 2.5 (a). It suggested that the proposed  $\Omega$ -SMA actuators have the maximum torque at around  $-90^\circ$  and minimum torque output while actuators were open (at  $0^\circ$ ) and closed (at  $-150^\circ$ ). We further examined the maximum torque output in the direction opposite from the programmed direction with a circular SMA with  $1 \text{ mm}^{-1}$  curvature at the bending angles that range from  $-40^\circ$  to  $40^\circ$ . We got comparable results for the range from  $0^\circ$  to  $-40^\circ$ . However, we also find that the torque output is weak while bending towards the direction that opposites to the programmed direction.

We would like to know how we can increase the maximum torque output while we bend the SMA towards the direction that opposite to the programmed direction. In [147], it suggested that the larger the difference between the programmed radius of curvature and current radius of curvature, the larger the output moment can be obtained. Thus, we tested circular SMA actuators within with  $0.345 \text{ mm}^{-1}$  curvature, which was wrapped around a 2.9 mm rod during the annealing process. From the modeling prediction, we should have a smaller torque output at the direction that is opposite to the programmed direction since we have a smaller curvature difference. However, it has surprisingly high torque outputs at the bending angles that range from  $0^\circ$  to  $50^\circ$ , as shown in figure 2.6. A possible reason is that the way we fixed the SMA on the experimental setup, which refined the boundary condition of the model, has a great impact on the maximum torque output. The results suggest that the maximum torque output of SMA torsional actuators may be varied from modeling if we consider the integrating methods with the structural materials.

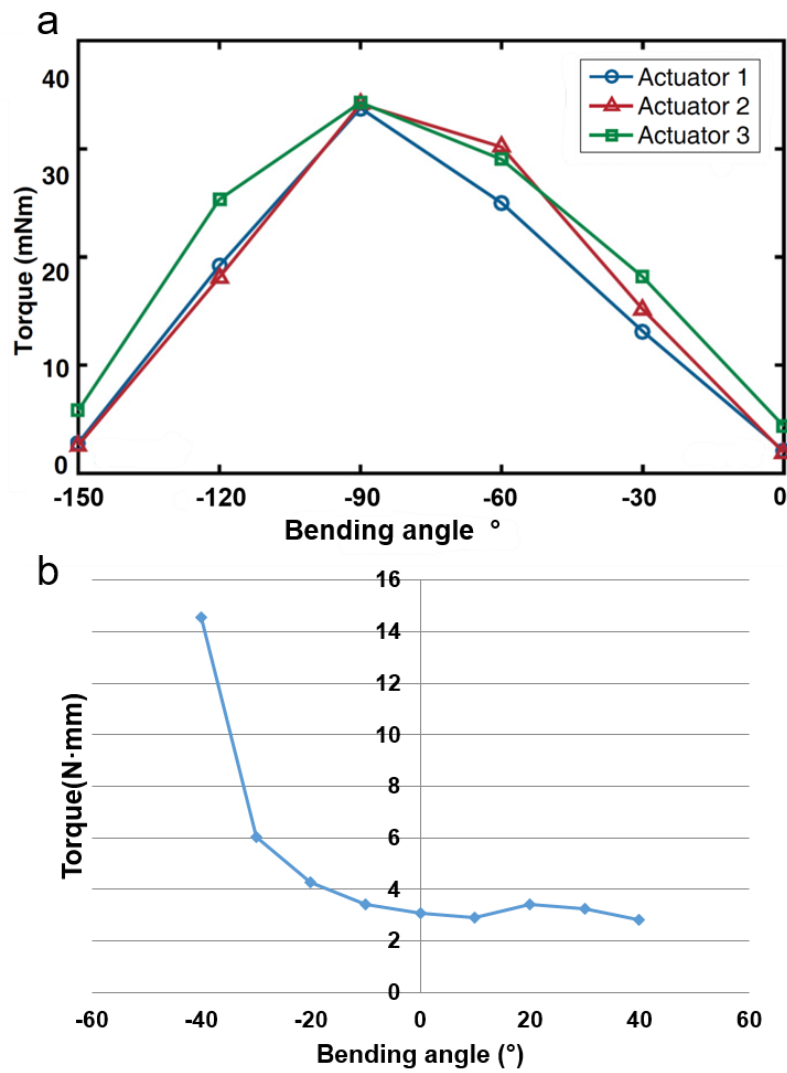


**Figure 2.5 The maximum torque output with SMA torsional actuators.** (a) The maximum torque output of  $\Omega$ -SMA torsional actuators with  $1 \text{ mm}^{-1}$  curvature at the bending angles from  $0^\circ$  to  $-150^\circ$  (b) The maximum torque output of circular SMA torsional actuators with  $1 \text{ mm}^{-1}$  curvature from at the bending angles  $-40^\circ$  to  $40^\circ$

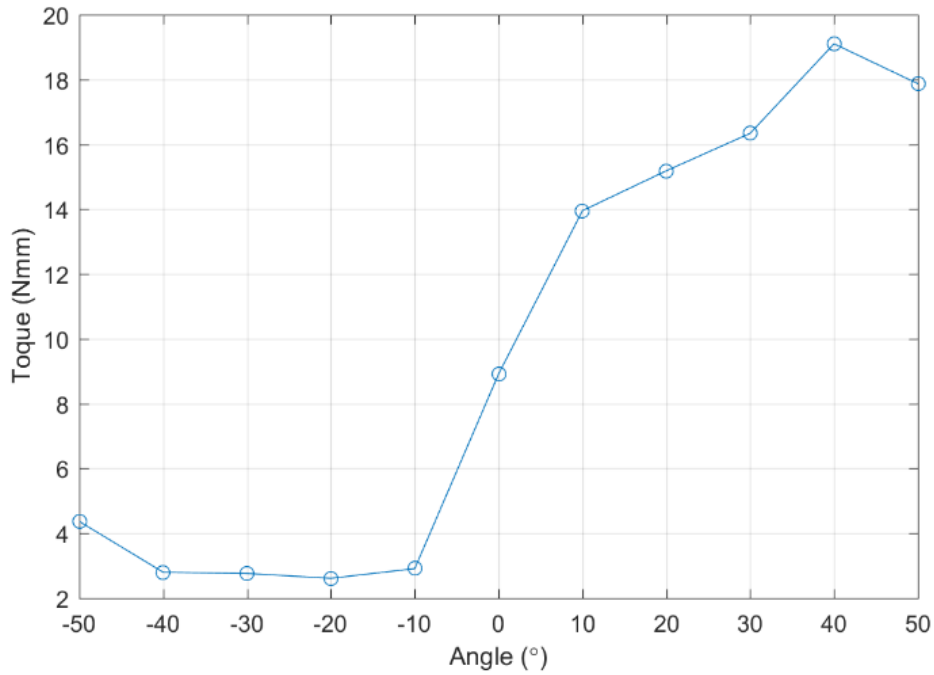
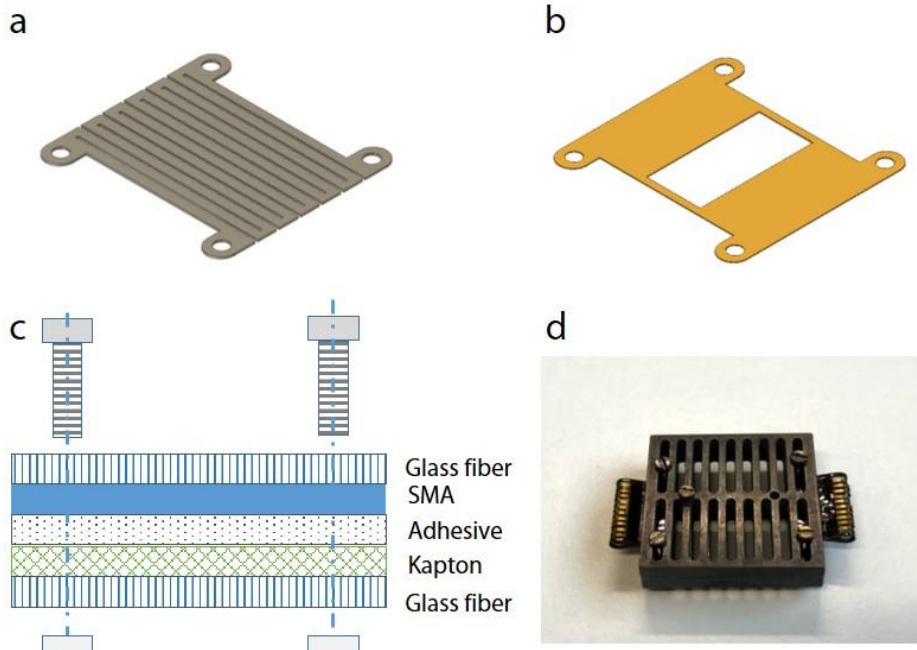


Figure 2.6 Maximum output of circular torsional SMA actuator with  $0.345 \text{ mm}^{-1}$  curvature

### Self-heating SMA torsional actuators design and fabrication

The torsional SMA actuators we proposed in the previous sections need an external heater for realizing thermal activation. The customized heaters can produce heat more quickly and more power-efficient since it has a higher resistance than SMA actuator which is the essential parameter for Joule heating. But it also adds difficulty for the subsequent assembly and integration processes. Thus, we also developed a low-profile self-heating torsional SMA actuator as an alternative solution. The design and working principle are the same as the circular-shaped SMA proposed in the previous sections. We designed a zigzag pattern, as shown in Figure 2.7(a). Then, we cut the SMA sheet and remove the unwanted part to get the desired geometry. The zigzag geometry provides a higher resistance for Joule heating. A similar idea has been presented in [153]. The main challenge for this design is to keep the SMA in the shape of ensuring there is not short (no contact between lines) during the programming processes. Thus, we design a Kapton layer for fixing the SMA shape while bending to the programmed shape and during the annealing process, as shown in Figure 2.7(b). We design a mold for assembly and binding the Kapton layer with the SMA actuator with adhesive layers, as shown in Figure 2.7(c). We put the mold in the heat press machine at  $125^\circ\text{C}$  for 20 minutes. Then, remove the screws, nuts, and glass fiber layers after cooling down. Finally, the SMA actuator with the Kapton layer is wrapped around a 2-mm metal rod and fixed in the clamping jig, as shown in Figure 2.7(d). Then, it is ready for annealing. The fabricated self-heating SMA torsional actuators have the dimension  $14 \times 9.4 \times 0.1 \text{ mm}$ . However, the effective width is  $0.6 \text{ mm} \times 12 = 0.72 \text{ mm}$  since we have removed some materials to form the zigzag geometry. The performance of self-heating SMA actuator will be discussed in the Chapter 3.3.





**Figure 2.7 Design and fabrication of self-heating torsional SMA actuators.** (a) The schematic of SMA actuators, (b) the Kapton layer design for keeping the shape of SMA during the programming process, (c) Mold for attaching the Kapton layer, and (d) Clamping jig for annealing.

### Design of Shape memory alloy spring actuators

SMA wires have been widely applied in robotics applications thanks to their high force to volume ratio [154]–[156]. However, it has suffered from the recoverable strain in the range of 4–8%, which limits the applications that need a larger displacement. SMA coil spring actuator that designed for generates 200% to even 1600% deformation, which can provide an alternative for robotic applications. The design principle is that wrap SMA wire along with a stick for forming a helical geometry during the training process, as shown in Figure 2.5. The design and model of SMA spring actuators have been demonstrated and validated [157]. SMA spring actuators can also be used for generating folding motions, whether it is embedded in the hinge or mounted externally of hinge body.

There are main design parameters of SMA spring actuators for deciding the maximum force and the maximum deflections. They are spring diameter  $D$ , wire diameter  $d$ , active coil numbers  $n$ , and the pitch angle  $\alpha$ , as shown in Figure 2.5. To determine the force output of SMA spring actuators in the full austenitic state, we could use the following formula.

$$F = \frac{\pi d^4}{8D^2} G_A \frac{\cos^3 \alpha_i}{\cos^2 \alpha_f (\cos^2 \alpha_f + \sin^2 \alpha_f / (1 + \nu))} \delta \quad (2.6)$$

Where  $F$  is the axial force generated by the SMA spring actuator.  $G_A$  is the elastic shear modulus of the austenitic phase.  $\alpha_i$  and  $\alpha_f$  are initial and final pitch angles.  $\delta$  is the deflection of the spring actuator. Then we can find the design parameters for the desired stroke and force output from this formula.



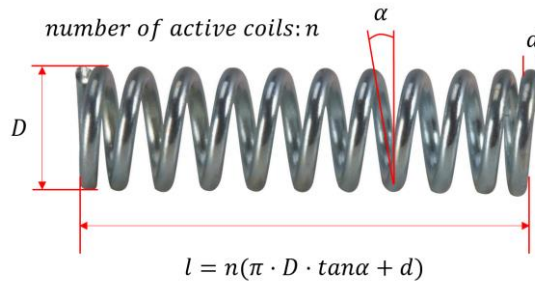


**Figure 2.8** Design parameter of SMA spring

### Characterization of shape memory alloy spring actuators

We have fabricated and programmed several SMA spring actuators using Ni-Ti SMA wire (FLEXINOL, Dynalloy, Inc.) with different sets of design parameters. The fabrication process is similar to how we obtain torsional SMA actuators, as described in the previous sections. And we measured the force-deflection relation both for the full martensitic phase and the full austenitic phase. The test setup consisted of a force transducer (Nano17, ATI industrial automation) and a one-DoF moving stage with a micrometer for controlling the displacement. We attach one end of the SMA spring to the transducer, and the other end is fixed with the moving stage. Then, we stretch the spring actuators for the length range from the length of active programmed active coil  $l_0$  to approximately 1.5 times  $l_0$ , depending on the application scenario. The force-deflection relation characterization test was conducted three cycles for each phase. We present the experimental results as shown in Figures 2.9 and 2.10 for the prototype with  $D=1.77$  mm,  $d=0.35$  mm,  $l_0=18.3$  mm,  $n=40$  mm. The experimental results meet with the model so that we can ensure the use of the model for the design guideline of SMA spring actuators.

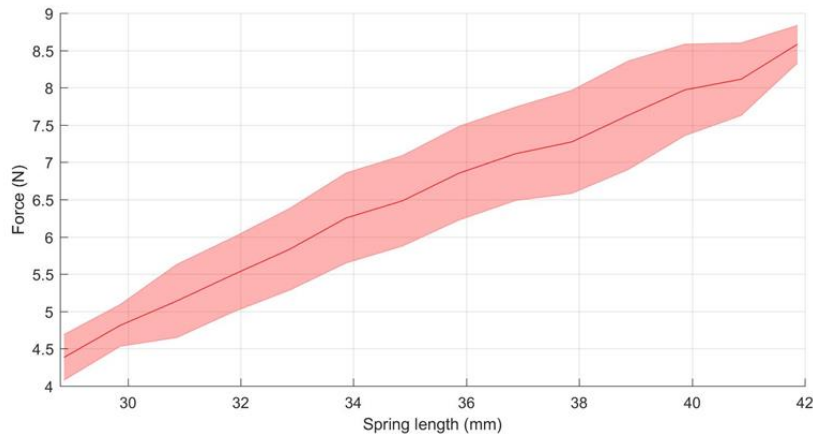


**Figure 2.9** Force output of SMA spring at austenite phase in the loading direction.

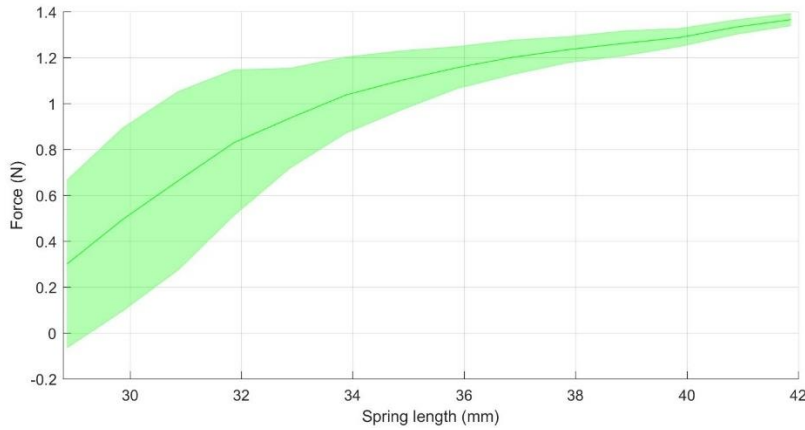


**Figure 2.10** Force-deflection characterization of SMA spring at martensite state at loading direction

### 2.1.3 Low-profile functional layer development

One of the grand challenges for soft robotics is to have controllability on the compliance and deformabilities. Thus, several stiffening technologies such as Shape memory materials, material jamming, low-melting-point materials, and electroactive polymers have been proposed for partially/entirely adjusting the stiffness of the soft robot body [158] [159]. The variable stiffness enables to strengthen the structure while needed or increasing the efficiency for performing desired tasks. There are also examples that employ SMP for changing the stiffness of folding hinges resulting in various grasping modes for robotic gripping applications[86], [139], [160], [161].

We design and fabricate a low-profile variable stiffness component for embedding in the folding hinge. This component consists of a SMP layer with a copper-Kapton layer attached for self-heating. The fabrication process is shown in Figure 2.11. First, we disperse the SMP pellets (MM 5520 from SMP Technologies Inc.) on a metal plate and use two spacers consisted of several layers of Teflon tapes. Then we put the SMP pellets with another metal plate on the top into a heat press machine at 160 °C temperature for 15 minutes. And then, we put a copper-Kapton layer on top of the formed SMP plate. The next step is to form a bonding between SMP and copper-Kapton layer by putting both layers in the heat press machine again at 160 °C for 5 minutes. The final step is to cut and engrave the heater pattern on the copper-Kapton layer by UV laser machining station. Since the SMP is almost transparent with a 0.5 mm thickness, the reflection rate differences allow us selectively engraving and cutting the multi-layer material easily. The prototyped self-heating SMP components have a dimension: 14 mm x 8 mm with the SMP thickness of 500 μm and copper-Kapton thickness of 50 μm. We also characterized the bending stiffness by the measurement setup proposed in the previous sections. The glass state bending stiffness is 0.11 N/°, as shown in Figure 2.12. Bending stiffness is almost neglectable comparing with hinge materials while the temperature higher than the glass transition temperature.

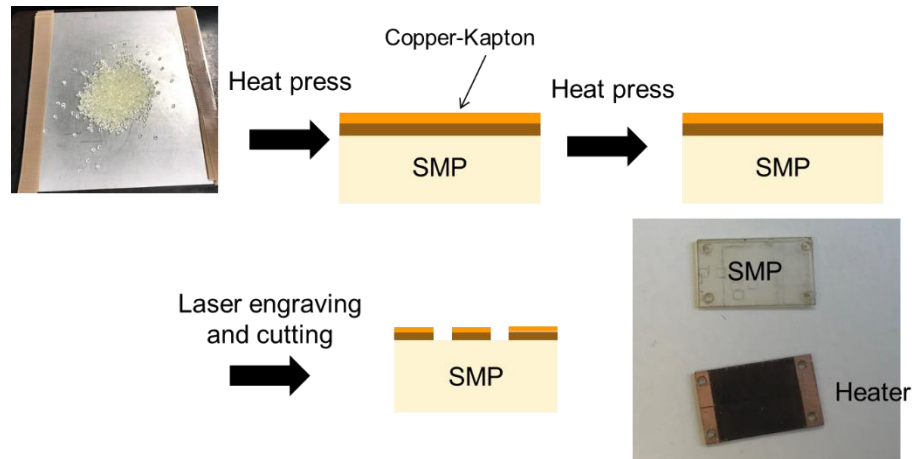


Figure 2.11 Fabrication process of SMP with customized heater attached

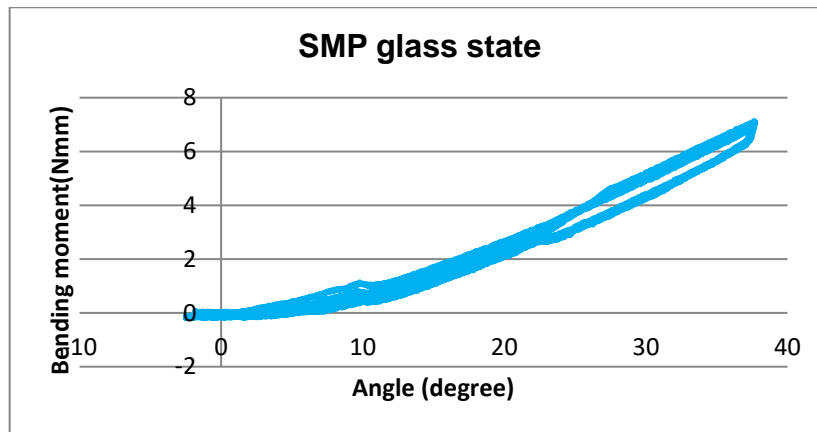


Figure 2.12 Bending stiffness of SMP at glass state

### Heaters and circuit layers

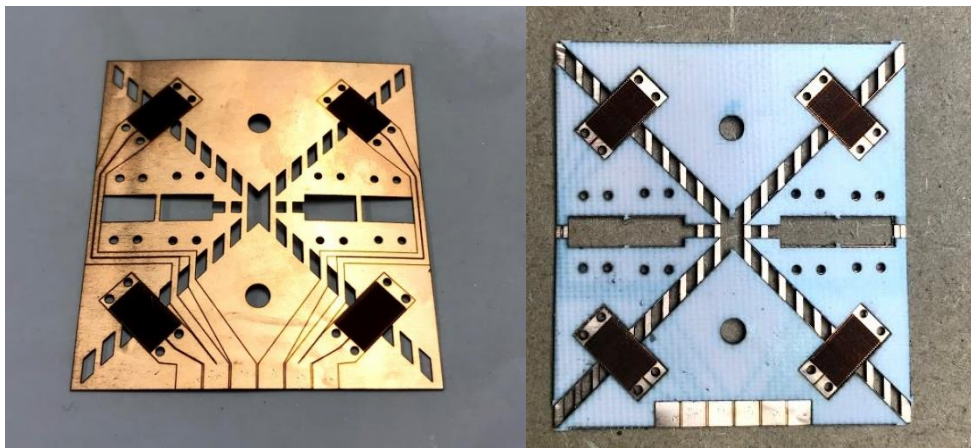


Figure 2.13 Laser engraved copper-Kapton flexible circuit and heaters

We are able to selectively engraving the multi-layer material by fine-tuning the laser control parameters and also thanks to the lower-cutting efficiency with transparent materials. Thus, a customizable, flexible circuit layer can be achievable with UV machining, as shown in Figure 2.13.

### 2.2 Flexural hinge design and characterization

In the second part, we focus on testing and characterizing the mechanical properties of flexural hinges so that our findings could have immediate applications in 3D-printed origami structures. We introduce an aramid fiber composite hinge and compare it to a single-material polyamide and a multi-material photopolymer hinge. We investigate the impact of the materials and geometric design parameters on the load-carrying capability and flexural properties of the hinge. Furthermore, the fatigue behavior of the hinges is characterized, identifying the constitutive mechanisms.

#### 2.2.1 An overview of additive manufactured hinges

Additive manufacturing (AM), also known as 3D printing, offers possibilities for overcoming some challenges in conventional fabrication technologies. The ability to fabricate complex structures in a single step relieves the difficulty for the post-assembly process. As a result of the lower volume that origami-inspired structures could have, AM is uniquely suited to fabricate origami-inspired structures. A variety of studies have shown that AM can be used to fabricate origami-inspired structures with properties hitherto not observed (shape-changing capability[162], tunable bi-stability[163], or deployable robotic systems[35]). However, it is rare to have these structures finding their way into real-life applications. This disparity is mainly due to the low load-carrying capability and fatigue resistance of the folding joints: these two main obstacles need to be overcome in order to bring origami structures closer to applications.

Origami is the art of paper folding. The principal mechanism is folding, which can be discovered in nature within different scales. Folding plays a crucial role in DNA packaging and the organization of three-dimensional structures of proteins at the molecular scale. At cellular and tissue scale, plants fold pollen to prevent it from drying up due to evaporation [164]. At the mesoscale, insects fold their wings for expediting the storage while rest as well as deployment while flying. [165]. Not only being explored in nature, but modern manufacturing and engineering applications have also been inspired by the original form of origami art. Namely, various complex shapes can be folded from a single sheet, which implies the significant volumetric changes can be adapted from simplification in assembly and manufacturing processes [166].

The elementary component in mechanical designs is a hinge that allows localized deformation in a defined area. There are two major design principles for realizing folding mechanisms. The first one is a pin joint usually consisted of a cylindrical stud to constrain the motions of two components to pure single DoF rotational movements [167]. This design provides advantages that low-torsional resistance by proper surface treatment on the contact area or employment of bearing systems. However, lubricant or additional surface treatments and maintenance for preventing wear are required for this design [168]. Another design, flexure hinges, provides an alternative for low-wear or even wear-free for rotary motions. Flexure hinge consists of a segment of compliant materials allowing large strain for bending movements. It is generally easier to manufacture and miniaturize due to the fact that it can be fabricated in a single step without post-assembly processes and external bearing components. Nonetheless, there are

also some drawbacks that need to address. The unstable center of rotation and induced uncontrollable parasitic DoF might create undesired and unpredicted motions [169]. In addition, localized strain-induced fatigue should be aware for designing a flexure hinge.

The research on 3D-printed flexural hinges is scarce. It is known that specific cutout patterns in the hinge can prescribe motions[169]. In a recent study, a 3D-printed flexural hinge was simulated using finite element analysis and compared to a non-linear beam model[170]. Others use an analytical model composed of a rotational and a tension spring to model the behavior of hinges fabricated by fused deposition modeling (FDM)[171]. [172] reviewed the suitability of different AM polymers for application in hinges. Polyethylene, polypropylene, and polyamide showed the most promising properties. Furthermore, the flexural behavior of photopolymer hinges fabricated on an inkjet 3D printer was examined experimentally. In that study, the blocked force was measured for different hinge thicknesses, and the experimental results were compared to the finite element simulations.

While AM is prevalent in various structural manufacturing and research efforts in their new application fields, to date, there is no research describing the load-carrying capability and fatigue properties of hinges manufactured by AM. In this work, we perform an in-depth investigation of these disregarded but essential aspects. Three classes of hinges fabricated by different AM processes are characterized experimentally (Figure 2.14). The relation between mechanical properties and design parameters is studied. Further, the fatigue mechanisms in the different hinge classes are examined.

The concept of an aramid composite hinge is introduced and compared to two existing hinge classes, i.e. a single-material polyamide (PA) and a multimaterial photopolymer hinge. This allows a benchmark of the mechanical properties.

### 2.2.2 Hinge design, material, and fabrication

In this study, three classes of flexural hinges fabricated are investigated, each fabricated by AM (Figure 2.14). The concept of an aramid composite hinge is introduced and compared to two existing hinge classes, i.e., a single-material polyamide (PA) and a multi-material photopolymer hinge. This allows a benchmark of the mechanical properties.

The aramid hinge consists of two rigid polyamide segments, which are connected in the hinge region by bundles of continuous aramid fibers impregnated by a polyamide matrix (Figure 2.14a). The hinge was fabricated from the commercial materials “tough nylon” and continuous aramid fiber filaments (Markforged Ltd.). Carbon and glass fiber composite filaments showed a fracture in the first folding cycles, proving as unsuitable for the application in hinges. Both the aramid and the PA hinges were fabricated on a Markforged Mark II FDM 3D printer.

The second class is a single material hinge consisting of the commercial PA6 (“tough Nylon” Markforged Ltd.) (Figure 2.14b). The flexible hinge region was designed as a sheet with a reduced thickness, shifted to the bottom of the rigid segment. This allows printing the hinge without support structures, which results in improved mechanical properties. To maximize the strength of the hinges, the long axis was aligned with the direction of the print head movement. In the FDM printing process, a nozzle with a 0.4 mm diameter was used. The layer height

was 0.1 mm for the hinges with the thickness of 0.1 mm and 0.2 mm for the ones with a hinge thickness of 0.2 mm.

The third hinge class is a multimaterial photopolymer hinge (Figure 2.14c). The rigid segments of the hinge are made from a UV curable rigid thermoset (VeroWhite+ Stratasys Ltd.) and the flexural hinge consists of the flexible thermoset (Agilus30 Stratasys Ltd.).

The photopolymer hinges were fabricated on a Stratasys Connex3 Objet500 inkjet 3D printer. Small gaps were introduced in the hinge region to reduce the concentration of stresses. Upon bending, the material on the compression side expands laterally and contracts on the tension side due to the Poisson effect. This introduces stress concentrations, which accumulate along the hinge width. To reduce these stress concentrations, cut-outs were introduced into the flexible materials, which prevent the accumulation of lateral strains and stresses. This effect is prevalent in hinges high thickness of the flexible segment. In this study, this holds true for the photopolymer hinges.

The Connex polyjet process is known to produce parts with varying mechanical properties due to variation in UV dosage dependent on the print job. To minimize this effect, all photopolymer specimens were printed with the matte surface finish option and thus encapsulated in a shell of hydrogel support material (SUP706 Stratasys Ltd. ). After printing the support material was removed mechanically, and the specimen was stored in a dark environment to avoid post-curing. To minimize the influence of aging, the time between printing and testing was kept as constant as possible throughout all experiments.

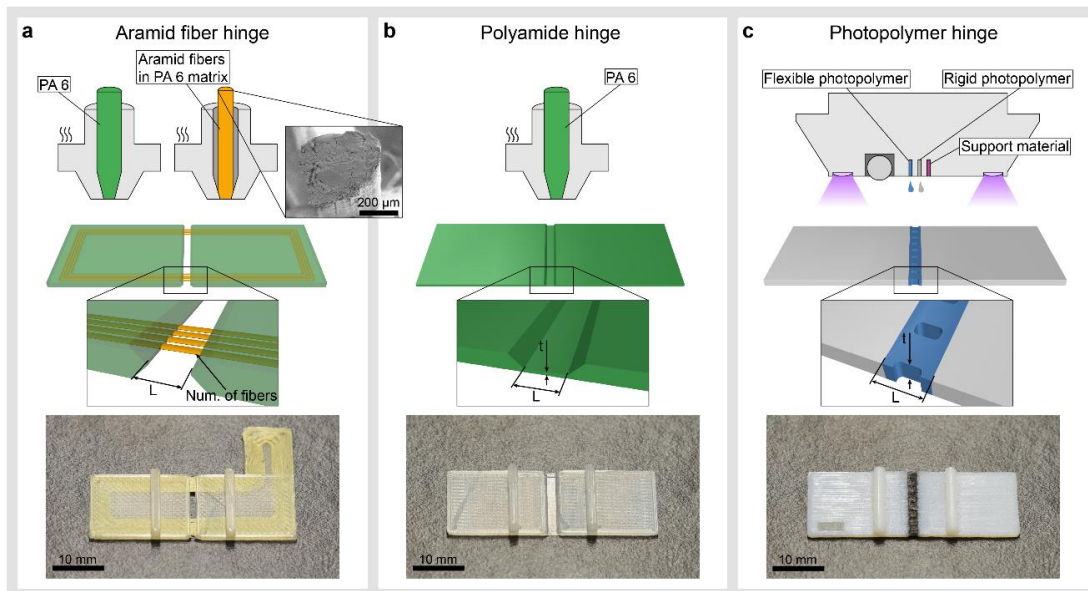


**Figure 2.14 Investigated hinge classes, processes and design parameters.** (a) Aramid hinge, (b) PA hinge and (c) photopolymer hinge. The top row illustrates the respective manufacturing technologies, (a) multimaterial FDM, (b) single-material FDM and (c) multimaterial inkjet. The middle row indicates the design parameters varied, hinge length and number of fiber bundles (a) respectively hinge thickness (b, c). The bottom row shows images of the 3D-printed specimen. The ridge on the top side of the hinge was added to facilitate accurate repeatable positioning in the experimental investigation. Note that the hinge region of the PA hinge (b) is shifted to the bottom. Thus, it can be fabricated without requiring support material, which improves the mechanical properties. This Figure is made by M. Wagner [173]

### 2.2.3 Experimental characterization

The set-up of the folding experiments is shown in Figure 2.15. The specimen was clamped to the rotating wing. During the test, the wing rotates by  $160^\circ$  and pushes the specimen onto the load cell, where the normal force is measured for calculation of the bending moment. The hinge geometry was adjusted for the fatigue tests on the Hydropuls fatigue testing machine. Two additional hinges were introduced in order to convert the uniaxial motion of the testing machine into folding deformation (Fig 2.15 c). These changes lead to a changing in loading conditions of the hinge. Particularly for small angles of folding, the hinge is subjected to compressive loading. Comparison of the results with hinges folded manually suggests that this does not significantly affect the fatigue in the hinge. The direction of folding was defined by initial manual-folding the hinge once before mounting in the setup. The fatigue proceeds faster for the middle hinge than in the outer two since the maximum folding angle, and consequently, the strain amplitude in one deformation cycle is higher.

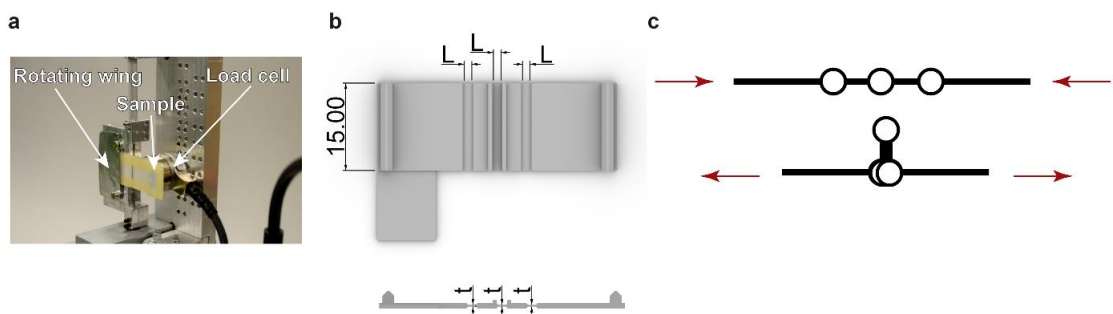


**Figure 2.15 The custom-built setup used for characterization of the flexural properties** is shown in (a). For the fatigue tests on the Hydropuls fatigue testing machine the hinge geometry was adjusted according (b). The folding induced by uniaxial motion is illustrated in (c). The experimental setup is built by J.L. Huang, and the figure is edited by M. Wagner [173]

The load-carrying capability of the hinges is described in terms of the ultimate line load (ULL), which is defined as the maximum load divided by the width of the hinge and has the dimensions N/mm. The line load notation is useful for the description of the loads and properties of “two-dimensional” structures like hinges, which have a much lower thickness compared to their in-plane dimensions. The ULL was characterized depending on the design parameters and the number of folding cycles. Tensile tests were performed on an Instron E3000 testing machine equipped with a 5 kN load cell, at a controlled strain rate of  $1 \text{ s}^{-1}$ . The photopolymers of the Connex 3D printer are highly viscoelastic and thus rate dependent [174]. This dependence is outside of the scope of this study.

### Flexural properties

The flexural properties of the hinges are measured using a custom-built setup, consisting of a motor, a rotating wing and a stationary load cell. One side of the hinge is fixed to the moving wing, while the other side is pushed against the load cell. The maximum folding angle of  $160^\circ$  and an angular velocity of  $5^\circ/\text{s}$  are selected. All hinges are folded towards the side, which faced the print bed during fabrication. The bending moment is calculated from the normal force and the distance from the center of rotation to the contact point on the load cell. For each set of parameters, we test three specimens. Since the different hinges show non-linear behavior in the characteristic bending moment – folding angle curves, the definition and comparison of the bending stiffness is difficult. Therefore, the area under the loading curve, representing the



work required for folding, is used as a comparable measure. Similar to the load carrying capability, the folding work is normalized by dividing through the hinge width, which yields the line folding work (*LFW*). The *LFW* has the dimensions ( $\text{mJ rad mm}^{-1}$ ).

### Fatigue

The influence of fatigue on the tensile and flexural properties was characterized by performing the experiments as described above after subjecting the specimen to a certain number of folding cycles. One cycle consists of folding the hinge from flat the as-printed state to the maximum folded state (folding angle  $180^\circ$ ) and back. This corresponds to strain-controlled fatigue with an R-ratio of zero, as long as the material behaves elastically. Since the polymers investigated exceed the limit of elastic strain and exhibit viscoelastic properties, stress with the opposite sign (tension on the compression side and vice versa) will be generated in the unloading step. This results in  $-1 < R < 0$ . Fatigue is highly sensitive to the amplitude of stress and strain and, therefore to the selected design parameter. The nominal strain amplitude in the material at complete folding varies greatly between the hinge classes and depends on the design parameters. In the fatigue specimen, the nominal strain amplitude amounts to 31% for the aramid and PA hinge and 87% for the photopolymer hinge. Particularly the strain in the aramid hinges deviates from this theoretical value, which will be discussed later. Manual folding was performed for the specimen up to 200 cycles. A Hydropuls fatigue testing machine (Instron structural testing systems) was used to achieve higher numbers of folding cycles at a frequency of 10 Hz. In the fatigue study, five specimens were tested for each respective set of parameters.

A sole description of the flexural fatigue by measuring the reduction of *LFW* with increasing numbers of folding cycles is not sufficient, since it is impossible to differentiate between the distinct phenomenological mechanisms leading to the decrease in *LFW*. A reduction in *LFW* results either from the accumulation of plastic deformation leading to a decrease in the effective angle of folding in the experiment (defined as  $160^\circ$  maximum folding angle of the setup minus the residual angle of the hinge), or reduction in stiffness of the hinge itself. Examining the folding work versus the residual angle allows to determine whether the residual angle or a stiffness decreasing mechanism is prevalent for the reduction in *LFW*. The black solid lines in Figure 2.16i describe how the *LFW* would decrease due to increasing residual angle for a material that exhibits a stable stiffness. For sake of simplicity, the stiffness curves are approximated as linear, quadratic (progressive) and square root (degressive). The normalized *LFW* as a function of the effective folding angle can be calculated as:

$$LFW_l = n_l \int_0^{\alpha_{eff}} x \, dx \quad (2.7)$$

$$LFW_p = n_p \int_0^{\alpha_{eff}} x^2 \, dx \quad (2.8)$$

$$LFW_d = n_d \int_0^{\alpha_{eff}} \sqrt{x} \, dx \quad (2.9)$$

With  $\alpha_{eff} = 160^\circ - \alpha_{residual}$  and  $n$  being normalization factors, such that  $LFW_l(160) = LFW_p(160) = LFW_d(160) = 1$ . The introduction of  $n$  allows the comparison of the *LFW* for the different curve shapes. The theoretical model is illustrated in Figure 2.16(h). The stiffness of the hinge remains constant, and the area under the loading curve (i.e., the *LFW*) is only



reduced by a change in the folding angle. Depending on the shape of the moment–angle curve, the decrease in  $LFW$  is due to the residual angle changes. A material can deviate from this either by a cyclic decrease in stiffness (red region) or by a cyclic stiffness increase related to a hardening effect (yellow region), as shown in Figure 2.16(i). If the reduction in  $LFW$  from the experiments appears below the theoretical model, this is a sufficient condition to identify a stiffness decrease. On the other hand, for stable stiffness, it is necessary to have the hinge data in this cyclic stable regime. Since the exact shape of the moment–angle curve is only roughly approximated in the model, a slight reduction in stiffness could be present, even if the data lies inside the cyclic stable region. Further clarification can be achieved by examining the hysteresis loops for increasing numbers of folding.

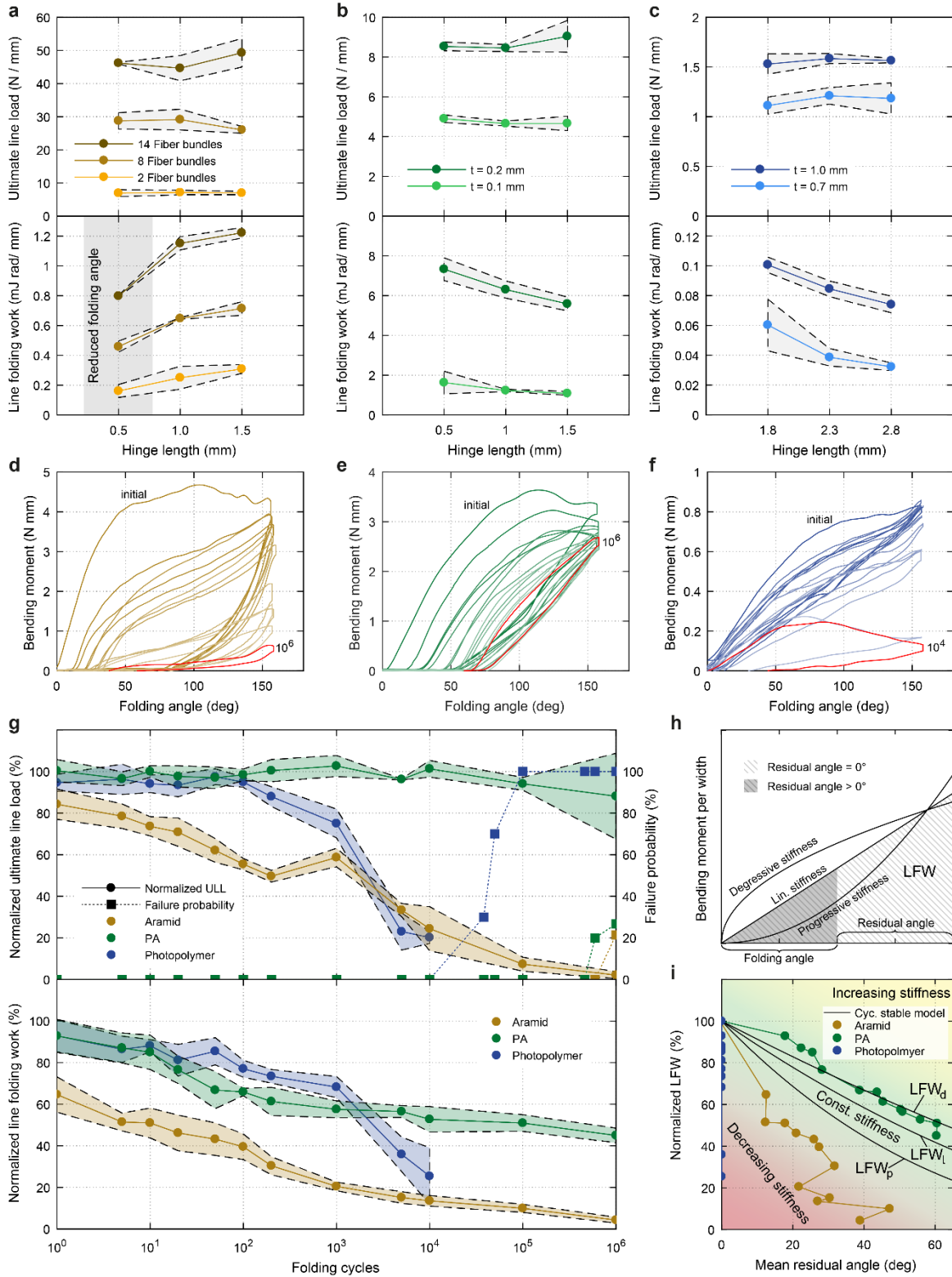


**Figure 2.16 Mechanical properties of the different hinge classes.** (a-c) The ultimate line load (ULL) (top row) and line folding work (LFW) (bottom row) depend strongly on the design parameters number of fiber bundles, respectively hinge thickness. (d-f) The different hinges show varying hysteresis loops, which change significantly with an increasing number of folding cycles. (g) Fatigue can be quantified by investigating the decrease of ULL and LFW depending on the cyclic deformation. (h) The theoretical model of constant elastic properties can be applied to determine the source of LFW decay. (i) The experimental data applied to the theoretical model indicates a stiffness reduction for PA and photopolymer hinges and a constant stiffness for the PA hinges. The experiments were conducted by J. L. Huang and M. Wagner. Data processing is done by J. L. Huang and M. Wagner. The figure is made by M. Wagner [173].

## 2.2.4 Results, discussion, and design guidelines

### Results

The tested ultimate line load ( $ULL$ ) based on the design parameters is shown in Figure 2.16a – c top row. The solid points represent the mean of three experiments and the dashed line shows the standard deviation. Unsurprisingly, the  $ULL$  of the aramid fiber hinge largely depends on the amount of fiber bundles, which are placed across the hinge. The same holds true for the thickness of the hinge region for polyamide (PA) hinges and photopolymer hinges. The hinge length is found to not significantly affect the  $ULL$  for all three materials in the range investigated.

The line folding work ( $LFW$ ), depending on the design parameters, is shown in Figure 2.16a – c (bottom row). The number of fibers and the thickness of the hinge has a large influence on the  $LFW$ . The aramid hinges with a length of 0.5 mm cannot be folded up to an angle of  $160^\circ$ , as the rigid segments collide (Figure 2.16a bottom). Therefore, the folding angle in the experiment is reduced from  $160^\circ$  to  $120^\circ$ . For this reason, the  $LFW$  is not comparable, and these data points are excluded from the discussion. The PA and the photopolymer hinges show a decrease in  $LFW$  for an increase in hinge width. For the aramid hinges, the opposite relation is found; an increase in hinge length leads to increasing  $LFW$ . Figure 2.16d – f shows the characteristic moment – folding angle curves depending on the number of folding cycles for the respective hinge classes: Aramid hinges and photopolymer hinges show a pronounced decrease of the slope, while the accumulation of plastic deformation prevails for PA hinges. The darkest color represents the first folding cycles. The number of folding cycles increases with the brightness of the color of the curves, up to  $10^6$  cycles for aramid and PA hinges and  $10^4$  cycles for the photopolymer hinge (marked red).

The  $ULL$  and  $LFW$  show a decrease with increasing numbers of folding cycles, which can be attributed to fatigue (Figure 2.16g). The top graph shows the  $ULL$  normalized by the as-printed properties (round data points) and the failure probability (square data points) of the hinges versus the number of folding cycles. The  $LFW$  normalized by the as-printed properties is shown in the bottom graph. A decreasing trend for all hinge classes is found. When comparing the  $LFW$  and the residual angle with the theoretical model of constant stiffness, a reduction in stiffness can be observed for the aramid and photopolymer hinges, while the stiffness of the PA hinges does not change greatly (Figure 2.16i). In spite of the viscoelastic material properties, we do not observe a significant effect of the strain rate on the fatigue, which would appear as a discontinuity in the data from 200 to 1000 folding cycles.

The results of the different experiments are combined in Figure 2.17. The  $LFW$  is plotted against the  $ULL$  for the three hinge classes. The grey shaded zones indicate the change in properties due to fatigue. The length of the shadow provides information about the extent of fatigue and greyscale the number of the elapsed folding cycles. The dashed lines illustrate the change in properties resulting from a change in the respective design parameter.

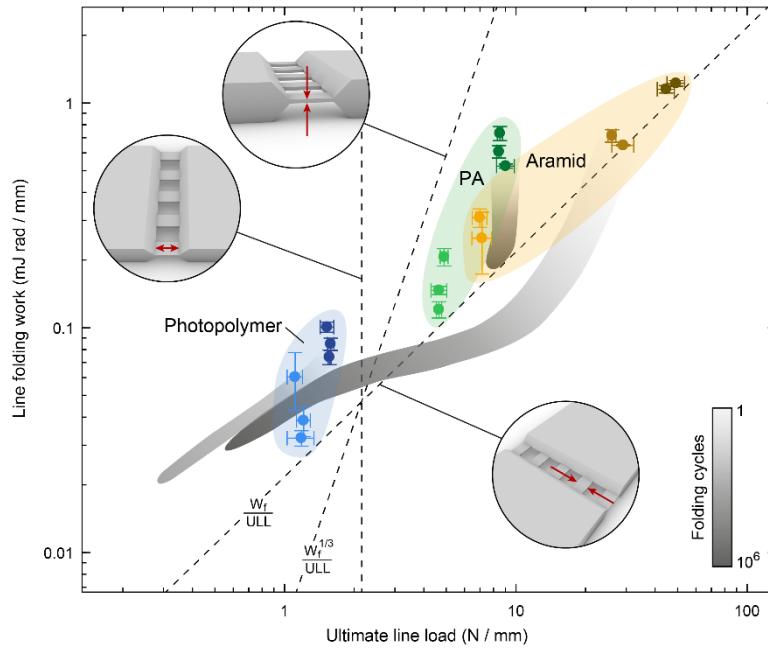


**Figure 2.17 Property map comparing ULL and LFW of the different hinge classes.** Fatigue is indicated as grey shadows. The greyscale provides information about the number of folding cycles. The dashed lines mark the change in ULL and LFW due to variation of the respective design parameter. Large regions of the property space can be accessed by materials selection and optimization of the design parameters. Modifying the hinge thickness leads to changing LFW while the ULL remains unaffected (vertical dashed line). A change in the amount of material in the hinge region with constant thickness leads to a linear scaling of both ULL and LFW. Thus, the properties change along the dashed line with slope one. Tuning the hinge thickness results in a linear change in ULL and the LFW changes with the power of three. The dashed line with slope three illustrates this scaling. The experiments are conducted by J. L. Huang and M. Wagner. Data processing is done by J. L. Huang and M. Wagner. The figure is made by M. Wagner [173].

### Influence of design parameters on mechanical properties

The mechanical properties of the hinge can be tailored by the design parameters (Figure 2.16a-c). The ultimate line load (*ULL*) of the hinges strongly depends on the amount of material in the hinge region. The experimental results shown in Figure 2.16a-c (top row) indicate a linear relationship between the *ULL* and both the number of fiber bundles and the thickness of the hinge. For the aramid hinges, an increase in load carrying capability of 50 N per aramid fiber bundle is found. This corresponds to a nominal tensile strength of 408 MPa, which is well below the 610 MPa reported by the supplier [21]. This discrepancy can be explained by the fact that not all fibers carry the same amount of load. The fibers at the bottom side of the hinge sag downwards, due to a lack of support while printing. Therefore, not all fibers are loaded equally under the uniaxial tension. This could be improved by the introduction of supports for printing the fibers across the hinge gap. However, the removal of these supports could lead to surface imperfections. Especially under flexural loading, this would lead to stress concentrations. The nominal tensile strength of the polyamide (PA) hinges has been found to be 43.4 MPa for a thickness of 0.2 mm and 47.4 MPa for a thickness of 0.1 mm. Literature suggests a slightly higher value of approximately 54 MPa [22]. This discrepancy originates from local stress concentrations near the interface to rigid segments due to the asymmetric design of the hinge. This is also the region where failure is observed in the tensile tests. The maximum stress at the interface between the rigid segments and the hinge region is considerably higher than the nominal stress calculated. A brief examination of the stress concentration in the PA hinges by means of finite element simulation can be found in the SI. The photopolymer hinges

show an average nominal tensile strength of 2.4 MPa. This value coincides with the 2.4 – 3.1 MPa reported by the supplier. The hinges failed inside the flexible polymer, not at the interface between the rigid and the flexible photopolymer, which is in accordance with literature[175].

The work required for folding the hinge strongly depends on both the number of fiber bundles and the hinge thickness (Figure 2.16a-c bottom row). While this finding coincides with expectation, the influence of the hinge length appears to be counterintuitive at first glance. The line folding work (*LFW*) of PA and photopolymer hinges decreases with the increase in the hinge length. This finding is in accordance with intuition since longer hinge areas lead to lower strains, stresses, and thus a lower *LFW*. For the aramid hinges, however, the opposite trend can be observed. An increase in hinge length leads to an increase in *LFW*. This alleged inconsistency can be explained by looking at the local deformation in the material for the respective hinges. The PA and photopolymer hinges exhibit a continuous strain distribution throughout the whole length of the bent segment. In contrast to that, the aramid hinges deform predominantly at a localized spot close to the rigid segment. In this region, the thickness of the aramid fiber bundle is lower than in the center of the hinge. The strain in the fibers exceeds the elastic limit, and plastic hinging occurs at the location with the lowest resistance, e.g. the reduced thickness region. Naturally, fiber composites exhibit a much higher stiffness under tensile loading than in compression. This stiffness disparity leads to a shift of the neutral axis towards the tension side. Compression of the fibers accommodates most of the deformation. The compressive stress results in buckling of the fibers, causing large deformation and inter-fiber failure of the PA matrix. For increasing hinge lengths, the stress and strain due to fiber buckling on the compression side are distributed to a larger volume of the matrix material, and thus the *LFW* increases.

The mechanical properties for the different classes of hinges span an enormous range. Both the *ULL* and the *LFW* vary by almost one and a half orders of magnitude. Further, the properties can be tailored precisely by the careful design of the hinge. The composite hinge greatly outperforms both PA and photopolymer hinges in terms of maximum achievable *ULL* in the as-printed state. Its tensile and flexural properties are highly controllable by the design of the hinge region.

### **Fatigue mechanisms and their impact on mechanical properties**

The fatigue of the flexural hinges is studied by analyzing changes in *ULL* and *LFW*, by investigation of the characteristic moment-angle curve, and by inspection using SEM. The combination of the findings from these three approaches allows the inference of the fatigue mechanisms.

The aramid hinges show an increase in *ULL* between 200 and 1000 folding cycles (Figure 2.16 g). This most likely originates from the different folding procedures. The samples up to 200 folding cycles are folded manually, whereas the other samples are folded on the Hydropuls fatigue testing setup. From the jump in the data, it can be concluded that manual-folding leads to a more rapid decrease in *ULL*, most likely because of slight variations in the folding axis.

Both the *ULL* and the *LFW* of the aramid hinges show a strong decrease with an increasing number of folding cycles. Starting from the first cycle, a stiffness decrease in the hysteresis loops can be observed (Figure 2.16d). Similarly, the strong deviation from the theoretical model of constant stiffness indicates a stiffness decreasing fatigue mechanism in the aramid hinges (Figure 2.16i). This originates from the deformation mode of the fiber bundles upon folding, which is examined in the previous section. Fiber buckling under compression results in high tensile stresses in the PA matrix. This leads to excessive plastic deformation and the formation of inter-fiber cavities in the matrix. Upon unfolding, the cavities close, and the resistance of the cavity walls under compressive stress conditions is small. The variation in deformation mechanism for tension and compression results in an enormous hysteresis, which can be observed most significantly in the initial folding cycles. With the increasing number of cycles, an interconnected network of voids between the aramid fibers forms due to the breaking of the PA. Consequently, the resistance to folding decreases strongly (Figure 2.16d). Moreover, the *ULL* is affected by this fatigue mechanism. With increasing plastic deformation, the load distribution in the fibers becomes progressively inhomogeneous under tensile loading conditions, lowering the *ULL*. Besides the failure of the PA matrix, fiber fracture in the region's maximum tensile stress is observed. The fiber ruptures at a later stage of the fatigue life than the fiber buckling. After folding the aramid hinge  $10^4$  times, no indication of fiber rupture is present, whereas the sample after  $10^6$  folding cycles exhibits large quantities of ruptured fibers. This is the fatigue mechanism, which eventually results in the failure of the hinge. Overall, the aramid hinges show low resistance to fatigue. There is no stable regime, and constant reduction of *ULL* and *LFW* prevail. The enormous hysteresis loop in the early folding cycles makes the aramid hinges uniquely suited for energy absorption applications.

The fatigue behavior of the PA hinges deviates strongly from the one discussed previously. The *ULL* is stable up to  $10^4$  folding cycles (Figure 2.16g). Subsequently, only a slight decrease in the *ULL* can be observed. The *LFW* shows a decreasing trend. However, the reduction in *LFW* can be attributed to the accumulation of plastic deformation, lowering the effective folding angle (Figure 2.16i) rather than to a reduction of the hinge stiffness. The very onset of crack nucleation is observed on the surface of the hinge specimen after  $10^6$  folding cycles. Parallel surface cracks are visible perpendicular to the tensile stresses on the surface, spanning a width of only 50 – 500 nm. These imperfections form in the center of the hinge region at the location of maximum tensile stress. The scission and relative sliding of single molecular chains lead to the formation of nucleation sites on the surface. Hence, a multi-axial stress-state develops and the material yields locally. These steps amplify the local stress concentration, resulting in a self-catalyzing propagation of the surface crack perpendicular to the tensile stress in plane and through the thickness of the hinge. This marks the transition from the cyclic stable stage of the fatigue life to the crack initiation stage. At this point, the mechanical properties are not yet affected significantly. Under further cyclic loading, the cracks will propagate deeper into the material and start to coalesce. The onset of fatigue crack initiation in PA depends strongly on the environmental conditions, e.g. absorbed humidity from the air acting as a plasticizer. While the specimen exhibits only the first signs of a fatigue crack, other samples showed failure after  $10^6$  cycles.

The fatigue fracture surface of a failed specimen is found in SEM image. During initial folding, the top side of the fracture surface was loaded in tension and the bottom side in compression.

As the crack initiates at the top and propagates through the thickness of the hinge, the neutral axis and hence the tensile and compression region shift downwards. Characteristic fatigue striations, which originate from consecutive crack arrest and growth, can be found on a large portion of the surface. Other than in metals, each line does not necessarily correspond to a single cycle of loading. The width of the bands decreases towards the lower side of the fracture surface. Under the assumption that the crack initiated at the top tensile sides and propagated through the thickness, the change in the width of the bands can be explained by the reduction of the peak stress, as the effective thickness gets smaller. In the upper half of the fracture surface, a large feature of yielded material can be found, spanning across the complete width of the hinge. Ledges are visible, which form when cracks originating from different planes, approach one another and coalesce. PA is known for its good fatigue properties with a life of up to several million cycles. In this study, PA hinges exhibit stable properties up to 105 folding cycles. After that, the crack initiation and cyclic growth might begin depending on the conditioning of the specimens. Under the right conditions (e.g. sufficiently high humidity), the hinges can withstand 106 folding cycles without deterioration of their mechanical properties.

The photopolymer hinges exhibit the lowest resistance to fatigue. A decrease in *ULL* beginning already at 100 folding cycles can be observed. Since the elastomeric photopolymer consists of a cross-linked network, there is essentially no plastic deformation (Figure 2.16f). The residual folding angle remains zero up to the point of failure. The photopolymer has the interesting property that the two surfaces of a crack adhere to each other when the crack is closed. After closure of the crack during unfolding, a significant amount of stress can be carried across the adhering crack surfaces. If the stress is sufficiently high, the crack opens and the stiffness drops. This explains why the moment at low folding angles changes less than the moment at folding angles above 70°.

The side surface of the photopolymer hinges appears very rough and irregular. This can originate either from the printing process or from the cleaning procedure, which was applied to the specimens before SEM imaging. The residues of the hydrogel support material on the specimen surface is dissolved chemically by immersion in a solution of 2 vol.% sodium hydroxide and 1 vol.% sodium silicate for 5 hours. It is unclear to which extent this procedure affects the surface of the photopolymer. Cracks are exclusively found on hinges, which have been subjected to fatigue testing. Thus, they should not originate from the cleaning procedure. After  $10^3$  cycles, cracks are visibly initiating from sites of stress concentrations, where the tensile stress and the stress caused by the Poisson effect superimpose. With increasing cyclic deformation, the cracks propagate through the thickness direction as well as in the plane. Cracks initiate at different locations, grow and approach. Thus, the loading conditions change, resulting in the formation of bifurcations and alternating propagation directions. This proceeds until the cracks coalesce, forming an interconnected network across the hinge width, significantly weakening the hinge and ultimately resulting in failure. The fracture surface after  $10^4$  folding cycles exhibits no signs of fatigue striations. The overall morphology of the surface appears rough, with marks similar to ledges. These features originate from changes in propagation direction and coalescence of cracks. The photopolymer hinges exhibit an accelerated decay of the *ULL* and *LFW* after 100 folding cycles, which can be attributed to the formation and propagation of cracks.

The investigated hinges behave fundamentally differently when subjected to cyclic deformation. The aramid hinges and the photopolymer hinges show limited resistance to fatigue. Most of the fatigue life is spent in crack propagation, which results in steadily decreasing mechanical properties. This is a characteristic of low cycle fatigue. The PA hinges in contrast, exhibits crack initiation and growth at a much higher number of folding cycles, indicating a high cycle fatigue behavior.

In general, it can be observed that a drop in  $ULL$  is always accompanied by the reduction in the bending stiffness and hence the  $LFW$ . This relation offers the opportunity to develop a smart hinge concept, in which the  $LFW$  is monitored to predict the residual  $ULL$  of the hinge and prevent failure in duty. This concept will be addressed in future studies.

### A guideline for the design of flexural hinges

All the experimental data is condensed into a double logarithmic representation of the  $ULL$  and  $LFW$  (Figure 2.17). This graph enables the comparison of the achievable properties for the different classes of hinges. Thus, it provides a tool to select the material and design parameters based on the target properties of the hinge. The change in mechanical properties due to fatigue is illustrated as grey shadows. The greyscale indicates the number of folding cycles. The shorter and darker the shadow, the higher if the resistance to fatigue of the hinge. The dashed lines represent the scaling of the mechanical properties depending on the change of the respective design parameter. If the hinge length is changed, the  $LFW$  can be tuned while the  $ULL$  remains unaffected. Thus, we move along the vertical dashed line. A change in the amount of material in the hinge with constant thickness, as is the case for the different numbers of fiber bundles of the aramid hinges, results in a linear scaling of both the  $ULL$  and the  $LFW$  (dashed line with slope 1). An increase in thickness, as for the PA and the photopolymer hinges, leads to a linear scaling of the  $ULL$ , while the  $LFW$  scales with the power of three (dashed line with slope 1/3).

Even though the linearized beam equations are generally not valid for structures undergoing large deformations, the observed relationship suggests that the stiffness of the PA and photopolymer hinges can be described by the analytical equations of the bending beam. Hence, the hinge can be modeled with a bending stiffness:

$$k_b = \frac{EI}{L} \quad (2.10) \quad \text{with} \quad I = \frac{b t^3}{12} \quad (2.11)$$

$k_b$  represents the bending stiffness,  $E$  is Young's modulus, and  $I$  is the area moment of inertia of a bending beam with rectangular cross-section,  $L$  is the length of the hinge,  $b$  is the width of the hinge and  $t$  is the thickness. The work required for folding the hinge is directly related to the bending stiffness of the hinge by:

$$W_f = \frac{1}{2} k_b \alpha^2 = \frac{E b t^3}{24 L} \alpha^2 \quad (2.12)$$

With the folding angle  $\alpha$ . This equation applies to the dashed lines in Figure 2.17 for scaling of the design parameters hinge width  $b$ , length  $L$ , and thickness  $t$ .



When tuning the individual design parameters, the  $ULL$  and  $LFW$  change along linearly independent vectors in the 2D property space. Therefore, the  $ULL$  and  $LFW$  can be decoupled when designing the hinge. This is only valid for a certain range of values, set by physical limitations, e.g. at a certain hinge thickness, the strain during folding will exceed the failure strain of the material.

Figure 2.17 property map implies that the selection of the hinge material depends on the requirements set by the application. The aramid hinges are the first choice for high loading scenarios with low numbers of folding. PA hinges show the best performance over elevated numbers of cyclic deformation, and the photopolymer hinges exhibit the lowest resistance to folding, which allows the use of low-power actuators.

### 2.3 Integration of active components and additive manufactured flexure hinge

We have discussed the design, model, and characterization of the key components for multi-DoF origami-inspired robots, including actuators, adjustable stiffness components, and additive manufactured hinges. However, are the active components still behave similarly while integrating into structural materials? In [176], we proposed a model that analyzes the mechanics of origami folding joints consist of multi-material layers that have semi-rigid connections at the material interfaces. The model suggests that localized bending at folding hinges, the semi-rigid, flexible behavior on the material interface, results in different bending behavior from the mono-material hinge proposed in sections 2.2.

#### 2.3.1 Characterization of SMA torsional actuators embedded with flexure hinge

First, we design prototypes that allow us to measure the maximum torque output of SMA torsional actuators with different where SMA is embedded between two glass fiber layers(Figure 2.18). The measurement results are shown in Figure 2.19. We can already found that the measurement results are quite different from the results shown in Figure 2.6 since they have different boundary conditions. The SMA torsional actuators can have a higher maximum torque output with a shorter hinge gap thanks to bigger bending curvature. It is Induced by constraining of the semi-rigid material interface and localized bending.

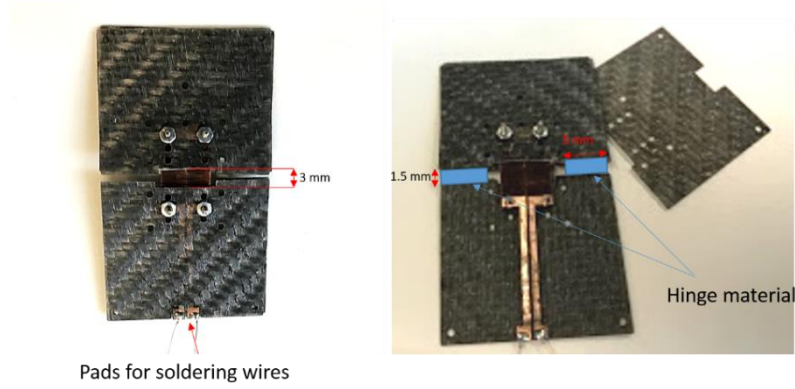


**Figure 2.18** The prototypes for measuring torque output for SMA torsional actuators with different hinge gaps

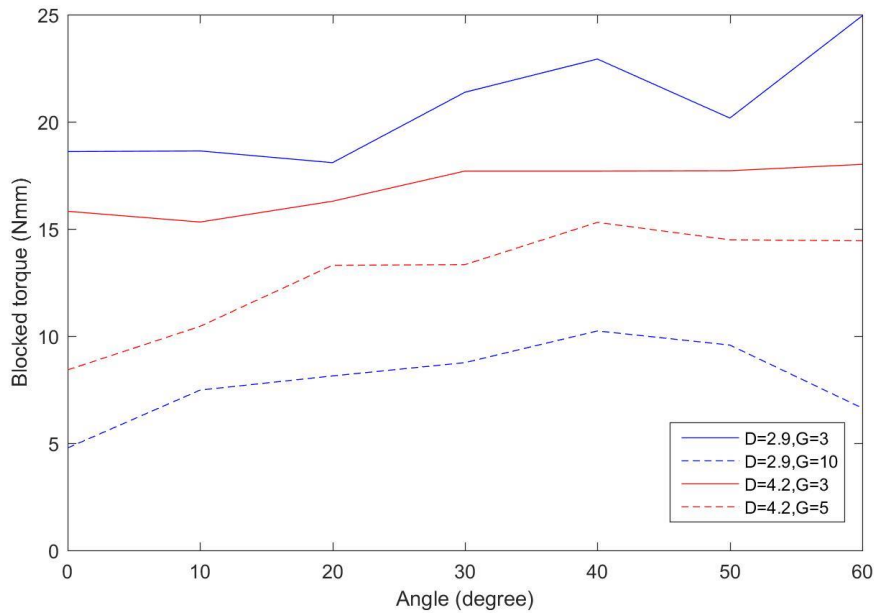


**Figure 2.19** Circular SMA actuator with different diameters and hinge gaps. D: Diameter of circular SMA, G: Hinge gap. We have test 4 prototypes with varying parameters of design to evaluate the torque output performance.

Then, we examine the performance of additive manufactured active hinges consisted of 3D printed hinges with torsional SMA actuators and heaters embedded. The design and fabricated prototypes are shown in Figure 2.20. We first 3D print Nylon base material and stop the printing work for drop-in of SMA and heaters. Then, we put nylon insulation layers to prevent the SMA actuator from being activated by the extruded materials in the subsequent printing process. Finally, we continue the printing job for sandwiching the SMA actuator between the 3D printed structure. The design parameter is shown in Table 2.1. The bending stiffness and Maximum torque output are shown in Figure 2.21. We can find the residual angle is around 40 to 45° for the polyamide hinges and aramid hinges shown in the bending stiffness test results. And the residual angles are smaller than the results we found in the previous section (Figure 2.16 d,e ) due to the hyperelastic properties of SMA. The constraints from the 3D printed hinge have a huge impact on the torque output of SMA. Although the aramid hinge

has a lower bending stiffness, the torque output aramid hinge is smaller than the polyamide hinges. And this may be due to the localized bending behavior and larger axial strength for the aramid hinge, which contributed extra resistance for SMA bending. We can also find that polyamide hinge even amplifying the torque output. The change of the rotational axis also has a great influence on the blocked torque, which needs to be further investigated.

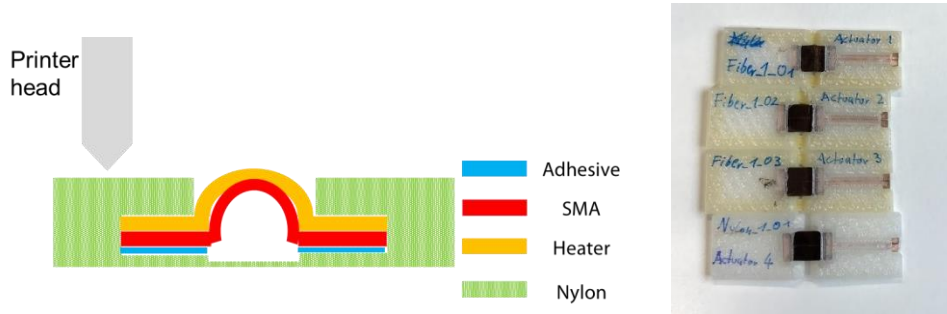


**Figure 2.20 3D printed active hinges with actuators and heaters embedded**

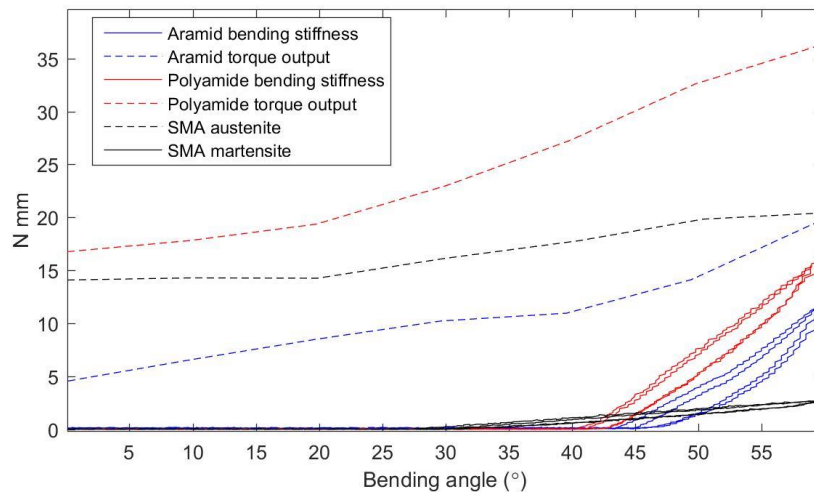


**Figure 2.21 Torque output and torsional stiffness of the 3D printed active hinge**

**Table 2.1 The radius of torsional SMA actuators and hinge material for each sample**

	SMA Radius (mm)	Hinge material
Sample 1	0.5	Aramid fiber
Sample 2	1.45	Aramid fiber
Sample 3	2.1	Aramid fiber
Sample 4	1.45	Polyamide

### 2.3.2 Development of actuated reconfigurable mechanisms

We would like to combine the understanding of previous parts in this chapter for building an integrated origami mechanism that consists of low-profile actuators and flexure hinges as an example. We quantitatively study the bistable behavior of a six-bar kinematic chain origami

prototype based on the water-bomb pattern by conducting a geometric and potential energy analysis of the pattern and its stable positions. We developed a kinematic model to describe the behavior of the joint and suitable actuators that generate desired motions. Secondly, an SMA-actuated solution was proposed to change between the two stable states our structure possesses and to control its end-effector position. The lightweight SMA-actuated origami bi-stable two-mode stiffness joint with a high workspace that can rapidly change between its two stiffness modes and which can be a reconfigurable mechanism for robotic applications.

### Waterbomb pattern-based origami mechanisms overview

Waterbomb origami pattern is one of the most commonly applied origami patterns. It is a single-vertex origami pattern with bistability. It has been used in the applications such as bio-medical robots, robotic grasper, and locomotion[34], [177], [178]. Waterbomb patterns can behave similarly to a spherical mechanism and bistable states critical can be helpful for different applications[46]. That is bistability can amplify displacements by small incremental force to release the stored energy. Also, the transition of bistability could also possibly provide extra DoFs to the structure in some origami structures[163]. In this section, we would like to explore and study the behavior of bistability in actuated waterbomb-based origami structures.

### System design and model

Three-dimensional structures can be obtained through origami techniques by erecting and folding a 2D arrangement of rotational joints, in this case, origami creases. We present the origami pattern, which is used to achieve the two-mode stiffness bistable behavior, its degrees of freedom, and we propose an actuation solution that will later be used to control the structure, which is realized to a layer-by-layer fabrication method. Our crease pattern is schematically represented in Figure 2.22, in which the six creases are symmetrically distributed with respect to the axis defined by the line passing through points  $B$  and  $E$ . The pattern is also symmetrical with respect to the axis created by the crease lines  $l_1$ ;  $l_4$  that is perpendicular to the axis  $BE$ . The six creases have a single common vertex  $V$  that will later be used to analyze the pattern geometrically. The employed foldable serial structure is composed of one spherical six-bar kinematic chain, as shown in Figure 2.22. The structure possesses two different ranges of motions depending on the angle between lines  $BV$  and  $EV$ , as shown in Figure 2.23.

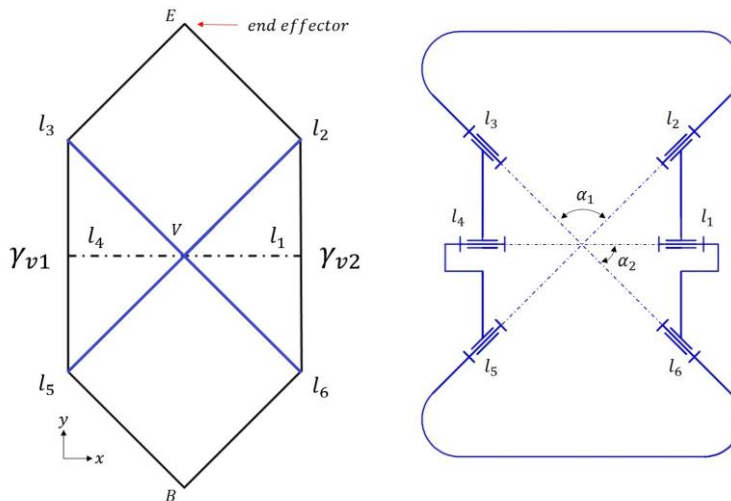


Figure 2.22 Water-bomb based origami joint and equivalent kinematic chain

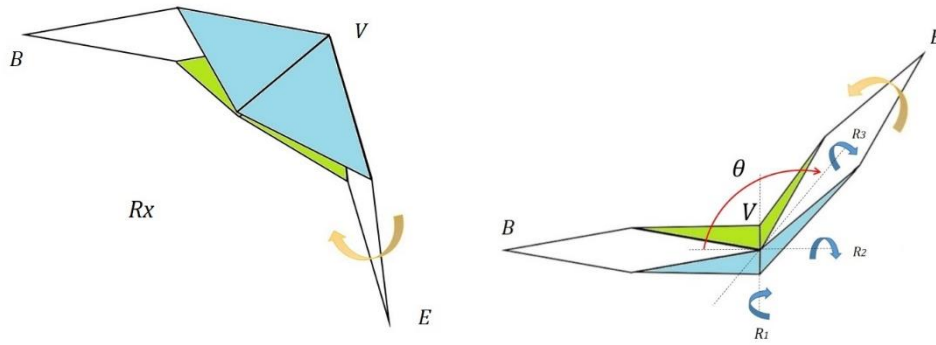


Figure 2.23 Two range of motion due to different bistable states

### Actuation design

For actuating the waterbomb origami in and switching between the two bistable states, we proposed the actuation design, which consists of two  $\Omega$ -SMA torsional actuators for end-effector positioning and two SMA springs actuators for changing bistable states, as depicted in Figure 2.24.

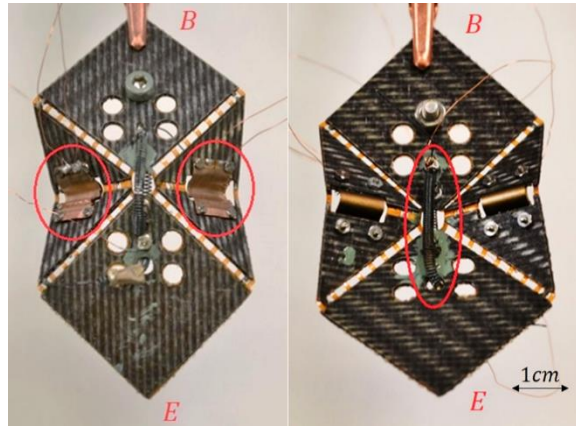


Figure 2.24 Actuators for control the origami joints in two bistable states

### Single-vertex fold analysis

For understanding the kinematic behavior and find the design parameters for actuators, we studied the analytical model of waterbomb pattern. Single-vertex fold of the model in its state A, as shown in Figure 2.25 (the left pattern). State B has a much simpler pattern, making the structure act as a simple small-length flexural hinge, as shown in Figure 25 (the right pattern).

We describe the movement by two main folds: (1) Movement across a face of the crease pattern: rotation of  $\alpha_i$  on xy plane denoted by  $A_i$  (2) Movement of crossing a fold line  $l_i$ : rotation of  $\rho_i$ , denoted by  $C_i$ . The matrix represents a rotation in the yz-plane (around the x-axis) by the folding angle  $\rho_i$ . Then, we can denote the counter-clockwise rotation of angle  $\rho_i$  around the axis corresponding to the crease line  $l_i$  as

$$\chi_i = A_i C_i A_i^{-1} \quad (2.13)$$

Where  $A_i$  and  $C_i$  can be denoted by

$$C_i(\rho_i) = \begin{bmatrix} 1 & 0 & 0 \\ 0 & \cos \rho_i & -\sin \rho_i \\ 0 & \sin \rho_i & \cos \rho_i \end{bmatrix} \quad (2.14) \quad \text{and} \quad A_i(\alpha_i) = \begin{bmatrix} \cos \alpha_i & -\sin \alpha_i & 0 \\ \sin \alpha_i & \cos \alpha_i & 0 \\ 0 & 0 & 0 \end{bmatrix} \quad (2.15)$$

As described in [179], when executing a circular closed path around a single vertex, we can define that  $\chi_n \chi_{n-1} \cdots \chi_1 = I$ . Then, we can obtain the relation between mountain angle  $\rho_m$  and valley angle  $\rho_v$  in state A. The modeling results are shown in Figure 2.26.

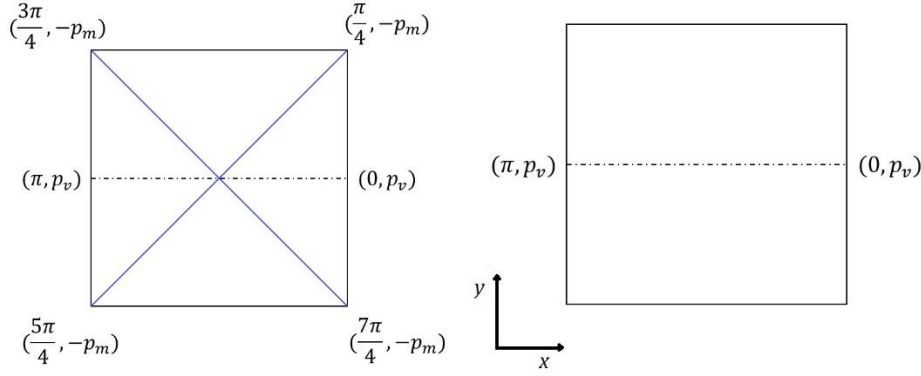


**Figure 2.25 Schematics of the crease pattern.** Solid-lines are mountain-fold and dashed-lines are valley-folds.

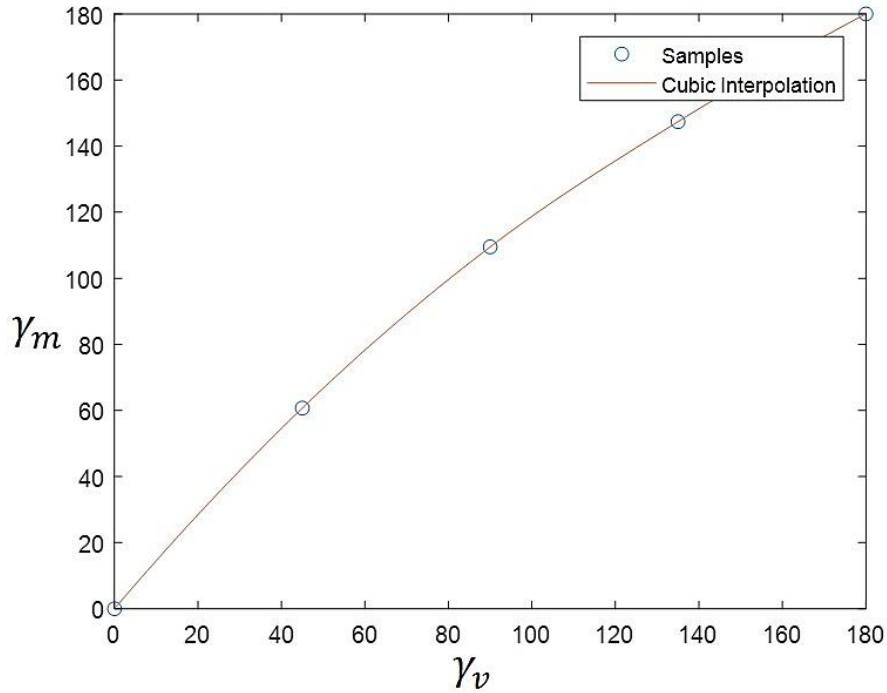


**Figure 2.26 Interpolated curve for mountain and valley folding angles.**

### Potential energy model for changing the bistable states

The potential energy analysis was executed by representing each fold as a compliant small-length flexural hinge with the parameters. Then, the potential energy stored in a small-length flexural hinge, and therefore in each fold, is expressed by

$$V = \frac{1}{2}k(\Theta)^2, k = \frac{EI}{l} \quad (2.16)$$

where  $\Theta$  is the rotational deflection away of the stable position and the stiffness  $k$ . where  $E$  is Young's modulus of the material,  $I$  is the moment of inertia, and  $L$  is the length of the hinge.

### The potential energy of origami structure and SMA

We assume a symmetry condition that all the mountain folds have the same parameters and angle value, and the same condition has to be true for all valley angles. In this case, we have two different types of hinges (valley and mountain) whose stiffness constants will be denoted  $k_v$  and  $k_m$ , respectively. With these two constants, we can express the total potential energy of the structure by the following equations for range A and range B, respectively.

$$\begin{aligned} V_{structure} &= k_v(\gamma_v - \gamma_{v0})^2 + 2k_m(\gamma_m - \gamma_{m0})^2 \\ V_{structure} &= k_v(\gamma_v - \gamma_{v0})^2 \end{aligned} \quad (2.17)$$

The total potential energy of origami structure with embedded actuators can then be expressed as the sum of the potential energy of the structure and the potential energy generated by all the non-actuated SMA actuators on their martensitic state, as shown in Eq 2.8. With the modeling results proposed in the previous sections(for SMA spring and torsional actuators), we can obtain the potential energy of origami structure with actuator mounted, as shown in Figure 2.27.

$$V_{Total} = V_{structure} + V_{torsional\ SMA} + V_{spring\ SMA} \quad (2.18)$$

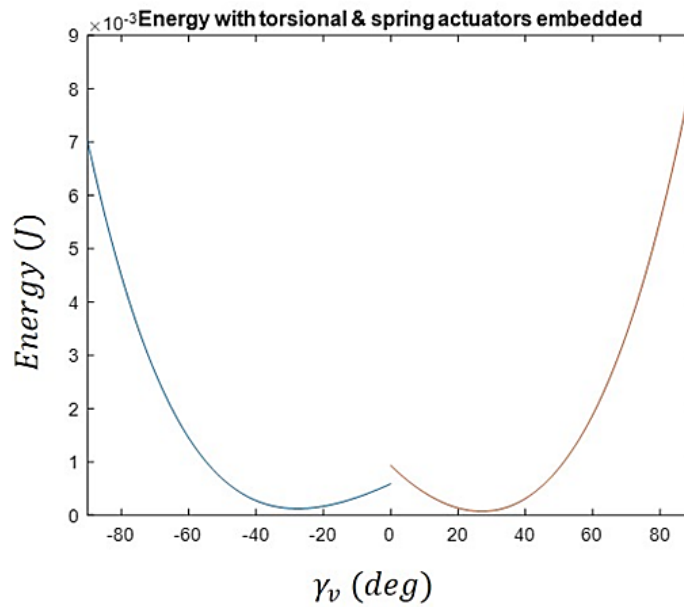


**Figure 2.27 Potential energy of origami structure.** The different colors show the potential energy in two different bistable states.

### SMA spring for changing the bistable states

Since we have the potential energy required for changing the state, we can compute the design parameters for SMA spring actuators. We introduce a schematic representation of our

structure on its highest energetic configuration, where the actuator  $SMA_{spring2}$  is in its compressed (either austenitic or twinned martensitic) state, and the other actuator  $SMA_{spring1}$  is on its elongated (detwinned martensitic) state, as shown in Figure 2.28. Where  $l/2$  is defined as the distance between the point where the spring actuator is attached to the structure and the central vertex. Then, for making the SMA spring actuator function as desired, the design parameter should satisfy the formula 2.19.

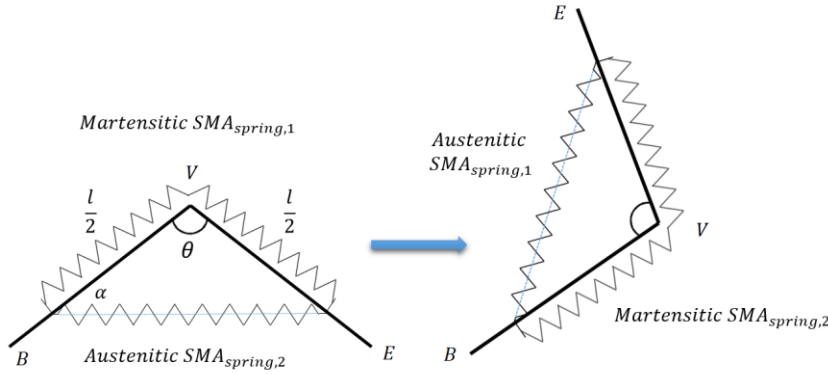


**Figure 2.28 Schematic of two different bistable states**

$$\frac{1}{D^3 n} = \frac{16(k_v(\gamma_v - \gamma_{v0})^2 + 2k_m(\gamma_m - \gamma_{m0})^2)}{d^4(G_{aus} - G_{mar})\delta^2} \quad (2.19)$$

### 2.3.3 Prototyping and characterization

#### Fabrication

We developed a prototype to validate the functionality and to compare it with the modeling results. The method we used for fabrication is based on a layer-by-layer fabrication, but the robot design can be fabricated as well following the additive manufacturing process for reducing fabrication time and complexity by reducing the number of layers.

We employed a CO2 laser micro-machining station (Trotec Speedy 400). The different layers of the structure are illustrated in Figure 2.29. The structure contains two layers of glass fiber, one layer of Kapton, and two adhesive layers to integrate the separate layers together.

The first step of the process was to prepare the structure. We cured two 250  $\mu\text{m}$  glass fiber layers together at 160  $^\circ\text{C}$  and 500 lbs of pressure for 30 min by using a heat press (Carver 3853CE). Secondly, the desired crease pattern in 2D is generated on the previously cured glass fiber using the CO2 laser (Trotec Speedy 400). Similarly, the Kapton layer with 75  $\mu\text{m}$  of thickness is the foldable joints between the glass fiber tiles, deploying the role of the hinge. Afterward, the adhesive layers are cut, concluding the preparation of all the separate layers. Then, all the layers are aligned and placed in the heat press at 130  $^\circ\text{C}$  for 30 min to be cured.



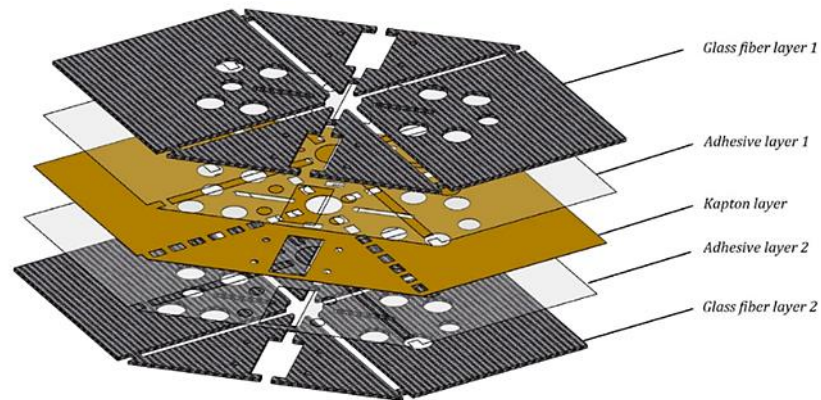


Figure 2.29 Schematics for the design of functional layers

### Experiments

In order to measure the stiffness of the origami joints and their output torque, a customized 3D printed fixing plate has been made and mounted on the setup we proposed in the previous sections, as shown in Figure 2.30.

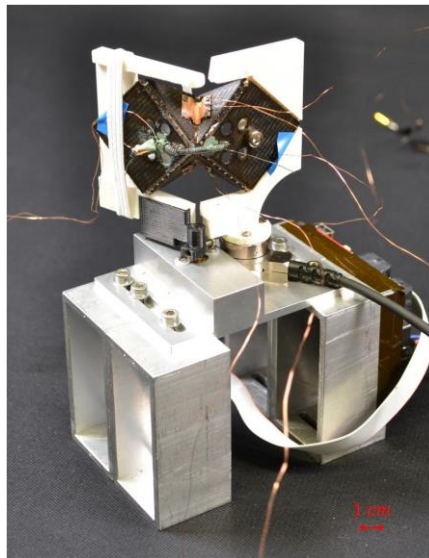
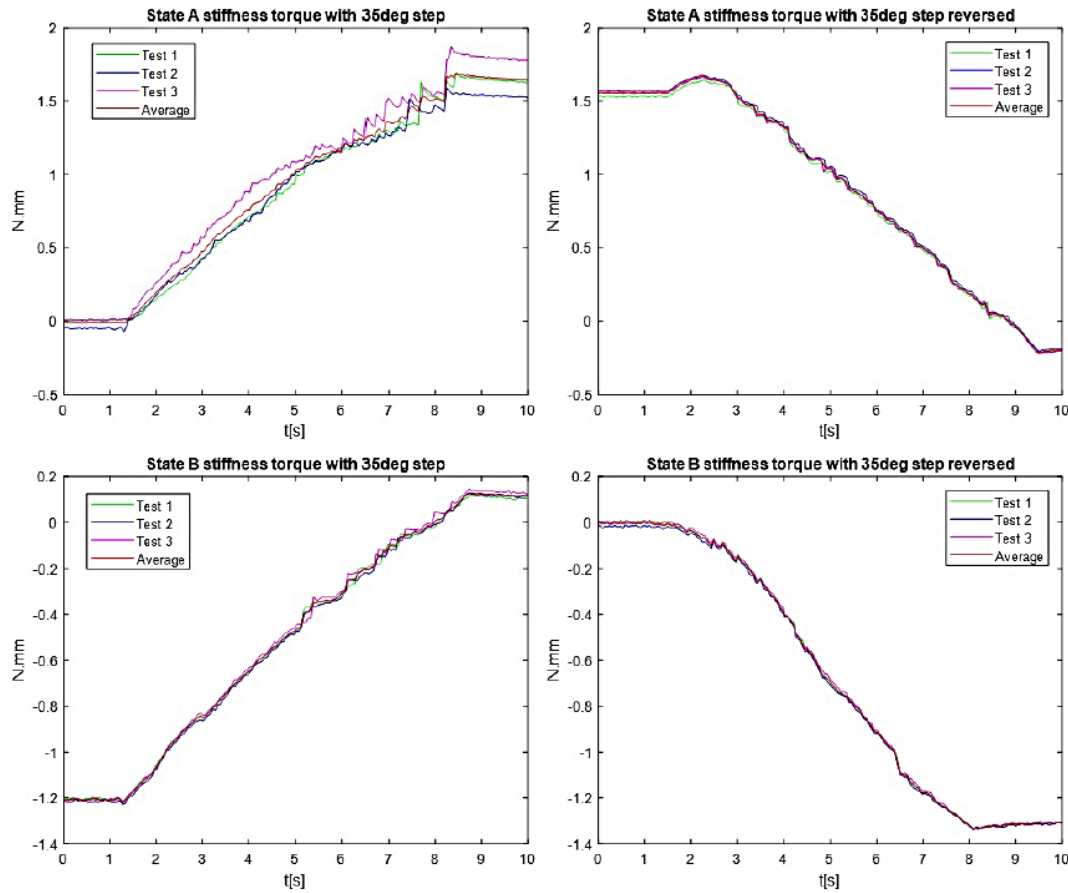
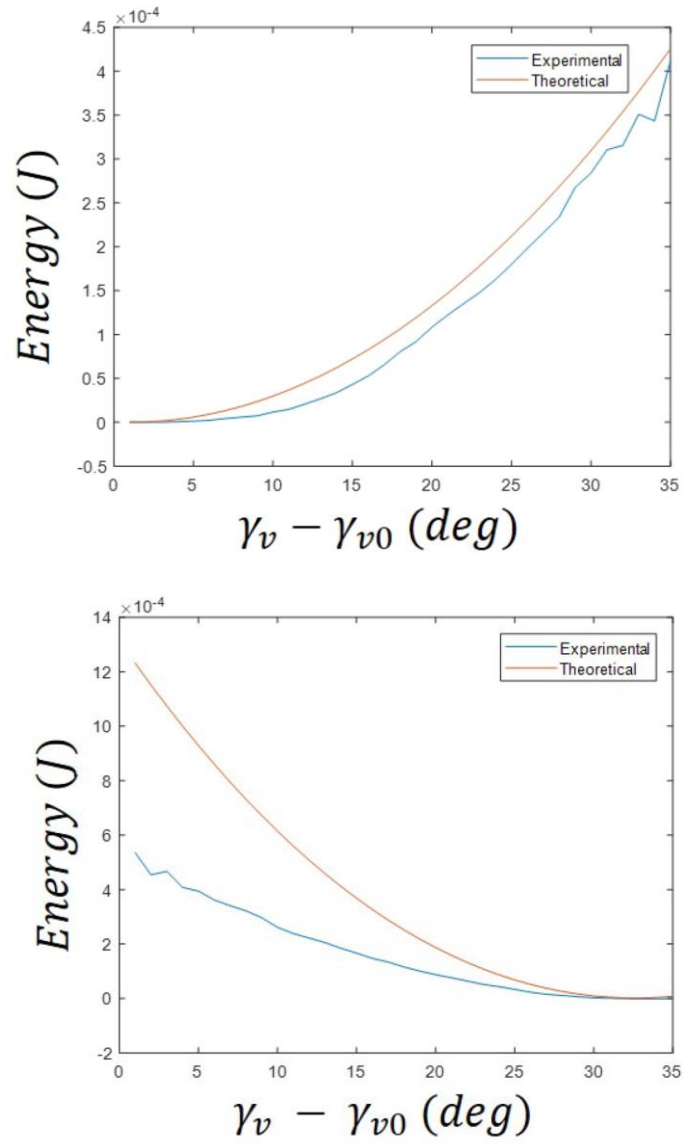


Figure 2.30 Characterization setup for bistable origami joints with customized holder



**Figure 2.31 Torsional stiffness measurement of bistable origami joints**

In order to characterize the two-mode stiffness of our joint, two different tests were made for each state where none of the embedded actuators were activated. First, the moving plate was brought to the stable angle position, where the measured torque was as close to 0 Nm as possible. Once the zero position was established, we folded the joint with  $5^\circ/\text{sec}$  speed by the DC motor until it reached  $35^\circ$ , and the output torque was measured throughout the displacement. A reverse test was conducted as well, where the moving plate was brought from  $35^\circ$  to the previously established zero position so that the hysteresis could be analyzed. Both tests were repeated three times for states A and B, and the mean value curve of each was used for determining each state stiffness. The measured stiffness is shown in Figure 2.31. There is a slight difference between both loading and unloading tests, but both are similar to the modeling value that was previously calculated. Furthermore, the experimental torque found for state B was used as well to calculate the potential energy of the structure in this state. With the comparison shown in Figure 2.32, we can observe that the stated modeling presents a satisfactory description of the potential energy of the structure.



**Figure 2.32 Comparison between theoretical and experimental energy values**

For validating the performance of torsional SMA, we measured the blocked while activating both torsional SMA actuators. The measured result is shown in Figure 2.33. The torque output generated by the -SMA actuators in state B was expected to be higher than the torque generated in state A, as the latter one has a bigger stiffness.

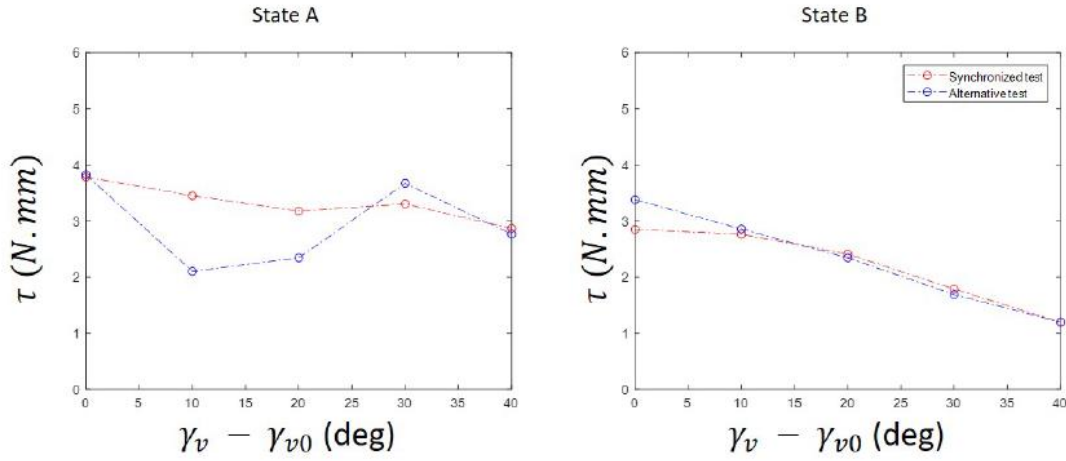


Figure 2.33 End-effector torque generated by the two torsional SMA actuators.

### 2.3.4 Conclusion

We developed analytical models to describe the behavior of the bistable origami joint from the component level like actuators and hinge stiffness to the overall behavior of the active origami mechanisms. Secondly, an SMA-actuated solution was proposed where spring SMA for switching between the two stable states and torsional SMA for controlling the end-effector position. The range of motion can be switched, and bending stiffness can be changed by switching the bistable states. These results give us a trace for designing a dual stiffness joint, shock-absorbing, explosive movements such as jumping, and dual operation for creating different motions for gripping applications. Current implementation and analysis are for layer-by-layer fabricated prototypes. The methodology for designing and building additive manufactured prototypes needs to be further investigated. For example, the design of 3d printed hinge with desired potential energy and residual angle for generating bistable properties would be an interesting topic to study.

# The design and demonstration of multi-DoF reconfigurable systems for customizable functionalities

In this chapter, we demonstrate the capabilities of design methods for reconfigurable robotic systems for additive manufactured structures across various applications. To overcome additive manufactured active structures' current limitations, we investigate the fabrication process, which has included additive manufactured structures with subtractive manufactured embeddable functional components. We also propose a strategy to configure functional components in order to achieve desired functionalities. There are three applications, wrist for a robotic gripper, space hinge for orientating the solar panel, and self-assembly floating solar panel.

## 3.1 The multi-function enhancement of a 4D printed 3DoF origami module

In the first part of Chapter 3, we investigate the design of a 4D printed, lightweight, reconfigurable, and reversible actuated 3DoF origami module. We integrate low-profile functional components—such as actuators—and variable stiffness components into the printing process. Moreover, we study functionality enhancements, such as tunable compliance and self-assembly, with different configurations of embedded components. Then, we investigate 3D printed active systems' behavior and systems.

### 3.1.1 An overview of 4D printed structures and mechanisms

Additive manufacturing (AM), also known as 3D printed technology, has offered opportunities for the rapid design and fabrication of highly customized components and structures, which are popular and heavily used in research. Furthermore, it has also allowed the manufacture of complex structures or mechanisms in a single step, without a post-process or assembly. The fabrication of complex and multi-articulated mechanisms is often regarded as time-consuming

---

The material of this chapter is adopted from the following self-authored publications.

Oleg Testoni, Thomas Lumpe, **Jian-Lin Huang**, Marius Wagner, Sampada Bodkhe, Zhenishbek Zhakypov, Ralph Spolenak, Jamie Paik, Paolo Ermanni, Luis Muñoz, and Kristina Shea 'A 4D printed active compliant hinge for space using shape memory alloys and polymers' *Smart materials and structures*, 2021

The contribution of Jian-Lin Huang were concept and design of hinge, design and fabrication of actuators and heaters, energy consumption evaluation, all experiments, results analysis, and partial writing.

and demanding. Work in this field has also paired rigid materials with uncured resins as a function of designed compliance through AM. These methods, though novel, have relied heavily on human labor for controlled postprocessing techniques, assembly, and deployment.

3D printing fabrication has not yet been massively applied to industrial manufacturing due to some drawbacks. Costs, limited material choices, build sizes, and production speeds remain uncompetitive with traditional fabrication methods. Nevertheless, growing interest in different applications' development persists as new printable materials are investigated.

More recently, the new concept of 4D printing—with an extra dimension, time—was proposed, extending printed systems' capabilities, thanks to the development of printable smart material[180]–[182]. 4D printed systems can achieve morphological changes through external excitations, such as heat, light, and magnetic fields. However, smart-material-based and additive manufactured interactive systems remain in their infancy; many recent studies have had limited capabilities to create repeatable, reversible, and controllable motions. In most 4D printing cases, actions are triggered by environmental excitation. How to implement in-situ, multi-stage, programmable, and controllable actuation for desired functionalities is one of 4D printing's great challenges. Furthermore, the technology's limited force output due to inherent material properties has also hindered its potential applications.

#### **3.1.2 Design of multi-functional 4D printed origami module**

We aim to investigate the strategy of how to implement additional functionalities for a known multi-DoF mechanism and overcome conventional limitations via the synergy of additive manufacturing technologies and functional materials. We chose a 3DoF origami-inspired parallel mechanism for studying its behavior. This robotic origami mechanism has been proposed for the robotic arm and grasper for medical applications with SMA actuators [183], pneumatic actuators[141], or tendon-driven systems[184]. However, the challenges for assembly of modules, integration of actuators, and the capability for withstanding external loading have still remained. Here we propose a strategy that suggests the synergy of additive manufacturing origami structures and low-profile functional materials. And a study of the configuration of functional components and control schemes gives a hint for functional enhancement for integrated multi-DoF reconfigurable systems.

##### **Variable stiffness origami module**

The variable stiffness enables to strengthen the structure while needed or increasing the efficiency for performing desired tasks. There are also examples that employ SMP for changing the stiffness of folding hinges resulting in various grasping modes for robotic gripping applications. Thus, we implement the variable stiffness SMP components proposed in Chapter 2 for achieving partial stiffening in multi-DoF reconfigurable robotic systems.

##### **Design and stiffness modeling**

We design an origami-inspired parallel mechanism as depicted in Figure 3.1. The 3 DoF reconfigurable robotic module can be designed and fabricated with a quasi-2D origami pattern and then folded up to a 3D structure. The functional components, SMA for activating the origami

### 3 Design and demonstration of multi-DoF reconfigurable systems for customizable functionalities

structure and SMP for stiffening the hinges, are embedded during the 3D printing process. For realizing the behavior of origami module embedded with stiffness changing elements on the hinge. We derive a model base on the repelling-screw theory proposed in [185].

When an origami structure is deformed, torques generated from folded creases result in an integrated reaction force to counter the external force applied at the origami structure. The reaction force of the linear-motion mode of the origami mechanism is simulated by adding the same displacement loads at three prismatic joints. The resistive torque generated by crease  $i$  can be expressed by:

$$\tau_i = k_0 l_i (\theta_{s,i} - \theta_{s,i}(0)) \quad (3.1)$$

Where  $k_0$  and  $l_i$  are the stiffness coefficient of the hinge and length of crease  $i$ , respectively.  $\theta_{s,i}(0)$  is the initial angle between two panels of crease  $i$ .  $\theta_{s,i}$  is the angle at the current stage and determined by the position of waterbomb linkage, as shown in Figure 3.2. There are some assumptions in [185] which is not suitable for our design: (1) Stiffnesses of creases include  $B$  and  $P$  (as shown in Figure 3.2), are omitted to simplify the comparison procedure. (2) Resistive torques  $\tau_i$  purely based on the geometry and position of folded origami structure (3) Stiffness coefficient  $k_0$  of a single crease is assumed to be constant. We have modified the model accordingly for our design. Nylon hinge bending stiffness are calculated from previous experiment results for 3D printed hinge by linearized beam equations.

$$k_0 = \frac{EI}{L} \text{ with } I = \frac{b t^3}{12} \quad (3.2)$$

Where  $b$  and  $t$  are the width and thickness of the hinge, respectively, we set the initial configuration with module height as the initial condition of the model, and input for the model is vertical distance  $h$  between the top and bottom panel, as shown in Figure 3.2. Then, the reaction force along the vertical axis of the moving platform can be computed as:

$$f_e = \frac{3}{b \cos \theta_1} \frac{(2 \sin \gamma_1 \cdot \tau_L + 2 \cos \beta_1 \sin \alpha_1 \cdot \tau_S)}{\cos \beta_1 \sin(\gamma_1 - \alpha_1)} \quad (3.3)$$

With this formula, we can calculate the axial stiffness of the origami module by giving geometrical parameters and materials stiffness of SMA, SMP, and Nylon hinge as model input.

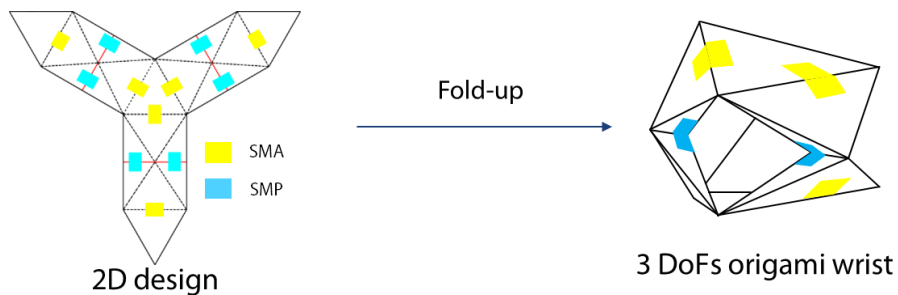


**Figure 3.1 Design of 3 DoF origami module.** Blue and yellow rectangles are represent SMP and SMA, respectively. Dashed lines are valley folds and red lines are mountain folds.

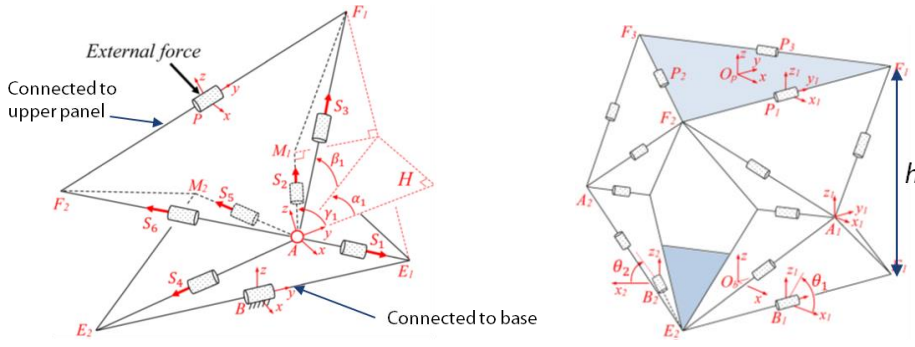
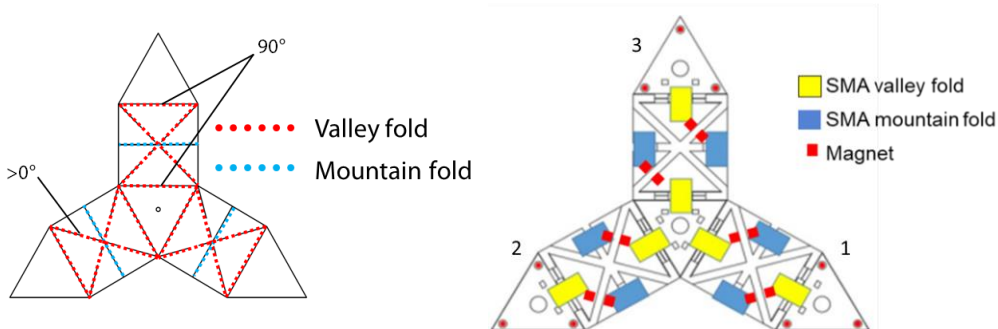


Figure 3.2 Geometrical relationships of the equivalent spherical joint, adapted from [185]

### Self-assembly of origami module

Self-assembly is one of the core functions that can be achieved by 4D printing. With proper design of pattern and folding sequence, arbitrary 3D geometries can be achieved by self-folding from a 2D origami design[186]. Many works have been done regarding self-folding to the desired shapes for different scales, from DNA folding, MEMS structures to Mesoscale self-folding structures [10], [11], [187]–[191]. Relatively less work has been done for self-folding/assembly to achieve a functional mechanism or robot. [192], [193] present the robot that can self-assemble by folding. However, both works need extra motors installed after the self-assembly process for actuating the robots. [33], [194] present self-folding robots that can fold themselves to a robot shape and functional for medical applications. However, the requirement of an external magnetic field for actuating and controlling the robots may not be applicable for larger-scale applications and limited control of DoF for an individual robot.

Here, we propose a self-assembly 3 DoF origami module with exactly the same crease pattern as the origami module we proposed in the previous sections. By changing the configuration of the functional components, the origami module can print with 2D design and self-fold and assemble to a 3DoF self-actuated origami module. The crease pattern and configuration of the functional components are shown in Figure 3.3. Since the SMA actuators can be embedded with heaters or self-heating with a zigzag pattern during the 3D printing process, distributed controllable actuation can be accomplished. The square magnets shown in Figure 3.3 are designed for creating initial valley folding on the limbs. Once initial foldings were made by square magnet (attraction), the continued SMA mountain folds can establish the water bomb pattern folding on the limbs. Circular magnets are designed for top plate assembly, as shown in Figure 3.3.





**Figure 3.3 Design of self-assembly origami module**

We conducted self-assembly experiments by sequential folding, as shown in Figure 3.4. The origami module starts with a 2D flat configuration (Figure 3.4a). Then, activations of the mountain and valley folds of SMA on limb 1, which bring it to the assembly position, as shown in Figure 3.4b. Afterward, we activate the valley fold SMA connected to the central triangle on limb 2 and mountain fold SMAs at the same time for lifting limb 2. We activate the other valley fold SMA while the base valley fold SMA bends around  $80^\circ$ . The assembly of top plates can be carried out by the attraction of circular magnets (Figure 3.4c). The same control sequence for limb 3 is carried out for accomplishing self-assembly (Figure 3.4d-f). The assembled origami module can have 3DoF controllable motion while activating SMAs.

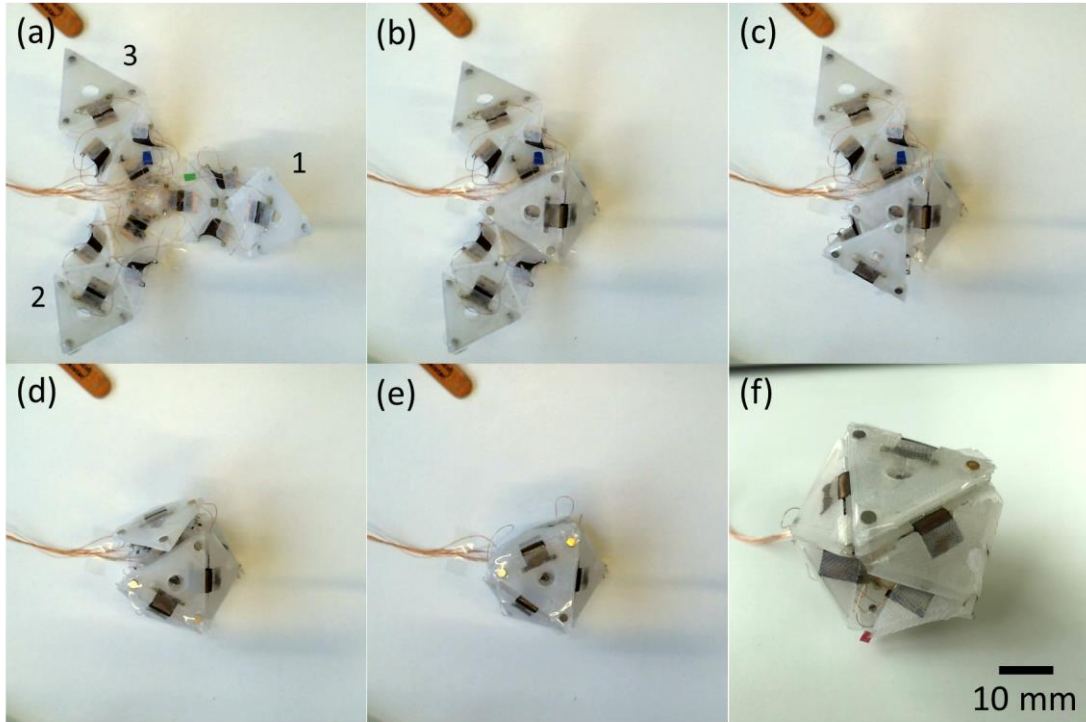


**Figure 3.4 Self-assembly sequence**

### **3.1.3 Characterization and function validation of 4D printed origami module**

In the characterization section, we start with the validation of variable stiffness property. We measure the axial and lateral stiffness of the origami module. Then, we examine the load-carry capability of the module. Last, we implement a closed-loop control system for controlling the module.

#### **Experimental platform**

For the experiments, the purpose was to constraint the robot to move in predefined directions while measuring the various forces thanks to a sensor. The purpose was to understand and characterize the robot stiffness and, more generally, its behavior. In order to do so, three stepper motors were attached to the robot using strings (nylon fishing wire). The three motors were necessary in order to simulate a movement in the XYZ plane. The experimental setup for

### 3 Design and demonstration of multi-DoF reconfigurable systems for customizable functionalities

1 DoF and 3DoF measurements are shown in Figure 3.4 and Figure 3.5. For the closed-loop control system, we install the camera on top of the module for tracking the motion.

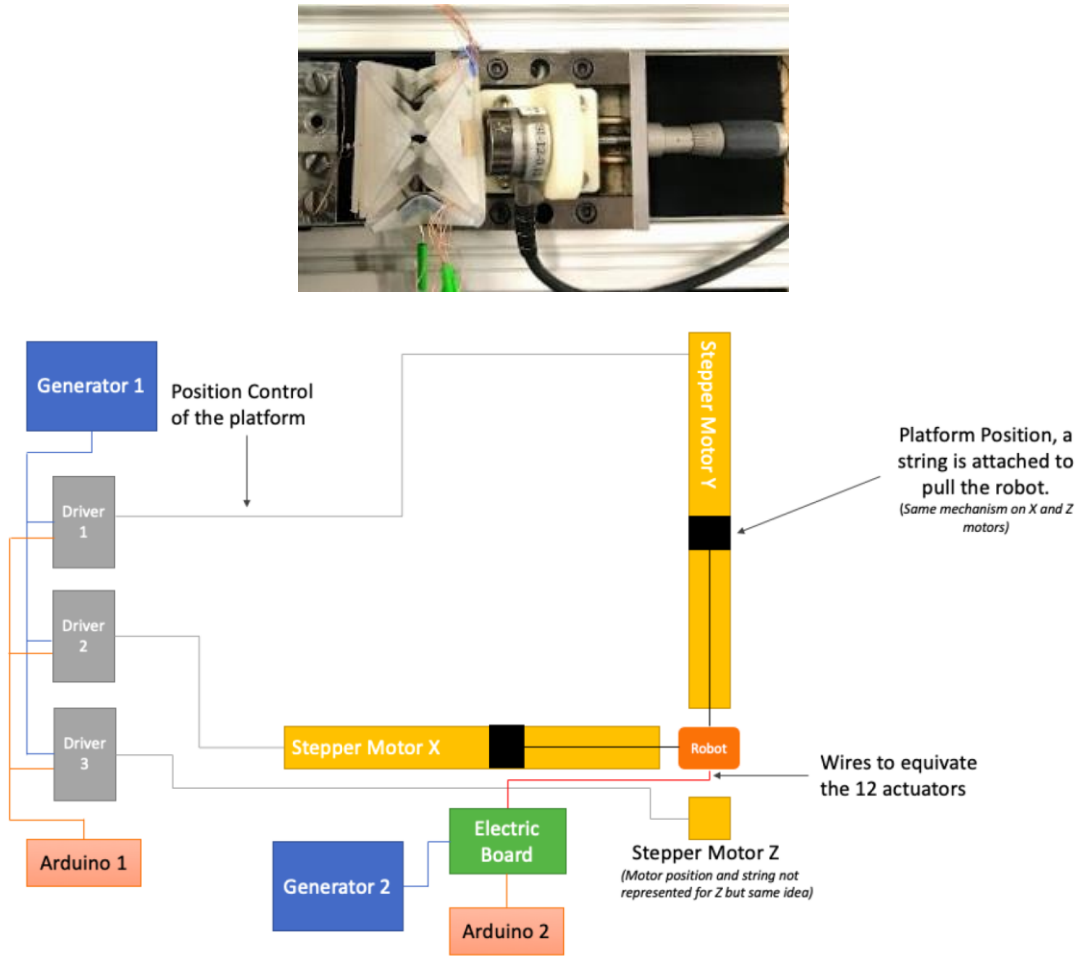


Figure 3.5 3-DoF force-displacement characterization setup

### Experimental results

Firstly, a single-axis force-displacement experiment was carried out for characterizing the axial stiffness of the structure.

#### Axial stiffness

In Figure 3.6, we can find that the overall axial stiffness of the origami module can be adjusted during turn on and off the heating for the SMPs. The axial Stiffness can vary from 250% to 300% both for tension and compression direction. We found that the modeling results have a lower stiffness comparing with experimental results while SMP is at a glass state, as shown in Figure 3.7. The misalignment of the hinges could be the reason for the higher stiffness obtained in the experimental results.

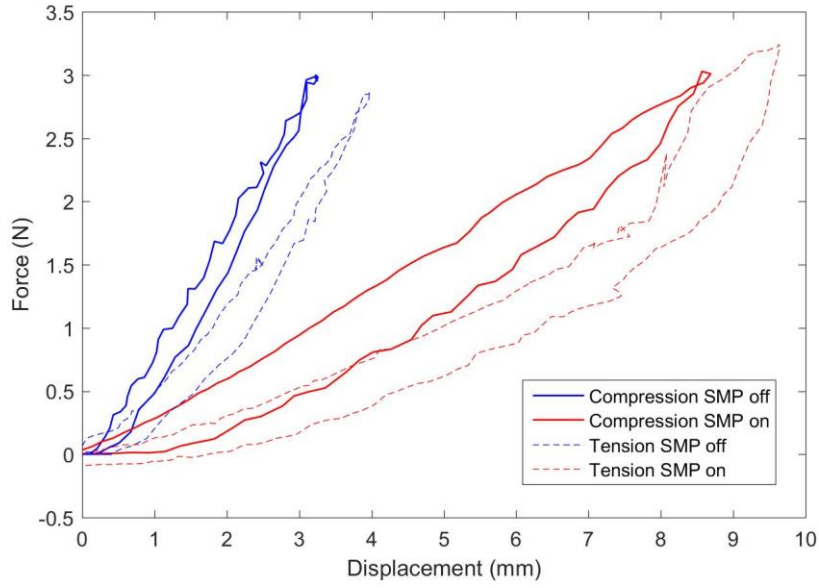


Figure 3.6 Axial stiffness measurements

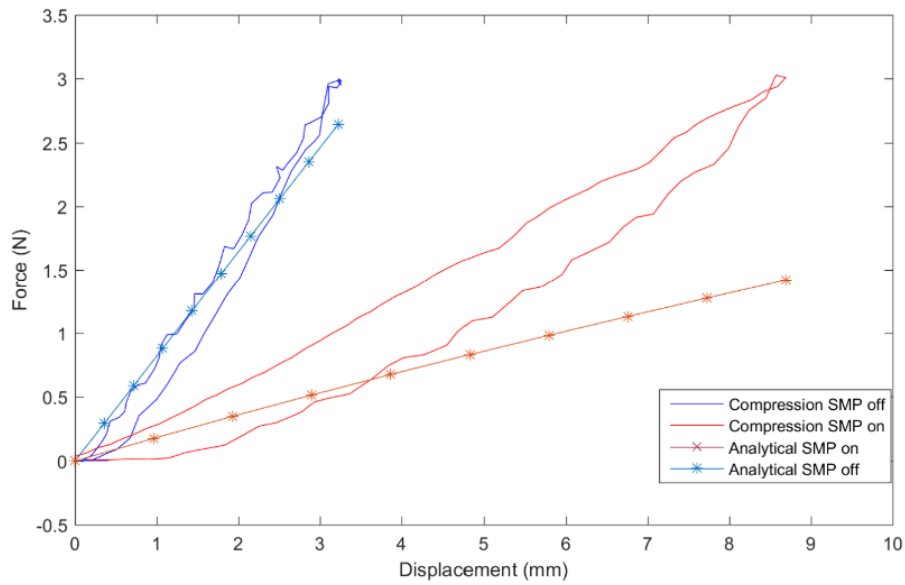
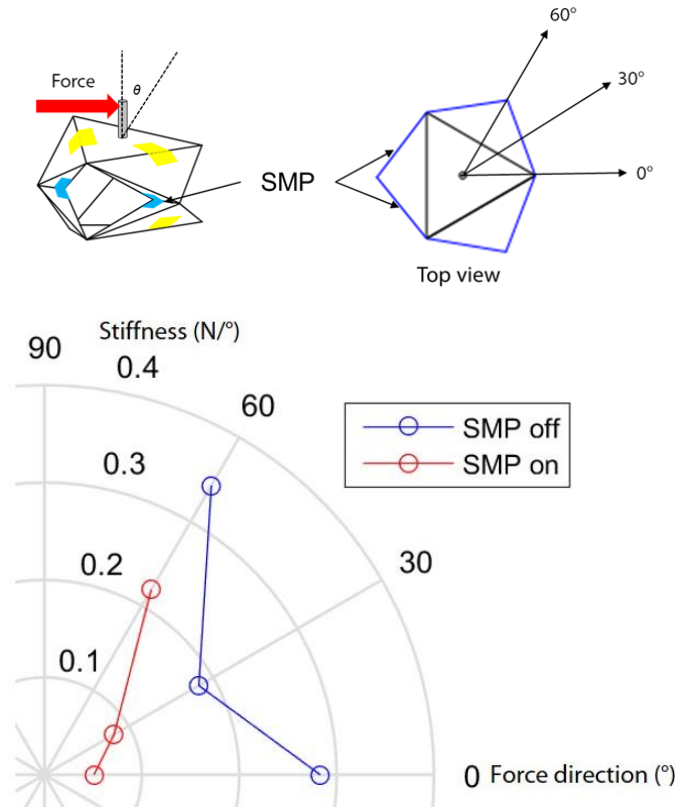


Figure 3.7 Modeling results of linear axial stiffness

#### Lateral stiffness measurements

The lateral stiffness could be varied in different directions due to the kinematics constraints of the origami structure itself. However, not only the kinematic constraints dominate the stiffness behavior in our prototype but also the activation of SMPs. Here, we want to evaluate the impact of SMP on lateral stiffness within different activation strategies. The lateral stiffness measurements were carried out for examining the lateral stiffness change while SMPs were heated and not at heated states. We applied the force on a metal pin which is installed on the top plate of the origami module, as shown in Figure 3.8. Then, we measured the lateral stiffness from different directions while all SMPs were turned on or off. The results are shown in Figure 3.8. The stiffness changes not only due to kinematics configuration but also the stiffness of the joints.



**Figure 3.8 Lateral stiffness measurement with all SMP turned on/off**

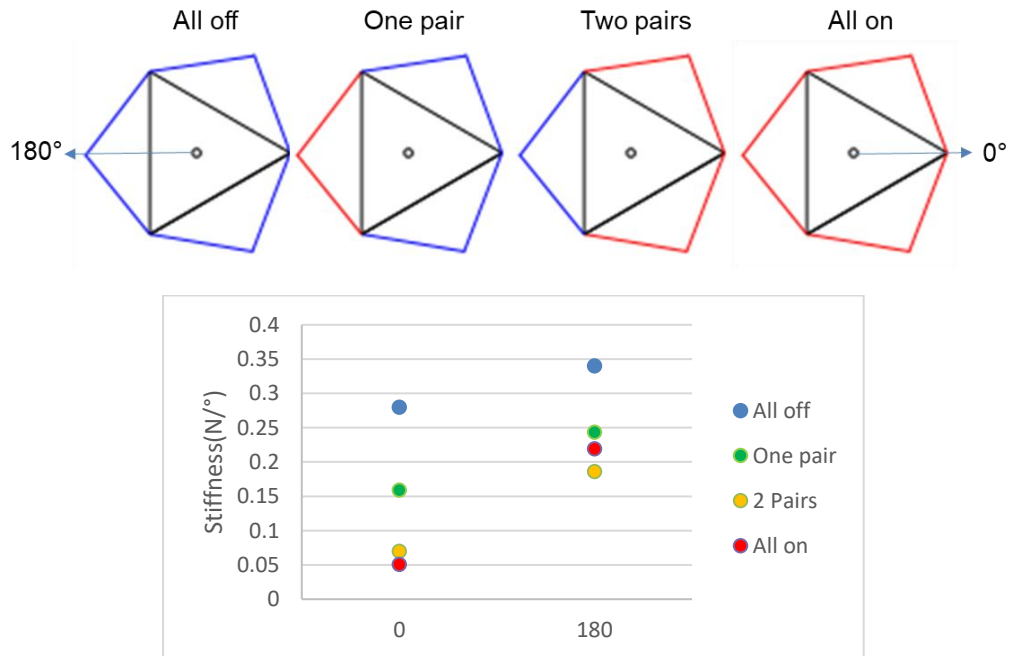


**Figure 3.9 Lateral stiffness measurement with selectively activated SMPs**

Then, we selectively activated one pair, two pairs, and all SMPs to evaluate the effect of partial stiffening of the origami module, as shown in Figure 3.9. From the experimental results shown in Figure 3.9. Selectively activated SMPs could have potentially larger load-carrying capacity and range of motion with additional lateral loading, as shown in Figure 3.9 and 3.10.

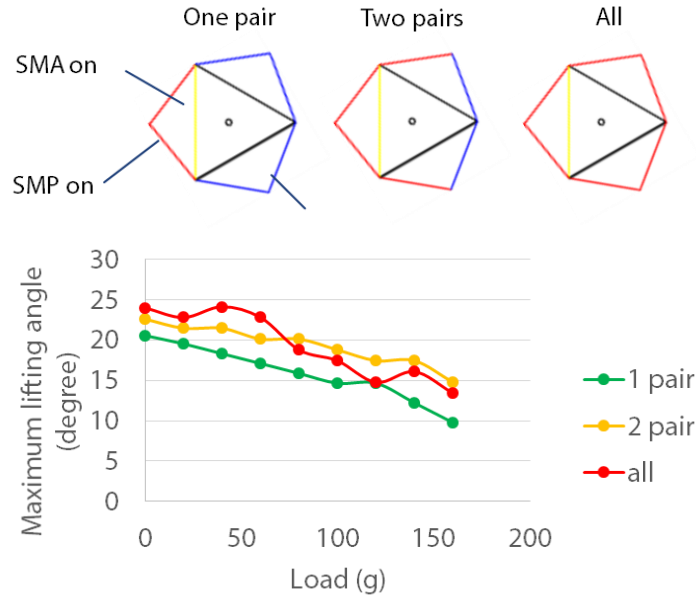


Figure 3.10 External load effect on the range of motion while selectively activating SMPs.

### Reversibility of variable stiffness origami wrist

The reversibility of 4D printed structures was rarely being addressed. However, it is important for many engineering applications since the active structure may not only be one-time deployment but also repeated actuations. We characterize the reversibility of variable stiffness origami wrist both by natural recovery which the reversible motion is achieved by the structural stiffness and by antagonistic actuation. Natural recovery can only recover to 30% of total displacement, as shown in Figure 3.11. However, the antagonistic actuation can provide enough recovery force for back to the central position in 2D, as shown in Figure 3.12. 3D position needs to be further investigated since the actuation always compresses the entire device.

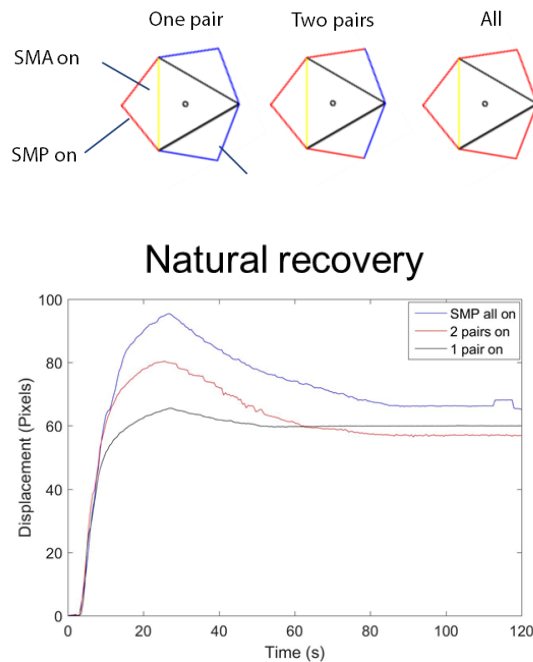


Figure 3.11 Reversibility of origami module by natural recovery

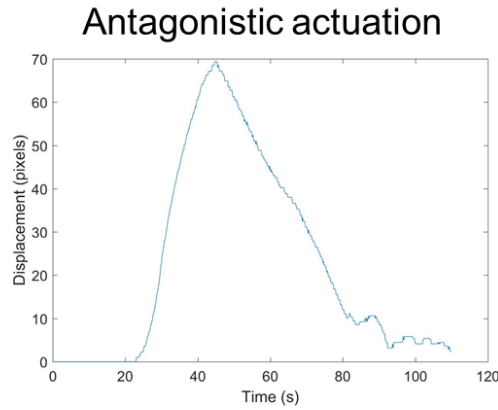


Figure 3.12 Reversibility of origami module by antagonistic actuation

### Control experiments

In this section, we would like to examine the controllability of distributed actuation for the 4D printed structures. We build a setup for closed-loop control by computer vision feedback, as shown in Figure 3.13. The control system can track the central position on top of the origami module precisely to a 0.1 mm scale. We gave step input to see if a single actuation direction (2 SMAs) can be controlled precisely by our control system. The results show that single-direction displacement can be controlled, as shown in Figure 3.14.

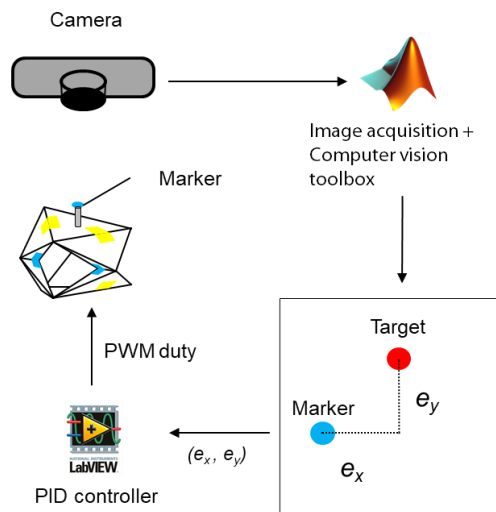
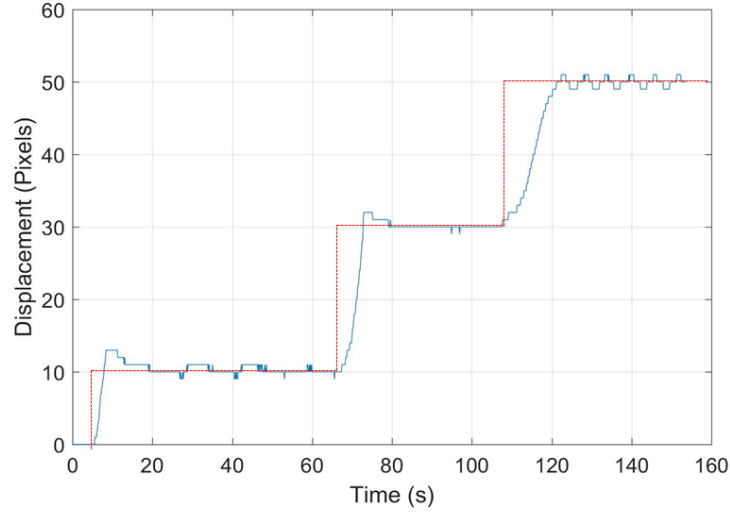
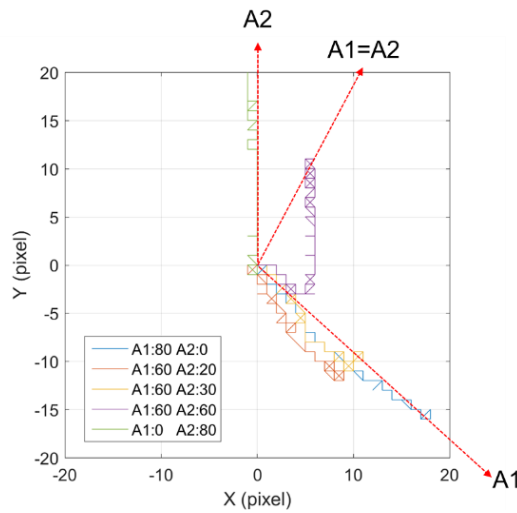


Figure 3.13 Schematic of setup for closed-loop control experiments



**Figure 3.14 Control results for closed loop with step input**

However, a high degree of coupling between the states makes it challenging to model and control in 3D space as well as with loading conditions. There is no model and control algorithm for distributed activated origami parallel mechanisms as well as considering the variable stiffness of hinge. We've conducted dual actuation experiments where activate actuators for two directions with different power inputs, as shown in Figure 3.15. The 2D bending direction between directions A1 and A2 is not proportional to the power input. This is due to the non-linearity between bending angle vs. power input over time, as shown in Figure 3.16.



**Figure 3.15 Dual actuation experiments**

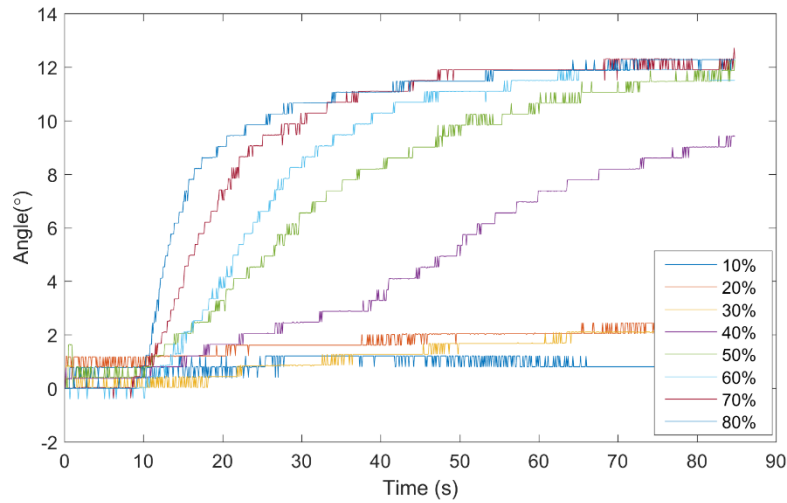


**Figure 3.16 The bending angle of origami module with different power input**

The control and behavior of 4D printed active structures in 3D space are not easy to be realized due to the nonlinearity of thermal-mechanical properties of smart materials and coupled kinematics. Predicting precisely the behavior when activating several actuators in a multi-DoF system is a critical challenge.

#### 3.1.4 Conclusion

In this section, we developed The lightweight 4D printed reconfigurable robotic origami module with three degrees of freedom which can be applied for changing the orientation of the end-effector, as shown in Figure 3.17. The origami module can be fully printed in 2D with the SMA actuators and SMP components “drop-in” during the 3D printing process. And it could later fold up to a 3D structure with 3-DoF mobility. The enhanced functionality like adjustable stiffness and range of motion, extra loading capability without additional energy consumption, and self-assembly can be achieved first-ever on a single origami module by the configuration and control design of functional components. Current evaluations are majorly limited to 2D directions. Further characterization and control experiments can be done with 3D motion tracking system. The demonstration of the use scenarios could be implemented with an end-effector.



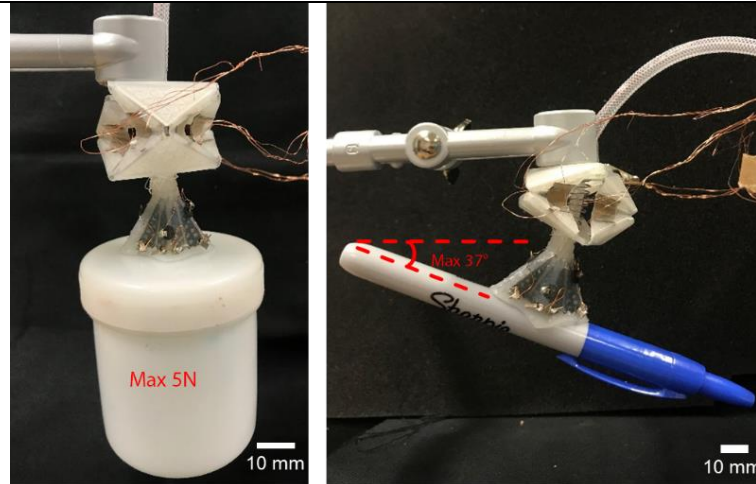


Figure 3.17 Integration with a suction cup gripper

### 3.2 A 4D printed active compliant hinge for space applications

In the second part, we present the concept of a 3D printed, active compliant hinge with variable stiffness suitable for deployment as well as the reorientation of satellite appendices. The concept has no moving parts, hence requires no lubrication and prevents shocks allowing for smooth and controlled movements. The deployment and the reorientation of the hinge are achieved by exploiting the thermally induced variation in stiffness of one of the constituting materials and using two antagonists shape memory alloy springs as actuators.

#### 3.2.1 An overview of 4D printed active hinge for space applications

In recent years, the reduction of mission costs resulting from the development of CubeSats [195] and new business opportunities related to Earth observation and satellite communication systems has raised the interest of a broad number of private companies in the space economy [196]–[198]. As a result, the number of nanosatellites launched has boomed since 2013, and the forecasts seem to confirm an increasing trend also for the next years [199].

CubeSats are mostly made of commercial off-the-shelf components [200] and usually avoid complex and expensive tailored-made solutions [201]. As a result, a trade-off between cost and performance has to be achieved. Power management is a crucial aspect of satellite design [202]. On CubeSats, solar panels are typically the only source of energy on board and limit the power to the payload [203]. A commonly used solution to increase power collection is deployable solar panels. The deployment mechanisms generally rely on revolute joints with pre-compressed torsional springs [204]–[206]. Nevertheless, compliant solutions based on tape springs [207]–[210] or on SMA [211], [212], and SMP [213] have also been proposed. However, all these designs are suitable only for one-time deployment and cannot be used to vary the orientation of the panels. This possibility to tailor the orientation of the panels would further increase the amount of energy collected and allow for the installation of more powerful payloads or for the reduction in the size of the solar panels saving weight and costs. Nevertheless, current solutions rely on complex mechanisms, which require lubrication and are affected by thermal expansion, galling and cold welding [214], [215] [21-25].

4D printing, namely the 3D printing of components able to change their properties when subjected to an external stimulus, might be a possible solution to circumvent this problem [216]. In the literature, there are various examples of how different types of stimuli, such as heat, UV light or humidity, can be used to induce a change in shape in 3D printed objects. Even though 4D printing is still at a proof of concept stage, it has the potential to revolutionize the aerospace sector adding new functionalities and improving the performance of current systems thanks to pre-programmed components able to achieve the desired response in a challenging environment such as in space. The concept proposed in this work takes advantage of this novel technology and combines 3D printed SMP with “drop-in” SMAs, added in a second manufacturing step, to realize an active compliant hinge with variable stiffness. Being capable of bending multiple times in a slow and controlled manner and retaining the deformed shape, the proposed concept prevents the destabilization of the satellite through snap movements and is suitable for both deployment and reorientation of satellite appendices.

In this work, we present and discuss the design of a new active compliant hinge applied to a 6U CubeSat with orientable solar panels. However, the same hinge concept could be applied to other satellite appendices such as antennas, booms or even thrusters. In the following sections, we first introduce the hinge concept, explain its working principle and describe the treated case study, also assessing the possible increase in energy introduced by the hinge. Secondly, we evaluate the feasibility of the concept both experimentally by fabricating and testing a prototype and numerically by calculating the influence of the hinge on the Eigenmodes of a panel of the considered CubeSat. Finally, we discuss the applicability of the hinge concept considering the achievable range of motion, power consumption, and stiffness.

#### 3.2.2 Case study and function evaluation

We evaluate the feasibility of the proposed hinge concept considering the case of a 6U CubeSat with two orientable solar panels. The architecture of the considered CubeSat is depicted in Figure 3.18. The orientable panels are connected to the satellite on the longest edges with two active hinges each. For the sake of simplicity, we assume that all solar cells mounted on the satellite are placed on the upper side of the orientable panels; no solar cell is installed on the main structure of the satellite. The hinges must be bendable at  $90^\circ$  to allow for the folding of the panels and stowing the satellite in the dispenser (Figure 3.18-a). After the satellite ejection, the hinges can be activated to deploy the panels and point them in the desired direction (Figure 3.18-b, 3.18-c, and 3.18-d).

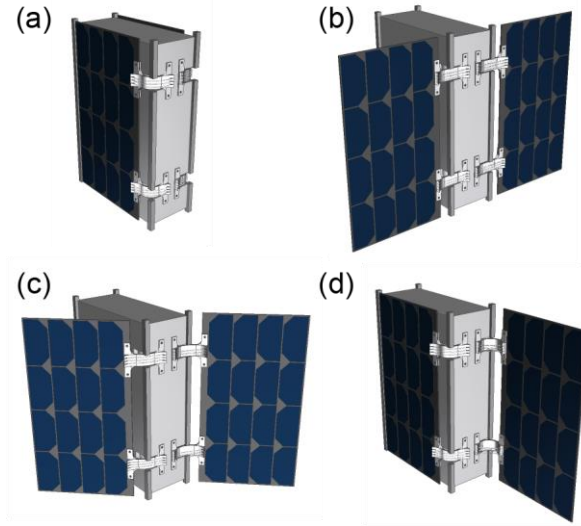


**Figure 3.18 CubeSat hinge case study**, (a) stowed satellite, (b) fully deployed panels (reference position), (c) panels oriented at 45°, and (d) panels oriented at 90°.

### Energy collection estimation

The theoretical increase in energy collected per orbit achievable using the active compliant hinge is calculated and compared to a satellite with fixed panels. As a reference, we assume a sun-synchronous Low Earth Orbit (LEO) with 40% of the orbital period in eclipse and neglect the effect of penumbra and albedo. Moreover, we assume that both panels are oriented with the same angle concerning the sun. In the fixed configuration, the panels are perpendicular to the local vertical of the satellite.

Referring to Figure 3.19, we define  $\vartheta$  as the angle between the solar flux  $\Phi$  and the local vertical axis of the satellite,  $\beta$  is the angle between the normal to the panels and the vertical axis of the satellite, and  $\alpha$  the angle of incidence of the solar flux on the panels.  $\alpha$  depends on the position of the satellite along the orbit and on the orientation of the panels and can be expressed as:

$$\alpha = \vartheta - \beta \quad (3.4)$$

Assuming that the solar cells installed on the panels have an area  $A$  and an efficiency  $\varepsilon$ , independent of the inclination angle  $\alpha$ , the power collected by the satellite  $W$  can be expressed as:

$$W_{(\vartheta, \beta)} = \Phi \cdot \varepsilon \cdot A \cdot \cos \alpha_{(\vartheta, \beta)} \quad (3.5)$$

The energy collected per orbit is the integral of the power absorbed over the orbital period. Considering a circular orbit, the angular speed is constant and equivalent to:

$$\dot{\vartheta} = \frac{d\vartheta}{dt} = \frac{2\pi}{T} \quad (3.6)$$

where  $T$  is the orbital period, the collected energy  $E$  can then be expressed as:

$$E = \int_T W_{(\vartheta, \beta)} dt = \int_0^{2\pi} W_{(\vartheta, \beta)} \frac{T}{2\pi} d\vartheta \quad (3.7)$$

The energy collected is a function of the inclination of the panels  $\beta$  and can be maximized using the active hinges to adjust the value of  $\beta$  along the satellite's orbit (see Figure 3.19). The maximum amount of energy is collected when the panels are always perpendicular to the solar flux: this corresponds to the condition  $\beta = \vartheta$ . Nevertheless, this situation implies that the hinges have to be constantly supplied with energy to track the Sun. For this reason, we consider repositioning the hinges in multiple discrete steps, activating them only for few seconds to rotate the panels of a given angle at each step. We use equation (3.7) to calculate the energy collected with three and with five actuation steps per orbit (Figure 3.20-c and 3.20-d, respectively), and we compared the energy collected to that obtained in the case of fixed (Figure 3.20-a) and of sun-tracking panels (Figure 3.20-b).

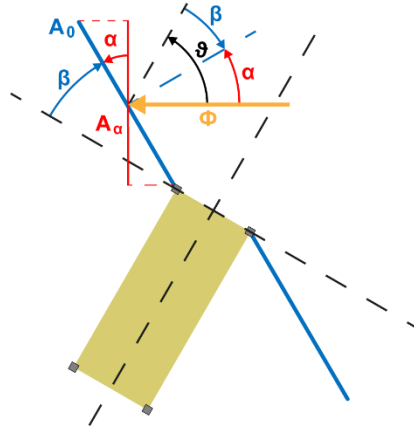


**Figure 3.19** Orientation of the satellite  $\vartheta$  and of its panels  $\alpha$  with respect to the incoming solar flux  $\Phi$ .  $\beta$  angular position of the solar panels with respect to the reference position.

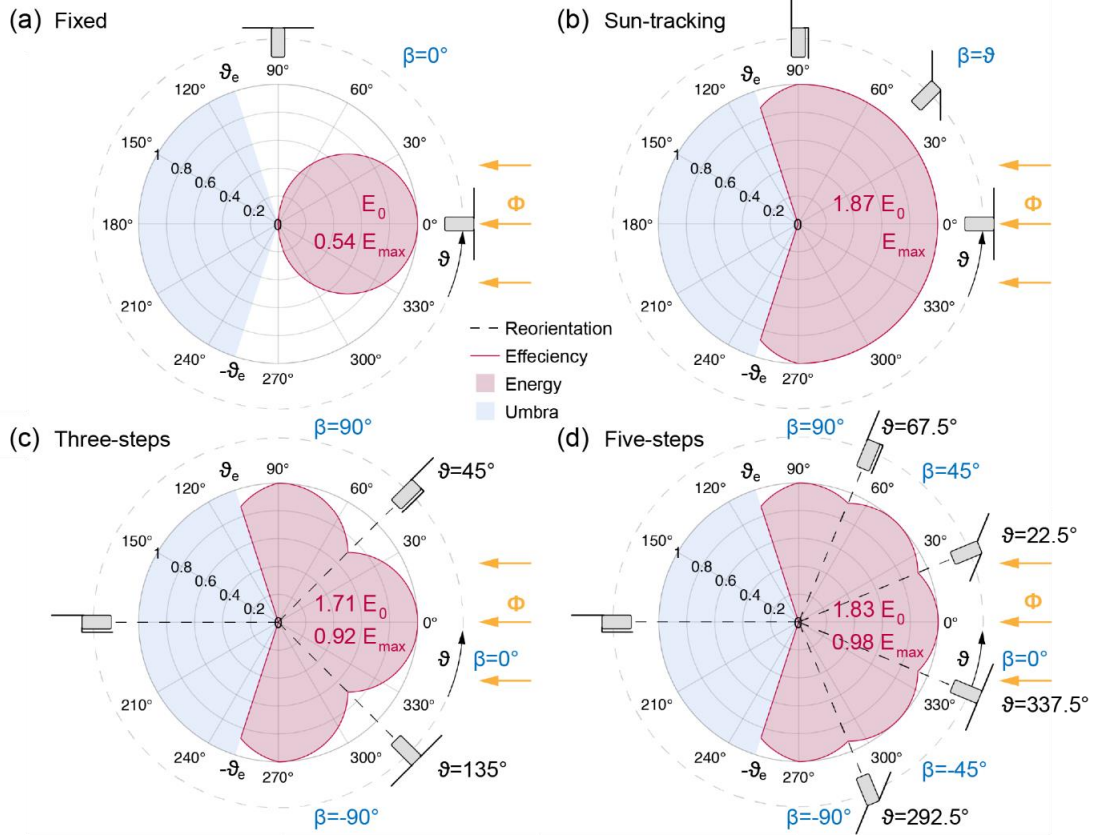


**Figure 3.20 Schematic representation of the actuation strategies** of the active hinges and of the corresponding orientation of the solar panels along the orbit of the satellite: (a) fixed panels, (b) sun-tracking panels, (c) three-step actuation, and (d) five-step actuation.

The estimation of the energy collection is carried out assuming asymmetric orientation of the satellite in the first and in the second half of the orbit with respect to the solar flux. Therefore, the energy collection is calculated between  $0^\circ \leq \theta \leq 180^\circ$  and multiplied by a factor two to account for the other half of the orbit.

### Energy collection estimation

#### Fixed panels

In the case of fixed panels,  $\beta = 0^\circ$  throughout the entire orbit of the satellite. Since the panels rotate with the satellite, the solar flux has an angle of incidence  $\alpha = \theta$  only for half of the orbital period (see Figure 3.20-a). Therefore, the energy collected by the satellite can be calculated as:

$$E_0 = \int_{-\frac{\pi}{2}}^{\frac{\pi}{2}} W_{(\vartheta)} \frac{T}{2\pi} d\vartheta = 2 \int_0^{\frac{\pi}{2}} \Phi \cdot A_0 \cdot \cos \vartheta \cdot \varepsilon \cdot \frac{T}{2\pi} d\vartheta = \frac{1}{\pi} \cdot \Phi \cdot A_0 \cdot \varepsilon \cdot T \quad (3.8)$$

#### Sun-tracking panels

If the panels of the satellite are continuously oriented perpendicularly to the solar flux,  $\beta = \theta$  and the energy collected is maximized. Nevertheless, this condition does not occur for the entire orbit since the active compliant hinges have a maximum angular position, which is assumed to be  $90^\circ$  in this calculation. Once the hinges have reached this limit position, they cannot bend further and the panels stay fixed in this position until the satellite enters in the umbra, condition that occurs in the first half orbit at  $\theta_e = 108^\circ$  in orbit with 40% of its period

in eclipse (see Figure 3.20-b). Moreover, at values of  $\theta$  larger than  $90^\circ$ , the satellite would project its shadow on one of the panels, reducing the panel area exposed to the solar flux with increasing  $\theta$  until a panel is completely darkened. We calculate the reduction in panel surface exposed to the solar flux and the angle  $\theta_s$  at which a panel is completely darkened by assuming a ratio between the length of the panel and that of the side of the satellite projecting its shadow of 2:1. The area exposed to the solar flux  $A_\theta$  is calculated as the difference between the total area of the two panels  $A_0$  and the panel area in the shadow  $A_s$ :

$$A_\theta = A_0 - A_s = 2 \cdot w \cdot l_0 - w \cdot \frac{l_0}{2} \tan\left(\vartheta - \frac{\pi}{2}\right) = A_0 \left(1 + \frac{1}{4} \frac{1}{\tan \vartheta}\right) \quad (3.9)$$

Where  $w$  is the width of the panels and  $l_0$  is the length of the side of the satellite, assumed equal to the length of the panel. The angle at which the shadow of the satellite darkens entirely a panel corresponds to the condition:

$$\frac{l_0}{2} \tan\left(\vartheta - \frac{\pi}{2}\right) = l_0 \quad (3.10)$$

which return an angle  $\theta_s = 153.43^\circ$ . Being  $\theta_s > \theta_e$ , the shadow of the satellite never darkens completely a panel in the considered orbit, since the eclipse of the satellite occurs before  $\theta_s$  is reached. Finally, the collected energy can be calculated as:

$$\begin{aligned} E_{max} &= 2 \int_0^{\frac{\pi}{2}} \Phi \cdot A_0 \cdot \varepsilon \cdot \frac{T}{2\pi} d\vartheta + 2 \int_{\frac{\pi}{2}}^{\frac{3\pi}{5}} \Phi A_\theta \cos\left(\vartheta - \frac{\pi}{2}\right) \varepsilon \frac{T}{2\pi} d\vartheta = \\ &= \frac{1}{2} \cdot \Phi \cdot A_0 \cdot \varepsilon \cdot T + \frac{\sqrt{\frac{5}{8} + \frac{\sqrt{5}}{8}} + \sqrt{5} - 2}{4\pi} \cdot \Phi \cdot A_0 \cdot \varepsilon \cdot T = \\ &= \frac{2\pi + \sqrt{\frac{5}{8} + \frac{\sqrt{5}}{8}} + \sqrt{5} - 2}{4\pi} \cdot \Phi \cdot A_0 \cdot \varepsilon \cdot T \end{aligned} \quad (3.11)$$

### Three-step actuation

In the three-step actuation, the following strategy is adopted:  $\beta = 0^\circ$  for  $0^\circ \leq \theta < 45^\circ$  and  $\beta = 90^\circ$  for  $45^\circ \leq \theta \leq 180^\circ$ . The collected energy results:

$$\begin{aligned}
 E_{3 \text{ steps}} &= 2 \int_0^{\frac{\pi}{4}} \Phi A_0 \cos \vartheta \varepsilon \frac{T}{2\pi} d\vartheta + 2 \int_{\frac{\pi}{4}}^{\frac{\pi}{2}} \Phi A_0 \cos \left( \vartheta - \frac{\pi}{2} \right) \varepsilon \frac{T}{2\pi} d\vartheta + \\
 &\quad + 2 \int_{\frac{\pi}{2}}^{\frac{3\pi}{5}} \Phi A_0 \cos \left( \vartheta - \frac{\pi}{2} \right) \varepsilon \frac{T}{2\pi} d\vartheta = \\
 &= \frac{\sqrt{2}}{2\pi} \cdot \Phi \cdot A_0 \cdot \varepsilon \cdot T + \frac{\sqrt{2}}{2\pi} \cdot \Phi \cdot A_0 \cdot \varepsilon \cdot T + \frac{\sqrt{\frac{5}{8} + \frac{\sqrt{5}}{8}} + \sqrt{5} - 2}{4\pi} \cdot \Phi \cdot A_0 \\
 &\quad \cdot \varepsilon \cdot T = \\
 &= \frac{4\sqrt{2} + \sqrt{\frac{5}{8} + \frac{\sqrt{5}}{8}} + \sqrt{5} - 2}{4\pi} \cdot \Phi \cdot A_0 \cdot \varepsilon \cdot T
 \end{aligned} \tag{3.12}$$

### Five-step actuation

In the five-step actuation, the following strategy is adopted:  $\theta = 0^\circ$  for  $0^\circ \leq \theta < 22.5^\circ$ ,  $\theta = 45^\circ$  for  $22.5^\circ \leq \theta < 67.5^\circ$  and  $\theta = 90^\circ$  for  $67.5^\circ \leq \theta \leq 180^\circ$ . The collected energy results:

$$\begin{aligned}
 E_{5 \text{ steps}} &= 2 \int_0^{\frac{\pi}{8}} \Phi A_0 \cos \vartheta \varepsilon \frac{T}{2\pi} d\vartheta + 2 \int_{\frac{\pi}{8}}^{\frac{3\pi}{8}} \Phi A_0 \cos \left( \vartheta - \frac{\pi}{4} \right) \varepsilon \frac{T}{2\pi} d\vartheta + \\
 &\quad + 2 \int_{\frac{3\pi}{8}}^{\frac{\pi}{2}} \Phi A_0 \cos \left( \vartheta - \frac{\pi}{2} \right) \varepsilon \frac{T}{2\pi} d\vartheta + 2 \int_{\frac{\pi}{2}}^{\frac{3\pi}{5}} \Phi A_0 \left( 1 + \frac{1}{4} \frac{1}{\tan \vartheta} \right) \sin \vartheta \varepsilon \frac{T}{2\pi} d\vartheta = \\
 &= \frac{\sqrt{2 - \sqrt{2}}}{2\pi} \cdot \Phi \cdot A_0 \cdot \varepsilon \cdot T + \frac{\sqrt{(2 - \sqrt{2})}}{\pi} \cdot \Phi \cdot A_0 \cdot \varepsilon \cdot T + \\
 &\quad + \frac{\sqrt{2 - \sqrt{2}}}{2\pi} \cdot \Phi \cdot A_0 \cdot \varepsilon \cdot T + \frac{\sqrt{\frac{5}{8} + \frac{\sqrt{5}}{8}} + \sqrt{5} - 2}{4\pi} \cdot \Phi \cdot A_0 \cdot \varepsilon \cdot T \\
 &= \\
 &= \frac{8\sqrt{2 - \sqrt{2}} + \sqrt{\frac{5}{8} + \frac{\sqrt{5}}{8}} + \sqrt{5} - 2}{4\pi} \cdot \Phi \cdot A_0 \cdot \varepsilon \cdot T
 \end{aligned} \tag{3.13}$$

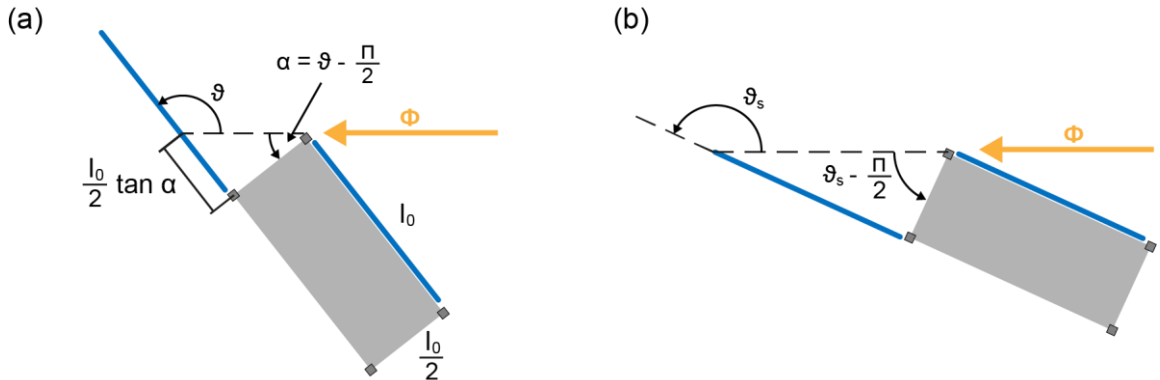


**Figure 3.21 Orientation of the satellite** (a) at  $\vartheta > 90^\circ$  and (b) at the critical angle  $\vartheta = \vartheta_s$ , at which one solar panel is completely darkened by the shadow of the satellite.

### Materials and manufacturing



### 3 Design and demonstration of multi-DoF reconfigurable systems for customizable functionalities

The stiffness of the joints is majorly dominated by the stiffness of Verowhite. The stiffness of Verowhite could be changed repeatedly and reversibly by thermal activation. It transfers from the rigid glassy state to a rubbery deformable state once its temperature is above the glass transition temperature ( $T_g$ ). In order to control the stiffness of the joint, we customized, designed, and manufactured heater layers and embedding the heater layers inside the 3D printed multi-material hinge. The heater layers should be able to heat up the hinges uniformly and also flexible and stretchable that allows the hinge to bend. Thus, the customized heaters are composed of a Copper-polyimide thin-film layer with a zigzag path that increases the resistance by making a longer path for better heating efficiency and provides additional flexibility while the heater is being bent and stretched. The zigzag paths were created by a laser micromachining station (LAB 3550, Inno6 Inc.). Here we use laser micromachining the thin film material for rapid prototyping and better robustness. The material heater could be changed to 3D printable for easier and faster integration.

For space applications, smart material such as shape memory alloy (SMA) is a promising option thanks to its high power-to-weight ratio and power-to-volume ratio. Furthermore, SMA actuators could provide smooth and shockless actuation that is essential for keeping satellites stable while deploying and orientating the solar panels. Thus, we selected SMA spring actuators for achieving the bending motion of the hinge. The design principle and fabrication process are described in the previous chapter. We customized the design of SMA spring actuator according to the desired stroke, force output as well as power efficiency. We used the commercial NiTi wires with 380  $\mu\text{m}$  diameter (Dynalloy Inc.) for fabricating the SMA spring actuators. The SMA wires were wound around a rod with a 1.6 mm diameter and annealed at 405  $^{\circ}\text{C}$  for 30 mins. Then, the SMA spring actuators are programmed and ready for integrating with the hinge.

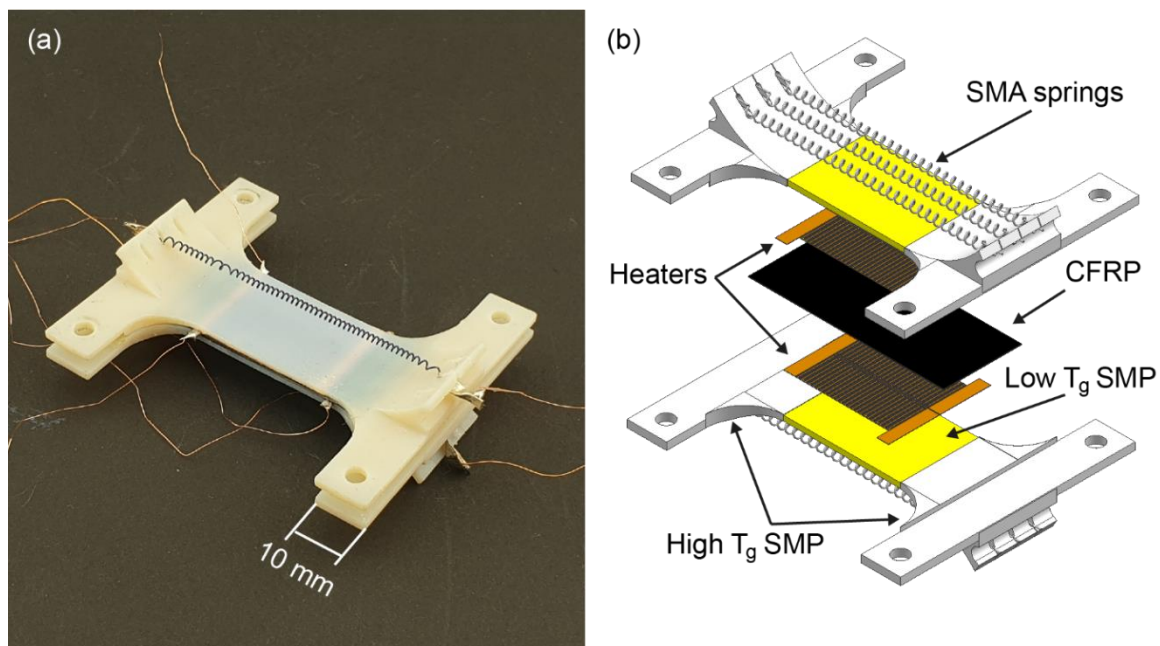
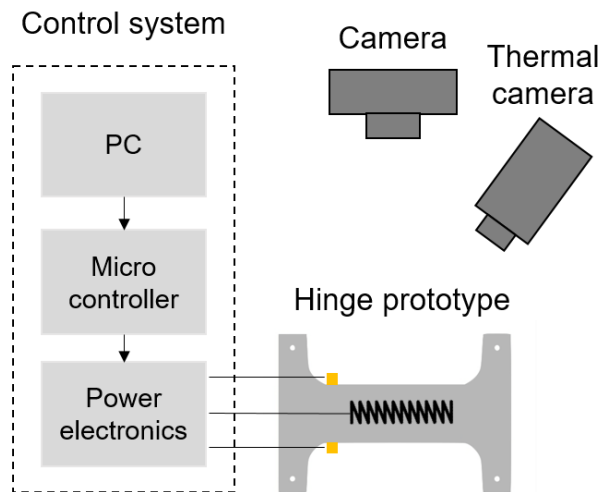


Figure 3.22 (a) Demonstrator of the active compliant hinge, (b) exploded view of the active compliant hinge.



### 3.2.3 Experimental validation

A prototype of the hinge is built and tested to simulate three actuation scenarios: the deployment of the solar panel from the stowed configuration, the bending at the maximum angular position, and the locking at a target angular position. The three tests are performed by fixing one end of the hinge prototype to vertical support and measuring the angular position of the other end by tracking its displacement on camera, as shown in Figure 3.23. The heaters and the SMAs are actuated via a microcontroller (Arduino Mega) and power electronics using a LabView interface. The microcontroller receives the command and generates the pulse-width modulation (PWM) with adjusted duty cycles for regulating the input power of SMA actuators and heaters. The power electronics consist of a DC power supply (RND 320-KD3005P, RDN LAB) and transistor switches. The PWM signal is sent to the transistors so that the power level can be regulated proportionally to the duty value. Therefore, the power consumption can be easily controlled. The detailed electronics setup is described in the [78]. Additionally, a thermal imaging camera (FLIR A35, FLIR Systems Inc.) is used for monitoring the temperature of the different components. All tests are performed at ambient temperature and pressure.



**Figure 3.23 The schematics of the experimental setup.** A control system for powering the heaters and the SMA spring actuators of the hinge. The camera and thermal camera are employed for motion and temperature monitoring.

First, we start with the characterization of SMA energy consumption and the heating/cooling cycle of SMP.

#### SMA spring energy consumption

We measure the force output of SMA with different power inputs and record the force over time. With the maximum force, the designed SMA spring should be strong enough according to the model described in Chapter 2. The measurement results are shown in Figure 3.25. Although given power above 1.44 W can achieve higher force output, 1.44 W is sufficient enough to achieve maximum bending angle without extra energy cost, which will be discussed in the following experiments.

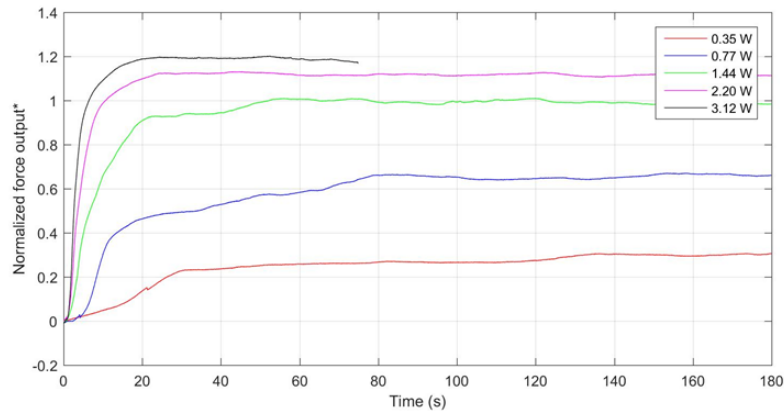


**Figure 3.24** SMA spring force output with different power input and maximum force of 1.44 W for normalization

#### SMP heating cycle

Then we evaluate the heating/cooling efficiency of the embedded heaters for SMP. We attached a thermal couple for comparing with the measurement results from the thermal camera. We also compare the experimental results with numerical simulation results executed by COMSOL, as shown in Figure 3.25. The simulation heating rate is lower than the experimental results, while the results of cooling rate quite match with experimental results. This is might due to the inhomogenous of the printed SMP results in a lower density of SMP structure. And higher heater efficiency due to the higher resistance of the heaters, which may be caused by the over engraving induced narrower electrical path.

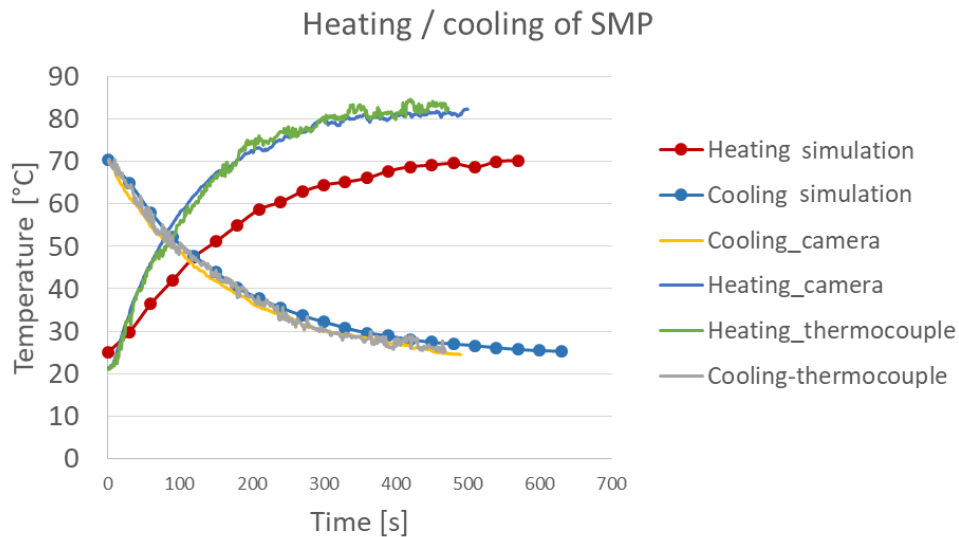




Figure 3.25 Heating/cooling cycle test of SMP

Then, five testing scenarios considered are described as follows:

### Deployment

This scenario represents the ejection of the satellite from its dispenser and the deployment of the solar panels, as illustrated in Figure 3.18-b. In order to reproduce the stowed configuration, the hinge is heated up, folded manually at an angular position of 90°, and allowed to cool down while constraining it in the deformed shape. The constraint is then removed, and the hinge is deployed only by powering the heaters with a total power of 1.5 W. In this test, no SMA is actuated in order to measure the natural recovery of the hinge.

### Bending at the maximum angular position

This test aims to measure the maximum angular position achievable by the hinge and that at which the hinge can be locked. Starting from a flat configuration and at room temperature, the hinge is first heated above the  $T_g$  of VeroWhite by switching on both heaters and by powering them with 0.75 W each for 180 s. Then, the heaters are switched off, and a single SMA spring is actuated with 1.45 W. Once the SMA bent the hinge to the maximum angular position, the heaters are turned off while keeping the SMA spring contracted until the SMP cooled down. Finally, the power to the SMA actuator is turned off, and the maximal locking angular position is measured.

### Bending and locking at a target angular position

The test reproduces the pointing and the locking of the hinge at a target angular position of 50° and assesses the precision of the hinge when used for pointing. Similar to the previous scenario, the hinge is first heated above the  $T_g$  of VeroWhite by powering both heaters with 0.75 W each for 180 s. Then, the heaters are switched off, and the power provided to the SMA actuator is carefully tuned to lock the hinge at the target angular position. It has to be pointed out that no closed-loop control system is implemented and that the power provided to the SMA is tuned manually.

### **Gradual increase in angular position**

The possibility to precisely control the hinge by actuating a single SMA spring is investigated. The controller tunes the value of  $i_{SMA}$  to vary the angular position  $\theta$  of the prototype from  $0^\circ$  to  $90^\circ$  in steps of  $10^\circ$ .

### **Multi-step actuation**

The possibility to actuate the hinge in multiple steps coordinating both SMA springs to implement the suggested actuation strategies is investigated. The control algorithm adjusts the input power for activating SMA to bend the hinge at the following angular positions:  $45^\circ$ ,  $90^\circ$ ,  $-90^\circ$ , and  $45^\circ$ . Moreover, at each angular position, the power consumed by the prototype to hold its position is measured and used in the estimation of the energy consumption.

## **3.2.4 Results and discussion**

### **Deployment**

The angular position of the hinge measured from the actuation of the heaters is plotted in Figure 3.26a. Starting from a stowing angle close to  $90^\circ$ , the hinge gradually unfolds until it reaches an angle of natural recovery of about  $15^\circ$  after 400 seconds. Considered that the heaters are powered at 0.75 W each, the full deployment of the hinge requires 600 J.

### **Bending at the maximum angular position**

Figures 3.26b and 3.27a report the angular position of the hinge starting from the actuation of the SMA spring. The activation of the latter leads to a smooth bending of the hinge, which reaches a maximum bending angle of approximately  $100^\circ$ . After being locked, the hinge recovers part of its deformation and stabilizes at an angular position of  $71^\circ$ . In this scenario, the SMA spring is activated at the maximum power of 1.44 W (0.9 A at 1.6 V) for 240 s, returning an energy consumption of 348 J. Considering that the heaters require 270 J, the total energy consumption of this scenario is 618 J, while the actuation time amounts to 420 s.

### **Gradual increase in angular position**

Figure 3.27-c shows the gradual increase in angular position of the prototype from  $0^\circ$  to  $90^\circ$ . The results show that the prototype can achieve the target angular positions with an accuracy of  $\pm 3^\circ$  over the entire range of angular positions considered.

### **Multi-step actuation**

Figure 3.27d shows the angular position of the prototype in the multi-step actuation test. The results show that the prototype can achieve the target angular positions of  $\pm 45^\circ$  within an actuation time of 30 s when starting from an angular position of  $0^\circ$  and  $-90^\circ$ , respectively. On the other hand, the plot shows that the control algorithm takes about 120 s to bend to the prototype at the maximum angular positions of  $\pm 90^\circ$  and to move from  $-45^\circ$  to  $+45^\circ$  (Figure 7-c). The power required by the SMA springs to hold the prototype at an angular position of  $\pm 45^\circ$  and  $\pm 90^\circ$  amounts to 0.25 W and 1 W, respectively.

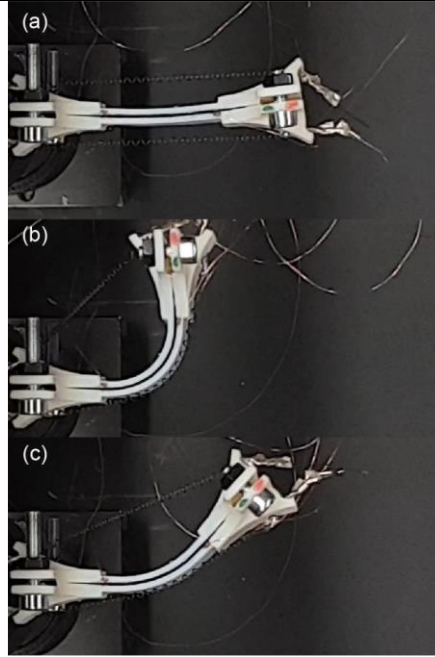


**Figure 3.26** Deployment from the stowed configuration, (a) zero position (b) bending at the maximum angular position and (c) locking at a target angular position of 45°.

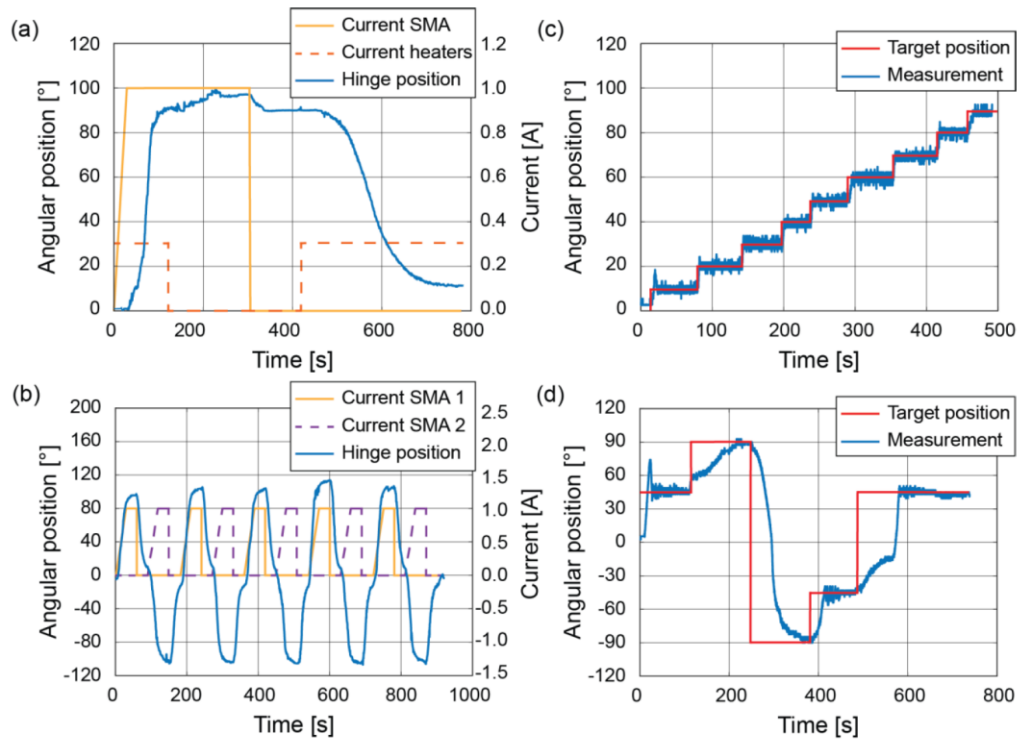


**Figure 3.27** Bending and locking test of the active hinge (a) at maximum angular position (b) multiple actuation, (c) gradual increase in angular position, and (d) multi-step actuation.

### Estimation of energy performance and actuation time

The orbital period calculated with Eq. 5 amounts to  $T = 5801$  s, with a corresponding full-light exposure time  $T_S = 3481$  s, and energy collected per orbit  $E_0 = 116$  kJ. The energy collected by the proposed actuation strategies is reported in Table 3.1.

**Table 3.1 Energy gained by proposed actuation strategies**

Fixed panels	$\beta = 0$	$0 \leq \vartheta \leq 2\pi$	$E_0$	$0.54 E_{max}$
Two steps	$\beta = 0$ $\beta = \frac{\pi}{2}$	$0 \leq \vartheta \leq \frac{\pi}{4} \wedge \frac{7}{4}\pi \leq \vartheta \leq 2\pi$ $\frac{\pi}{4} < \vartheta < \frac{7}{4}\pi$	$1.70 E_0$	$0.92 E_{max}$
Three steps	$\beta = 0$ $\beta = \frac{\pi}{4}$ $\beta = \frac{\pi}{2}$	$0 \leq \vartheta \leq \frac{\pi}{6} \wedge \frac{11}{6}\pi \leq \vartheta \leq 2\pi$ $\frac{\pi}{6} < \vartheta \leq \frac{\pi}{3} \wedge \frac{5}{3}\pi \leq \vartheta < \frac{11}{6}\pi$ $\frac{\pi}{3} < \vartheta < \frac{5}{3}\pi$	$1.84 E_0$	$0.98 E_{max}$
Sun tracking panels	$\beta = \vartheta$	$0 \leq \vartheta \leq 2\pi$	$1.85 E_0$	$E_{max}$

In a single actuation step, the heaters consume 450 J ( $2 \cdot 0.75 \text{ W} \cdot 300 \text{ s}$ ), while the SMA springs 75 J ( $0.25 \text{ W} \cdot 300 \text{ s}$ ) or 300 J ( $1 \text{ W} \cdot 300 \text{ s}$ ) according to the target angular position of  $\pm 45^\circ$  and  $\pm 90^\circ$ , respectively. Considering all four hinges, the satellite requires 2.1 kJ and 3.0 kJ to reorient the panels at  $\pm 45^\circ$  and  $\pm 90^\circ$ , respectively. Therefore, the total energy consumption of the three- and of the five-step actuation strategy amounts to 9.0 kJ and 13.2 kJ, respectively. In the case of sun-tracking actuation, the heaters and the SMA springs require respectively 5.22 kJ ( $2 \cdot 0.75 \text{ W} \cdot 3481 \text{ s}$ ) and 3.48 kJ ( $1 \text{ W} \cdot 3481 \text{ s}$ ) in full-light. Considering four hinges, the energy required in full-light amounts to 34.8 kJ. By adding the 3.0 kJ required in eclipse to reorient the panels, the total energy consumption of the sun-tracking actuation strategy amounts to 37.8 kJ.

The maximum allowable actuation time to implement the three- and the five-step actuation strategy amounts to 1'740 s and 870 s, respectively, while the time required by a single step is 500 s: 180 s to heat up the hinge and 320 s to bend and lock the hinge.

**Table 3.2** Energy collected, energy consumed, net energy gain and allowable actuation time for the considered actuation strategies. The net energy gain is calculated with respect to a satellite configuration with fixed panels

	Energy collected	Energy consumed	Net energy gain	Actuation time
Fixed panel	116 kJ	0 kJ	0 kJ (+ 0%)	-
Sun-tracking	217 kJ	37.8 kJ	63.2 kJ (+ 52%)	-
Three steps	198.5 kJ	9.0 kJ	73.5 kJ (+65 %)	1740s
Five steps	212.5 kJ	13.2 kJ	83.3 kJ (+72%)	870s

## Discussion

The results obtained demonstrate that 4D printing is a suitable method for the realization of an active compliant hinge that, combining active materials and 3D printing, shows a unique palette of properties, such as compliance, variable stiffness and multiple actuation, not achievable by any other type of hinge. Our approach based on the combination of SMPs and SMAs allows for the realization of an active compliant hinge capable of varying its bending stiffness to achieve angular positions larger than  $90^\circ$  in both directions and to hold any target position in its range of motion without consuming energy. Moreover, 3D printing of multi-material components and the use of embedded heaters enable the implementation of

thermally induced stiffness modulation without compromising the mechanical properties of the components of the hinge and of the adhesive used to join them.

The tests performed also demonstrate the feasibility of our hinge concept to be deployed and reoriented multiple times. On the one hand, the functional prototype is capable of holding an angular position of  $90^\circ$  for stowing without consuming energy and of deploying to a neutral position of  $0^\circ$  if the SMA spring under tension is actuated. In addition, even if only the heaters are powered, the prototype is still capable of deploying and recovering almost  $80^\circ$ , returning a feature that might be useful to reorient the hinge towards the neutral position in case of failure of the actuation system. On the other hand, the prototype shows a predictable and repeatable behavior, and it is capable of reorienting itself in different angular positions multiple times in a controlled manner and with a precision of  $3^\circ$ .

The tests carried out on the prototype show that, under standard temperature and pressure conditions, the actuation speed and the energy consumption of the hinge are compatible with all proposed actuation strategies. The time necessary to reorient and lock the hinge in a new angular position is 500 s. This value is lower than the 870 s required by the five-step actuation strategy, which is the most demanding among the strategies proposed. In addition, the actuation time might be further reduced by monitoring the temperature of the hinge and optimizing the actuation accordingly.

The energy requirements of the three- and of the five-step actuation strategy are about eight and six times lower than the corresponding gain in energy collection theoretically achievable. If compared with the reference satellite configuration with the fixed panel, these two actuation strategies lead to a net increase in energy collected of about 63% and 72%, respectively. On the other hand, the sun-tracking actuation strategy has a power consumption of only 1.7 times lower than the increase in energy collection and a gain with respect to the reference configuration of 54%. However, the power consumption of this actuation strategy might be overestimated since it is assumed that heaters and SMA springs are always activated at constant power when the satellite is in full light. In reality, this condition might not be necessary, and the power consumption of heaters and SMA springs might be reduced. Therefore, the increase in energy collection calculated represents the minimum value achievable under standard temperature and pressure conditions.

### **3.3 Multi-agent control for reconfigurable power harvesting modules**

We investigate multi-DoF reconfigurable systems' scalability on a larger scale and bring the system to real-world applications. We are especially interested in the systems' self-assembly function. Self-assembly is the autonomous organization of components into patterns without human intervention. This idea has been proposed for years and is widely applied, especially to micro and nanometer scales, since the force needed for self-assembly is small and achievable by van der Waals's forces, magnetic force, electrical charge, et cetera. However, applying self-assembly to a mesoscale or even a meter-scale is difficult since the components may be too heavy to move[59], [217]. Reconfigurable modular robotics has indicated a promising solution

to achieve self-assembly at a larger scale. We want to examine the possibility of solving real-world problems at a larger scale with a reconfigurable robotic system.

#### 3.3.1 An overview of power harvest modules and water management

Since water resource management has become a serious issue due to climate change, overdevelopment, and the destruction of the natural environment, reservoirs' storage efficiency has garnered great importance in recent years. One crucial approach to saving water is reducing evaporation loss in reservoirs, especially in high-radiation and dry regions. Several approaches to evaporation reduction have been developed, such as suspended shade cloth covers and float covers that serve as impermeable barriers and even long-chain alcohols in thin-layer chemical covers [218], [219]. More recently, well-known "shade balls [220]" were distributed to a reservoir in California, not only to reduce evaporation but also to improve water quality by preventing algae growth and reducing bromates.

These concepts could be extended by integrating additional functionalities to shielding structures to better use space. The concept of floating photovoltaic power plants has introduced several advantages, such as higher efficiency due to the lower operating temperatures through water cooling[221], [222]. Furthermore, floating photovoltaic power plants could even produce more energy than other renewable energy sources, such as hydropower and evaporation engines installed at reservoirs [223]. However, most current floating photovoltaic power plants are time-consuming to install and uninstall, leading to a lack of mobility for their transportation and inflexibility in changing their deployment locations.

Many recent research projects and patents have focused more on floating photovoltaic power plants' overall design [7-8] and sun-tracking techniques to improve efficiency [9]. Several patents have proposed deployment methods for these plants [10-11] and a modular design to adapt to different geometries [12-13]. Furthermore, two patents have proposed motorized modules [13] and magnet-mounted modules [14], which provide possibilities for these plants' self-assembly. However, these solutions also entail some drawbacks, such as high costs, high energy consumption, and highly complex control systems for motorized modules. For magnetic self-assembly, external disturbances may be required due to the short effective distance of magnetic attraction. Although magnetic self-assembly could offer lower energy consumption, the assembly process could be time-consuming [15]. Self-assembly has already been widely applied to the fabrication process of nano- and micro-engineering. However, self-assembly mechanisms' scalability in larger-scale applications (e.g., cm to m ranges) remains problematic [16-17]. Therefore, we combine the two main mechanisms—pneumatic actuation and magnetic attractions—to propose a scalable, customizable, lower-energy-consumption, and rapid-self-assembly modular floating photovoltaic power system.

#### 3.3.2 Reconfigurable power module (RoPoM) design

We developed a modular floating photovoltaic power system, which is able to self-reconfigure, forming a 2D surface in order to adapt to water storage with different sizes and shapes. This surface can float on a farming reservoir and acts as a protective layer between the water and



### 3 Design and demonstration of multi-DoF reconfigurable systems for customizable functionalities

the sun's radiation. By reducing the sun exposition, the evaporation process is lessened, allowing better conservation of the water resources.

This chain is composed of modules, each one carrying a solar cell mounted on a deployable origami floating structure, as shown in Figure 3.28. Once assembled and the reservoir covered, the surface created can be considered as a solar panel composed of the solar element of all the modules. The electricity generated by the modules can be gathered at one end of this chain and use to power supply dams' pumps or charge batteries. The power generated by the modules is directly proportional to the surface of the reservoir that sets the number of modules to use.

This robotic chain is composed of modules linked together by flexible joints or torsional actuators. This ensures the overall structure cover any kind of reservoir form, even complex. All the links between modules and actuators can be disconnected, allowing an easy intervention in case of dysfunction and an efficient chain assembly.

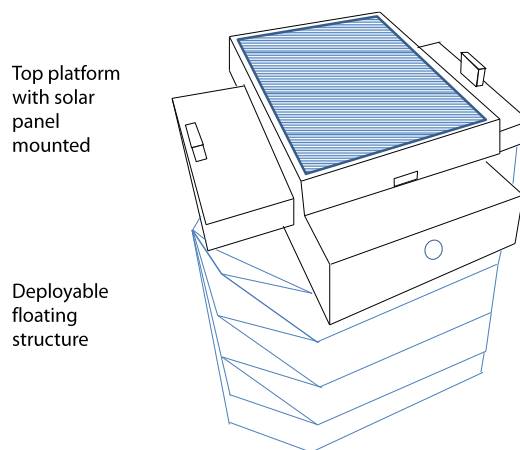


**Figure 3.28** The schematics of the reconfigurable power module, which consists of two main components, top platform and deployable floating structure.

#### Design and fabrication of RoPoM

Every module contains an inflatable structure for storage and transport convenience made from an accordion fold origami pattern, as shown in Figures 3.30. Indeed, origami allows the creation of light and low-cost structures with a fast and straightforward fabrication process. Its design is flexible was chosen depending on the desired module's overall shape and size. It is conceived in order to ensure an easy and waterproof assembly. This structure must be sealed to guarantee the floatability once deployed onto the water, but also the compression and expansion if pneumatically power supplied. The parameters of the inflatable origami have a direct impact on its deployability. Depending on the weight every module has to carry, the volume and, therefore, the deployability of the origami has to be adjusted to ensure the best buoyancy possible. The final design allows the module with optimal floatability when deployed while ensuring a compact design when compressed, as shown in Figure 3.29. Every module contains a platform plugged on top of the deployable origami structure. It is used to carry the solar panel, the associated electronics, the electric and pneumatic cables, and the magnets, as shown in Figures 3.31. A solar cell is equipped on every platform and used to collect energy,

**3 Design and demonstration of multi-DoF reconfigurable systems  
for customizable functionalities**

---

as shown in Figure 3.29. Ensuring an easy way to plug and unplug the solar system on the platform allows an easy replacement of the broken part in case of dysfunction. In this sense, it must also be easy to disconnect the electronics, the electric cables, and the solar cells.

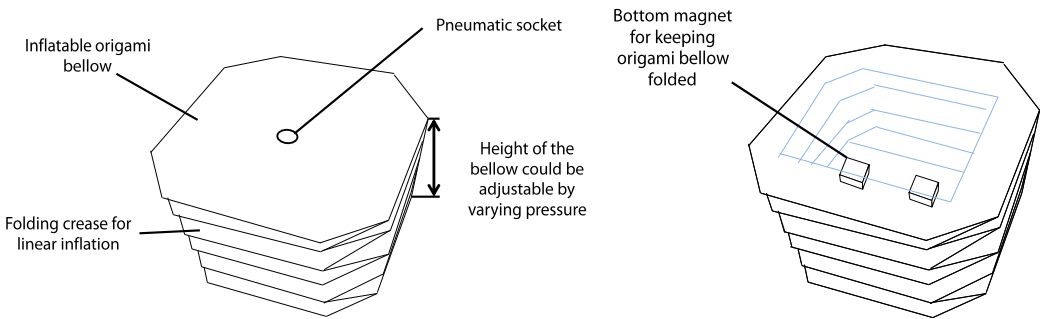


**Figure 3.29 The schematics of deployable origami floating structure**

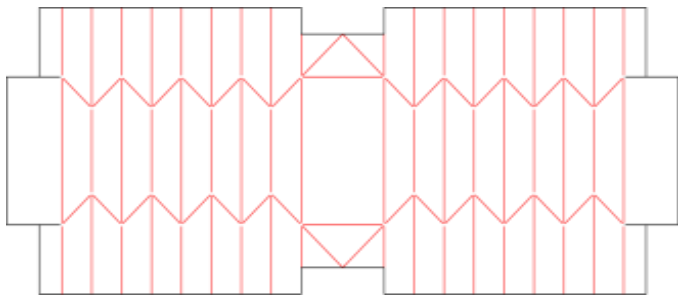


**Figure 3.30 Folding pattern for origami module**

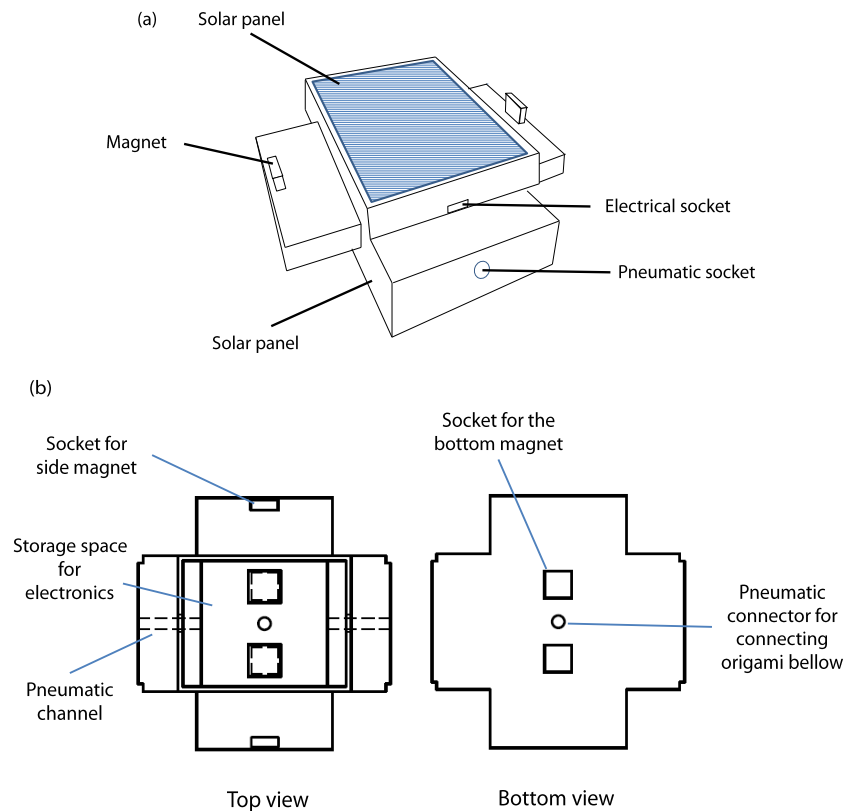


**Figure 3.31** The schematic of the top platform (a), and (b) the drawing of the platform.

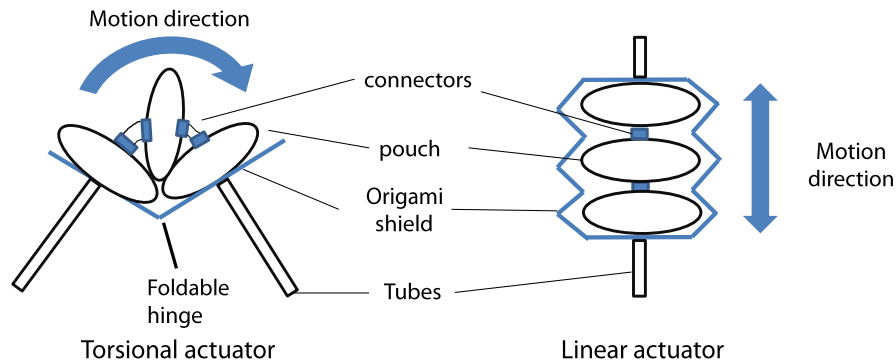


**Figure 3.32** The schematics of modular pneumatic actuators. The desired motion could be programmed by varying the number of modules and the design of the origami shield

Pneumatic actuators installed between modules enable the reconfiguration of the connected chain modules. The geometries of the chain structure can be reconfigured for adapting to different shapes of reservoirs by changing the positions installed in the chain and the types of pneumatic actuators. While the pneumatic actuator can actively change the entire configuration of the chain, magnets equipped on edge could assist the assembly precisely and engagement of the modules, as shown in Figure 3.33. Furthermore, the optimization of energy and time consumption of self-assembly can be achieved by combining the magnetic

attractions and pneumatic actuators, as shown in Figure 3.34. There is also an alternative approach for covering reservoirs by employing the reconfigurable power modules connected with permeable sheets. The modules serve as a moveable buoy to deploy the permeable sheets. The modularity of the system brings the flexibility to deploy different sizes and multiple sheets.

This pneumatic actuator design contains replaceable and customizable pouch modules. An origami shield is implemented for constraining and defining the motion of actuation, which could be linear motion or bending motion etc., as shown in Figure 3.32. The replaceable pouch modules allow adjustable bending angle or linear displacement by altering the number of pouches and regulating the corresponding origami shield design.

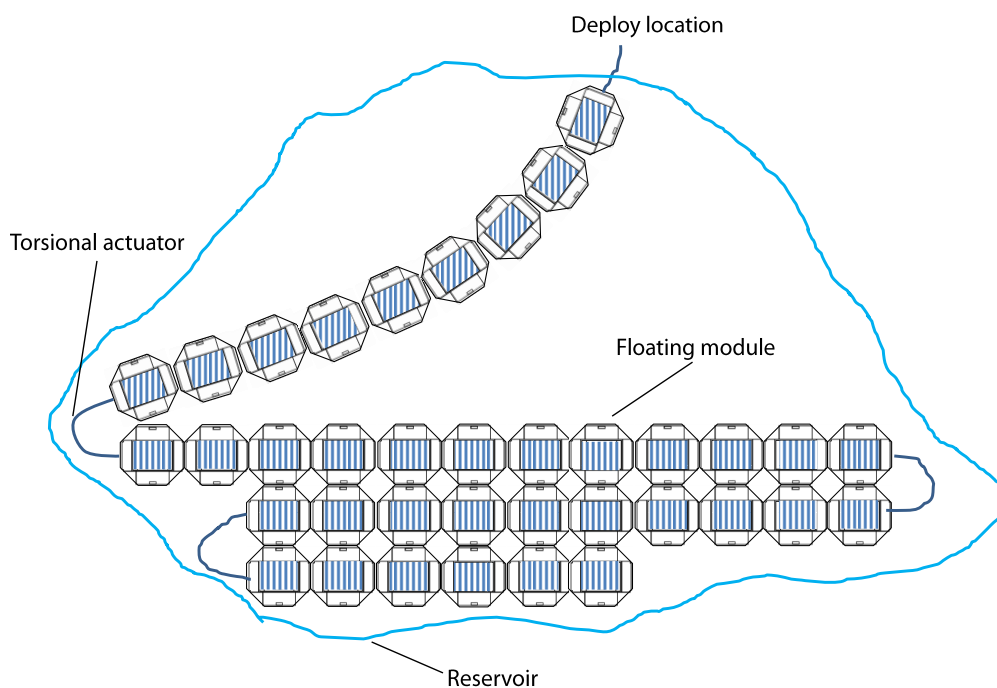


**Figure 3.33** The first self-assembly scenario of the floating modules on a reservoir with arbitrary geometry. The self-assembly one deployment location.

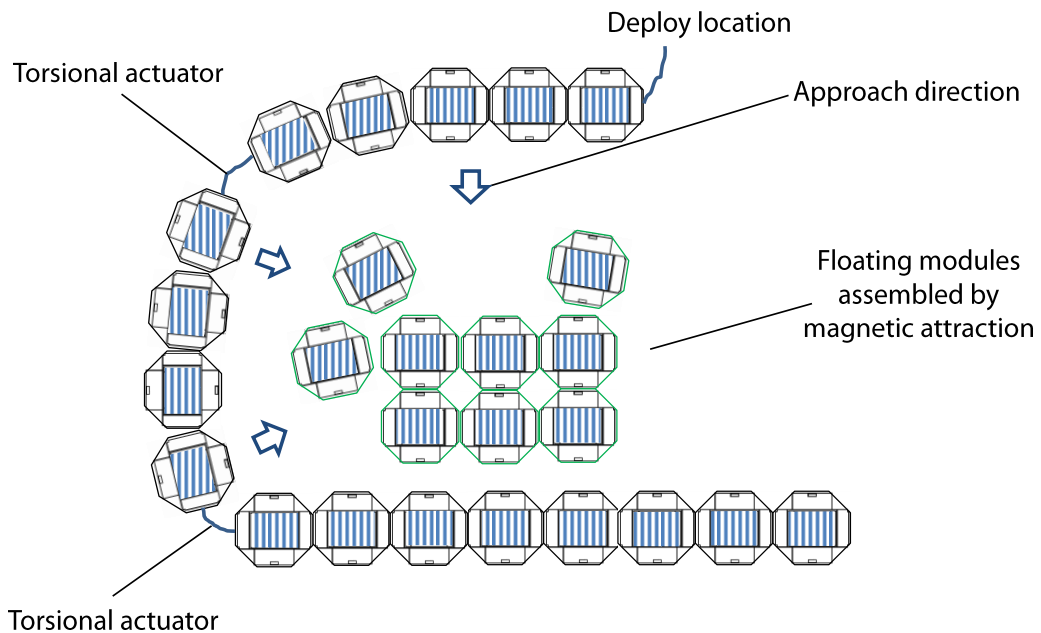


**Figure 3.34 The second self-assembly scenario of the floating modules.** Pneumatic actuations give the constraints of the boundary for magnetic self-assembly that accelerates the assembly process without giving external disturbance.

### 3.3.3 Results and discussion

#### Scalability of self-assembly technology

Self-assembly is the autonomous organization of components into patterns or geometries without human intervention. Most of the current self-assembly technology focuses on micro or nanometer scales, but the needs, technologies, and applications for self-assembly should be further investigated. We reviewed several self-assembly technologies such as magnetics attractions and self-reconfigurable robotics systems. However, these solutions also have some drawbacks such as high cost, high energy consumption, and high complexities of the control system for and self-reconfigurable robotics systems. For magnetic self-assembly, external disturbances may be required due to the short effective distance of magnetic attraction. Although magnetic self-assembly could have potentially lower energy consumption, the assembly process could be very time-consuming. So, we proposed a soft-pneumatics actuation combines with magnetic attractions to have a scalable, efficient, and controllable self-assembly.

#### Fabrication difficulties

The main problems we encountered in this project arise from manufacturing. There are different steps that require manual assembly and where time-consuming during design iterations. For example, the sealing steps are also particularly crucial and might lead to the failure of the whole structure if not done correctly. Therefore, a lot of time has been spent on improving the fabrication method and making it more efficient and reliable. The fact that water resistance of 2D manufacturing structures is challenging due assembly and attachment of multiple layers of material in 3D space. First, the waterproof of the inflatable bellow is essential

and should resist a long water exposition. In this regard, suitable material choices and correspond assembly methods have been developed. Secondly, the electronic system and power supply need to be water-resistant and involved the use of special kinds of connectors and a way to keep the PCB dry by encapsulating it. Finally, the system needs to be stable on the water and not disturbed by potential small waves. This is still a problem for individual modules, but it is working as expected when modules are grouped together.

#### **Practical applications for the target country and local context**

We choose Chile as the target country for studying our design. There are three distinct hydrological regions: (1) The dry northern regions, (2) The temperate central regions (3) the humid southern regions in Chile. In the northern part, the limited water resources sustain a few coastal cities, some specialized agriculture, and large mining operations such as the main copper mining, which is a high energy consumption industry, and the need for affordable clean energy are rising. Since northern Chile is one of the very few regions in the world with annual global irradiance values exceeding 2500 kWh/m<sup>2</sup>, solar energy has become a promising solution in recent years. In the central part, the rainfall is concentrated in winter, so water storage reservoirs have been constructed to support these irrigation systems. However, there have been significant decreases in rainfall in central Chile over the last 40 years. Water management became a serious issue, especially for these high-radiation and dry areas. Furthermore, the local small farms typically have to use fossil fuels to make water pumps work or have to afford the high cost of electricity during dry seasons. This situation not only increases the cost, but also hinders the chances to develop sustainable agriculture. The development of sustainable agriculture and the access to electricity is the issues we tackled with this project by developing a single device that provided a simple solution to both problems.

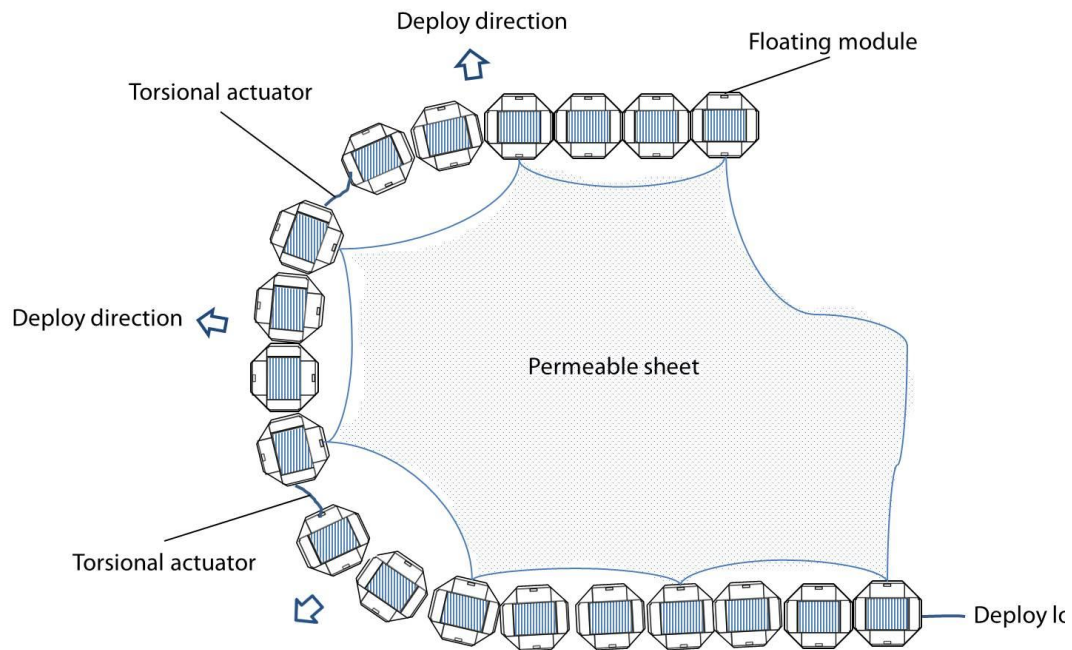


**Figure 3.35 The third self-assembly scenario of the floating modules.** The floating modules serve as buoy for deploying the covering sheet to shade the reservoir.

### 3.3.4 Conclusion

We developed a modular floating photovoltaic power system, which is able to self-reconfigure its overall geometry forming a 2D surface in order to adapt to the reservoirs with different shapes and sizes. This system is made with inflatable origami-inspired modules linked together by cables or torsional pneumatic actuators. The configuration of modules is chosen by adjusting the position and the number of actuators in the chain. An inflatable origami bellow, part of every module, is used to ensure the overall stability and buoyancy of the system. Pneumatically powering the modules with a positive pressure both deploy the modules and actuate the joint, transforming this chain in a 2D surface configuration. Once assembled, magnets equipped onto the modules allow them and their neighbors to be mechanically connected. Solar cells are placed on the top of every module. Electric cables are part of the liaisons between modules and connect all the solar cells of the robotic chain in a parallel configuration. Storage or electric device can be connected at one of the ends of the chain to use the power generated. By pneumatically powering the modules by negative pressure, the structure adopts its initial chain configuration breaking the magnetic interactions. This vacuum allows every module to deflate in compact dimensions to improve storage and transport. Once compressed, magnets placed inside modules make them keep their flattened configuration in a passive way. The capabilities and concepts of the prototype have been validated by both experiments in the lab and field tests. The results have been collected for patent application and further determination of possible commercialization of the system

# Conclusion and future directions

## 4.1 Conclusion

In this thesis, we have investigated, developed, and explored multi-DoF reconfigurable interactive robotic systems. We have aimed to overcome current limitations in terms of the control, design, and evaluation of interactive robotic systems, unleashing these systems' potential for real-world applications. Moreover, we have answered our three research questions described in the introduction of this thesis. Below, we summarize these answers to each research question.

- ***What design approaches enable direct human-robot interaction with the morphological transformations and constraints of multi-DoF distributed activated systems?***

In Chapter 1, we started by discussing the design of interactive interfaces to realize and control multi-DoF robotic systems' morphological deformation. This proposed interface comprises a graphical interface with a physical robot. The graphical interface displays a real-time simulation of physical robots, and the physical robot can serve as either an input or an output for the virtual simulation. We employed origami-inspired multi-DoF robots as a platform for this interface design. Morphological changes can be achieved by folding hinges. This simulation extracts physical parameters from the characteristics of core components, such as actuators, sensors, and hinge properties, which are seldom found in the literature on origami simulation. We built a kinematic model for origami robots, based on the distributed sensing system to realize real-time simulation. This simulation allows users to fold the physical robot, and a virtual simulation is simultaneously shown on the graphical interface. Additionally, we developed another interaction mode that enables users to use hand gestures to manipulate and fold the virtual origami model directly. This interactive interface allows for direct interaction and manipulation of multi-DoF robotic systems, both virtually and physically.

In the second part of Chapter 1, we explored the design space of the proposed interactive interface for reconfigurable modular robotic systems. Morphological transformations can be generated by distributed actuation, as well as the connection or disconnection of self-sustained modules. We designed gesture sets that allowed us to investigate modular robotic systems' unique characteristics and constraints—particularly their modularity, reconfigurability, and functional adaptability. This functionality can be achieved using the proposed interaction modes, including module reassembly, individual module control, and global geometry control.

Then, we designed and validated a haptic system in which the delivery of tactile feedback and spatial accuracy was quantitatively studied for a bi-directional human-in-the-loop system. With the designed soft haptic interface, we can reconstruct sensation of morphology defined in virtual environments. We designed an evaluation protocol and conducted an experimental evaluation. A 2D planar platform was used to physicalize a given virtual shape using a soft test



object, based on two-level tactile cues to guide human actions. The molding of the test object, Play-Doh, provided a sense of shape and size, whereas active tactile feedback from SPA-skin overlaid its texture cues. We employed two-stage actuation with low-frequency stimulation when approaching the contour shape, followed by high-frequency vibration when reaching the actual contour for ease of exploration. The proposed haptic interface and evaluation protocol could allow for a quantitative evaluation of the interactive user interface for multi-DoF robotic systems.

- ***How can the controllable actuation of complex ranges of motions and functionalities be implemented?***

Distributed, controllable actuation in robotic systems remains a challenge, especially in small scales, down to a mesoscale or even a microscale. Novel smart materials and advances in AM technology led us to build a compact distributed actuated system. We adapted the idea of 4D printing, integrating active and functional materials during the 3D printing process with our origami design. However, the materials' nonlinearity, coupled with kinematics, made the multi-DoF control difficult and unpredictable, especially with external loading. Thus, we started with designing, modeling, and characterizing the functional components. Low-profile functional components for origami folding, as well as adaptation to 3D printing processes, were developed. We also conducted parameterized studies on 3D printed flexure hinges. Moreover, we investigated the impact of the materials and geometric design parameters on the hinge's load-carrying capability and flexural properties. Furthermore, the hinge's fatigue behavior was characterized, identifying constitutive mechanisms. Since every manufacturing step could significantly influence the fabricated prototypes' overall performance, we created origami mechanisms both by AM and subtractive layer-by-layer manufacturing processes. Characterization for the hinge's output force, range of motion, and stiffness were conducted and compared with analytical models. We also explored bistability-induced motion range changes and adjustable stiffness to withstand external loading, enhanced load-carrying capability, and kinematics changes.

- ***How can the multi-DoF robotic systems needed to operate in distinct, real-world applications be designed?***

Multi-DoF brings adaptivity and versatility to morphological transformation and task requirements. However, how to generate a useful configuration and suitable design for desired tasks remains a great challenge. We conducted three case studies—a 3DoF origami module for orientating the robotic end-effector, an active compliant hinge for space applications, and modular origami floating robots for power harvesting. Starting with function definitions, we defined the requirements for scales of motion, structure, power, and force. Then, we designed suitable mechanisms, together with actuation solutions, to generate desired motion (translation, rotation, bending, etc.), based on our prior studies of origami mechanisms and actuator designs. We needed to investigate material properties with component fabrication and the integration of all mechanisms since every step was cross-linked and influenced each other step. We achieved self-assembly from mesoscale to meter-scale problems by delicately designing actuators' configurations. Variable stiffness components provided the flexibility needed to ad-

just structures' overall stiffness in order to prevent unwanted distortion due to external loading or locking morphological transformations to desired positions. Partial stiffening of the structure also can be conducted to change kinematics behaviors, which can enhance ranges of motion and load-carrying capabilities.

### 4.2 Future research directions

We have presented an interactive control interface for multi-DoF robotic systems and modular self-reconfigurable robotic systems. The current kinematics of interaction is managed by a physics engine built in the Unity system. However, numerous mechanical constraints increase the calculation load for real-time simulations. The interaction model's simplification may increase the tool's robustness and relieve computation loading to handle more complex structures. However, the current virtual environment still entails some restrictions, including soft material modeling, and a higher-DoF interaction is challenging or even impossible to simulate accurately. Algorithms, control methodologies, and the integration of a soft material simulation engine are needed for higher-DoF origami structures, as well as nonlinear actuators and components. For modular robot control, the module assembly function should be further validated using mobile prototypes with automated attachment mechanisms. Another goal is to amalgamate the gesture and autonomous control modes in order to achieve intuitive high-level task programming. Also, we intend to introduce a robot operating system (ROS) for better management and flexibility in the integration of both software and hardware.

This thesis presents significant scope for further studies on multimodal perception with wearable soft haptic devices due to the customizability of both material properties and control frequencies. For example, we only evaluated 2D geometry; the evaluation protocol's integration in a 3D VR environment could help us understand the tangible interaction's effectiveness. Furthermore, these preliminary studies open a discussion on the next generation of haptic feedback devices, which are not only mechanically transparent for human wearability but also provide ranges of tactile sensations inherent to objects and perceived by human touch.

For hardware design, we have proposed a low-profile actuation and function layer design to achieve a distributed, controllable multi-DoF active system at a mesoscale. However, despite studies on material properties, fabrication techniques, and integrated mechanisms, the control and behavior of 4D printed multi-DoF active structures are not difficult to realize due to the nonlinearity of smart materials' and coupled kinematics' thermal-mechanical properties. We conducted a preliminary study, integrating a neural network-based control algorithm to model and control 4D printed active structures. The results revealed opportunities to solve high-dimensional problems.

Finally, we proposed three case studies to address real-world challenges. The current work has focused mainly on the ideation of our design and proof of our concept. To further examine the proposed design's applicability, appropriate experimental environments must be established. For example, the space hinge could be evaluated in a vacuum environment to examine the effects on thermal transfer and energy efficiency. On the other hand, manufacturing technologies' scalability—as well as the actuation mechanism—should be further investigated.

# References

- [1] C. Laschi, B. Mazzolai, and M. Cianchetti, "Soft robotics: Technologies and systems pushing the boundaries of robot abilities," *Sci. Robot.*, vol. 1, no. 1, Dec. 2016, doi: 10.1126/scirobotics.aah3690.
- [2] A. Brunete, A. Ranganath, S. Segovia, J. P. de Frutos, M. Hernando, and E. Gambao, "Current trends in reconfigurable modular robots design," *Int. J. Adv. Robot. Syst.*, vol. 14, no. 3, p. 1729881417710457, May 2017, doi: 10.1177/1729881417710457.
- [3] S. Hauser, M. Mutlu, P.-A. Léziart, H. Khodr, A. Bernardino, and A. J. Ijspeert, "Roombots extended: Challenges in the next generation of self-reconfigurable modular robots and their application in adaptive and assistive furniture," *Robot. Auton. Syst.*, vol. 127, p. 103467, May 2020, doi: 10.1016/j.robot.2020.103467.
- [4] J. Seo, J. Paik, and M. Yim, "Modular Reconfigurable Robotics," *Annu. Rev. Control Robot. Auton. Syst.*, vol. 2, no. 1, pp. 63–88, 2019, doi: 10.1146/annurev-control-053018-023834.
- [5] E. A. Peraza-Hernandez, D. J. Hartl, R. J. M. Jr, and D. C. Lagoudas, "Origami-inspired active structures: a synthesis and review," *Smart Mater. Struct.*, vol. 23, no. 9, p. 094001, Aug. 2014, doi: 10.1088/0964-1726/23/9/094001.
- [6] L. M. Fonseca, G. V. Rodrigues, M. A. Savi, and A. Paiva, "Nonlinear dynamics of an origami wheel with shape memory alloy actuators," *Chaos Solitons Fractals*, vol. 122, pp. 245–261, May 2019, doi: 10.1016/j.chaos.2019.03.033.
- [7] J. Koh, S. Kim, and K. Cho, "Self-Folding Origami Using Torsion Shape Memory Alloy Wire Actuators," presented at the ASME 2014 International Design Engineering Technical Conferences and Computers and Information in Engineering Conference, Jan. 2015. doi: 10.1115/DETC2014-34822.
- [8] P. Motzki, F. Khelfa, L. Zimmer, M. Schmidt, and S. Seelecke, "Design and Validation of a Reconfigurable Robotic End-Effector Based on Shape Memory Alloys," *IEEEASME Trans. Mechatron.*, vol. 24, no. 1, pp. 293–303, Feb. 2019, doi: 10.1109/TMECH.2019.2891348.
- [9] H. Rodrigue, W. Wang, M.-W. Han, T. J. Y. Kim, and S.-H. Ahn, "An Overview of Shape Memory Alloy-Coupled Actuators and Robots," *Soft Robot.*, vol. 4, no. 1, pp. 3–15, Mar. 2017, doi: 10.1089/soro.2016.0008.
- [10] M. T. Tolley, S. M. Felton, S. Miyashita, D. Aukes, D. Rus, and R. J. Wood, "Self-folding origami: shape memory composites activated by uniform heating," *Smart Mater. Struct.*, vol. 23, no. 9, p. 094006, Aug. 2014, doi: 10.1088/0964-1726/23/9/094006.
- [11] S. M. Felton *et al.*, "Self-folding with shape memory composites," *Soft Matter*, vol. 9, no. 32, pp. 7688–7694, 2013, doi: 10.1039/C3SM51003D.
- [12] T. Chen, O. R. Bilal, R. Lang, C. Daraio, and K. Shea, "Autonomous Deployment of a Solar Panel Using Elastic Origami and Distributed Shape-Memory-Polymer Actuators," *Phys. Rev. Appl.*, vol. 11, no. 6, p. 064069, Jun. 2019, doi: 10.1103/PhysRevApplied.11.064069.
- [13] R. Fernandes and D. H. Gracias, "Self-folding polymeric containers for encapsulation and delivery of drugs," *Adv. Drug Deliv. Rev.*, vol. 64, no. 14, pp. 1579–1589, Nov. 2012, doi: 10.1016/j.addr.2012.02.012.
- [14] S. Ahmed, E. Arrojado, and Z. Ounaies, "Realization of Origami-Inspired Smart Structures Using Electroactive Polymer (EAP)," presented at the ASME 2016 Conference on

## References

- Smart Materials, Adaptive Structures and Intelligent Systems, Nov. 2016. doi: 10.1115/SMASIS2016-9202.
- [15] W. Zhang, S. Ahmed, S. Masters, J. Hong, Z. Ounaies, and M. Frecker, "Finite element analysis of electroactive and magnetoactive coupled behaviors in multi-field origami structures," *J. Intell. Mater. Syst. Struct.*, vol. 29, no. 20, pp. 3983–4000, Dec. 2018, doi: 10.1177/1045389X18803451.
- [16] S. Ahmed, E. Arrojado, N. Sigamani, and Z. Ounaies, "Electric field responsive origami structures using electrostriction-based active materials," in *Behavior and Mechanics of Multifunctional Materials and Composites 2015*, Apr. 2015, vol. 9432, p. 943206. doi: 10.1117/12.2084785.
- [17] "Controlled Flight of a Biologically Inspired, Insect-Scale Robot | Science." <https://science.sciencemag.org/content/340/6132/603> (accessed Jun. 10, 2021).
- [18] A. T. Baisch, O. Ozcan, B. Goldberg, D. Ithier, and R. J. Wood, "High speed locomotion for a quadrupedal microrobot," *Int. J. Robot. Res.*, vol. 33, no. 8, pp. 1063–1082, Jul. 2014, doi: 10.1177/0278364914521473.
- [19] M. K. Rasmussen, E. W. Pedersen, M. G. Petersen, and K. Hornbæk, "Shape-changing interfaces: a review of the design space and open research questions," in *Proceedings of the SIGCHI Conference on Human Factors in Computing Systems*, New York, NY, USA, May 2012, pp. 735–744. doi: 10.1145/2207676.2207781.
- [20] "Grand Challenges in Shape-Changing Interface Research | Proceedings of the 2018 CHI Conference on Human Factors in Computing Systems." <https://dl.acm.org/doi/abs/10.1145/3173574.3173873> (accessed Jun. 09, 2021).
- [21] M. Coelho and J. Zigelbaum, "Shape-changing interfaces," *Pers. Ubiquitous Comput.*, vol. 15, no. 2, pp. 161–173, Feb. 2011, doi: 10.1007/s00779-010-0311-y.
- [22] S. Haddadin and E. Croft, "Physical Human–Robot Interaction," in *Springer Handbook of Robotics*, B. Siciliano and O. Khatib, Eds. Cham: Springer International Publishing, 2016, pp. 1835–1874. doi: 10.1007/978-3-319-32552-1\_69.
- [23] A. Cherubini, R. Passama, A. Crosnier, A. Lasnier, and P. Fraisse, "Collaborative manufacturing with physical human–robot interaction," *Robot. Comput.-Integr. Manuf.*, vol. 40, pp. 1–13, Aug. 2016, doi: 10.1016/j.rcim.2015.12.007.
- [24] T. B. Sheridan, "Human–Robot Interaction: Status and Challenges," *Hum. Factors*, vol. 58, no. 4, pp. 525–532, Jun. 2016, doi: 10.1177/0018720816644364.
- [25] L. Prusko, C. Coutrix, Y. Laurillau, B. Piranda, and J. Bourgeois, "Molecular HCI: Structuring the Cross-disciplinary Space of Modular Shape-changing User Interfaces," *Proc. ACM Hum.-Comput. Interact.*, vol. 5, no. EICS, pp. 1–33, May 2021, doi: 10.1145/3461733.
- [26] I. P. S. Qamar, R. Groh, D. Holman, and A. Roudaut, "HCI meets Material Science: A Literature Review of Morphing Materials for the Design of Shape-Changing Interfaces," in *Proceedings of the 2018 CHI Conference on Human Factors in Computing Systems*, New York, NY, USA, Apr. 2018, pp. 1–23. doi: 10.1145/3173574.3173948.
- [27] Z. Pan, J. Polden, N. Larkin, S. Van Duin, and J. Norrish, "Recent progress on programming methods for industrial robots," *Robot. Comput.-Integr. Manuf.*, vol. 28, no. 2, pp. 87–94, Apr. 2012, doi: 10.1016/j.rcim.2011.08.004.
- [28] A. Billard, S. Calinon, R. Dillmann, and S. Schaal, "Robot Programming by Demonstration," in *Springer Handbook of Robotics*, B. Siciliano and O. Khatib, Eds. Berlin, Heidelberg: Springer, 2008, pp. 1371–1394. doi: 10.1007/978-3-540-30301-5\_60.
- [29] "Real-time photorealistic virtualized reality interface for remote mobile robot control - Alonzo Kelly, Nicholas Chan, Herman Herman, Daniel Huber, Robert Meyers, Pete Rander, Randy Warner, Jason Ziglar, Erin Capstick, 2011." <https://journals.sagepub.com/doi/10.1177/0278364910383724> (accessed Apr. 18, 2021).
- [30] J. Alonso-Mora, S. H. Lohaus, P. Leemann, R. Siegwart, and P. Beardsley, "Gesture based human - Multi-robot swarm interaction and its application to an interactive display," in

- 2015 *IEEE International Conference on Robotics and Automation (ICRA)*, May 2015, pp. 5948–5953. doi: 10.1109/ICRA.2015.7140033.
- [31] G. F. Rossano, C. Martinez, M. Hedelind, S. Murphy, and T. A. Fuhlbrigge, “Easy robot programming concepts: An industrial perspective,” in *2013 IEEE International Conference on Automation Science and Engineering (CASE)*, Aug. 2013, pp. 1119–1126. doi: 10.1109/CoASE.2013.6654035.
- [32] J. K. Paik, A. Byoungkwon, D. Rus, and R. J. Wood, “Robotic Origamis: Self-morphing Modular Robot,” presented at the ICMC, 2012. Accessed: Apr. 18, 2021. [Online]. Available: <https://infoscience.epfl.ch/record/206919>
- [33] S. Miyashita, S. Guitron, K. Yoshida, Shuguang Li, D. D. Damian, and D. Rus, “Ingestible, controllable, and degradable origami robot for patching stomach wounds,” in *2016 IEEE International Conference on Robotics and Automation (ICRA)*, May 2016, pp. 909–916. doi: 10.1109/ICRA.2016.7487222.
- [34] C. D. Onal, R. J. Wood, and D. Rus, “An Origami-Inspired Approach to Worm Robots,” *IEEEASME Trans. Mechatron.*, vol. 18, no. 2, pp. 430–438, Apr. 2013, doi: 10.1109/TMECH.2012.2210239.
- [35] S. Felton, M. Tolley, E. Demaine, D. Rus, and R. Wood, “A method for building self-folding machines,” *Science*, vol. 345, no. 6197, pp. 644–646, Aug. 2014, doi: 10.1126/science.1252610.
- [36] E. A. Peraza Hernandez, D. J. Hartl, R. J. Malak Jr., E. Akleman, O. Gonen, and H.-W. Kung, “Design Tools for Patterned Self-Folding Reconfigurable Structures Based on Programmable Active Laminates,” *J. Mech. Robot.*, vol. 8, no. 031015, Mar. 2016, doi: 10.1115/1.4031955.
- [37] A. Roudaut, A. Karnik, M. Löchtefeld, and S. Subramanian, “Morphees: toward high” shape resolution” in self-actuated flexible mobile devices,” in *Proceedings of the SIGCHI Conference on Human Factors in Computing Systems*, 2013, pp. 593–602.
- [38] B. An and D. Rus, “Designing and programming self-folding sheets,” *Robot. Auton. Syst.*, vol. 62, no. 7, pp. 976–1001, Jul. 2014, doi: 10.1016/j.robot.2013.06.015.
- [39] M. E. W. Nisser, S. M. Felton, M. T. Tolley, M. Rubenstein, and R. J. Wood, “Feedback-controlled self-folding of autonomous robot collectives,” in *2016 IEEE/RSJ International Conference on Intelligent Robots and Systems (IROS)*, Oct. 2016, pp. 1254–1261. doi: 10.1109/IROS.2016.7759208.
- [40] L. A. Bowen, C. L. Grames, S. P. Magleby, L. L. Howell, and R. J. Lang, “A Classification of Action Origami as Systems of Spherical Mechanisms,” *J. Mech. Des.*, vol. 135, no. 111008, Oct. 2013, doi: 10.1115/1.4025379.
- [41] L. A. Bowen, W. L. Baxter, S. P. Magleby, and L. L. Howell, “A position analysis of coupled spherical mechanisms found in action origami,” *Mech. Mach. Theory*, vol. 77, pp. 13–24, Jul. 2014, doi: 10.1016/j.mechmachtheory.2014.02.006.
- [42] R. J. Lang, *Origami 4*. CRC Press, 2009.
- [43] H. C. Greenberg, M. L. Gong, S. P. Magleby, and L. L. Howell, “Identifying links between origami and compliant mechanisms,” *Mech. Sci.*, vol. 2, no. 2, pp. 217–225, Dec. 2011, doi: 10.5194/ms-2-217-2011.
- [44] E. A. Peraza-Hernandez, D. J. Hartl, and R. J. M. Jr, “Design and numerical analysis of an SMA mesh-based self-folding sheet,” *Smart Mater. Struct.*, vol. 22, no. 9, p. 094008, Aug. 2013, doi: 10.1088/0964-1726/22/9/094008.
- [45] N. An, M. Li, and J. Zhou, “Predicting origami-inspired programmable self-folding of hydrogel trilayers,” *Smart Mater. Struct.*, vol. 25, no. 11, p. 11LT02, Oct. 2016, doi: 10.1088/0964-1726/25/11/11LT02.
- [46] B. H. Hanna, J. M. Lund, R. J. Lang, S. P. Magleby, and L. L. Howell, “Waterbomb base: a symmetric single-vertex bistable origami mechanism,” *Smart Mater. Struct.*, vol. 23, no. 9, p. 094009, Aug. 2014, doi: 10.1088/0964-1726/23/9/094009.

## References

---

- [47] C. Qiu, V. Aminzadeh, and J. S. Dai, "Kinematic Analysis and Stiffness Validation of Origami Cartons," *J. Mech. Des.*, vol. 135, no. 111004, Sep. 2013, doi: 10.1115/1.4025381.
- [48] C. Sung and D. Rus, "Foldable Joints for Foldable Robots," *J. Mech. Robot.*, vol. 7, no. 021012, May 2015, doi: 10.1115/1.4029490.
- [49] J. S. Dai and F. Cannella, "Stiffness Characteristics of Carton Folds for Packaging," *J. Mech. Des.*, vol. 130, no. 022305, Dec. 2007, doi: 10.1115/1.2813785.
- [50] L. Bowen, K. Springsteen, M. Frecker, and T. Simpson, "Trade Space Exploration of Magnetically Actuated Origami Mechanisms," *J. Mech. Robot.*, vol. 8, no. 031012, Mar. 2016, doi: 10.1115/1.4032406.
- [51] R. Watanabe, Y. Itoh, M. Asai, Y. Kitamura, F. Kishino, and H. Kikuchi, "The soul of ActiveCube: implementing a flexible, multimodal, three-dimensional spatial tangible interface," *Comput. Entertain.*, vol. 2, no. 4, p. 15, Oct. 2004, doi: 10.1145/1037851.1037874.
- [52] Y. Huang and M. Eisenberg, "Easigami: virtual creation by physical folding," in *Proceedings of the Sixth International Conference on Tangible, Embedded and Embodied Interaction*, New York, NY, USA, Feb. 2012, pp. 41–48. doi: 10.1145/2148131.2148143.
- [53] K. Nakagaki, S. Follmer, and H. Ishii, "LineFORM: Actuated Curve Interfaces for Display, Interaction, and Constraint," in *Proceedings of the 28th Annual ACM Symposium on User Interface Software & Technology*, New York, NY, USA, Nov. 2015, pp. 333–339. doi: 10.1145/2807442.2807452.
- [54] A. Dementyev, H.-L. (Cindy) Kao, and J. A. Paradiso, "SensorTape: Modular and Programmable 3D-Aware Dense Sensor Network on a Tape," in *Proceedings of the 28th Annual ACM Symposium on User Interface Software & Technology*, New York, NY, USA, Nov. 2015, pp. 649–658. doi: 10.1145/2807442.2807507.
- [55] C. Rendl *et al.*, "FlexSense: a transparent self-sensing deformable surface," in *Proceedings of the 27th annual ACM symposium on User interface software and technology*, New York, NY, USA, Oct. 2014, pp. 129–138. doi: 10.1145/2642918.2647405.
- [56] C. Chien, R.-H. Liang, L.-F. Lin, L. Chan, and B.-Y. Chen, "FlexiBend: Enabling Interactivity of Multi-Part, Deformable Fabrications Using Single Shape-Sensing Strip," in *Proceedings of the 28th Annual ACM Symposium on User Interface Software & Technology*, New York, NY, USA, Nov. 2015, pp. 659–663. doi: 10.1145/2807442.2807456.
- [57] O. Shaer and E. Hornecker, "Tangible User Interfaces: Past, Present, and Future Directions," *Found. Trends® Human-Computer Interact.*, vol. 3, no. 1–2, pp. 4–137, Mar. 2010, doi: 10.1561/11000000026.
- [58] K. Nakagaki, A. Dementyev, S. Follmer, J. A. Paradiso, and H. Ishii, "ChainFORM: A Linear Integrated Modular Hardware System for Shape Changing Interfaces," in *Proceedings of the 29th Annual Symposium on User Interface Software and Technology*, New York, NY, USA, Oct. 2016, pp. 87–96. doi: 10.1145/2984511.2984587.
- [59] H. S. Raffle, A. J. Parkes, and H. Ishii, "Topobo: a constructive assembly system with kinetic memory," in *Proceedings of the SIGCHI Conference on Human Factors in Computing Systems*, New York, NY, USA, Apr. 2004, pp. 647–654. doi: 10.1145/985692.985774.
- [60] K. Nakagaki *et al.*, "Materiable: Rendering Dynamic Material Properties in Response to Direct Physical Touch with Shape Changing Interfaces," in *Proceedings of the 2016 CHI Conference on Human Factors in Computing Systems*, San Jose California USA, May 2016, pp. 2764–2772. doi: 10.1145/2858036.2858104.
- [61] D. Lindlbauer, J. E. Grønbaek, M. Birk, K. Halskov, M. Alexa, and J. Müller, "Combining Shape-Changing Interfaces and Spatial Augmented Reality Enables Extended Object Appearance," in *Proceedings of the 2016 CHI Conference on Human Factors in Computing Systems*, New York, NY, USA, May 2016, pp. 791–802. doi: 10.1145/2858036.2858457.
- [62] D. Leithinger, S. Follmer, A. Olwal, and H. Ishii, "Physical telepresence: shape capture and display for embodied, computer-mediated remote collaboration," in *Proceedings*

- of the 27th annual ACM symposium on User interface software and technology - UIST '14, Honolulu, Hawaii, USA, 2014, pp. 461–470. doi: 10.1145/2642918.2647377.
- [63] P. Strohmeier, J. P. Carrascal, B. Cheng, M. Meban, and R. Vertegaal, “An Evaluation of Shape Changes for Conveying Emotions,” in *Proceedings of the 2016 CHI Conference on Human Factors in Computing Systems*, New York, NY, USA, May 2016, pp. 3781–3792. doi: 10.1145/2858036.2858537.
- [64] A. Martin and M. R. Emami, “An Architecture for Robotic Hardware-in-the-Loop Simulation,” in *2006 International Conference on Mechatronics and Automation*, Jun. 2006, pp. 2162–2167. doi: 10.1109/ICMA.2006.257628.
- [65] “DESIGNING A MIXED REALITY FRAMEWORK FOR ENRICHING INTERACTIONS IN ROBOT SIMULATION,” in *Proceedings of the International Conference on Computer Graphics Theory and Applications*, Angers, France, 2010, pp. 331–338. doi: 10.5220/0002817903310338.
- [66] D. J. Balkcom and M. T. Mason, “Robotic origami folding,” *Int. J. Robot. Res.*, vol. 27, no. 5, pp. 613–627, May 2008, doi: 10.1177/0278364908090235.
- [67] T. Tachi, “Geometric Considerations for the Design of Rigid Origami Structures,” p. 13, 2010.
- [68] R. Viswanathan and P. K. Varshney, “Distributed detection with multiple sensors Part I. Fundamentals,” *Proc. IEEE*, vol. 85, no. 1, pp. 54–63, Jan. 1997, doi: 10.1109/5.554208.
- [69] S. S. Skiena, *The Algorithm Design Manual*. Springer Nature, 2020.
- [70] W. Schiehlen, “Multibody System Dynamics: Roots and Perspectives,” *Multibody Syst. Dyn.*, vol. 1, no. 2, pp. 149–188, Jun. 1997, doi: 10.1023/A:1009745432698.
- [71] E. D. Demaine and J. O’Rourke, *Geometric Folding Algorithms: Linkages, Origami, Polyhedra*. Cambridge University Press, 2007.
- [72] S. R. Gray, J. Seo, P. J. White, N. J. Zeichner, M. Yim, and V. Kumar, “A Toolchain for the Design and Simulation of Foldable Programmable Matter,” Mar. 2011, pp. 1167–1176. doi: 10.1115/DETC2010-28838.
- [73] M. Müller, B. Heidelberger, M. Hennix, and J. Ratcliff, “Position based dynamics,” *J. Vis. Commun. Image Represent.*, vol. 18, no. 2, pp. 109–118, Apr. 2007, doi: 10.1016/j.jvcir.2007.01.005.
- [74] J. Bender, M. Müller, and M. Macklin, “Position-Based Simulation Methods in Computer Graphics,” *EG 2015 - Tutor.*, 2015, doi: 10.2312/EGT.20151045.
- [75] C. Deul, P. Charrier, and J. Bender, “Position-based rigid-body dynamics,” *Comput. Animat. Virtual Worlds*, vol. 27, no. 2, pp. 103–112, 2016, doi: <https://doi.org/10.1002/cav.1614>.
- [76] W. Goldstone, *Unity Game Development Essentials*. Packt Publishing Ltd, 2009.
- [77] “Characterization of Creases in Polymers for Adaptive Origami Structures | SMASIS | ASME Digital Collection.” <https://asmedigitalcollection.asme.org/SMASIS/proceedings-abstract/SMASIS2014/46148/V001T01A009/286411> (accessed Apr. 18, 2021).
- [78] Z. Zhakypov, J. Huang, and J. Paik, “A Novel Torsional Shape Memory Alloy Actuator: Modeling, Characterization, and Control,” *IEEE Robot. Autom. Mag.*, vol. 23, no. 3, pp. 65–74, Sep. 2016, doi: 10.1109/MRA.2016.2582868.
- [79] A. Firouzeh and J. Paik, “Robogami: A Fully Integrated Low-Profile Robotic Origami,” *J. Mech. Robot.*, vol. 7, no. 021009, May 2015, doi: 10.1115/1.4029491.
- [80] Z. Zhakypov, M. Falahi, M. Shah, and J. Paik, “The design and control of the multi-modal locomotion origami robot, Tribot,” in *2015 IEEE/RSJ International Conference on Intelligent Robots and Systems (IROS)*, Sep. 2015, pp. 4349–4355. doi: 10.1109/IROS.2015.7353994.
- [81] M. Yim *et al.*, “Modular Self-Reconfigurable Robot Systems [Grand Challenges of Robotics],” *IEEE Robot. Autom. Mag.*, vol. 14, no. 1, pp. 43–52, Mar. 2007, doi: 10.1109/MRA.2007.339623.

## References

- [82] “Transforming architectures inspired by origami | PNAS.” <https://www.pnas.org/content/112/40/12234.short> (accessed Apr. 18, 2021).
- [83] M. Schenk, S. G. Kerr, A. M. Smyth, and S. D. Guest, “Inflatable Cylinders for Deployable Space Structures,” p. 6, 2013.
- [84] Z. Zhakypov and J. Paik, “Design Methodology for Constructing Multimaterial Origami Robots and Machines,” *IEEE Trans. Robot.*, vol. 34, no. 1, pp. 151–165, Feb. 2018, doi: 10.1109/TRO.2017.2775655.
- [85] Z. Zhakypov, C. H. Belke, and J. Paik, “Tribot: A deployable, self-righting and multi-locomotive origami robot,” in *2017 IEEE/RSJ International Conference on Intelligent Robots and Systems (IROS)*, Sep. 2017, pp. 5580–5586. doi: 10.1109/IROS.2017.8206445.
- [86] A. Firouzeh and J. Paik, “An under-actuated origami gripper with adjustable stiffness joints for multiple grasp modes,” *Smart Mater. Struct.*, vol. 26, no. 5, p. 055035, Apr. 2017, doi: 10.1088/1361-665X/aa67fd.
- [87] “The flying monkey: A mesoscale robot that can run, fly, and grasp.” [https://ieeexplore.ieee.org/abstract/document/7487667/?casa\\_token=goNjb1c5WhgAAAAA:gnlltmBw-uVL89g7HvgYdgVuguOJVn3y-6Cp5yDI26okKgAhnxbupJh3jOBcYFiro8PwmeNMSQ](https://ieeexplore.ieee.org/abstract/document/7487667/?casa_token=goNjb1c5WhgAAAAA:gnlltmBw-uVL89g7HvgYdgVuguOJVn3y-6Cp5yDI26okKgAhnxbupJh3jOBcYFiro8PwmeNMSQ) (accessed Apr. 18, 2021).
- [88] C. H. Belke and J. Paik, “Mori: A Modular Origami Robot,” *IEEEASME Trans. Mechatron.*, vol. 22, no. 5, pp. 2153–2164, Oct. 2017, doi: 10.1109/TMECH.2017.2697310.
- [89] G. Biggs and B. MacDonald, “A Survey of Robot Programming Systems,” p. 10.
- [90] M. Mutlu, S. Bonardi, M. Vespignani, S. Hauser, A. Bernardino, and A. J. Ijspeert, “Natural user interface for lighting control: Case study on desktop lighting using modular robots,” in *2016 25th IEEE International Symposium on Robot and Human Interactive Communication (RO-MAN)*, Aug. 2016, pp. 288–293. doi: 10.1109/RO-MAN.2016.7745144.
- [91] M. Pielot, S. Diefenbach, and N. Henze, Eds., “Natural 3D Interaction Techniques for Locomotion with Modular Robots,” in *Mensch und Computer 2015 – Tagungsband*, De Gruyter, 2015, pp. 133–142. doi: 10.1515/9783110443929-015.
- [92] “ChiroBot | Proceedings of the 2014 conference on Interaction design and children.” [https://dl.acm.org/doi/abs/10.1145/2593968.2610454?casa\\_token=axaK2LwZHIU-AAAAA:dC9Ps2hRpnY0iYibvonYQxd--oc8IU21\\_y9M\\_kvSrT766eAGFlr8RXpgk6GZ7GXVsRe81kSsMByN](https://dl.acm.org/doi/abs/10.1145/2593968.2610454?casa_token=axaK2LwZHIU-AAAAA:dC9Ps2hRpnY0iYibvonYQxd--oc8IU21_y9M_kvSrT766eAGFlr8RXpgk6GZ7GXVsRe81kSsMByN) (accessed Apr. 18, 2021).
- [93] A. Özgür, S. Bonardi, M. Vespignani, R. Möckel, and A. J. Ijspeert, “Natural user interface for Roombots,” in *The 23rd IEEE International Symposium on Robot and Human Interactive Communication*, Aug. 2014, pp. 12–17. doi: 10.1109/ROMAN.2014.6926223.
- [94] “Ani-Bot | Adjunct Publication of the 30th Annual ACM Symposium on User Interface Software and Technology.” [https://dl.acm.org/doi/abs/10.1145/3131785.3131833?casa\\_token=Aje4iRXKnZcAAAAA:CCZx6p\\_GMe387XpMb-fQvh8x1d9IXvM7orHw4gQXswisBwZR9FS3LIQ477HUFbNcq1YO3FlcTBpyH](https://dl.acm.org/doi/abs/10.1145/3131785.3131833?casa_token=Aje4iRXKnZcAAAAA:CCZx6p_GMe387XpMb-fQvh8x1d9IXvM7orHw4gQXswisBwZR9FS3LIQ477HUFbNcq1YO3FlcTBpyH) (accessed Apr. 18, 2021).
- [95] V. Nigolian, M. Mutlu, S. Hauser, A. Bernardino, and A. Ijspeert, “Self-reconfigurable modular robot interface using virtual reality: Arrangement of furniture made out of roombots modules,” in *2017 26th IEEE International Symposium on Robot and Human Interactive Communication (RO-MAN)*, Aug. 2017, pp. 772–778. doi: 10.1109/RO-MAN.2017.8172390.
- [96] A. M. Mehta and D. Rus, “An end-to-end system for designing mechanical structures for print-and-fold robots,” in *2014 IEEE International Conference on Robotics and Automation (ICRA)*, May 2014, pp. 1460–1465. doi: 10.1109/ICRA.2014.6907044.
- [97] G. Jing, T. Tosun, M. Yim, and H. Kress-Gazit, *An End-To-End System for Accomplishing Tasks with Modular Robots*. 2016. doi: 10.15607/RSS.2016.XII.025.



- [98] "A reconfiguration strategy for modular robots using origami folding - Meibao Yao, Christoph H. Belke, Hutao Cui, Jamie Paik, 2019." <https://journals.sagepub.com/doi/full/10.1177/0278364918815757> (accessed Apr. 18, 2021).
- [99] B. M. C. A. and L. G. "A Survey of Augmented Reality," 2015, doi: 10.1561/1100000049.
- [100] "Grand Challenges in Shape-Changing Interface Research | Proceedings of the 2018 CHI Conference on Human Factors in Computing Systems." [https://dl.acm.org/doi/abs/10.1145/3173574.3173873?casa\\_token=oiEL-jqzibMQAAAAA:LFsOPZosfrhdc6ArXg5UOaFPCWnw1IBI2cNoZmGIK9ybYi1mWg-ZE-raPafSE4zNfVOcXUUiGWvld](https://dl.acm.org/doi/abs/10.1145/3173574.3173873?casa_token=oiEL-jqzibMQAAAAA:LFsOPZosfrhdc6ArXg5UOaFPCWnw1IBI2cNoZmGIK9ybYi1mWg-ZE-raPafSE4zNfVOcXUUiGWvld) (accessed Apr. 18, 2021).
- [101] "Robotic Assembly of Haptic Proxy Objects for Tangible Interaction and Virtual Reality | Proceedings of the 2017 ACM International Conference on Interactive Surfaces and Spaces." [https://dl.acm.org/doi/abs/10.1145/3132272.3134143?casa\\_token=pSQAfas8KksAAAAA:6e2ImZ1TxjEbdjcd8QZfSQcyonkx5oi76p6PwGy7Ay-TiGmK3bEflcfaz6uqG5LMPBg4wVMspx03](https://dl.acm.org/doi/abs/10.1145/3132272.3134143?casa_token=pSQAfas8KksAAAAA:6e2ImZ1TxjEbdjcd8QZfSQcyonkx5oi76p6PwGy7Ay-TiGmK3bEflcfaz6uqG5LMPBg4wVMspx03) (accessed Apr. 18, 2021).
- [102] A. Roudaut, D. Krusteva, M. McCoy, A. Karnik, K. Ramani, and S. Subramanian, "Cubimorph: Designing modular interactive devices," in *2016 IEEE International Conference on Robotics and Automation (ICRA)*, May 2016, pp. 3339–3345. doi: 10.1109/ICRA.2016.7487508.
- [103] S. Musić and S. Hirche, "Control sharing in human-robot team interaction," *Annu. Rev. Control*, vol. 44, pp. 342–354, Jan. 2017, doi: 10.1016/j.arcontrol.2017.09.017.
- [104] A. Kolling, P. Walker, N. Chakraborty, K. Sycara, and M. Lewis, "Human Interaction With Robot Swarms: A Survey," *IEEE Trans. Hum.-Mach. Syst.*, vol. 46, no. 1, pp. 9–26, Feb. 2016, doi: 10.1109/THMS.2015.2480801.
- [105] C. Bartneck, M. Soucy, K. Fleuret, and E. B. Sandoval, "The robot engine — Making the unity 3D game engine work for HRI," in *2015 24th IEEE International Symposium on Robot and Human Interactive Communication (RO-MAN)*, Aug. 2015, pp. 431–437. doi: 10.1109/ROMAN.2015.7333561.
- [106] J.-L. Huang, Z. Zhakypov, H. Sonar, and J. Paik, "A reconfigurable interactive interface for controlling robotic origami in virtual environments," *Int. J. Robot. Res.*, vol. 37, no. 6, pp. 629–647, May 2018, doi: 10.1177/0278364918769157.
- [107] P. MILGRAM and F. KISHINO, "A Taxonomy of Mixed Reality Visual Displays," Dec. 1994. [https://search.ieice.org/bin/summary.php?id=e77-d\\_12\\_1321](https://search.ieice.org/bin/summary.php?id=e77-d_12_1321) (accessed Apr. 18, 2021).
- [108] Y. Jansen *et al.*, "Opportunities and Challenges for Data Physicalization," in *Proceedings of the 33rd Annual ACM Conference on Human Factors in Computing Systems*, Seoul, Republic of Korea, Apr. 2015, pp. 3227–3236. doi: 10.1145/2702123.2702180.
- [109] D. Wang, K. Ohnishi, and W. Xu, "Multimodal Haptic Display for Virtual Reality: A Survey," *IEEE Trans. Ind. Electron.*, vol. 67, no. 1, pp. 610–623, Jan. 2020, doi: 10.1109/TIE.2019.2920602.
- [110] F. Vidal-Verdu and M. Hafez, "Graphical Tactile Displays for Visually-Impaired People," *IEEE Trans. Neural Syst. Rehabil. Eng.*, vol. 15, no. 1, pp. 119–130, Mar. 2007, doi: 10.1109/TNSRE.2007.891375.
- [111] S. Follmer, D. Leithinger, A. Olwal, A. Hogge, and H. Ishii, "inFORM: dynamic physical affordances and constraints through shape and object actuation," in *Proceedings of the 26th annual ACM symposium on User interface software and technology - UIST '13*, St. Andrews, Scotland, United Kingdom, 2013, pp. 417–426. doi: 10.1145/2501988.2502032.
- [112] D. Leithinger, D. Lakatos, A. DeVincenzi, M. Blackshaw, and H. Ishii, "Direct and gestural interaction with relief: a 2.5D shape display," p. 8, 2011.

## References

---

- [113] K. Nakagaki, D. Fitzgerald, Z. (John) Ma, L. Vink, D. Levine, and H. Ishii, "inFORCE: Bi-directional 'Force' Shape Display for Haptic Interaction," in *Proceedings of the Thirteenth International Conference on Tangible, Embedded, and Embodied Interaction*, Tempe Arizona USA, Mar. 2019, pp. 615–623. doi: 10.1145/3294109.3295621.
- [114] L. Yao, R. Niiyama, J. Ou, S. Follmer, C. Della Silva, and H. Ishii, "PneUI: pneumatically actuated soft composite materials for shape changing interfaces," in *Proceedings of the 26th annual ACM symposium on User interface software and technology - UIST '13*, St. Andrews, Scotland, United Kingdom, 2013, pp. 13–22. doi: 10.1145/2501988.2502037.
- [115] J. Ou *et al.*, "aeroMorph - Heat-sealing Inflatable Shape-change Materials for Interaction Design," in *Proceedings of the 29th Annual Symposium on User Interface Software and Technology*, Tokyo Japan, Oct. 2016, pp. 121–132. doi: 10.1145/2984511.2984520.
- [116] N. Takizawa, H. Yano, H. Iwata, Y. Oshiro, and N. Ohkohchi, "Encountered-Type Haptic Interface for Representation of Shape and Rigidity of 3D Virtual Objects," *IEEE Trans. Haptics*, vol. 10, no. 4, pp. 500–510, Oct. 2017, doi: 10.1109/TOH.2017.2740934.
- [117] S. Follmer, D. Leithinger, A. Olwal, N. Cheng, and H. Ishii, "Jamming user interfaces: programmable particle stiffness and sensing for malleable and shape-changing devices," in *Proceedings of the 25th annual ACM symposium on User interface software and technology*, 2012, pp. 519–528.
- [118] L.-K. Ma, Y. Zhang, Y. Liu, K. Zhou, and X. Tong, "Computational design and fabrication of soft pneumatic objects with desired deformations," *ACM Trans. Graph.*, vol. 36, no. 6, pp. 1–12, Nov. 2017, doi: 10.1145/3130800.3130850.
- [119] M. Koehler, N. S. Usevitch, and A. M. Okamura, "Model-Based Design of a Soft 3-D Haptic Shape Display," *IEEE Trans. Robot.*, vol. 36, no. 3, pp. 613–628, Jun. 2020, doi: 10.1109/TRO.2020.2980114.
- [120] F. Chinello, M. Malvezzi, D. Prattichizzo, and C. Pacchierotti, "A Modular Wearable Finger Interface for Cutaneous and Kinesthetic Interaction: Control and Evaluation," *IEEE Trans. Ind. Electron.*, vol. 67, no. 1, pp. 706–716, Jan. 2020, doi: 10.1109/TIE.2019.2899551.
- [121] F. Chinello, M. Malvezzi, C. Pacchierotti, and D. Prattichizzo, "A three DoFs wearable tactile display for exploration and manipulation of virtual objects," in *2012 IEEE Haptics Symposium (HAPTICS)*, Mar. 2012, pp. 71–76. doi: 10.1109/HAPTICS.2012.6183772.
- [122] M. Gabardi, M. Solazzi, D. Leonardis, and A. Frisoli, "A new wearable fingertip haptic interface for the rendering of virtual shapes and surface features," in *2016 IEEE Haptics Symposium (HAPTICS)*, Apr. 2016, pp. 140–146. doi: 10.1109/HAPTICS.2016.7463168.
- [123] H. Benko, C. Holz, M. Sinclair, and E. Ofek, "NormalTouch and TextureTouch: High-fidelity 3D Haptic Shape Rendering on Handheld Virtual Reality Controllers," in *Proceedings of the 29th Annual Symposium on User Interface Software and Technology*, Tokyo Japan, Oct. 2016, pp. 717–728. doi: 10.1145/2984511.2984526.
- [124] S. Okamoto, H. Nagano, and Y. Yamada, "Psychophysical Dimensions of Tactile Perception of Textures," *IEEE Trans. Haptics*, vol. 6, no. 1, pp. 81–93, First 2013, doi: 10.1109/TOH.2012.32.
- [125] S. Choi and K. J. Kuchenbecker, "Vibrotactile Display: Perception, Technology, and Applications," *Proc. IEEE*, vol. 101, no. 9, pp. 2093–2104, Sep. 2013, doi: 10.1109/JPROC.2012.2221071.
- [126] B. Ward-Cherrier *et al.*, "The TacTip Family: Soft Optical Tactile Sensors with 3D-Printed Biomimetic Morphologies," *Soft Robot.*, vol. 5, no. 2, pp. 216–227, Apr. 2018, doi: 10.1089/soro.2017.0052.
- [127] "Soft Touch using Soft Pneumatic Actuator–Skin as a Wearable Haptic Feedback Device - Sonar - 2021 - Advanced Intelligent Systems - Wiley Online Library." <https://onlinelibrary.wiley.com/doi/full/10.1002/aisy.202000168> (accessed Apr. 18, 2021).

- [128] S. Mueller *et al.*, “FormFab: Continuous Interactive Fabrication,” in *Proceedings of the Thirteenth International Conference on Tangible, Embedded, and Embodied Interaction*, Tempe Arizona USA, Mar. 2019, pp. 315–323. doi: 10.1145/3294109.3295620.
- [129] A. F. Siu, J. Miele, and S. Follmer, “An Accessible CAD Workflow Using Programming of 3D Models and Preview Rendering in A 2.5D Shape Display,” in *Proceedings of the 20th International ACM SIGACCESS Conference on Computers and Accessibility*, Galway Ireland, Oct. 2018, pp. 343–345. doi: 10.1145/3234695.3240996.
- [130] Z. Gao, H. Wang, G. Feng, F. Guo, H. Lv, and B. Li, “RealPot: an immersive virtual pottery system with handheld haptic devices,” *Multimed. Tools Appl.*, vol. 78, no. 18, pp. 26569–26596, Sep. 2019, doi: 10.1007/s11042-019-07843-3.
- [131] “Frontiers | Soft Pneumatic Actuator Skin with Piezoelectric Sensors for Vibrotactile Feedback | Robotics and AI.” <https://www.frontiersin.org/articles/10.3389/frobt.2015.00038/full> (accessed Apr. 18, 2021).
- [132] J.-L. Rodríguez, R. Velázquez, C. Del-Valle-Soto, S. Gutiérrez, J. Varona, and J. Enríquez-Zarate, “Active and Passive Haptic Perception of Shape: Passive Haptics Can Support Navigation,” *Electronics*, vol. 8, no. 3, Art. no. 3, Mar. 2019, doi: 10.3390/electronics8030355.
- [133] A. M. Smith, G. Gosselin, and B. Houde, “Deployment of fingertip forces in tactile exploration,” *Exp. Brain Res.*, vol. 147, no. 2, pp. 209–218, Nov. 2002, doi: 10.1007/s00221-002-1240-4.
- [134] L. St»hle and S. Wold, “Analysis of variance (ANOVA),” *Chemom. Intell. Lab. Syst.*, vol. 6, no. 4, pp. 259–272, Nov. 1989, doi: 10.1016/0169-7439(89)80095-4.
- [135] S.-J. Kim, D.-Y. Lee, G.-P. Jung, and K.-J. Cho, “An origami-inspired, self-locking robotic arm that can be folded flat,” *Sci. Robot.*, vol. 3, no. 16, Mar. 2018, doi: 10.1126/scirobotics.aar2915.
- [136] D. Rus and M. T. Tolley, “Design, fabrication and control of origami robots,” *Nat. Rev. Mater.*, vol. 3, no. 6, Art. no. 6, Jun. 2018, doi: 10.1038/s41578-018-0009-8.
- [137] K. Zhang, C. Qiu, and J. S. Dai, “An Origami Parallel Structure Integrated Deployable Continuum Robot,” presented at the ASME 2015 International Design Engineering Technical Conferences and Computers and Information in Engineering Conference, Jan. 2016. doi: 10.1115/DETC2015-46504.
- [138] M. Luo *et al.*, “OriSnake: Design, Fabrication, and Experimental Analysis of a 3-D Origami Snake Robot,” *IEEE Robot. Autom. Lett.*, vol. 3, no. 3, pp. 1993–1999, Jul. 2018, doi: 10.1109/LRA.2018.2800112.
- [139] A. Firouzeh and J. Paik, “Grasp Mode and Compliance Control of an Underactuated Origami Gripper Using Adjustable Stiffness Joints,” *IEEEASME Trans. Mechatron.*, vol. 22, no. 5, pp. 2165–2173, Oct. 2017, doi: 10.1109/TMECH.2017.2732827.
- [140] R. Niiyama, X. Sun, C. Sung, B. An, D. Rus, and S. Kim, “Pouch Motors: Printable Soft Actuators Integrated with Computational Design,” *Soft Robot.*, vol. 2, no. 2, pp. 59–70, May 2015, doi: 10.1089/soro.2014.0023.
- [141] M. A. Robertson, O. C. Kara, and J. Paik, “Soft pneumatic actuator-driven origami-inspired modular robotic ‘pneumagami,’” *Int. J. Robot. Res.*, vol. 40, no. 1, pp. 72–85, Jan. 2021, doi: 10.1177/0278364920909905.
- [142] Z. Zhakypov, M. Mete, J. Fiorentino, and J. Paik, “Programmable Fluidic Networks Design for Robotic Origami Sequential Self-Folding,” in *2019 2nd IEEE International Conference on Soft Robotics (RoboSoft)*, Apr. 2019, pp. 814–820. doi: 10.1109/ROBOSOFT.2019.8722798.
- [143] S. M. Felton *et al.*, “Self-folding with shape memory composites,” *Soft Matter*, vol. 9, no. 32, pp. 7688–7694, 2013, doi: 10.1039/C3SM51003D.
- [144] “A method for building self-folding machines | Science.” <https://science.sciencemag.org/content/345/6197/644.abstract> (accessed Apr. 20, 2021).

## References

- [145] D.-Y. Lee, S.-R. Kim, J.-S. Kim, J.-J. Park, and K.-J. Cho, "Origami Wheel Transformer: A Variable-Diameter Wheel Drive Robot Using an Origami Structure," *Soft Robot.*, vol. 4, no. 2, pp. 163–180, Jun. 2017, doi: 10.1089/soro.2016.0038.
- [146] J. K. Paik and R. J. Wood, "A bidirectional shape memory alloy folding actuator," *Smart Mater. Struct.*, vol. 21, no. 6, p. 065013, May 2012, doi: 10.1088/0964-1726/21/6/065013.
- [147] Y. She, J. Chen, H. Shi, and H.-J. Su, "Modeling and Validation of a Novel Bending Actuator for Soft Robotics Applications," *Soft Robot.*, vol. 3, no. 2, pp. 71–81, May 2016, doi: 10.1089/soro.2015.0022.
- [148] J. Sheng and J. P. Desai, "Design, modeling and characterization of a novel meso-scale SMA-actuated torsion actuator," *Smart Mater. Struct.*, vol. 24, no. 10, p. 105005, Aug. 2015, doi: 10.1088/0964-1726/24/10/105005.
- [149] S. Kim, E. Hawkes, K. Choy, M. Joldaz, J. Foley, and R. Wood, "Micro artificial muscle fiber using NiTi spring for soft robotics," in *2009 IEEE/RSJ International Conference on Intelligent Robots and Systems*, Oct. 2009, pp. 2228–2234. doi: 10.1109/IROS.2009.5354178.
- [150] J. Koh and K. Cho, "Omega-Shaped Inchworm-Inspired Crawling Robot With Large-Index-and-Pitch (LIP) SMA Spring Actuators," *IEEEASME Trans. Mechatron.*, vol. 18, no. 2, pp. 419–429, Apr. 2013, doi: 10.1109/TMECH.2012.2211033.
- [151] "One-Dimensional Thermomechanical Constitutive Relations for Shape Memory Materials - C. Liang, C. A. Rogers, 1997." [https://journals.sagepub.com/doi/abs/10.1177/1045389X9700800402?casa\\_token=YjttCr8EBOE-AAAAA:iz015CPiedJx1YgGfzBnLDnvL7K0pBrFr6Qpbffu-pGKWmlg2Yv-w-2vuOqxd-dUaf9pxdth4HB9](https://journals.sagepub.com/doi/abs/10.1177/1045389X9700800402?casa_token=YjttCr8EBOE-AAAAA:iz015CPiedJx1YgGfzBnLDnvL7K0pBrFr6Qpbffu-pGKWmlg2Yv-w-2vuOqxd-dUaf9pxdth4HB9) (accessed Jun. 13, 2021).
- [152] J. Ortín and L. Delaey, "Hysteresis in shape-memory alloys," *Int. J. Non-Linear Mech.*, vol. 37, no. 8, pp. 1275–1281, Dec. 2002, doi: 10.1016/S0020-7462(02)00027-6.
- [153] J. K. Paik, E. Hawkes, and R. J. Wood, "A novel low-profile shape memory alloy torsional actuator," *Smart Mater. Struct.*, vol. 19, no. 12, p. 125014, Nov. 2010, doi: 10.1088/0964-1726/19/12/125014.
- [154] Z. Wang, G. Hang, J. Li, Y. Wang, and K. Xiao, "A micro-robot fish with embedded SMA wire actuated flexible biomimetic fin," *Sens. Actuators Phys.*, vol. 144, no. 2, pp. 354–360, Jun. 2008, doi: 10.1016/j.sna.2008.02.013.
- [155] A. Villanueva, C. Smith, and S. Priya, "A biomimetic robotic jellyfish (Robojelly) actuated by shape memory alloy composite actuators," *Bioinspir. Biomim.*, vol. 6, no. 3, p. 036004, Aug. 2011, doi: 10.1088/1748-3182/6/3/036004.
- [156] K. Yang and C. L. Gu, "A novel robot hand with embedded shape memory alloy actuators," *Proc. Inst. Mech. Eng. Part C J. Mech. Eng. Sci.*, vol. 216, no. 7, pp. 737–745, Jul. 2002, doi: 10.1243/09544060260128788.
- [157] S.-M. An, J. Ryu, M. Cho, and K.-J. Cho, "Engineering design framework for a shape memory alloy coil spring actuator using a static two-state model," *Smart Mater. Struct.*, vol. 21, no. 5, p. 055009, Apr. 2012, doi: 10.1088/0964-1726/21/5/055009.
- [158] M. Manti, V. Cacucciolo, and M. Cianchetti, "Stiffening in Soft Robotics: A Review of the State of the Art," *IEEE Robot. Autom. Mag.*, vol. 23, no. 3, pp. 93–106, Sep. 2016, doi: 10.1109/MRA.2016.2582718.
- [159] Y.-F. Zhang *et al.*, "Fast-Response, Stiffness-Tunable Soft Actuator by Hybrid Multimaterial 3D Printing," *Adv. Funct. Mater.*, vol. 29, no. 15, p. 1806698, 2019, doi: 10.1002/adfm.201806698.
- [160] "A novel design of shape-memory alloy-based soft robotic gripper with variable stiffness - Mingfang Liu, Lina Hao, Wei Zhang, Zhirui Zhao, 2020." <https://journals.sagepub.com/doi/full/10.1177/1729881420907813> (accessed Jun. 15, 2021).
- [161] "Shape Memory Alloy-Based Soft Gripper with Variable Stiffness for Compliant and Effective Grasping | Soft Robotics."

- <https://www.liebertpub.com/doi/full/10.1089/soro.2016.0081> (accessed Jun. 15, 2021).
- [162] J. T. B. Overvelde, J. C. Weaver, C. Hoberman, and K. Bertoldi, "Rational design of reconfigurable prismatic architected materials," *Nature*, vol. 541, no. 7637, Art. no. 7637, Jan. 2017, doi: 10.1038/nature20824.
  - [163] J. L. Silverberg *et al.*, "Origami structures with a critical transition to bistability arising from hidden degrees of freedom," *Nat. Mater.*, vol. 14, no. 4, Art. no. 4, Apr. 2015, doi: 10.1038/nmat4232.
  - [164] P. Hunter, "Nature's origami," *EMBO Rep.*, vol. 16, no. 11, pp. 1435–1438, Nov. 2015, doi: 10.15252/embr.201541390.
  - [165] F. Haas, S. Gorb, and R. J. Wootton, "Elastic joints in dermapteran hind wings: materials and wing folding," *Arthropod Struct. Dev.*, vol. 29, no. 2, pp. 137–146, Apr. 2000, doi: 10.1016/S1467-8039(00)00025-6.
  - [166] R. J. Lang, "From flapping birds to space telescopes: the modern science of origami," in *Proceedings of the 6th international symposium on Non-photorealistic animation and rendering - NPAR '08*, Annecy, France, 2008, p. 7. doi: 10.1145/1377980.1377983.
  - [167] B. G. Winder, S. P. Magleby, and L. L. Howell, "A Study of Joints Suitable for Lamina Emergent Mechanisms," Jul. 2009, pp. 339–349. doi: 10.1115/DETC2008-49914.
  - [168] "Compliant Mechanisms | SpringerLink." [https://link.springer.com/chapter/10.1007/978-1-4471-4510-3\\_7](https://link.springer.com/chapter/10.1007/978-1-4471-4510-3_7) (accessed Jun. 15, 2021).
  - [169] I. L. Delimont, S. P. Magleby, and L. L. Howell, "Evaluating compliant hinge geometries for origami-inspired mechanisms," *J. Mech. Robot.*, vol. 7, no. 1, 2015, doi: 10.1115/1.4029325.
  - [170] Z. Zhao *et al.*, "3D printing of complex origami assemblages for reconfigurable structures," *Soft Matter*, vol. 14, no. 39, pp. 8051–8059, Oct. 2018, doi: 10.1039/C8SM01341A.
  - [171] J. A. Faber, A. F. Arrieta, and A. R. Studart, "Bioinspired spring origami," *Science*, vol. 359, no. 6382, pp. 1386–1391, Mar. 2018, doi: 10.1126/science.aap7753.
  - [172] I. Gibson, G. Goenka, R. Narasimhan, and N. Bhat, "Design Rules for Additive Manufacturing," p. 12.
  - [173] M. A. Wagner, J.-L. Huang, P. Okle, J. Paik, and R. Spolenak, "Hinges for origami-inspired structures by multimaterial additive manufacturing," *Mater. Des.*, vol. 191, p. 108643, Jun. 2020, doi: 10.1016/j.matdes.2020.108643.
  - [174] "Origami Inspired Mechanics: Measuring Modulus and Force Recovery with Bent Polymer Films | Macromolecules." <https://pubs.acs.org/doi/10.1021/acs.macromol.8b02002> (accessed Jun. 15, 2021).
  - [175] T. S. Lumpe, J. Mueller, and K. Shea, "Tensile properties of multi-material interfaces in 3D printed parts," *Mater. Des.*, vol. 162, pp. 1–9, Jan. 2019, doi: 10.1016/j.matdes.2018.11.024.
  - [176] H. Zhang, H. Feng, J.-L. Huang, and J. Paik, "Generalized modeling of origami folding joints," *Extreme Mech. Lett.*, vol. 45, p. 101213, May 2021, doi: 10.1016/j.eml.2021.101213.
  - [177] M. Johnson *et al.*, "Fabricating biomedical origami: a state-of-the-art review," *Int. J. Comput. Assist. Radiol. Surg.*, vol. 12, no. 11, pp. 2023–2032, Nov. 2017, doi: 10.1007/s11548-017-1545-1.
  - [178] "Addressable wireless actuation for multijoint folding robots and devices | Science Robotics." [https://robotics.sciencemag.org/content/2/8/eaan1544.short?casa\\_token=jWAtP1\\_JvdQAAAA:KgQKsWzlk1aT9upsC\\_LFdByXRb0XC8SkFXjz-SiyXKDMQEv-TXns1S0hUPy2idOfLIQ-CMZftzmPsSw](https://robotics.sciencemag.org/content/2/8/eaan1544.short?casa_token=jWAtP1_JvdQAAAA:KgQKsWzlk1aT9upsC_LFdByXRb0XC8SkFXjz-SiyXKDMQEv-TXns1S0hUPy2idOfLIQ-CMZftzmPsSw) (accessed Jun. 16, 2021).
  - [179] sarah-marie belcastro and T. C. Hull, "Modelling the folding of paper into three dimensions using affine transformations," *Linear Algebra Its Appl.*, vol. 348, no. 1, pp. 273–282, Jun. 2002, doi: 10.1016/S0024-3795(01)00608-5.

## References

---

- [180] X. Kuang *et al.*, “Advances in 4D Printing: Materials and Applications,” *Adv. Funct. Mater.*, vol. 29, no. 2, p. 1805290, 2019, doi: 10.1002/adfm.201805290.
- [181] S. Tibbitts, “4D Printing: Multi-Material Shape Change,” *Archit. Des.*, vol. 84, no. 1, pp. 116–121, 2014, doi: 10.1002/ad.1710.
- [182] F. Momeni, S. M. Mehdi Hassani, N. X. Liu, and J. Ni, “A review of 4D printing,” *Mater. Des.*, vol. 122, pp. 42–79, May 2017, doi: 10.1016/j.matdes.2017.02.068.
- [183] M. Salerno, K. Zhang, A. Menciassi, and J. S. Dai, “A Novel 4-DOF Origami Grasper With an SMA-Actuation System for Minimally Invasive Surgery,” *IEEE Trans. Robot.*, vol. 32, no. 3, pp. 484–498, Jun. 2016, doi: 10.1109/TRO.2016.2539373.
- [184] K. Zhang, C. Qiu, and J. S. Dai, “An Extensible Continuum Robot With Integrated Origami Parallel Modules,” *J. Mech. Robot.*, vol. 8, no. 3, Mar. 2016, doi: 10.1115/1.4031808.
- [185] C. Qiu, K. Zhang, and J. S. Dai, “Repelling-Screw Based Force Analysis of Origami Mechanisms,” *J. Mech. Robot.*, vol. 8, no. 3, Mar. 2016, doi: 10.1115/1.4031458.
- [186] B. An *et al.*, “An end-to-end approach to making self-folded 3D surface shapes by uniform heating,” in *2014 IEEE International Conference on Robotics and Automation (ICRA)*, May 2014, pp. 1466–1473. doi: 10.1109/ICRA.2014.6907045.
- [187] J.-H. Na *et al.*, “Programming Reversibly Self-Folding Origami with Micropatterned Photo-Crosslinkable Polymer Trilayers,” *Adv. Mater.*, vol. 27, no. 1, pp. 79–85, 2015, doi: 10.1002/adma.201403510.
- [188] J. Rogers, Y. Huang, O. G. Schmidt, and D. H. Gracias, “Origami MEMS and NEMS,” *MRS Bull.*, vol. 41, no. 2, pp. 123–129, Feb. 2016, doi: 10.1557/mrs.2016.2.
- [189] Y. Liu, J. K. Boyles, J. Genzer, and M. D. Dickey, “Self-folding of polymer sheets using local light absorption,” *Soft Matter*, vol. 8, no. 6, pp. 1764–1769, Jan. 2012, doi: 10.1039/C1SM06564E.
- [190] S. Pandey, M. Ewing, A. Kunas, N. Nguyen, D. H. Gracias, and G. Menon, “Algorithmic design of self-folding polyhedra,” *Proc. Natl. Acad. Sci.*, vol. 108, no. 50, pp. 19885–19890, Dec. 2011.
- [191] B. An, N. Benbernou, E. D. Demaine, and D. Rus, “Planning to fold multiple objects from a single self-folding sheet,” *Robotica*, vol. 29, no. 1, pp. 87–102, Jan. 2011, doi: 10.1017/S0263574710000731.
- [192] S. Miyashita, C. D. Onal, and D. Rus, “Multi-crease Self-folding by Global Heating,” *Artif. Life*, vol. 21, no. 4, pp. 398–411, Nov. 2015, doi: 10.1162/ARTL\_a\_00183.
- [193] S. M. Felton, M. T. Tolley, C. D. Onal, D. Rus, and R. J. Wood, “Robot self-assembly by folding: A printed inchworm robot,” in *2013 IEEE International Conference on Robotics and Automation*, May 2013, pp. 277–282. doi: 10.1109/ICRA.2013.6630588.
- [194] S. Miyashita, S. Guitron, M. Ludersdorfer, C. R. Sung, and D. Rus, “An untethered miniature origami robot that self-folds, walks, swims, and degrades,” in *2015 IEEE International Conference on Robotics and Automation (ICRA)*, May 2015, pp. 1490–1496. doi: 10.1109/ICRA.2015.7139386.
- [195] “DigitalCommons@USU - Small Satellite Conference: CubeSat: The Development and Launch Support Infrastructure for Eighteen Different Satellite Customers on One Launch.” <https://digitalcommons.usu.edu/smallsat/2001/All2001/59/> (accessed Jun. 17, 2021).
- [196] M. Johnson, “The Emerging Commercial Marketplace in Low-Earth Orbit,” NASA, Feb. 27, 2019. [http://www.nasa.gov/mission\\_pages/station/research/news/b4h-3rd/ev-emerging-commercial-market-in-leo](http://www.nasa.gov/mission_pages/station/research/news/b4h-3rd/ev-emerging-commercial-market-in-leo) (accessed Jun. 17, 2021).
- [197] “Space Economy: The New Global Space Age | Morgan Stanley.” <https://www.morganstanley.com/Themes/global-space-economy> (accessed Jun. 17, 2021).
- [198] M. Sheetz, “An investor’s guide to space, Wall Street’s next trillion-dollar industry,” *CNBC*, Nov. 09, 2019. <https://www.cnbc.com/2019/11/09/how-to-invest-in-space-companies-complete-guide-to-rockets-satellites-and-more.html> (accessed Jun. 17, 2021).

- [199] A. Poghosyan and A. Golkar, "CubeSat evolution: Analyzing CubeSat capabilities for conducting science missions," *Prog. Aerosp. Sci.*, vol. 88, pp. 59–83, Jan. 2017, doi: 10.1016/j.paerosci.2016.11.002.
- [200] R. Nugent, R. Munakata, A. Chin, R. Coelho, and P. Puig-suari, "CubeSat: The Pico-Satellite Standard for Research and Education," Sep. 2008, doi: 10.2514/6.2008-7734.
- [201] "CubeSat 101: Basic Concepts and Processes for First-Time CubeSat Developers," p. 96.
- [202] E. Mostacciuolo, L. Iannelli, S. Sagnelli, F. Vasca, R. Luisi, and V. Stanzione, "Modeling and power management of a LEO small satellite electrical power system," in *2018 European Control Conference (ECC)*, Jun. 2018, pp. 2738–2743. doi: 10.23919/ECC.2018.8550095.
- [203] S. Sanchez-Sanjuan, J. Gonzalez-Llorente, and R. Hurtado-Velasco, "Comparison of the Incident Solar Energy and Battery Storage in a 3U CubeSat Satellite for Different Orientation Scenarios," *J. Aerosp. Technol. Manag.*, vol. 8, pp. 91–102, Mar. 2016, doi: 10.5028/jatm.v8i1.531.
- [204] F. Santoni, F. Piergentili, S. Donati, M. Perelli, A. Negri, and M. Marino, "An innovative deployable solar panel system for Cubesats," *Acta Astronaut.*, vol. 95, pp. 210–217, Feb. 2014, doi: 10.1016/j.actaastro.2013.11.011.
- [205] P. Senatore, A. Klesh, T. H. Zurbuchen, D. McKague, and J. Cutler, "Concept, Design, and Prototyping of XSAS: A High Power Extendable Solar Array for CubeSat Applications," p. 14.
- [206] "Conceptual design and finite element method validation of a new type of self-locking hinge for deployable CubeSat solar panels - Arturo Solís-Santomé, Guillermo Urriolagoitia-Sosa, Beatriz Romero-Ángeles, Christopher Rene Torres-San Miguel, Jorge J Hernández-Gómez, Isaac Medina-Sánchez, Carlos Couder-Castañeda, Jesús Irán Grageda-Arellano, Guillermo Urriolagoitia-Calderón, 2019." <https://journals.sagepub.com/doi/full/10.1177/1687814018823116> (accessed Jun. 17, 2021).
- [207] Ö. Soykasap, "Analysis of tape spring hinges," *Int. J. Mech. Sci.*, vol. 49, no. 7, pp. 853–860, Sep. 2007, doi: 10.1016/j.ijmecsci.2006.11.013.
- [208] E. Ziade, C. S. Patmont, and T. A. Fritz, "Design and Characterization of a Spring Steel Hinge for Deployable CubeSat Structures," p. 12.
- [209] J. Sicre, D. Givois, and A. Emerit, "APPLICATION OF 'MAEVA' HINGE TO MYRIADE MICRO-SATELLITES DEPLOYMENTS NEEDS," p. 8.
- [210] K.-W. Kim and Y. Park, "Systematic design of tape spring hinges for solar array by optimization method considering deployment performances," *Aerosp. Sci. Technol.*, vol. 46, pp. 124–136, Oct. 2015, doi: 10.1016/j.ast.2015.06.013.
- [211] J. W. Jeong, Y. I. Yoo, J. J. Lee, J. H. Lim, and K. W. Kim, "Development of a Tape Spring Hinge with a SMA Latch for a Satellite Solar Array Deployment Using the Independence Axiom," *IERI Procedia*, vol. 1, pp. 225–231, Jan. 2012, doi: 10.1016/j.ieri.2012.06.035.
- [212] J. W. Jeong, Y. I. Yoo, D. K. Shin, J. H. Lim, K. W. Kim, and J. J. Lee, "A novel tape spring hinge mechanism for quasi-static deployment of a satellite deployable using shape memory alloy," *Rev. Sci. Instrum.*, vol. 85, no. 2, p. 025001, Feb. 2014, doi: 10.1063/1.4862470.
- [213] Y. Liu, H. Du, L. Liu, and J. Leng, "Shape memory polymers and their composites in aerospace applications: a review," *Smart Mater. Struct.*, vol. 23, no. 2, p. 023001, Jan. 2014, doi: 10.1088/0964-1726/23/2/023001.
- [214] F. Santoni, F. Piergentili, G. P. Candini, M. Perelli, A. Negri, and M. Marino, "An orientable solar panel system for nanospacecraft," *Acta Astronaut.*, vol. 101, pp. 120–128, Aug. 2014, doi: 10.1016/j.actaastro.2014.04.020.
- [215] "Towards the use of diamond-like carbon solid lubricant coatings in vacuum and space environments - J Fontaine, 2008." <https://journals.sagepub.com/doi/abs/10.1243/13506501JET323> (accessed Jun. 17, 2021).

## References

---

- [216] A. Mitchell, U. Lafont, M. Hołyńska, and C. Semprimoschnig, “Additive manufacturing — A review of 4D printing and future applications,” *Addit. Manuf.*, vol. 24, pp. 606–626, Dec. 2018, doi: 10.1016/j.addma.2018.10.038.
- [217] M. Boncheva and G. M. Whitesides, “Making Things by Self-Assembly,” *MRS Bull.*, vol. 30, no. 10, pp. 736–742, Oct. 2005, doi: 10.1557/mrs2005.208.
- [218] X. Yao, H. Zhang, C. Lemckert, A. Brook, and P. Schouten, “Evaporation Reduction by Suspended and Floating Covers: Overview, Modelling and Efficiency,” *Urban Water Secur. Res. Alliance Tech. Aust.*, Jan. 2010.
- [219] M. Benzaghta and T. Mohamad, “Evaporation from reservoir and reduction methods: An overview and assessment study,” May 2009.
- [220] E. Haghighi, K. Madani, and A. Y. Hoekstra, “The water footprint of water conservation using shade balls in California,” *Nat. Sustain.*, vol. 1, no. 7, Art. no. 7, Jul. 2018, doi: 10.1038/s41893-018-0092-2.
- [221] A. Sahu, N. Yadav, and K. Sudhakar, “Floating photovoltaic power plant: A review,” *Renew. Sustain. Energy Rev.*, vol. 66, pp. 815–824, Dec. 2016, doi: 10.1016/j.rser.2016.08.051.
- [222] R. Cazzaniga, M. Cicu, M. Rosa-Clot, P. Rosa-Clot, G. M. Tina, and C. Ventura, “Floating photovoltaic plants: Performance analysis and design solutions,” *Renew. Sustain. Energy Rev.*, vol. 81, pp. 1730–1741, Jan. 2018, doi: 10.1016/j.rser.2017.05.269.
- [223] M. Perez, R. Perez, C. R. Ferguson, and J. Schlemmer, “Deploying effectively dispatchable PV on reservoirs: Comparing floating PV to other renewable technologies,” *Sol. Energy*, vol. 174, pp. 837–847, Nov. 2018, doi: 10.1016/j.solener.2018.08.088.



# Curriculum Vitae

## Jian-Lin Huang

**Address:** EPFL STI IGM RRL, MED 12313, Station 9, CH-1015 Lausanne, Switzerland

**Mobile:** +41 78 828 5970

**Email:** jian-lin.huang@epfl.ch

---

### Education

---

**Ph.D. candidate in Microsystems and Microelectronics** **2015-Present**

École Polytechnique Fédérale de Lausanne (EPFL), Lausanne, Switzerland

**Master of Science, Mechanical Engineering** **2008-2010**

National Taiwan University, Taipei, Taiwan

- Dissertation "Carbon nanocoils based thermal sensor and its applications"

**Bachelor of Science, Mechanical Engineering** **2004-2008**

National Chung-Chen University, Chiayi, Taiwan

---

### Experience

---

**Doctoral Assistant** **2015-Present**

Reconfigurable Robotics Lab, EPFL, Lausanne, Switzerland

- Development of origami-based interactive platform for creates a bidirectional relationship between physical and virtual environments.
- Study and development of compact actuators and mechanisms which can be integratable with multi-DoF reconfigurable system as well as additive manufacturing process.
- Design and demonstration of multi-DoF actuated reconfigurable systems with customizable functionalities for robotics, space, and energy harvesting applications.

**Associate Engineer** **2011-2014**

Center for Measurement Standards, Industrial Technology Research Institute (ITRI), Hsinchu, Taiwan.

- Conducted the metrology research project in the fields of force, vacuum, and nanomaterials.
- Participated in inter-comparison projects with other National Metrology Institute
- Constructed measurement systems and provided measurement services for industry

**Tutor** **2012-2014**

Chuhsin Life Education Association (NPO), Hsin-Chu, Taiwan

**Corporal** **2010-2011**

The Republic of China Army

---

### Research Experiences

---

**Doctoral Assistant** **2015-Present**

Reconfigurable Robotics Lab, EPFL, Lausanne, Switzerland

Project: Interactive interfaces for controlling reconfigurable robots

- Designed an gesture-based interactive interface intuitively controlling a multiple-DoF robotic system
- Developed algorithms for integrating mechanical characteristics of sensors, actuators, and joints for robotic origami into an existing physics engine and the physics-based simulation.
- Explored the design space of Human-robot interaction using reconfigurable modular robotic system integrated with multiple I/O modalities.

**Project: Sustainable Design of 4D Printed Active Systems**

- Developed self-assembly 3DoF origami module that can be fabricated in fully 2D and self-folding to active functional structure by selective distributed actuations
- Parametric studies of the folding joints and materials were performed for further investigating and controlling the behavior of 3D printed active system.
- Studied the compliance and performance of the origami module with different configuration of functional components and activation strategies

**Project: Harvesting solar energy and avoiding evaporation from water reservoirs by Reconfigurable Power Modules**

- Developed a modular floating photovoltaic power system, which is able to self-reconfigure its overall geometry forming a 2D surface in order to adapt to the reservoirs with different shapes and sizes

**Project Leader**

**2013-2014**

Center for Measurement Standards, Industrial Technology Research Institute, Hsinchu

**Project: Sub-picogram mass measurement**

- Conducted and managed the research project
- Designed the structure of high-Q micro-mechanical oscillator
- Designed MEMS process (cooperated with National Tsing Hua University, Taiwan)

**Associate engineer**

**2012-2013**

Center for Measurement Standards, Industrial Technology Research Institute, Hsinchu, Taiwan

**Project: Tactile Shear force sensing technology for robotic applications**

- Designed the fabrication process of tactile sensor with the application range 0 to 3 N, and a resolution of smaller than 5mN.
- Developed the program for sensor operation and sensor characterization system which consist of laser interferometers, force gauges, and precision motorized stage.

**Student assistant**

**2009-2010**

National Taiwan University, Taipei

**Project: Synthesis of Carbon Nanocoil and Development of Carbon Nanocoil Devices**

- Refined the synthesis process of carbon nanocoils to fit the dimensional requirements of electromagnetic wave absorber.
- Analyzed microwave absorption properties of single carbon nanocoil and nanocoils/ polymer composites.

## Teaching

---

**Teaching assistant for Master's-level graduate course:**

**2020**

**Mechanical product design and development**

Assisted the student to design and prototype with focus on wearable and assistive technology

**Teaching assistant for undergraduate course: Mechanical Engineering Principles**

**2015-2020**

Assisted the students to go through exercises session and define the design criteria, possible solutions and detailed CAD design for a mechanical design project

**Coach for STI Interdisciplinary Robot Competition**

**2017**

Assisted the students to build an autonomous robot that can collect bottles in a semi-structured environment with different terrains and obstacles

## Skills

---

- Mechanical design
- FEM modeling: ANSYS, COMSOL
- Metrology: Multi-scale force measurement
- CAD: Solidwork, AutoCad
- Microfabrication
- Manufacturing: Laser machining, 3D printing, CNC machining
- Programming: C/C++, C#, Python, Matlab, VBA, LabView

## Publications

---

- Oleg Testoni, Thomas Lumpe, Jian-Lin Huang, Marius Wagner, Sampada Bodkhe, Zhenishbek Zhakypov, Ralph Spolenak, Jamie Paik, Paolo Ermanni, Luis Muñoz, and Kristina Shea 'A 4D printed active compliant hinge for space using shape memory alloys and polymers' Smart materials and structures, 2021
- Hongying Zhang, Huijuan Feng, Jian-Lin Huang, and Jamie Paik 'Generalized modeling of origami folding joints' Extreme Mechanics Letters, 2021
- Harshal Sonar, Jian-Lin Huang, and Jamie Paik, 'Soft touch using soft pneumatic actuator (SPA)-skin as a wearable haptic feedback device' Advanced Intelligent systems, 2021
- Marius Wagner, Jian-Lin Huang, Philipp Okle, Jamie Paik, Ralph Spolenak 'Hinges for Origami-Inspired Structures by Multi-Material Additive Manufacturing' Materials and Design, 2020.
- Jian-Lin Huang, Zhenishbek Zhakypov, Harshal Arun Sonar, Jamie Paik 'A reconfigurable interactive interface for controlling robotic origami in virtual environments' The International Journal of Robotics Research, 2018
- Zhenishbek Zhakypov, Jian-Lin Huang, Jamie Paik 'A Novel Torsional Shape Memory Alloy Actuator: Modeling, Characterization, and Control' IEEE Robotics & Automation Magazine, 2016
- Sheng-Jui Chen, Gwo-Jen Wu, Chung-Lin Wu, Jian-Lin Huang 'Capacitive shear force sensor and method for fabricating thereof' US Patent 9,347,838B2, 2016
- Chih-Chung Su, Jian-Lin Huang, and Shuo-Hung Chang 'Fabrication of aligned carbon nanocoil thermal sensor with a high temperature coefficient of electrical resistance at 25 to 100 °C' IEEE Transactions on Nanotechnology, 2015
- Jian-Lin Huang, Sheng-Jui Chen, Gwo-Jen Wu, Chung-Lin Wu and Sheau-Shi Pan 'A PCB based capacitive shear force sensor developed for robotic gripper application' Asia-Pacific Symposium on Measurement of Mass, Force and Torque, Taipei, Taiwan, 2013